TOXICOLOGICAL ASSESSMENT OF GRAPHENE BASED NANOMATERIALS IN CELL CULTURE MODELS

BY

MOHAMED A ELHANEID

A thesis submitted to the University of Birmingham
For the degree of
DOCTOR OF PHILOSOPHY

School of Pharmacy
The Institute of Clinical Sciences
College of Medical and Dental Sciences
University of Birmingham

September 2018

Abstract

Graphene oxide (GO) and reduced GO (r-GO) nanomaterials exhibit great potential for several biomedical applications. Of foremost importance is to determine any potential health hazards related to their exposure. In this research, we hypothesised that the different material properties evidenced by GO and r-GO would elicit different biological responses. The first objective of this work was to synthesize GO and r-GO and characterize their physiochemical properties. The second aim was to investigate whether the two-distinct surface chemistries of GO and r-GO influenced their biological effect. The potential toxicity of these nanomaterials was investigated using the normal lung fibroblast cell line MRC-5 and cancerous epithelial lung cell line A549. The cytotoxicity of graphene derivatives was concentration-, time- and cell- dependent and varied according to the material used. Thus, the surface chemistry of graphene plays a critical role in its biocompatibility. Non-cancerous cells had a higher sensitivity to GO cytotoxicity than cancer cells. r-GO was highly biocompatible to MRC-5 cells and for A549 cells had a minimal effect on cell viability. At 37 C°, GO and r-GO were moderately hemolytic at concentration of 125 μg/ml and highly hemolytic at concentration of 300 μg/ml. Exposure of cells to both graphene derivatives led to reactive oxygen species (ROS) generation, without genotoxicity. GO, but not r-GO, led to autophagy in both cell lines, possibly *via* inhibiting the PIP3-Akt/mTOR pathway. For both cell lines and at non-lethal concentrations, GO downregulated the expression of glycogen synthase kinase-3 (GSK-3β). GO was also found to dysregulate both Wnt/β-catenin and Akt cell signalling pathways which are vital for cellular function. The finding relating to cell signalling provide an insight to the safety of GO which is important to its use in cancer therapy.

Acknowledgments

First, I would like to thank my parents for their love and support throughout my life.

I am heartily grateful to my supervisors (Dr Hanene Ali-Boucetta, Dr Marie-Christine Jones, Dr Geoffrey Brown) whose encouragement, guidance and support in the initial towards the final level enabled me to build up an awareness from the subject.

I would like to express my gratitude to the Libyan ministry of higher education and scientific research for providing the financial support of this project.

Finally, to all my friends and lab colleagues, thank you for your understanding and encouragement in many moments of crisis.

Table of Contents

List of Figures

List of tables

List of abbreviations

0D	Zero-dimensional
1D	One-dimensional
2D	Two-dimensional
3D	Three-dimensional
^{66}Ga	Gallium 66
A2780	Ovarian cancer cell line
A549	Human lung adenocarcinoma
AFM	Atomic Force Microscopy
ANOVA	Analysis of variance
APC	Adenomatosis polypsis coli
BSA	Bovine serum albumin
C/O	Carbon to oxygen atomic ratio
C_{60}	Fullerene
CRL-2522	Human skin fibroblast cells
DLS	Dynamic light scattering
DMSO	Dimethyl sulphoxide
EDTA	Ethylene-diamine-tetraacetic acid
EMEM	Eagle's minimum essential medium
FE1	Lung epithelial cell line
Fe_3O_4	Magnetite (iron oxide)
FRET	Fluorescence resonance energy transfer
FTIR	Fourier-transform infrared spectroscopy
Fz	Frizzled receptor
GBNs	Graphene-Based Nanomaterials
GO	Graphene oxide
GPCR	G protein coupled receptor
GSH	Reduced glutathione
GSK-3β	Glycogen synthase kinase-3
GSSG	Oxidised glutathione
H_2O_2	Hydrogen peroxide
H_2SO_4	Sulfuric acid
H9c2	Rat myocardial cell line
HA	Hydroxyapatite
HaCaT	Human skin keratinocytes
HCT116	Human colon cancer cells
Hela	Cervical cancer cells
HepG2	Human hepatoma cell line
HLF	Human lung fibroblast
HLF	human lung fibroblast
HMDMS	Human monocyte derived macrophages
HSP27	Heat shock protein 27
hTCEpi	Human corneal epithelial cell line
HUVEC	Human umbilical vein endothelial cells
IR	Infrared
IV	Intravenous injection
J774A.1	Mouse macrophage cell line
KBr	Potassium bromide
$KMnO_4$	Potassium permanganate

LC3	Light chain 3
MCF7	Breast cancer cell line
MDA-MB-231	Human breast cancer cells
m-LDH	Modified-lactate dehydrogenase
MRC-5	Foetal lung fibroblast cells
MRI	Magnetic resonance imaging
MSCs	Mesenchymal stem cells
mTOR	The mammalian target of rapamycin kinase
MWNT	Multi-walled nanotube
Na_3VO_4	Sodium orthovanadate
NAC	N-acetylcysteine
NaCl	Sodium chloride
NaN_3	Sodium azide
$NaNO_3$	Sodium nitrate
NIR	Near infrared regions
PARP	Poly (ADP-ribose) polymerase
PC12	Human neural cells
PDK1	3-phosphoinositide-dependent protein kinase-1
PEG	Poly ethylene glycol
PEG-GO	PEGylated graphene oxide
PEG-r-GO	PEGylated reduced graphene oxide
PI	Propidium iodide
PI3K- III	Phosphoinositide-3 kinase III
PIP3	Phosphatidylinositol triphosphates
PLGA	Poly lactic glycolic acid
PMSF	Phenylmethylsulfonyl fluoride
PTEN	Tumour suppressor phosphatase and tension homolog
PTT	Photothermal therapy
RAW 264.7	Murine macrophages
RBCs	Red blood cells
RBL	Rat basophilic leukaemia mast cells
r-GO	Reduced graphene oxide
RPE	Human-retinal pigment epithelium
RTK	Tyrosine kinase receptor
SD	Standard deviation
SEM	Standard error of mean
SKBR3	Breast cancer cells
SPIONs	Iron oxide particles
SQSTM1	Sequestosome 1
SWNT	Single-walled nanotube
TBHP	Tert-butyl hydroperoxide
TEM	Transmission Electron Microscopy
TEMED	Tetra-methyl-ethylene-diamine
TGA	Thermal gravimetric analysis
U87 and U118	Glioma cells
U87MG	Human glioblastoma cells
UV-Vis	Ultraviolet-Visible
XPS	X-ray photoelectron spectroscopy

Chapter 1

Introduction

1.1 Background

Nanoscience is a specific branch of material science that is interested in the behaviour and applications of materials in the nanoscale and spans across multiple disciplines including physic, chemistry, engineering and biomedical sciences. The interest in engineered nanomaterials is largely due to their small size (typically between 1-100 nm) and large surface area, both of which give nanoparticles distinguishable properties compared to the same bulk material (Klaessig et al., 2011, Gonsalves et al., 2007, Wang et al., 2009). A variety of materials have been used in the manufacture of nanoparticles, including, noble metals (e.g. gold and silver) (Jong and Borm, 2008), metal oxides (e.g. iron oxide, titanium dioxide, zinc oxide) (Huang et al., 2011), carbon derivatives (e.g. carbon nanotubes) (Lacerda et al., 2006), polymers (e.g. poly-lactic acid) (Rancan et al., 2009) and lipids (e.g. liposomes) (Daraee et al., 2016).

Depending on the material used, nanomaterials can be broadly classified as 'hard' or 'soft' (Sangtani et al., 2017). In general, hard nanomaterials, including metallic and carbon-based nanomaterials, are generated by physical, chemical and biological synthesis methods while soft, organic nanoparticles, such as lipid-based nanoparticles, often result from self-assembly/precipitation of the raw components in aqueous media (Das et al., 2017, Patil and Jadhav, 2014, Jones et al., 2006, Stout et al., 2013). Other than the method of production, hard nanomaterials often possess extraordinary structural, mechanical, electrical, thermal and optical properties that make them suitable for a wider range of applications, including in electronics, energy, optics, and biomedical applications (Jana et al., 2017, Guo et al., 2017, Molina et al., 2016, Kim et al., 2016).

Nowadays, engineered nanomaterials can be found in over 1800 consumer products (Vance et al., 2015) and, while interest in nanoscience shows no sign of slowing down, exposure and wide spread use of nanoparticles is becoming a concern, especially as the consequences

of long term exposure, both for humans and the environment, are unknown. These concerns have led to the rise of nanotoxicology as a specialised area of research in nanoscience (Donaldson et al., 2004). So far, most nanotoxicology studies have been performed to understand how environmental and occupational exposure to nanomaterials can affect human health and have focused mostly on hard nanomaterials. Despite this research effort, clear gaps remain in our understanding of the toxicity and fate of nanomaterials. Moreover, the lack of a standardised, definitive regulatory framework for nanoparticle-specific data on toxicity and environmental fate makes undertaking a full risk assessment even more difficult (White and Xing, 2016).

This absence of a clear understanding of the parameters that affect nanotoxicity can be particularly problematic due to the increasing number of nanomaterials being investigated for therapeutic/diagnostic applications (Ai et al., 2011, Yildirimer et al., 2011, Yang et al., 2017b) and cancer treatment in particular (Etheridge et al., 2013). Indeed, nanoparticles have shown remarkable promises to tackle cancer cells more specifically and effectively, and to minimise adverse side effects that are associated with the free drug (Chen et al., 2015c). However, these benefits must be weighed against potential toxicity and the risk that the nanoparticles themselves may be carcinogenic through disruption of cell function or genotoxicity (Wang et al., 2015b). Therefore, testing the toxicology of nanomaterials, in the context of biomedical applications, must aim to identify undesirable effects and facilitate their safe design. This concept known as ‘safe by design’ has become critically important in the risk assessment of nanomedicines (Accomasso et al., 2018, Fadeel, 2013).

The toxicity of nanoparticles is greatly controlled by their physicochemical properties including size, size distribution, particle shape, agglomeration, chemical composition, and surface area and chemistry (Oberdorster et al., 2005, Dobrovolskaia and Mcneil, 2007, Naahidi et al., 2013). Therefore, these parameters must be thoroughly investigated in order

to ensure the safe and effective use of nanomedicines (Fadeel and Garcia-Bennett, 2010, Fadeel et al., 2015).

All new nanomedicine formulations must go through various developmental phases in order to gain approval for use in the clinic (**Figure 1**). Nanoparticles can be found at different stages of the pharmaceutical pipeline, some have been approved for clinical use while others are being investigated and advanced through the approval process (Hare et al., 2017).

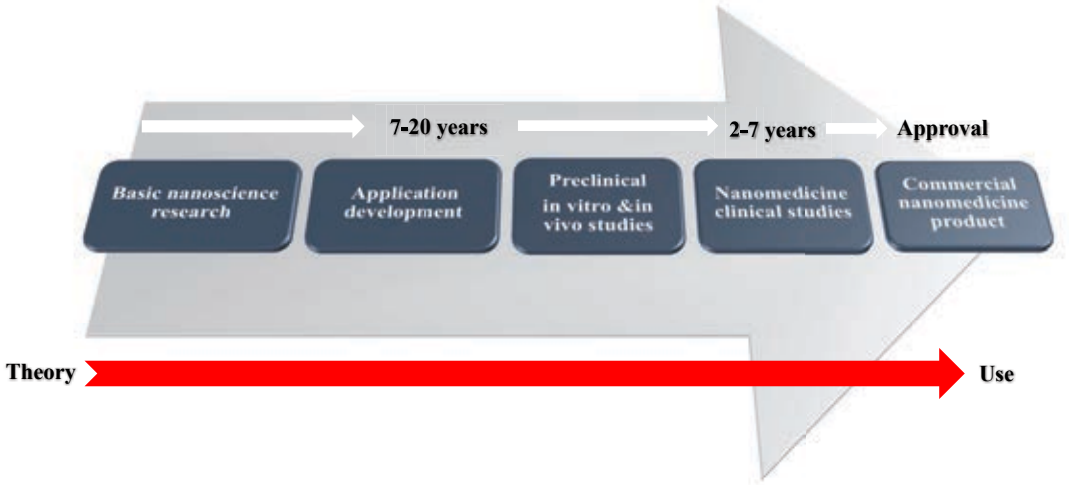

Figure 1. Nanomedicine technology development phases. All revolutionary nanomedicine technologies have to move through five developmental stages to get approval for the medical use. Adapted from (Etheridge et al., 2013).

Examples of hard material that have made it through to commercialisation include iron oxide particles (SPIONs). A number of SPIONs formulations have been suggested as magnetic resonance imaging (MRI) contrast agents (liver and reticulum endoplasmic system) (Taylor et al., 2012, Barrow et al., 2017). However, most agents have since been removed from the market due, in part, to side effects and poor efficacy (Wang, 2015). Others, like gold and silver colloids, have been used historically for medicinal purposes (e.g. anti-inflammatory (gold in rheumatoid arthritis) and antiseptic (silver) but have now been linked to safety concerns (Buzea et al., 2007). Indeed, cellular exposure to gold or silver nanoparticles appears to be associated with significant accumulation of reactive oxygen

species (ROS) leading to oxidative stress (Dos Santos et al., 2014, Alexander Gerber, 2013), although the exact mechanisms are still unknown. As the focus is shifting to newer bio-nanomaterials, such as carbon nanotubes and graphene derivatives (Bitounis et al., 2013, Chen et al., 2015a, Tonelli et al., 2015, Bhattacharya et al., 2016, Nasir et al., 2018), a detailed investigation of their toxicity and behaviour in a physiological environment will be crucial to avoid similar pitfalls.

1.2 Carbon-based nanomaterials

Carbon is known to exist as two natural, but distinct crystalline allotropes namely graphite and diamonds (Ferrari and Robertson, 2000, Nasir et al., 2018). Allotropes arise from the formation of covalent carbon-carbon bonds and, although chemically identical, they possess strikingly different physical properties due to the spatial arrangement of carbon atoms (Dai et al., 2012, Pang et al., 2015, Bitounis et al., 2013). In recent years, new carbon-based nano-allotropes were discovered including fullerenes (Smalley, 1991), carbon nanotubes (Iijima, 2002), nano-diamonds (Mochalin et al., 2011) and graphene (Geim and Novoselov, 2007), which together opened a new era in nanotechnology.

Fullerenes are entirely built up of carbon atoms in a form of a zero-dimensional (0D) hollow sphere or one-dimensional (1D) tube. The 0D fullerenes consist of sp^2 carbon with different sizes (C_{60}, C_{70} etc.), the C_{60} consists of 60 carbon atoms and it is considered the most abundant as-synthesized composition (Kroto et al., 1985, Smalley, 1991). Nano-diamonds are composed of sp^2 carbon on the surface and the core is built up by sp^3 carbon atoms (typically < 10 nm) (Mochalin et al., 2011). Tubular or cylindrical fullerenes are referred to as carbon nanotubes (Smalley, 1991). Carbon nanotubes are divided in two categories, single-walled nanotube (SWNT) and multi-walled nanotube (MWNT). The former is made of a rolled up single graphene sheet while multi-walled nanotube consists of several rolled-up concentric graphene sheets (Iijima, 2002) (**Figure 2**).

Graphene or graphene sheet represents the isolated two-dimensional (2D) single layer of graphite which itself is a three-dimensional structure (3D) formed by the stacking of multiple, one carbon-atom thick layers. For a long time, the existence of single graphene sheets was seen as theoretically possible, but their isolation was seen as physically impossible (Slonczewski and Weiss, 1958). However, in 2004, Novoselov and Geim were able to isolate and characterise a graphene sheet at University of Manchester (Novoselov et al., 2004) and won the Nobel award in Physics in 2010 for their innovative work on this material (The 2010 Nobel Prize in Physics) . This novel 2D one-atom thick sheet consist of a hexagonally- arranged, sp^2 –bonded carbon atoms with a large surface area on both sides of the planer axis (Novoselov et al., 2004).

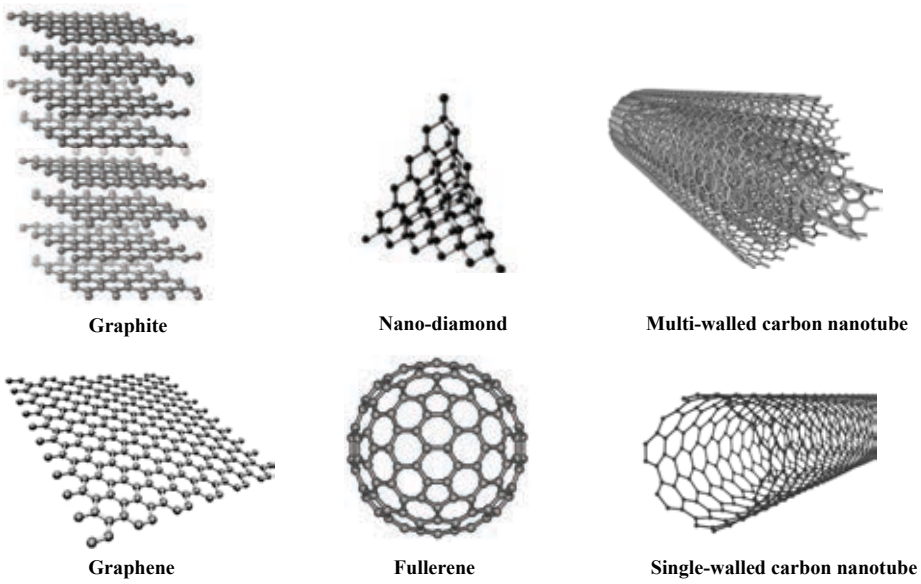

Figure 2. Schematic representation of carbon-based allotrope. Graphene is 2D nanostructure build up by a hexagonally arranged sp^2 –bonded carbon atoms and considered the parent of most of allotropic forms of carbon including graphite, nanotubes and fullerene. Adapted from (Tripathi et al., 2015)

Most of the carbon nano-allotropes listed above have been investigated for biomedical applications due to their extraordinary properties (Chen et al., 2015a, Tonelli et al., 2015, Bhattacharya et al., 2016, Nasir et al., 2018). These studies provided some preliminary

information about the toxicity of carbon nano-allotropes. While pristine fullerenes and their derivatives are still facing some safety concerns in regards to their bio-distribution and toxico-kinetic profiles (Hendrickson et al., 2014), the understanding of the toxicity of carbon nanotubes has vastly improved. Indeed, carbon nanotubes were initially shown to have similar carcinogenic potential as asbestos fibres (Poland et al., 2008). Later, it was revealed that pristine MWNTs with a length of more than 20 μm were responsible for granuloma formation, as a result of the inability of macrophages to digest the long fibres from the mesothelium (Kostarelos, 2008). A similar phenomenon was observed for hydrophobically-modified MWNTs, despite having a slightly smaller size (5-15 μm) (Ali-Boucetta et al., 2013c). In contrast, adding triethylene glycol to the surface has improved biocompatibility and prevented the inflammatory response (Ali-Boucetta et al., 2013c). In this case, MWNTs not only presented a more hydrophilic surface but were also shortened during the modification process (2-4 μm) (Ali-Boucetta et al., 2013c). *In vivo* toxicity of carbon nanotubes was related to their high aspect ratio, aggregations, length and manufacturing impurities (Lacerda et al., 2006, Muller et al., 2009). Of all the nano-allotropes, graphene nanomaterials particularly the oxidised derivatives may be the most promising, especially in nanomedicine, due to their inherently lower aspect ratio, and better dispersion in water compared to carbon nanotube (Bussy et al., 2013). This new class of carbon-based nanomaterials will be the focus of this study.

1.3 Graphene-based 2D-nanomaterials

A focus on graphene, for medical application, is attributed to its interesting properties such as mechanical strength and electronic capabilities coupled with high flexibility which render graphene a potential component of implants and bioelectronics devices (Reina et al., 2017, Kang et al., 2016). Furthermore, graphene has a tuneable surface chemistry which ease its functionalisation to form beneficial derivatives (Nanda et al., 2015).

Graphene exist in numerous forms; these forms belong to one family called Graphene-Based Nanomaterials (GBNs). GBNs include single sheet graphene, few layer graphene (2-10 sheets), ultrafine graphite (consist of more than 10 sheets being less than100 nm in thickness), graphene dots, graphene ribbons, graphene oxide (GO) and reduced graphene oxide (r-GO) sheets (Bianco, 2013, Wick et al., 2014).

Wick and colleagues considered three essential properties in the nomenclature of GBNs: the number of graphene layers, the average lateral size, and the carbon to oxygen atomic ratio (C/O). The number of layers was considered to define the thickness, the surface area, and the bending elasticity, while the lateral size determines the maximum size and degree of deformability of the material (Wick et al., 2014). The aforementioned characteristics of GBNs can influence their interactions with biological system such as cellular uptake and transport through biological barriers (Sanchez et al., 2012, Yue et al., 2012, Russier et al., 2013, Wick et al., 2014).

As the members of GBNs have different surface chemistry, it was important to include the C/O ratio for the classification of graphene materials (Wick et al., 2014). For example, pristine graphene has a hydrophobic surface while the surface of GO consists of hydrophobic moieties and hydrophilic clusters (Ali-Boucetta et al., 2013a, Jasim et al., 2016). GO could be considered as a graphene derivative with an extremely large number of oxygen functional groups. The C/O ratio of GO is usually in the range of 4:2 to 2:1, and for the r-GO is 12:1. Therefore, r-GO is hydrophobic and tends to form agglomerates in water while GO disperses well in water (Bianco, 2013, Wick et al., 2014, Gao et al., 2010). This wide variability of surface oxygen content can affect dispersion in water, colloidal stability and biocompatibility (Bitounis et al., 2013, Das et al., 2013, Sanchez et al., 2012, Mittal et al., 2016, Bianco, 2013).

The synthesis of graphene has developed very quickly and can be classified in two categories; top-down and bottom-up methods. The former synthesis methods are based on exfoliation of a layer of graphene from a graphitic material while bottom-up synthesis involves the building up of graphene using carbon materials (Kim et al., 2009, Zhu et al., 2012, Gurunathan and Kim, 2016). Top-down synthesis include electrochemical (Su et al., 2011) and mechanical exfoliation of graphite (Novoselov et al., 2004), ball milling (Leon et al., 2011), and unzipping of carbon nanotubes (Kosynkin et al., 2009) and the reduction of exfoliated graphite oxide (Pei and Cheng, 2012). The product of the latter method forms r-GO which has less oxygen atoms on its surface and mimics pristine graphene structure.

The morphology and dimensions of the obtained graphene *via* top-down methods are not uniform (Gurunathan and Kim, 2016). For this reason, this route is considered not appropriate for the synthesis of graphene-based bioelectronics devices due to the poor electronic properties of the obtained graphene (Reina et al., 2017), and would be unsuitable for biomedical applications as the morphology and dimensions of nanoparticles can have a big influence on biological interaction. On the other hand, bottom-up methods including chemical vapour deposition methods (Kim et al., 2009) are useful for the production of single or multiple layer graphene with a low number of defects which is suitable for the use in bioelectronics devices.

Graphene obtained by the aforementioned methods vary in morphologic and surface characteristics and some are associated with impurities. For this reason, further synthesis routes providing non-defective graphene and suitable for mass production are currently under scrutiny (Gurunathan and Kim, 2016, Reina et al., 2017).

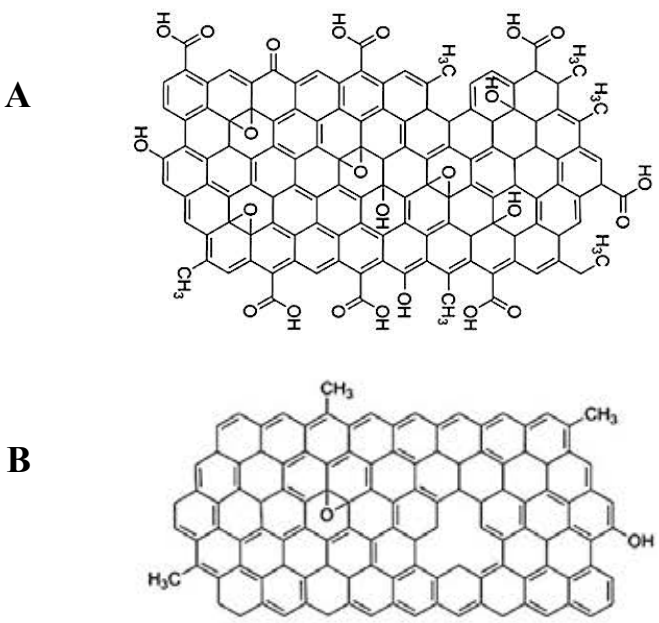

Figure 3. Graphical representation of GO and r-GO. **A**) GO sheet consisting of sp^2 or sp^3 hybridization, due to their derivatisation with epoxides, carbonyls and tertiary alcohol functional groups (Lerf-Klinowski model). **B**) r-GO sheet has similar structure of GO but with less oxygen containing functional groups. Adapted from (McCallion et al., 2016).

GO and r-GO are the most notable materials among GBNs. Both graphene derivatives have favourable physicochemical properties that make them promising candidates in nanomedicine applications and as starting building blocks for other GBNs (Gurunathan and Kim, 2016, Bitounis et al., 2013, Wick et al., 2014). To date, there is not a single and exact structure of GO as it can varies depending on the adapted protocols for its preparation, but surface characterisation can provide a rational idea of its structure (Bianco, 2013, Reina et al., 2017). The chemistry of GO sheet is commonly described by the Lerf-Klinowski model (Dreyer et al., 2010). GO can be distinguished by the existence of epoxy, tertiary hydroxyl, ketones and carboxylic acid groups on its surface (Szabo et al., 2006) (**Figure 3**). On the other hand, r-GO is the reduction product of GO, as a consequence r-GO surface has less oxygen functional groups than GO surface. Similar to GO, depending on the reduction method utilised to obtain r-GO, the structure and surface chemistry of the material can vary remarkably (Salas et al., 2010, Tiwari et al., 2012). GO sheets have shown to be more

hydrophilic than other carbon-based materials and hydrogen bonding between water molecules and their polar functional groups gives good colloidal dispersion under suitable pH conditions (Shen et al., 2012, Bitounis et al., 2013, Ali-Boucetta et al., 2013a). The enhanced dispersion in water, colloidal stability and the physicochemical advantages of GO materials render them one of the most important GBNs.

1.4 Biomedical application of GBNs

1.4.1 Bio-sensing and bio-imaging

Biosensors are generally made up of two major elements; a receptor and a transducer. The former provides the recognition sites (bioactive molecules) that interact with specific target while the transducer transforms the chemical information received into a detectable signal (Kang et al., 2016, Tiwari et al., 2016). Graphene has been used for bio-sensing applications as a transducer platform since it can be modified to allow attachment of the recognition sites. In particular, GO and r-GO are ideal graphene derivatives to be used in biosensors as they possess multiple sites for easy surface functionalisation with tuneable electric properties (Bitounis et al., 2013, Reina et al., 2017).

Current tools that are used to detect glucose are commonly based on the quantification of hydrogen peroxide (H_2O_2) formed through oxidation of glucose by the use of glucose oxidase (Zhou et al., 2015). The quantification of H_2O_2 is accomplished by electrochemical biosensors which are based on direct electron transfer between the sensing platform and target molecule (electroactive species). Liu and colleagues have deposited GO on carbon electrode and the amine groups of glucose oxidase were then covalently attached to the carboxyl acid groups of GO (Liu et al., 2010). The covalently linked GO-glucose oxidase enzyme electrode showed high sensitivity, indicating GO to be a highly efficient biosensor electrode. This high sensitivity is related to the high surface area and electron conductivity

of GBNs which are beneficial for electrode modification resulting in enhanced signal intensities (Kang et al., 2016) **(Figure 4)**.

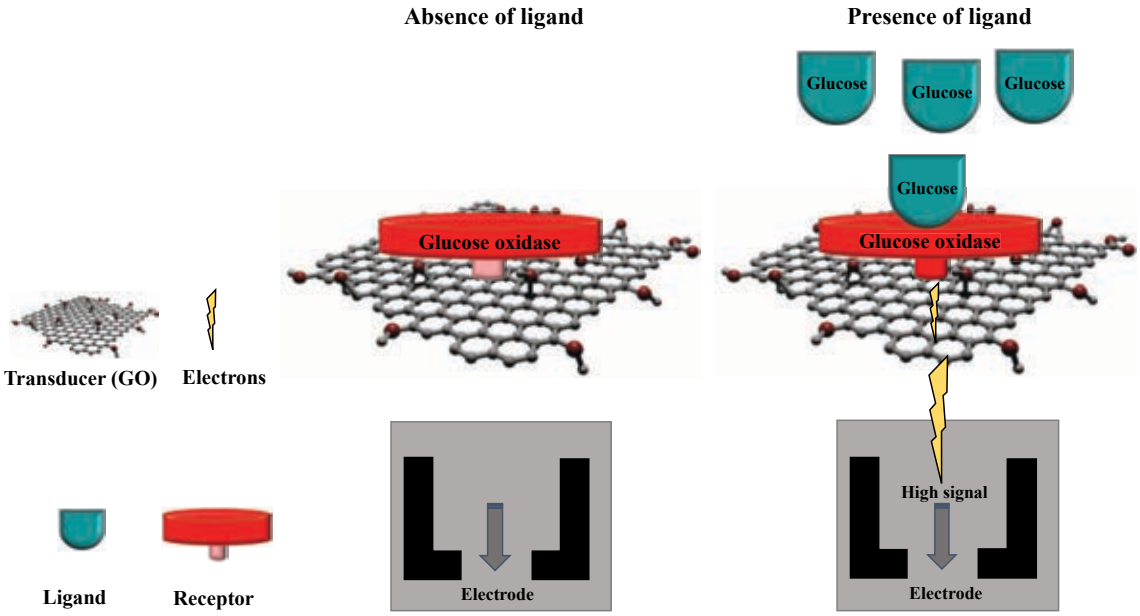

Figure 4. Schematic illustrations of GO-based glucose biosensor. The interaction of glucose molecules to the receptor molecules alters the electrical impedance and cyclic voltammetry readings of the electrode thus detecting the presence of the glucose molecules.

Several examples were reported in the literature using graphene-based electrodes for bio-sensing of glucose molecule where glucose oxidase was attached to graphene surface (Tiwari et al., 2016, Reina et al., 2017, Tadi et al., 2015). Also, graphene-based electrodes were applied to detect other small biomolecules released by living cells such as neurotransmitters and proteins which can be beneficial for diagnosis of neurological disorders and cancer (Cheemalapati et al., 2013, Shieh et al., 2015, Tiwari et al., 2016, Yáñez-Sedeño et al., 2017). The electrochemical graphene biosensors have also been employed for the detection of genetic materials (Graybill and Bailey, 2016, Ge et al., 2015, Reina et al., 2017).

In addition to the use of the electronic properties of graphene in bio-sensing, the excellent capability of graphene in fluorescence resonance energy transfer (FRET) render it an excellent quencher of excited state of dyes (Swathi and Sebastian, 2009, Bitounis et al.,

2013) (**Figure 5**). For instance, Chang and colleagues, reported high sensitivity to thrombin detection with high specificity in both buffer and blood serum using the graphene FRET strategy. GO was coated with dye-labelled bioactive molecules (recognition site for thrombin) through π–π stacking (Chang et al., 2010). The fluorescent signal of the dye was quenched due to the FRET effect with GO. However, once the thrombin molecule interacted with the dye-labelled recognition site, the latter dissociates from GO surface and the FRET effect is demolished enabling fluorescence signals to detectable levels (Chang et al., 2010). The graphene FRET strategy for bio-sensing has been applied to detect several enzymes, nucleic acids, proteins and cancer cells (Ge et al., 2015, Graybill and Bailey, 2016, Lee and Min, 2012). GBNs biosensors are proposed for *in situ* sensing implants, however, biocompatibility of these devices need to be thoroughly investigated (Dong and Qi, 2015, Reina et al., 2017).

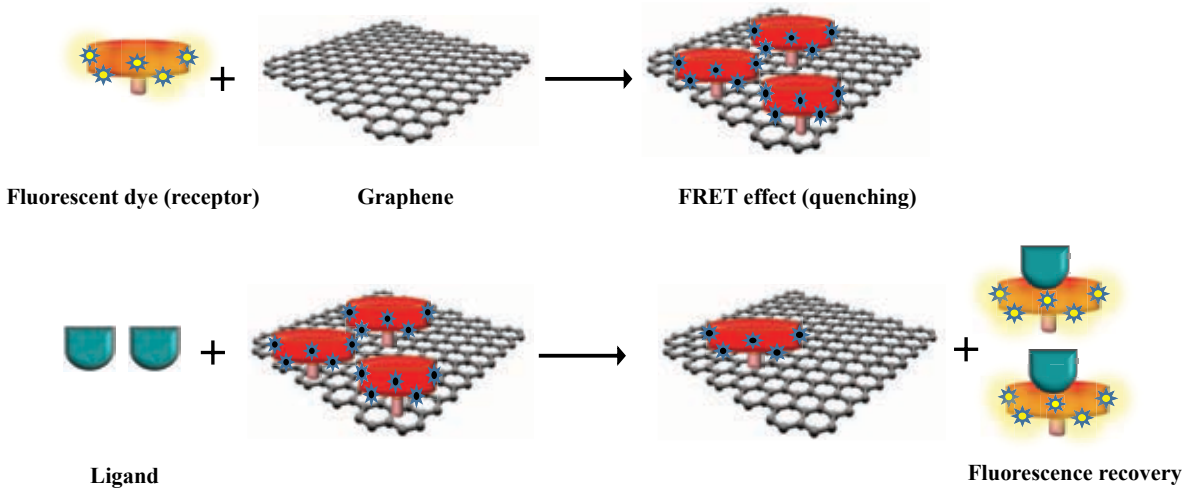

Figure 5. The fluorescence resonance energy transfer (FRET) strategy in graphene bio-sensing application. On interaction with a target molecule (ligand) complementary to the fluorescent dye receptor at graphene surface, strong complexation between the two occurs and as the newly formed complex desorbs from the graphene surface, the FRET effect is cancelled and fluorescence can be recovered.

In addition, GBNs have also been used as a tool for bio-imaging purposes (Lin et al., 2016). Similarly to carbon nanotubes, Raman vibrational signals exhibited by GBNs can be a useful tool to trace their pharmacokinetics *in vivo* (Liu et al., 2008a). Also, the ability to fluorescence in the visible and infrared regions can be applied in fluorescence imaging (Lee

et al., 2013, Welsher et al., 2009). For instance, PEGylated GO nanoparticles (GO coated with poly ethylene glycol) were intravenously injected into mice through the tail vein and their distribution and clearance from blood vessel were efficiently tracked by using a deep-penetrating two photon imaging techniques (Qian et al., 2012).

1.4.2 **Tissue engineering**

Tissue engineering applies biological materials to support and improve the functions of tissues or organs. Cells or tissues require a good substrate to proliferate, spread and function. GBNs have shown promise in the area of tissue engineering due to their mechanical properties which render them suitable for the structural reinforcement of medical scaffolds, such as biocompatible films and hydrogels (Gurunathan and Kim, 2016, Cheng et al., 2017). Although, carbon nanotube has similar mechanical properties as graphene and have been investigated as scaffold materials, they undergo structural collapse under cyclic strain which limited their applications (Abarrategi et al., 2008, Firkowska et al., 2006). Also, coating the scaffold's surface with graphene has been shown to improve the mechanical strength of carbon nanotubes. Hence, graphene becomes an attractive material for scaffolds engineering (Kim et al., 2012).

Mesenchymal stem cells (MSCs) are multipotent progenitor cells derived from bone marrow and have been investigated in tissue repair and cell therapies applications (da Silva Meirelles et al., 2006). The development of materials that can enhance MSC adhesion, proliferation and differentiation toward osteoblasts is of great interest in tissue engineering to induce healing and reconstruction of bone defects. Indeed, graphene and its derivatives have been found useful in bone tissue engineering applications (Gu et al., 2014, Singh, 2016, Fu et al., 2017, Dinescu et al., 2014). GBNs consist of many wrinkles and ripples (asymmetrical nanotopology) with a high surface area which might play a significant role in facilitating protein adsorption, cellular adhesion, proliferation and differentiation of

MSCs (Dong et al., 2010, Nayak et al., 2011, Kim et al., 2013). Also, Park and colleagues have reported that graphene substrate significantly increases cell attachment, neurite outgrowth and differentiation of human neural stem cells to neurons (Park et al., 2011). Furthermore, flexible and porous scaffolds composed of r-GO implanted in the injured rat spinal cord showed promising potential in neural regeneration (Elisa et al., 2015). A chitosan polyvinyl alcohol nano-fibrous scaffold was examined with and without graphene for wound healing. Findings from this study showed that graphene containing scaffold promoted fast wound healing compared to non-graphene scaffold (Lu et al., 2012). Li and colleagues have developed graphene foam scaffold loaded with MSCs to improve skin wound healing (Li et al., 2015). Graphene scaffold has facilitated biocompatible proliferation of different cell types, however additional extensive research is needed to understand the mechanisms of graphene-based scaffolds for tissue engineering. The mechanisms underlying the positive effect of GBNs on adhesion, proliferation and differentiation of cells are still under scrutiny. Additionally, there is the need to understand the possible risks from GBNs disintegrating from their scaffolds/films and being released into different body compartments.

1.4.3 **Drug delivery and Photo-thermal therapy in cancer**

The high surface area of GBNs offer high therapeutic molecule loading capacity and have been considered as potential carriers for drug delivery (McCallion et al., 2016, Zhang et al., 2017b). Among GBNs, GO nano-sheet has been investigated as a novel carrier for drug delivery due to its good dispersion in water and the existence of various surface functional groups (Bitounis et al., 2013). The versatile surface chemistry of GO facilitates conjugation with drugs, biomolecules, polymers and others (Reina et al., 2017). Also, the surface area of GO (≈ 2675 m^2/g) is higher than the surface area for the most of the available nanoparticles, providing a high drug loading capacity (Bussy et al., 2013, Kiew et al., 2016).

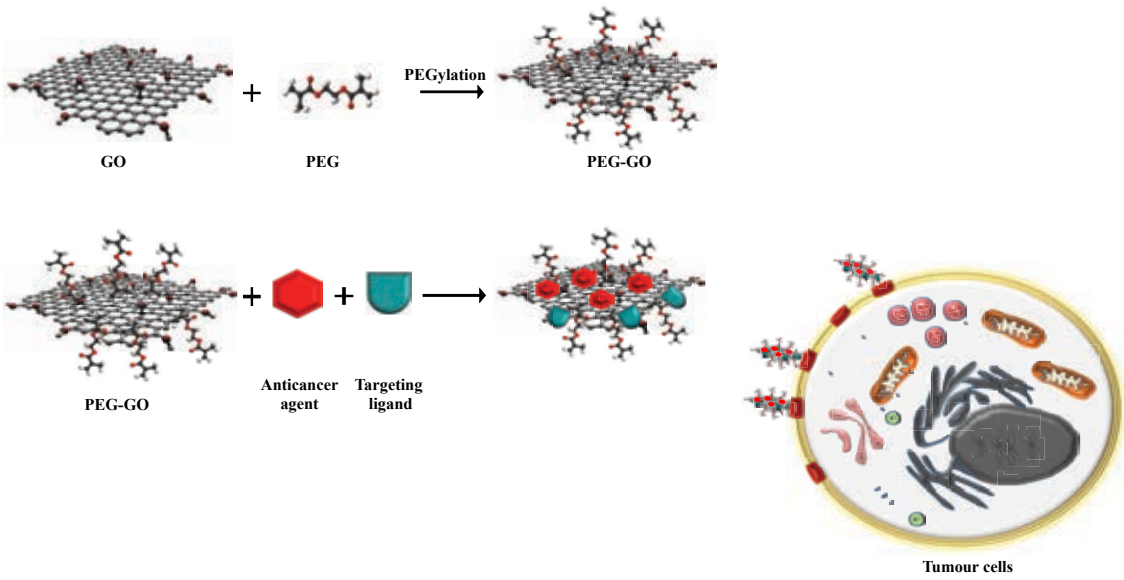

Figure 6. Schematic presentation of GO as platform for specific targeting drug delivery system. GO is PEGylated with poly ethylene glycol (PEG) to enhance its stability in biological solutions. PEG-GO conjugated with anticancer agent and specific targeting ligand via stable π–π stacking. Targeting ligand targets the drug delivery system against tumour cells overexpressed with its specific receptors.

Liu and colleagues were the first research group to use GO as a nano-carrier to load an anticancer drug *via* non-covalent van der Waals interaction (Liu et al., 2008b). In their work, GO nano-sheets (<50 nm) were conjugated with poly ethylene glycol (PEG) and then loaded with water-insoluble, an aromatic anticancer drug (SN38) *via* simple adsorption. After this study, other investigators modified this strategy by binding several aromatic molecules to graphene surface through stable π–π stacking. A specific interaction with particular tumour tissue type can be accomplished by incorporating targeting ligands that are recognised *via* receptors present at the surface of cancer cells (Song et al., 2011). Various tumour targeting ligands such as vitamins, proteins and antibodies, have been conjugated with graphene nano-sheet to achieve specific targeting (**Figure 6**) (Park et al., 2015b, Liu et al., 2013, Yang et al., 2016).

GBNs have also been investigated in photothermal therapy PTT due to their ability to absorb NIR and subsequent heat emission (Chen et al., 2016b). For example, Robinson and

colleagues have developed a new photothermal agent using r-GO coated with PEG as it has better stability in biological solutions than non-PEGylated r-GO. PEGylated r-GO (5-100 nm) was then conjugated with a Arg-Gly-Asp motif for selective cellular uptake and thermal ablation in human glioblastoma cells (U87MG). Upon irradiation, the PEG-r-GO showed high photothermal efficiency due to its high NIR absorbance (Robinson et al., 2011). Doxorubicin-loaded PEGylated-GO (GO-PEG-DOX) (100 nm) was developed by Zhang and colleagues to facilitate combined chemotherapy and PTT (Zhang et al., 2011). The GO-PEG-DOX treatment was investigated *in vivo* and induced complete destruction of the tumours without recurrence of tumours or weight loss, while doxorubicin chemotherapy alone or PEGylated-GO photothermal treatment did not (Zhang et al., 2011). This strategy can be more beneficial if a tumour-specific antibody is introduced onto the surface of GO-PEG-DOX complexes. Indeed, Lu and colleagues have developed magnetic PEGylated-GO doxorubicin complex (215.7 ± 18.4 nm) that combine co-precipitated Fe_3O_4 magnetic nanoparticles and CET (an EGFR antibody) for magnetic and receptor-mediated ligand-targeting of the CT-26 mouse colon carcinoma (Lu et al., 2018). This combined chemo-hyperthermia therapy with specific tumour targeting augmented the cytotoxicity in CT-26 *in vitro* and inhibited tumour recurrence *in vivo*. Overall, GBNs are very encouraging candidates as a drug delivery system and cancer therapy. Nonetheless, undesired effects induced by GBNs have also been reported, for instance hemolysis, platelet aggregation, serum protein adsorption, cytotoxicity and immunotoxicity (Luo et al., 2017b, Liao et al., 2011, Zhang et al., 2012a, Liu et al., 2018). Therefore, these toxicities need to be addressed to ensure safe design for biocompatible engineered nanoparticles.

1.5 Biocompatibility of GBNs

The increasing interest in the use of GBNs for biomedical applications provides a strong incentive for detailed investigation of their pharmacology and toxicity. These studies should

also consider the potential risk from occupational or environmental exposure as GBNs are produced on a larger scale. GBNs vary in structure and properties that can lead to completely different biological responses (Reina et al., 2017).

The first steps in exploring the safety profile of any new material often relies on the use of cell culture models as a critical part of safety and risk assessments (Stone et al., 2014, Nel et al., 2013). *In vitro* tests are useful to study cellular responses to nanoparticle exposure by identifying the key events that affect cell function. *In vitro* data also allow efficient screening and selection of subset of nanoparticles that can then be tested in *in vivo* studies using a limited number of mice (Kuempel et al., 2012, Stone et al., 2014). In this regard, the current body of literature relating to the *in vitro* toxicological evaluation of GBNs derivatives is considered essential as preliminary data. However, important differences in methodology and in the properties of the materials tested mean that definitive conclusions on the biocompatibility and toxicity of GBNs cannot be reached (Bussy et al., 2013, Bianco, 2013, Bitounis et al., 2013). Some studies have shown that graphene, GO and r-GO nanomaterials cause concentration- and time- dependent cytotoxicity while other studies revealed high biocompatibility at similar concentrations and times of exposure (**Table 1**)

Table 1. Different in vitro cytotoxicity studies with GBNs and their cellular effects.

Material	Size	Culture model	Tested concentrations	Cytotoxicity assays	Conclusions
Graphene	5-3 nm thick	Human neural cells (PC12)	0.01–100 µg/ml	MTT, LDH, ROS, Caspase 3/7 assays	Significant LDH release, increase in ROS and weak caspase-3 activation (Yongbin Zhang et al., 2010)
Carboxyl-graphene	349.5-4827.3 nm	Human hepatoma cell line (HepG2)	2-32 µg/ml	Alamar Blue assay, ROS	Concentration- and time- dependent cytotoxicity and increase in ROS. No cytotoxicity at low concentrations (≥ 4 µg/ml) (Lammel et al., 2013)
Graphene	500-1000 nm	Murine RAW 264.7 macrophages	20-100 µg/ml	ROS, MMP, Annexin-V/PI assays	ROS and apoptosis induced via mitochondrial cascade (Li et al., 2012)
Graphene	200-1200 nm	Human HaCaT skin keratinocytes	10-100 µg/ml	CCK-8 assay, ROS	induced a concentration-dependent cytotoxicity and ROS generation (Pelin et al., 2018)
GO	1 nm thick	Human-retinal pigment epithelium (RPE)	5-100 µg/ml	LDH assay	Good biocompatibility of GO to RPE cells (Yan et al., 2012)
GO	0.01 -0.02 μm^2	Human lung adenocarcinoma A549	7.8-125 µg/ml	Modified-LDH assay	Lack of cytotoxicity for up to 100 µg/ml dose exposure (Ali-Boucetta et al., 2013a)

Table 1. **Different in vitro cytotoxicity studies with GBNs and their cellular effects (continued)**

Material	Size	Culture model	Tested concentrations	Cytotoxicity assays	Conclusions
GO	342-765 nm	Human skin fibroblast cells (CRL-2522), red blood cells (RBCs)	3-200 µg/ml	MTT, LDH, WST-8, ROS hemolysis assay	Decreased cell viability, increased generation of ROS and induced hemolysis in RBCs (Liao et al., 2011)
GO with 3 different lateral dimensions	160 ± 90 nm 430 ± 300 nm 780 ± 410 nm	A549	10 -200 µg/ml	CCK-8, LDH, ROS, Annexin-V/PI	No cytotoxicity Dose dependent generation of ROS (Chang et al., 2011)
GO	592 ± 10.9 nm	Cervical cancer cells (Hela)	20-80 µg/ml	LDH, MTT, ROS	High toxicity at concentration equal or more than 40 µg/ml. (Zhang et al., 2012a)
GO	200-500 nm	Human lung fibroblast (HLF)	10-500 µg/ml	MTT, ROS, flow cytometry analysis, comet assay	GO induced significant ROS generation and cytotoxicity *via* apoptosis. Genotoxicity was remarkable even at the lowest concentration. (Wang et al., 2013)
GO	100-500 nm	A549	8-125 µg/ml	Modified-LDH assay, trypan blue exclusion assay	No cytotoxicity after 24 and 48 hours exposure (Jasim et al., 2016)

Table 1. **Different in vitro cytotoxicity studies with GBNs and their cellular effects (continued)**

Material	Size	Culture model	Tested concentrations	Cytotoxicity assays	Conclusions
GO with 3 different lateral dimensions	50-350 nm 350-750 nm 750-1300 nm	Mouse macrophage cell line J774A.1	20 μg/ml	Live-dead test, flow cytometry, confocal laser scanning, Western blot	All GO samples reduced cell viability of J774.A1 cells at 20 μg/ml, however, larger particles (750-1300nm) are significantly more toxic than smaller particles at 12 and 24 hours of exposure. larger GO significantly promoted macrophage M1 polarization through canonical NF-κB signalling, leading to enhanced pro-inflammatory responses (Ma et al., 2015)
GO	101.9- 586.4 nm	Mouse peritoneal macrophages	1-50 μg/ml	LDH, Western blot	Concentration dependent cytotoxicity was evident. GO caused significant release of LDH from cell cytosol at concentration of 10 μg/ml after 24 hours exposure. Increased autophagosome accumulation and decreased autophagic degradation (Wan et al., 2013)
GO	380 nm	Rat myocardial cell line H9c2	0.1-10000 μg/ml	Alamar Blue assay	Concentrations higher than 100 μg/mL induced cell death with IC_{50} of 652.1 ± 1.2 μg/ml (Contreras-Torres et al., 2017)
GO	> 1μm	Murine lung epithelial (FE1)	5-200 μg/ml	Nucleocounter NC-200, comet assay	No cytotoxicity or genotoxicity following 3 or 24 hours of exposure (Bengtson et al., 2016)

Table 1. **Different in vitro cytotoxicity studies with GBNs and their cellular effects (continued)**

Material	Size	Culture model	Tested concentrations	Cytotoxicity assays	Conclusions
GO with 3 different lateral dimensions	1-30 μm 50-2000 nm <500 nm	Human monocyte derived macrophages (HMDMS)	12.5-75 μg/ml	Alamar Blue assay	No cytotoxicity at concentrations up to 75 μg/ml (Rodrigues et al., 2018)
GO	400-1000 nm	Rat basophilic leukaemia mast cells (RBL), NIH-3T3 fibroblast cells, human breast cancer cells (MDA-MB-231	100 μg/ml	Confocal, live cell fluorescence microscopy, scanning electron microscopy	Plasma membrane ruffling and shedding was observed in all tested cell lines following 4 hours of exposure (Sun et al., 2016)
PEG-GO	500 nm	Raji lymphoma cells	10-100 μg/ml	CCK-8	Cell survival rate over 80% at 100 μg/ml after 24 hours of exposure (Du et al., 2014)
PEG-DSPE-GO	500 – 2500 nm	Breast cancer cells (SKBR3), NIH-3T3 fibroblast, Hela	10-400 μg/ml	Neutral red, Alamar Blue assay, LDH, clonogenic assay	Concentration- and, time-dependent cytotoxic effects on the four cell lines. HeLa cells, showed higher cytotoxicity compared to the other cells with 50% cell death at 200 μg/ml after 24 hours of exposure (Mullick Chowdhury et al., 2013)

Table 1. **Different in vitro cytotoxicity studies with GBNs and their cellular effects (continued)**

Material	Size	Culture model	Tested concentrations	Cytotoxicity assays	Conclusions
PEG-GO	5-50 nm	Human colon cancer cells (HCT116)	0.5-500 µg/ml	MTT	No cytotoxicity (Liu et al., 2008b)
r-GO	100-1500 nm	U87 and U118 glioma cells	5-100 µg/ml	BrdU, XTT, Annexin-V/PI	Concentration- dependent cell death *via* apoptosis (Jaworski et al., 2015)
r-GO	150 nm	Rat myocardial cell line H9c2	0.1-10000 µg/ml	Alamar Blue assay	Concentration dependent cytotoxicity with IC_{50} of 129.4 ± 1.2 µg/ml (Contreras-Torres et al., 2017)
r-GO	11 ± 4 nm	hMSCs	0.1-100 µg/ml	FDA, ROS, Comet assay	Cytotoxicity and DNA damage was observed at low concentrations of 0.1 and 1 µg/ml after 1-hour exposure (Akhavan et al., 2012)
r-GO	3.8 ± 0.4 µm	hMSCs	0.1-100 µg/ml	FDA, ROS, Comet assay	Cytotoxicity was only evident at 100 µg/ml after 1-hour exposure and no genotoxicity detected even at the highest concentration at all tested time points (Akhavan et al., 2012)
r-GO	> 1µm	FE1	5-200 µg/ml	Nucleocounter NC-200, comet assay	No cytotoxicity or genotoxicity following 3 or 24 hours of exposure (Bengtson et al., 2016)

Table 1. **Different in vitro cytotoxicity studies with GBNs and their cellular effects (continued)**

Material	Size	Culture model	Tested concentrations	Cytotoxicity assays	Conclusions
r-GO	4.23 nm thick	Breast cancer cells (MCF7)	20-100 µg/ml	WST-8, LDH, ROS	Concentration dependent cytotoxicity with 64.0% ± 2.0% cell death at 100 µg/ml after 24 hours of exposure. Increased levels of ROS were detected (Gurunathan et al., 2013)
r-GO	Not provided	Hela	10-100 µg/ml	MTT	Concentration dependent cytotoxicity with IC_{50} of 100 µg/ml (Luo et al., 2017a)
r-GO	180.55 nm	Ovarian cancer cell line A2780	20-100 µg/ml	MTT, LDH, ROS, WST-8, caspase-3 assay	Concentration dependent membrane damage and oxidative stress in cancer cells, and decreased their viability via apoptosis (Gurunathan et al., 2015)
PSU-r-GO	6-9 nm thick	Human corneal epithelial cell line (hTCEpi)	500 µg/ml	MTS	No negative effect on cells after 24 hours exposure (Peña-Bahamonde et al., 2017)
PEG-r-GO	791.57 nm	A549	1-200 µg/ml	MTT, ROS, MMP Neutral red, thymidine incorporation, Annexin-V/PI	Concentration dependent decrease in cell viability with more than 50% cell death at 50 µg/ml after 24 hours of exposure. Increased generation of ROS and apoptotic cell death (Reshma et al., 2016)

Symbol: PEG-DSPE = (1,2-distearoyl-sn-glycero-3-phosphoethanolamine-N- [amino (polyethylene glycol)]), PSU = poly- sulfone polymer.

So far, studies have suggested that GBNs toxicity may result from a number of different mechanisms, including a pro-inflammatory response, apoptosis, autophagy, necrosis, genetic damage (Ou et al., 2017, Bianco, 2013), although the link between GBNs and oxidative stress appears to be a common trend to studies. The lack of consistency in terms of the production and characterisation of GBNs makes a critical evaluation of their effect and properties more difficult.

Some data have revealed the vital influence of the dimensions of graphene materials on their biocompatibility profile. For instance, Ma and colleagues (2015) showed that GO nano-sheets with lateral sizes ranging from 750 to 1300 nm were more toxic than smaller particles for mouse macrophage cells (J774.A1), using the same dose and exposure times. In a recent study, large l-GO sheets (5-15 μm) induced greater ROS generation, inflammatory response, and cytotoxicity in human lung epithelial cells (BEAS-2B) than smaller s-GO sheets (50-200 nm) (Vranic et al., 2018). By contrast, GO with three different size ranges (1-30 μm, 50-2000 nm, <500 nm) showed no signs of toxicity against human monocyte derived macrophages (HMDMS) at concentrations up to 75 μg/ml (Rodrigues et al., 2018). Also, size has been reported to influence blood compatibility whereby smaller GO nano-sheets (342 nm) were linked to a more pronounced hemolytic activity compared to larger ones (765 nm) (Liao et al., 2011). In addition, it has been reported that r-GO with average lateral dimension of 11 ± 4 nm can enter the nucleus of human MSCs and cause DNA damage at low concentrations of 0.1 and 1μg/ml and by 1 hour. However, in the same study, r-GO with an average lateral dimension of 3.8 ± 0.4 μm showed no genotoxicity in the MSCs even at the highest tested concentration (100μg/ml) and after 24 hours (Akhavan et al., 2012). The latter study indicates that the genotoxicity of r-GO may depend on size.

In regard to size, several studies have measured the size of GBNs using dynamic light scattering (DLS) and this technique is unable to characterise the exact size of graphene sheets because of their anisotropic morphology (Liao et al., 2011). For this reason, comparing different studies should take into account differences in the characterisation techniques used.

The purity of GBNs is an important factor that should be considered while investigating their biocompatibility. GO samples obtained using a traditional synthesis method commonly contain a high level of impurities which can cause toxicity to cells (Wu et al., 2015). Indeed, highly purified GO with good colloidal stability, obtained after modification of the conventional method, appear to show a more consistent cytotoxicity profile (Ali-Boucetta et al., 2013b, Jasim et al., 2016, Rodrigues et al., 2018). Thereby, the purity of GBNs and methods used for their synthesis need more attention, to ensure more accurate and consistent results.

In addition to the size and purity, surface functionalisation of GBNs was reported to modulate its cytotoxicity (**Table 1**). For example, covalent PEGylation of GO was shown to further enhance its biological stability and biocompatibility (Liu et al., 2008b). In a different study, PEG-GO and lacto bionic acid-polyethylene glycol GO (LA-PEG-GO) had lower cytotoxicity and genotoxicity than non-functionalised GO (Wang et al., 2013). Also, coating GO surface with chitosan reduced its hemolytic activity against red blood cells (RBCs) (Liao et al., 2011). For targeted drug delivery and PTT, graphene derivatives were mostly conjugated with PEG to increase the circulation time and biocompatibility (Liu et al., 2013, Robinson et al., 2011, Zhang et al., 2017a, Lu et al., 2018). However, there are some concerns regarding surface functionalisation to enhance circulation time as this can lead to bioaccumulation of graphene nanoparticles (Yang et al., 2013b, McCallion et al.,

2016). Recently, protein coating of small s-GO sheets (50-200 nm) was shown to completely suppress the adverse effects exhibited by non-coated s-GO sheets while in the case of large l-GO sheets (5-15 μm), protein coating had slight impact on their toxicity (Vranic et al., 2018). Therefore, lateral dimension is a critical factor that governs biological responses to GBNs. Although most studies indicate that PEGylation has enhanced biocompatibility, recently PEG-GO (200 nm) was found to activate peritoneal macrophages by triggering a potent release of cytokines (Luo et al., 2017b). The latter finding indicates that PEGylation of GO can elicit an immunological response and caution and further studies in regards to biocompatibility of functionalised GBNs is required.

In biological systems, proteins can easily adsorb onto GBNs surface to form a "protein corona" around the graphene sheets (Peng and Mu, 2016, Wei et al., 2015). Protein corona formation has a great influence on the physiochemical properties, pharmacokinetic and toxicokinetic profile of the nanomaterials (Fadeel et al., 2013, Zhang et al., 2017c). Owing to the large surface area of GBNs, the corona phenomena could potentially limit their clinical use (Aggarwal et al., 2009). For example, corona formation can significantly increase the size of graphene nanoparticles which might lead to blockage of blood capillaries when delivering nanoparticles *via* intravenous injection (Liu et al., 2018).

So far, the number of *in vivo* biocompatibility studies remains limited, but current ones seem to reveal the lung as the organ most at risk of toxicity, irrespective of the administration route (Bussy et al., 2015, Bianco, 2013).

In summary, a number of factors can affect interpretation of the biocompatibility data obtained for GBNs (Ou et al., 2016). Contradictory data reported so far may be attributed to the large variability in physicochemical properties among GBNs, insufficient characterisation and differences in the methods used to produce the GBNs and models used

to test their cytotoxicity. These issues highlight the need for a standardised approach to the toxicological evaluation of new nanomaterials such as GBNs. More importantly, few studies have explored the complex signalling pathways relating to the toxicity of GBNs; such studies are critical to our understanding of the mechanisms that lead to changes in cell function following exposure to GBNs. Present research is motivated by the demands for a better understanding of the interaction and cytotoxic mechanisms of GBNs in cell culture models. To this end, GO and r-GO were selected as the most extensively investigated GBNs for potential biomedical applications. Highly purified GO and r-GO were synthesised and their physicochemical properties were extensively characterised. Hence, considering the revealed lung toxic responses by the *in vivo* studies of GBNs, the *in vitro* effects of GO and r-GO were evaluated using lung cell lines and without pre-modification of the nanoparticles.

1.6 Aims and objectives

Over the last eight years, there has been a considerable focus on the biomedical applications of GBNs, particularly GO and r-GO due to their extraordinary properties. However, more information about their toxicity and biocompatibility is crucially needed prior to their clinical use. We hypothesised that the different material properties evidenced by GO and r-GO would elicit different biological responses. The goal of this research was to synthesise and characterise GBNs with different oxygen content and to evaluate their potential toxicity using pulmonary cell lines as an *in vitro* model.

To achieve this goal:

- GO and r-GO were synthesized and characterised using a range of different techniques to elucidate their morphological and physicochemical properties.
- The cytotoxicity profile of both materials was assessed using foetal lung fibroblast cells and cancerous epithelial lung cells.
- Cellular uptake of graphene derivatives was assessed for both cell lines, as well as their interaction with RBCs.
- Mechanistic investigations of toxicity included oxidative stress and genotoxicity.
- The effect of GO and r-GO on the expression of cellular proteins, that are crucial to many cell signalling pathways, was investigated.

Chapter 2

Materials and methods

2.1 Materials

2.1.1 Cells

Foetal lung fibroblast cells (MRC-5) and epithelial lung carcinoma cells (A549) were obtained from Public Health England (Salisbury, UK). Sheep red blood cells (RBCs) were obtained from Innovative research INC (Michigan, USA).

2.1.2 Cell culture media and reagents

Eagle's minimum essential medium, glutamine and non-essential amino acid solution were from Sigma-Aldrich (Dorset, UK), and F-12 Nutrient Mixture Ham medium, RPMI medium 1640, 0.25% trypsin, Dulbecco's phosphate buffered saline, penicillin and streptomycin and foetal Bovine Serum were from Thermo Fisher Scientific (Paisley, UK).

2.1.3 Assay kits

Table 2. Assay kits.

Kit	Supplier
CytoTox 96 Non-Radioactive Cytotoxicity assay **RealTime-Glo™ MT Cell Viability assay** **CellTiter-Glo assay** **Caspase-Glo 3/7 assay** **GSH/GSSG-GloTM assay**	Promega (Southampton,UK)
CellROX assay	Thermo Fisher Scientific (Paisley, UK)
Annexin-V-FLUOS	Roche (Welwyn Garden City, UK)

2.1.4 **Chemicals**

Table 3. Chemicals.

Chemical	Supplier
Graphite powder **Sulfuric acid (H_2SO_4)** **Sodium nitrate ($NaNO_3$)** **30% Hydrogen peroxide (H_2O_2)** **Potassium permanganate ($KMnO_4$)** **Sodium orthovanadate (Na_3VO_4)** **Potassium bromide (KBr)** **Ethylene-diamine-tetraacetic acid (EDTA)** **Dimethyl sulphoxide (DMSO)** **Menadione** **Sodium azide (NaN_3)** **Anisomycin** **Tetramethylethylenediamine (TEMED)** **TritonTM X-100** **4-nitroquinoline N-oxide** **2-mercaptoethanol** **Bovine serum albumin (BSA)** **Bradford reagent**	Sigma- Aldrich (Dorset, UK)
Bovine serum albumin protein standard **SYBR Gold dye**	Thermo Fisher Scientific (Paisley, UK)
Tween-20 **Phenylmethylsulfonyl fluoride (PMSF)**	PanReac Applichem (Barcelona, Spain)

(Table 3 continued)

Table 3. Chemicals (continued)

Chemical	Supplier
Sodium chloride (NaCl) **Skim milk powder**	EMD Millipore (Watford, UK)
Staurosporine **Ponceau, 0.2% v/v solution**	Alfa Aesar (Heysham, UK).
ECL™ Western blot detection reagents **Amersham™ Hyperfilm™ ECL**	GE healthcare (Hatfield, UK).
Glycine	VWR (Bristol, UK)
Tris-base	Roche (Welwyn Garden City, UK)

2.1.5 **Buffers**

NP40 lysis buffer: 50 mM Tris-HCl (pH 7.5), 1 mM EDTA, 1 mM EGTA, 50 mM sodium fluoride, 5 mM sodium pyrophosphate, 1 mM sodium orthovanadate, 1% (w/v) Nonidet P40, and 0.27 M sucrose.

Gel running buffer: 25 mM Tris-base, 34.6 mM SDS and 1.92 M glycine.

Western transfer buffer: 48 mM Tris-base, and 39 mM glycine containing 20% (v/v) methanol.

Blocking buffer: 5% (w/v) dried skimmed milk in TBST.

TBST buffer: (0.2% (v/v) Tween-20, 50 mM Tris-HCl (pH 7.5), and 150 mM NaCl).

Cell lysis buffer: 2.5 M NaCl, 0.1 M Na_2EDTA, 8 mM Tris HCl, 1% sodium lauryl sarcosinate, 10% DMSO, Triton-X-100, and pH adjusted to 10.

Electrophoresis buffer: 300 mM NaOH, and 1 M Na_2EDTA.

Neutralisation buffer: 0.4 M Tris HCl.

2.1.6 **Antibody reagents**

Table 4. Antibodies used in Western blot and flow cytometry analysis.

Antibody	Reference number	Dilution
Cleaved-Caspase 3	9664	1:1000
Cleaved-PARP	5625	
GAPDH	5174	
LC3A/B	12741	
SQSTM1/p62	23214	
mTOR	2983	
Phospho-p38 MAPK	4511	
Phospho-HSP27	9709	
β-catenin	9582	
GSK-3β	9315	
PDK1	13037	
PTEN	9188	
Anti-rabbit IgG, HRP-linked Antibody	7074	1:2000
Anti-Rabbit Alexa Fluor RT (488)	4412	1:2000

* **Antibodies were purchased from cell signalling life technologies**

2.2 Methods

2.2.1 Synthesis and characterisation of GBNs

2.2.1.1 Preparation of GO and r-GO

GO was prepared from graphite powder following the modified Hummers method described by Ali-Boucetta et al (2013). The preparation of GO was carried out in a laminar flow hood. In brief, 0.2 g of graphite powder and 0.1 g of sodium nitrate ($NaNO_3$) were placed and mixed in a 125 ml conical glass flask. The temperature was kept below 5°C by placing the conical flask in an ice bath. A volume of 4.6 ml of concentrated sulphuric acid (H_2SO_4) was added to the mixture that was stirred constantly by using a magnetic stirrer. After 30 minutes, 0.6 g of potassium permanganate ($KMnO_4$) was added gradually to the above mixture while keeping the temperature below 5°C. The conical flask was taken out of the ice bath after the addition of $KMnO_4$, to return the temperature to room temperature and the flask was continuously stirred for 30 minutes. The mixture turned into a dark green thick paste. After that, 9.2 ml of deionised water were added slowly to the stirred mixture. A violent effervescence and a quick increase in temperature to approximately 50°C were observed. With the aid of a hot plate, the temperature was maintained around 95 to 100°C for 30 minutes. Then the mixture was diluted with 28 ml of warm deionised water with continuous mixing. In the next step, 3 ml of 30 % hydrogen peroxide (H_2O_2) were added gradually to the constantly stirred mixture. Dispersion of the thick paste together with the adoption of a yellow tint were observed. The mixture was transferred into two falcon tubes and vortexed for a few seconds.

In the following step, which is termed the washing step, 20 ml of warm sterile water were added to each tube which was then centrifuged at 8500 rpm for 40 minutes at 40°C. After centrifugation, the pH of the supernatant was measured and it was found to be extremely acidic. The supernatant was discarded and the washing step was repeated a number of times

as above. At each washing step, the acidity of the supernatant decreased gradually. Once the pH of the discarded supernatant achieved around 3 to 4, the washing step was repeated using cold sterile water instead of warm water and centrifugation at 8500 rpm for 40 minutes at 20°C. The washing step was ended once the pH was a neutral 6 and a brown viscose layer of GO had appeared on the top of the oxidation by-products. The supernatant was discarded and 1 ml of warm sterile water was added gently to the gel-like brown layer to suspend the GO. The collected GO suspension was purified from impurities by using a cell strainer of 100μm. The obtained GO suspension was centrifuged at 8500 rpm for 25 minutes at 40°C. Finally, the supernatant produced from the last centrifugation is the pure yellowish-brown GO dispersion. The GO dispersion was stored at 4°C. In order to determine the concentration of the pure GO, 1 ml of GO was transferred into a glass vial and left to dry at 40°C for 48 hours. The concentration of the original suspension (weight/volume) was obtained from the weight of the dry GO.

To prepare r-GO, GO was reduced *via* thermal reduction. The GO suspension was steam heated and the thick black dispersion produced, *via* steam heating, was dried in the oven at 180°C for 6 hours. The r-GO was scraped very carefully into a vial and the powder was weighed. In the final step, the r-GO flakes were dispersed in sterile water, sonicated for 1 hour and stored at 4°C until further use.

2.2.1.2 Raman spectroscopy

Aqueous dispersions of GO or r-GO were dried at 40°C for 24 hours before the samples (500 μg) were placed on a microscope slide for analysis. Raman spectra were recorded using a 100X objective lens at λ=633 nm on a Renishaw inVia Raman Microscope (RENISHAW). Data were analysed using WIRE 3.1 software. The Raman spectrum of graphite was measured for comparison.

2.2.1.3 Fourier-transform infrared (FTIR) spectroscopy

The GO dispersion (2 ml) was dried at 40°C in a glass vial for 24 hours. The dried GO (2 mg) was recovered, mixed with KBr (298 mg) and manually pressed into a pellet. Spectroscopy of the mid-infrared range was performed on a NICOLET 380 FTIR spectrophotometer (Thermo Fisher Scientific) and the transmittance results were analysed using OMNIC software. FTIR analysis was performed on the r-GO sample in a similar manner.

2.2.1.4 Zeta potential measurement

Particle charge was determined on a Malvern Zetasizer based on the electrophoretic mobility of the GO and r-GO samples in water (60 μg/ml). The electrophoretic mobility is converted automatically by the Zetasizer software to zeta potential (ζ) values using Henry's equation. All experiments were conducted in triplicate.

2.2.1.5 Thermal gravimetric analysis (TGA)

The TGA of graphite, GO and r-GO was performed using NETZSCH instrument. Measurement was obtained from 25 ℃ to 1000 ℃ at 10 ℃/min. Two mg of dried sample was placed into a ceramic crucible and nitrogen flow of 20 ml/min was used as a purge gas.

2.2.1.6 X-ray photoelectron spectroscopy (XPS)

The composition of graphene derivatives surfaces was analysed by Thermo Theta Probe XPS spectrometer at NEXUS facility. Spectra acquired at NEXUS were analysed using CasaXPS software.

2.2.1.7 Transmission Electron Microscopy (TEM)

TEM images were acquired on a Jeol 1200ex electron microscope (JEOL) operated at 80 kV beam energy. Ten μl of GO or r-GO sample were pipetted onto a formvar carbon coated

copper grid (Agar Scientific) and left to dry for 15 minutes. Size distribution analysis was carried out using ImageJ software for 100 individual graphene particles.

2.2.1.8 Atomic Force Microscopy (AFM)

AFM measurements were performed using the JPK microscope (JPK) and intermittent contact (taping mode) was utilised. Dip coating was used as the deposition method on a silicone substrate. JPK Nano-wizard 2 software was used to analyse the data. (This work was in collaboration with Paolo Passaretti).

2.2.1.9 Ultraviolet-Visible (UV-Vis) spectroscopy

Ultraviolet-Visible (UV-Vis) absorbance and the spectra of different concentrations of prepared GO and r-GO samples were collected on a UV-Vis spectrophotometer (UV-2600 SHIMADZU). Data were then analysed with UVProbe software.

2.2.1.10 Fluorescence spectroscopy

Fluorescence emission spectra were measured for GO and r-GO samples at room temperature at different concentrations (50-400 μg/ml) using a RF-S301 fluorescence spectrophotometer (SHIMADZU). The excitation wavelength used was 525 nm because it gave a maximum emission spectrum.

2.2.2 Toxicological Assessment of GBNs in cell culture models

2.2.2.1 Cell culture

MRC-5 cells are non-cancerous foetal lung fibroblast cells and they were maintained in Eagle's Minimum Essential Medium supplemented with 2 mM glutamine, 1% non-essential amino acids (NEAA),10% foetal bovine serum (FBS) and 1% penicillin and streptomycin. A549 cells are epithelial lung carcinoma cells and they were maintained in F-12 Nutrient Mixture Ham media supplemented with 10% FBS and 1% penicillin and streptomycin. Both

cell lines were kept at 37 °C in 5% CO_2 and passaged twice a week using 0.25% trypsin EDTA when the confluence of the cells reached around 75 to 85 %.

2.2.2.2 Modified LDH assay

The modified LDH assay was performed using the Promega Cytotox 96 non-radioactive cytotoxicity assay according to a protocol described by Ali-Boucetta and colleagues (Ali-Boucetta et al., 2011). MRC-5 cells were seeded at a density of 10000 cells per well in 96-well plates while A549 cells were seeded at a density of 7000 cells per well. These densities were selected to achieve 70% confluency of both cell lines when left to adhere overnight at 37°C in 5% CO_2 before incubation with the GO or r-GO dispersions. Stock dispersions of GO and r-GO were sonicated for 30 minutes prior to use in cell culture studies. Cells were then treated with graphene derivatives dispersions diluted in the complete media required for each cell type and at a concentration ranges from 31.25 to 600 μg/ml for 3, 24 and 48 hours. Control cells were incubated with complete media while positive controls were treated with 10% DMSO. Four replicate samples were performed for each treatment.

After 3 hours, the medium was aspirated and the cells were lysed with 10 μl of lysis buffer (0.9% Triton X100) mixed with 100 μl of phenol in serum free media and for 60 min at 37 °C in 5% CO_2. Cell lysate were collected and then centrifuged at 13000 rpm for 5 min in order to pellet down the GO. Fifty μl of the supernatant of the cell lysate were transferred into a new 96 well plate and mixed with 50 μl of the LDH substrate mix and then incubated for 15 min at room temperature. After this treatment, 50 μl of the stop solution were added to each well to stop the reaction and then the absorbance was read at 490 nm using a plate reader (FLUOstar Omega).

The amount of LDH detected represented the number of cells that survived the treatments. The above steps were performed for the 24 and 48 hours end time points. The following equation was used to calculate the percentage cell survival:

Percentage cell survival = (Sample absorbance /Mean control absorbance) x 100

2.2.2.3 RealTime-Glo TM MT cell viability assay

The MT cell viability assay was performed using the Promega RealTime-Glo™ MT cell viability kit according to the manufacturer instructions. At first, the assay linearity with regard to cell density for cells was evaluated. In order to investigate the assay's linearity for A549 cells, cells were plated at 5 different cell densities (2000 cells/well, 3000 cells/well, 4000 cells/well, 5000 cells/ well and 6000 cells/well) in 100 µl of cell culture medium in a white 96 well plate. Luminescence was read after the addition of the test reagents and at different times over the desired time course (3 hours, 24 hours, 48 hours, 72 hours). The average luminescence for each replicate group was calculated. A linear curve fit was applied for luminescence *versus* cell number plot. The cell density range that yields an R^2 value more than 0.95 is in the linear range of the assay according to the manufacturer instructions. After determining the linear range of cell density, the cell viability was monitored continuously following the protocol for Continuous-Read Format provided by the manufacturer where the MT Cell Viability Substrate and Nanoluc Enzyme were added at the same time as the test compound. The MT Cell Viability Substrate, Nanoluc Enzyme and cell culture medium were equilibrated to 37 °C. A549 cells were plated at cell density within the linear range (4000 cells/well) in 100 µl of cell culture medium in a white 96 well plate. 4 ml of 2X test compound diluent was prepared by adding 8 µl of MT Cell Viability Substrate and 8 µl of Nanoluc Enzyme to 3,984 µl of cell culture medium. Different concentrations of GO ranging from 7.8 to 125 µg/ml were prepared using the test compound

diluent prepared in the previous step to form the 2X test compound solution. After this, 100µl of 2X test compound containing RealTime-GloTM reagent were added to the cells. Healthy control cells were treated with the 2X test compound diluent while positive controls were treated with 10% DMSO prepared in the 2X test compound diluent. Four replicate samples were performed for each treatment. Luminescence was monitored at the desired time points (3 and 24 hours) using a plate reading luminometer (FLUOstar Omega).

To determine the potential interference of GO with luminescence, cells were plated with the assay reagent and luminescence was measured. After measurement, different concentrations of GO were added directly to the cells and luminescence was measured immediately without any incubation time.

2.2.2.4 CellTiter-Glo assay

The Promega CellTiter-Glo assay kit was used to determine the number of viable cells *in vitro* based on quantitation of the ATP present in cells. MRC-5 and A549 cells were seeded at cell densities of 10,000 and 7000 cells per well in 100 µl of cell culture medium in a white 96 well plate. Graphene derivatives were added at a concentration ranges from 31.25 to 600 µg/ml and the cells were incubated for 24 and 48 hours. Four replicate samples were performed for each treatment. After each time point, the plates were equilibrated at room temperature for 30 min. One hundred µl of the assay reagents were added to 100 µl of medium containing cells and graphene test material according to the kit protocol. However, a washing step was introduced to the original protocol as the medium containing the test material was removed and replaced with 100 µl of fresh medium followed by adding 100 µl of assay reagents. Both with and without washing step samples were compared to test for any potential interference of graphene nanomaterials with the assay and to assess the efficiency of the washing step to overcome such interference. After the addition of 100 µl of assay reagents, the contents of wells were mixed for 2 min using orbital shaker to induce

cell lysis. Plates were incubated at room temperature for 10 min to stabilise the luminescent signal and the luminescence was recorded using a plate reading luminometer (FLUOstar Omega).

2.2.2.5 Assessment of GBNs cellular uptake by flow cytometry

MRC-5 and A549 cells were plated into 24-well plates at a cell density of 50,000 cells per well in 500 µl of cell culture medium and left to attach overnight before incubation with the graphene derivatives. Cells were then incubated for 24 and 48 hours with GO (15.6 –125 µg/ml or the equivalent r-GO concentration (15.6 - 125 µg/ml) in complete media. Prior to analysis, cells were washed with 500 µl of PBS to remove unbound graphene derivatives. After washing with PBS, 100 µl of trypsin were added per well and the cells were incubated at 37°C in a humidified atmosphere (5% CO_2) incubator for 5 min followed by the addition of 500 µl of tissue culture media to detach cells by vigorous pipetting. Cells were then transferred into micro-centrifuge tubes, centrifuged at 350×g for 5 min at 4°C, resuspended in 500 µl of cold PBS and kept on ice for immediate analysis by flow cytometry.

2.2.2.6 Cytotoxicity analysis of GBNs after blocking cellular uptake by endocytosis inhibitors

MRC-5 and A549 cells/well were seeded in 96-well plates 24 hours prior to treatment as described previously for the modified LDH method. The cells were then pre-incubated with endocytosis inhibitors: sodium azide (7 µg/ml) for 1 hour followed by the addition of GO and r-GO (300 - 600 µg/ml) and incubation for 24 hours. The concentrations of the inhibitor were selected as described previously by other workers (Chatterjee et al., 2014, Macia et al., 2006).

2.2.2.7 Annexin V/PI flow cytometry Assay

The annexin V/PI staining assay was carried out following the instructions of the manufacturer. Both cell lines were seeded into 24-well plates as described in section 3.1. Cells were then incubated for 24 and 48 hours with GO and r-GO (125 - 300 μg/ml) in complete medium. Untreated cells were used as negative controls. Cells exposed to 20% DMSO or staurosporine (10 μM, 6 hours) were used as positive controls for necrosis and apoptosis, respectively. Cells were trypsinized, centrifuged at 350 *g* for 5 min at 4°C, washed with PBS, and stained with the annexin V/PI labelling solution for 15 min at 25 °C. Finally, the samples were diluted with HEPES incubation buffer immediately before analysis. Ten thousand events were collected on a Fortessa flow cytometer (BD Bioscience). Electronic compensation was applied to eliminate overlapping of the two emission spectra. The data generated were analysed by Flowing software.

2.2.2.8 Caspase-Glo 3/7 assay

This assay was performed using the Promega Caspase-Glo 3/7 kit according to the manufacturer instructions. This assay is based on luminescence and measures the activities of caspase-3 and -7. A washing step was introduced to the protocol to overcome any interference by the graphene nanomaterials. Caspase-Glo 3/7 was performed using MRC-5 and A549 cells incubated with GO and r-GO at concentrations ranging from 125 to 300 μg/ml and after 6, 24 and 48 hours exposure in a white 384-well plate. Staurosporine (10 μM) treated cells for 6 hours were used as a positive control for apoptosis. In brief, 384-well plates containing cells were incubated with graphene derivatives and allowed to equilibrate to room temperature. After this, the medium was removed and replaced with 25 μl of fresh medium (washing step). Twenty-five μl of caspase 3/7 reagent were added to each well and gently mixed using a plate shaker for 1 min and then incubated for 1 hour at

25°C followed by luminescence measurement using a plate reading luminometer (FLUOstar Omega).

2.2.2.9 Analysis of cleaved-caspase 3 and cleaved-PARP by flow cytometry

Both cell lines were plated into 12-well plates at a cell density of 100,000 cells per well in 1 ml of cell culture medium and left to attach overnight before incubation with the graphene derivatives. MRC-5 and A549 cells were incubated with GO and r-GO at concentrations ranging from 125 to 300 μg/ml and analysed at 24 and 48 hours post-exposure. Staurosporine (10 μM) treated cells for 6 hours were used as a positive control to induce cleaved caspase-3 and cleaved-PARP. Cells were trypsinized, centrifuged at 350 *g* for 5 min at 4°C, re-suspended in 500 μl of 4% of paraformaldehyde in PBS and kept for 10 min at 37°C for fixation. Fixed cells were then centrifuged, re-suspended in cold 90% methanol and incubated for 30 min on ice. For immunostaining, 3 ml of incubation buffer (0.5 g BSA in 100 ml PBS) were added to each sample and the cells were washed by centrifugation. Cells were then re-suspended in 100 μl and the primary antibody for the protein of interest was added (cleaved caspase-3/cleaved-PARP/non-specific antibody, [1:800 dilution]) and incubated for 1 hour at room temperature. Samples were washed with 3 ml of incubation buffer by centrifugation and then re-suspended in 100 μl of fluorochrome-conjugated secondary antibody and left for 30 min at room temperature. Finally, samples were washed and then re-suspended in 500 μl of PBS for immediate analysis on a flow cytometer. Ten thousand cells per sample were assessed using a Fortessa flow cytometer. Flowing software was used to analyse the data obtained.

2.2.2.10 Analysis of cleaved caspase-3 and cleaved PARP by western blot technique

For sample preparation, MRC-5 and A549 cells were seeded at a density of 400,000 cells per well in 6-well plates. Both the cell lines were left to adhere overnight at 37°C in 5% CO_2 before incubation with the GO or r-GO dispersions. MRC-5 and A549 cells were treated with the GO and r-GO at a concentration of 300 µg/ml for 24 hours. After incubation with the graphene derivatives for the desired time points, the medium was aspirated, cells were washed with PBS (1 ml/well) and the plates kept on ice. Cells were lysed by adding 100 µl of NP40 lysis buffer to each well. Protease inhibitors including 0.1 mM phenylmethanesulfonyl fluoride (PMSF), 1 mM Benzamidine and 0.1% (v/v) β-mercaptoethanol were added to the NP40 lysis buffer before lysing the cells. Cells were scraped off the plate and the extract was transferred to a 1.5 micro-centrifuge tube. Samples were centrifuged at 12000 g for 10 min at 4 °C and the protein concentration of the supernatant was measured using the Bradford assay.

Bradford assay: This test was performed in a non-sterile 96 well plate with blank, standard and test samples in triplicate. The standard BSA protein concentrations were 0.125, 0.2, 0.5, and 1 mg/ml. Five µl of protein standard were added per well and 2 µl per well of the test sample followed by the addition of 280 µl of Bradford reagent per well. Absorbance of the samples was measured using a plate reader (FLUOstar Omega). One µg/µl of protein samples in sodium dodecyl sulphate (SDS) were prepared. Samples were heated at 90 ºC for 5 min then left to cool and stored at -20ºC.

For immunoblotting, 20 µg of cell lysates in SDS sample buffer underwent electrophoresis on a polyacrylamide gel in running buffer. Gels were then transferred onto nitrocellulose membranes using transfer buffer. The Bonceau dye was then added to the nitrocellulose membranes to stain the protein bands followed by washing with distilled water. The

membranes were incubated for 1 hour with blocking buffer and washed 3 times with TBST buffer. The membranes were then incubated with the antibodies to cleaved-caspase 3 or cleaved-PARP overnight at 4ºC with gentle agitation, followed by washing 3 times with TBST buffer. The blots were then incubated with the secondary HRP-conjugated antibodies for 1 hour with gentle mixing at 25ºC. After membrane washing with TBST buffer, the signal was measured using the enhanced chemiluminescence reagent. Immunoblots were processed through a film automatic developer (SRX-101; Konica Minolta Medical), and films were scanned with a 300-dp1 resolution on a scanner (PowerLook 1000; UMAX).

Polyacrylamide gel preparation: The resolving gel percentage (%) was selected according to the molecular weight of protein being investigated and the lower the molecular weight the higher the gel percentage used. The protein of interest in experiments was cleaved caspase-3 which has low molecular weight (17,19 KDa). For this reason, a 15% gel was prepared. Tables 4 and 5 show the recipe to prepare the different resolving gel percentages and stacking gel, respectively.

Table 5. Formula of the different resolving gel percentages (15 ml).

Components	7.5%	10%	12%	15%
1.5M Tris (pH=8.8)	5 ml	5 ml	5 ml	5 ml
30% acrylamide	3.75 ml	4 ml	6 ml	7.5 ml
water	6.15 ml	5.9 ml	3.9 ml	2.4 ml
20% SDS	75 µl	75 µl	75 µl	75 µl
10% APS	75 µl	75 µl	75 µl	75 µl
TEMED	25 µl	25 µl	25 µl	25 µl

Table 6. Stacking gel formula (5 ml).

Components	
0.5 M Tris (pH= 6.8)	0.62 ml
30% acrylamide	0.833 ml
Water	3.82 ml
20% SDS	25 µl
10% APS	50 µl
TEMED	5 µl

2.2.2.11 Autophagy analysis

The levels of proteins that included light chain protein (LC3), sequestosome 1(SQSTM1/p62) and mammalian target of rapamycin kinase (mTOR) were measured by Western blot analysis to assess the autophagy process in cells exposed to graphene nanomaterials. MRC-5 and A549 cells incubated with different GO and r-GO concentrations for 24 hours. Fifty μM of chloroquine was used as control for the analysis of autophagy. The Western blot was performed as described in 3.10.

2.2.2.12 CellROX flow cytometry assay

The CellROX assay was performed as described by manufacturer. Both cell lines were seeded into 12-well plates and left to attach overnight before incubation with the graphene derivatives. MRC-5 and A549 cells were incubated with GO and r-GO at concentrations ranging from 125 to 300 μg/ml and exposed for 24 and 48 hours. The assay kit provided positive and negative controls for oxidative stress. Tert-butyl hydroperoxide (TBHP) was used as positive control to induce oxidative stress while N-acetylcysteine (NAC) was used as negative control as it increases the antioxidant capability of the cells. Cells were incubated with 400 μM of TBHP for 1 hour to create positive control. Negative control was prepared by incubating cells with 2500 μM of NAC for 1 hour followed by treatment with 400 μM of TBHP for 1 hour under normal growth conditions. After incubation, cells were trypsinized, centrifuged at 350 × g for 5 min at 4°C, and re-suspended with 1 ml phenol free media. CellROX stain was added to a final concentration of 500 nM to the cell suspension and incubated for 1 hour at 37°C, protected from light. Ten thousand cells were measured on a Fortessa flow cytometer using 488 nm excitation for the CellROX reagent and data generated analysed by Flowing software.

2.2.2.13 GSH/GSSG-Glo™ assay

This test was undertaken using the Promega GSH/GSSG-Glo™ kit. MRC-5 and A549 cells were seeded in a white 96 well plate. Graphene derivatives were added at a concentration ranging from 31.25 to 600 μg/ml and cells were incubated for 24 and 48 hours. At each time point, the medium was removed and the cells washed with PBS to remove any remaining nanoparticles, to overcome any possible interferences. Cells were divided into two groups; one group was lysed with total glutathione lysis reagent (50 μl/well) and the other group was lysed with oxidised glutathione lysis buffer (50 μl/well). The plates were placed on a plate shaker for 5 min at room temperature followed by the addition of 50 μl of luciferin reagent to each well and then incubated for 30 min at room temperature. The luciferin detection reagent was added (100 μl/well) and left for 15 min at room temperature. Luminescence was measured using a plate reading luminometer (FLUOstar Omega). The GSH/GSSG ratio was calculated from the net RLU (luminescence) using the following equation:

GSH/GSSG = (net total glutathione RLU – net oxidized glutathione RLU)/ (net oxidized glutathione/2)

2.2.2.14 The analysis of phosphor-p38 MAPK and phosphor-HSP27

Expression of phosphor-p38 MAPK and phosphor-HSP27 proteins was analysed for MRC-5 and A549 cells by Western blotting. Both cell lines were seeded in 6 well plates and left to adhere overnight at 37°C in 5% CO_2. Cells were then incubated with GO and r-GO at a concentration of 300 μg/ml for 24 hours. Positive control cells were incubated with 25 μg/ml of anisomycin for 30 minutes. Western blot was performed as described in section 3.10 using antibodies against phosphor-p38 MAPK and phosphor-HSP27.

2.2.2.15 Genotoxicity assessment

MRC-5 and A549 were seeded into 24-well plates as described previously. Cells were then incubated for 3 and 24 hours with GO and r-GO (125 - 300 μg/ml) in complete medium. Positive control cells were incubated with 0.2 μg/ml of 4-Nitroquinoline N-Oxide for 2 hours and untreated cells were used as a negative control. Cells were trypsinized, centrifuged at 350 × g for 5 min at 4°C, washed with PBS and re-suspended with 90 μl of warm low melting point agarose (0.7% LMA in PBS). Cells in LMA were mounted onto a normal melting point agarose (1% NMA in PBS) pre-coated microscopic glass slide, covered immediately with a glass coverslip and left to cool for 30 min at 4°C. The coverslip was gently removed and another 90 μl of LMA were added and coverslip was put back and slides were left to cool again for 30 min at 4°C. The coverslips were gently removed and then the slides were placed in the lysis buffer overnight at 4°C. After this, the slide was removed from the lysis solution and set parallel into the electrophoretic chamber followed by submerging the slides with electrophoretic buffer. The electrophoresis was conducted at 4°C for 20 min at 24 volts, 300 mA. After electrophoresis, the slides were then washed twice with neutralisation buffer for 5 min. Slides were then fixed with ethanol at -20°C for 5 min and left to dry on a flat surface for 4 hours at room temperature. Ninety μl of SYBR gold dye (1:1000 dilution) were added to each dry slide to stain cells that were covered immediately with a coverslip. The samples were examined using a fluorescence microscope, with a 560 nm excitation filter and 590 nm barrier filter and a comet assay IV software was used to analyse data. (This work was in collaboration with Dr. Alessio Perotti)

2.2.2.16 Impacts of GBNs on Wnt/β-catenin and Akt cell signalling pathways

Investigation on the effects of graphene nanomaterials on cell signalling was carried out by Western blot analysis of crucial proteins that play a major role in the Wnt/β-catenin and Akt

signalling pathway including; including β-catenin, glycogen synthase kinase-3 (GSK-3β), 3-phosphoinositide-dependent protein kinase-1 (PDK1), and tumour suppressor phosphatase and tension homolog (PTEN). Protein extracts from MRC-5 and A549 cells incubated with graphene derivatives were prepared and analysed as described previously in section 3.10.

2.2.2.17 Statistical analysis

All experiments were repeated at least 3 times and data are represented as the mean ± standard deviation (SD)/standard error of mean (SEM). Statistical analysis was selected according to the type of data and undertaken using GraphPad-Prism 7 software. The statistical significance of differences were determined using one-way analysis of variance (ANOVA) with Dunnett's comparison test while two-way ANOVA was performed with Tukey's multiple comparsion test. For non-parametric data, the Kruskal-wallis test was used alongside the Dunn's test.

Chapter 3

Synthesis and characterisation of GO and r-GO

3.1 Introduction

In nanomedicine, it is essential to evaluate a nanoparticle's biocompatibility to ensure effective use and minimise toxicity. Indeed, extensive evaluation of the factors that affect the biocompatibility of nanomaterials is critical. It is well established that the intrinsic physiochemical properties of nanoparticles (shape, size, surface chemistry) can dictate the biocompatibility degree of nanoparticles (Dobrovolskaia and Mcneil, 2007, Aggarwal et al., 2009, Naahidi et al., 2013). In this study, GO and its reduced form r-GO were synthesised to assess their biocompatibility in cell culture model. Therefore, it was very critical to characterise their inherent physiochemical properties.

This chapter will focus on the synthesis and characterisation of GO and r-GO, to gain a clear understanding of the differences between the two nanomaterials. GO was synthesised from graphite using the modified Hummers' method and then thermally reduced to produce r-GO. The two nanomaterials generated were characterised using a variety of methods to elucidate their surface chemistry, size & morphology as well as their optical properties.

3.2 Results and discussion

3.2.1 GO and r-GO synthesis

The chemical oxidation of graphite is the most common method used for the production of GO and a number of protocols have been described for oxidation, including the Staudenmaier (Dreyer et al., 2010), Hummers (Hummers and Offeman, 1958), and Tour (Marcano et al., 2010) protocols. The oxidising conditions employ exfoliate graphite and introduce oxygen functional groups that improve the surface hydrophilicity of GO (Dreyer et al., 2010, Ali-Boucetta et al., 2013a, Zhang et al., 2017b). Of the different protocols available, Hummers' method seems to be the most popular. This method involves the oxidation of graphite with potassium permanganate in concentrated sulphuric acid (Hummers and Offeman, 1958). However, the product from Hummers' method contains a large fraction of unreacted graphite and a mixture of oxidation by-product that disperse poorly in water. The presence of this might hinder the development of GO for biomedical applications (Ali-Boucetta et al., 2013a). Therefore and over the years, there has been a number of different modifications, with a view to enhancing the yield and purity of the final product.

In the present study, the synthesis of GO was achieved by following the modified Hummers' method described by Ali-Boucetta and colleagues (Ali-Boucetta et al., 2013a). In this modified protocol, additional purification and centrifugation steps were introduced, allowing efficient separation of the purest fraction of GO (Ali-Boucetta et al., 2013a, Jasim et al., 2016). By the end of the process, GO was isolated as a brownish gel-like layer that sits on the top of the impurities (**Figure 7A**). The light brown GO dispersion obtained (10% yield *vs*. graphite) dispersed well in water.

In addition, r-GO was studied to model pristine graphene, due to similarities between the two materials especially in terms of hydrophobicity. Removal of oxygen functional groups present in the GO structure gives rise to r-GO. The oxygen functional groups present on GO's surface can be efficiently eliminated by the use of reducing agents such as hydrazine and its derivatives (Stankovich et al., 2007). However, reduction with hydrazine was avoided in this study due to its high toxicity and the formation of C-N bonds which does not mimic the pristine graphene structure (Dreyer et al., 2010, Zhou et al., 2009). Also, GO has been successfully reduced *via* different methods using biomolecules and microorganisms, but these agents contaminate the end product (Zhu et al., 2010a, Wang et al., 2012, Roy et al., 2015).

Here, GO was subjected to hydrothermal reduction to produce r-GO (57 % yield *vs*. GO) (Zhou et al., 2009, Pei and Cheng, 2012, Bosch-Navarro et al., 2012). The reduction was successful, based on the change in colour (brownish to black) and increased hydrophobicity of the material (**Figure 7B**). The hydrothermal reduction uses only superheated water thereby eliminating the formation of C-N bonds or any other contaminants that are associated with the use of other reduction methods. The superheated water, formed under hydrothermal condition (temperature <200 ºC and autogenous pressure), act as a strong electrolyte with a high diffusion coefficient and dielectric constant that allow the catalysis of a variety of heterolytic bond cleavage reactions (Zhou et al., 2009, Díez et al., 2015).

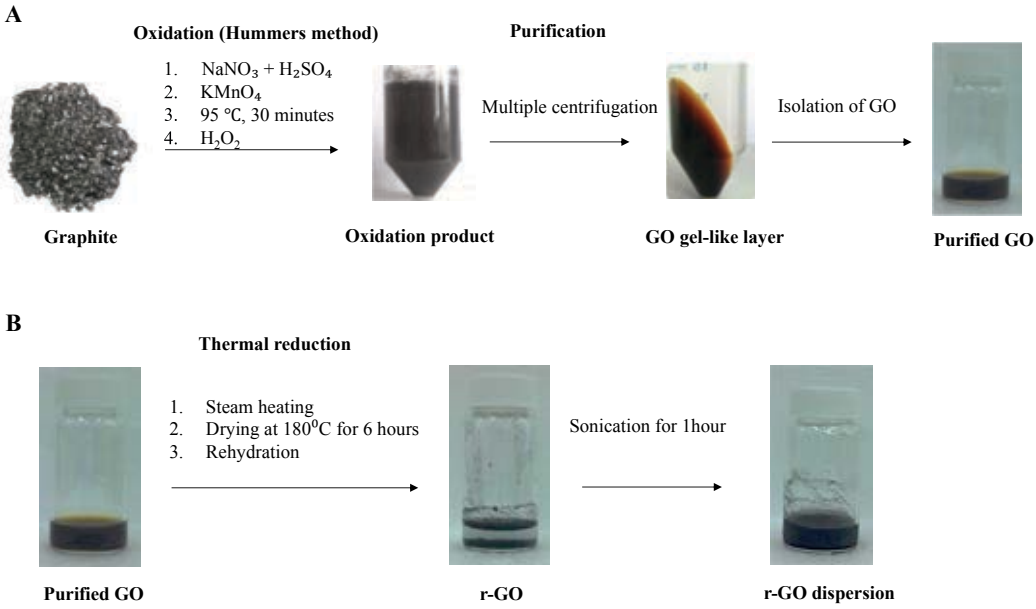

Figure 7. Schematic representation of A) the synthesis of GO by modified Hummers' method and, B) the preparation of r-GO through thermal reduction of GO. GO was obtained as a light brown material that dispersed well in water and was stable as a colloid for more than 12 months. r-GO particles were obtained by hydrothermal reduction of GO, and the material aggregated within 30 minutes in water.

3.2.2 **Surface characterisation**

The modification of graphite to GO and then of GO to r-GO was expected to lead to significant changes to the material's surface chemistry. These materials were assessed initially by Raman spectroscopy, and the particular interest is the identification of the G (1590 cm^{-1}) and D (1350 cm-1) bands. These two bands are characteristic of poly-aromatic hydrocarbons and are attributed to the vibrations of the double bonds (Ferrari, 2007, Casiraghi et al., 2009). The D band relates to the presence of defects on the surface of aromatic rings (Ferrari, 2007, Eda and Chhowalla, 2010).

The Raman spectra of GO, r-GO and graphite were compared and, as expected they all showed the G band (**Figure 8**), though it is broadened for GO and r-GO compared to graphite. The disorder band D was very distinct in the case of GO and r-GO samples, compared to graphite. This suggests the introduction of defects during the oxidation and exfoliation process of the graphite to form GO and a reduction in size of the in-plane sp^2 domains (Stankovich et al., 2007, Eda and Chhowalla, 2010, Jasim et al., 2016). The D to G band intensity ratio (I_D/I_G) of graphite was 0.2, while for GO and r-GO was 1.18 and 1.16, respectively. The increase in the I_D/I_G ratio relates generally to an increase in the degree of defects *via* the formation of sp^3 bonds (Casiraghi et al., 2009, Zhu et al., 2010b).

The 2D band near 2700 cm^{-1} was apparent only in the case of graphite; this band is a characteristic peak of graphite structure (Zólyomi et al., 2011, Kaniyoor and Ramaprabhu, 2012, Jasim et al., 2016). The 2D band is due to double resonance transitions that form two phonons with opposite momentum and is related to the number of graphene layers (Eda and Chhowalla, 2010). The weak and broad 2D bands are also another indication of disorder in the graphene structure (Robinson et al., 2009).

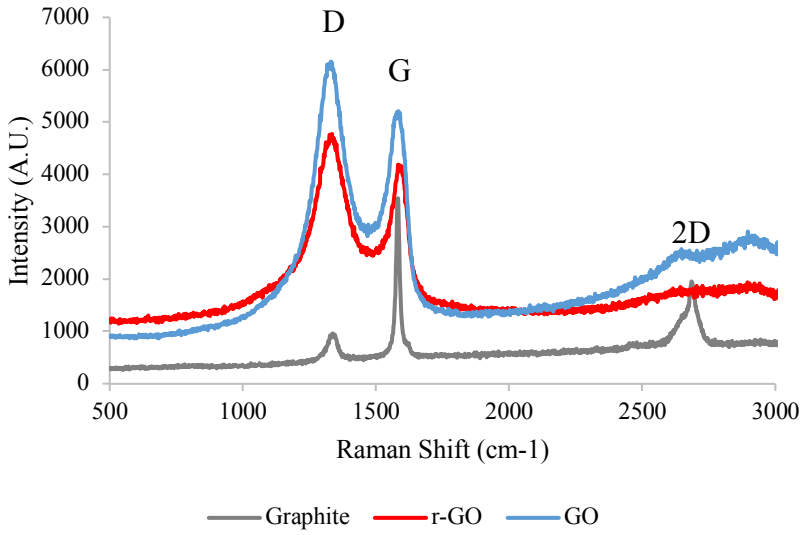

Figure 8. Raman spectra of GO, r-GO and graphite. Raman spectrum of GO and r-GO samples confirms the existence of the D and G bands.

To probe the surface chemistry in more depth, the Fourier-transform infrared (FTIR) spectra of GO and r-GO were recorded (**Figure 9**). GO's spectrum showed different oxygen configurations including the stretching vibrations of epoxide (**C-O-C**) at 1360 cm^{-1}, a broad peak between 3000- 3700 cm^{-1} and peak at 1030 cm^{-1}, corresponding to the stretching and bending vibration of hydroxyl O-H groups (namely phenol). Additionally, there are peaks at 1710 cm^{-1} for the carboxylic acids (**HO-C=O**) and bands corresponding to the stretching vibrations of sp^2 hybridized C-H (2840 and 2900 cm^{-1}). Aromatic **C=C** bonds (1610 cm^{-1}) were detected. The existence of the oxygen-containing functional groups confirmed the successful isolation of GO (Zhou et al., 2011, Song et al., 2014).

In contrast, r-GO's spectrum was a lot simpler (**Figure 9B**). Indeed, only two bands were visible after the disappearance of the **O-H** peaks (3000- 3700 cm^{-1} and1030 cm^{-1}), and epoxide bending (1360 cm^{-1}). The visible bands were corresponding to the vibrations of aromatic **C=C** bonds and carbonyl (**C=O**) groups, with decreased intensity *vs*. GO. This result indicates an effective elimination of some oxygenated groups *via* hydrothermal reduction on GO carbon planes.

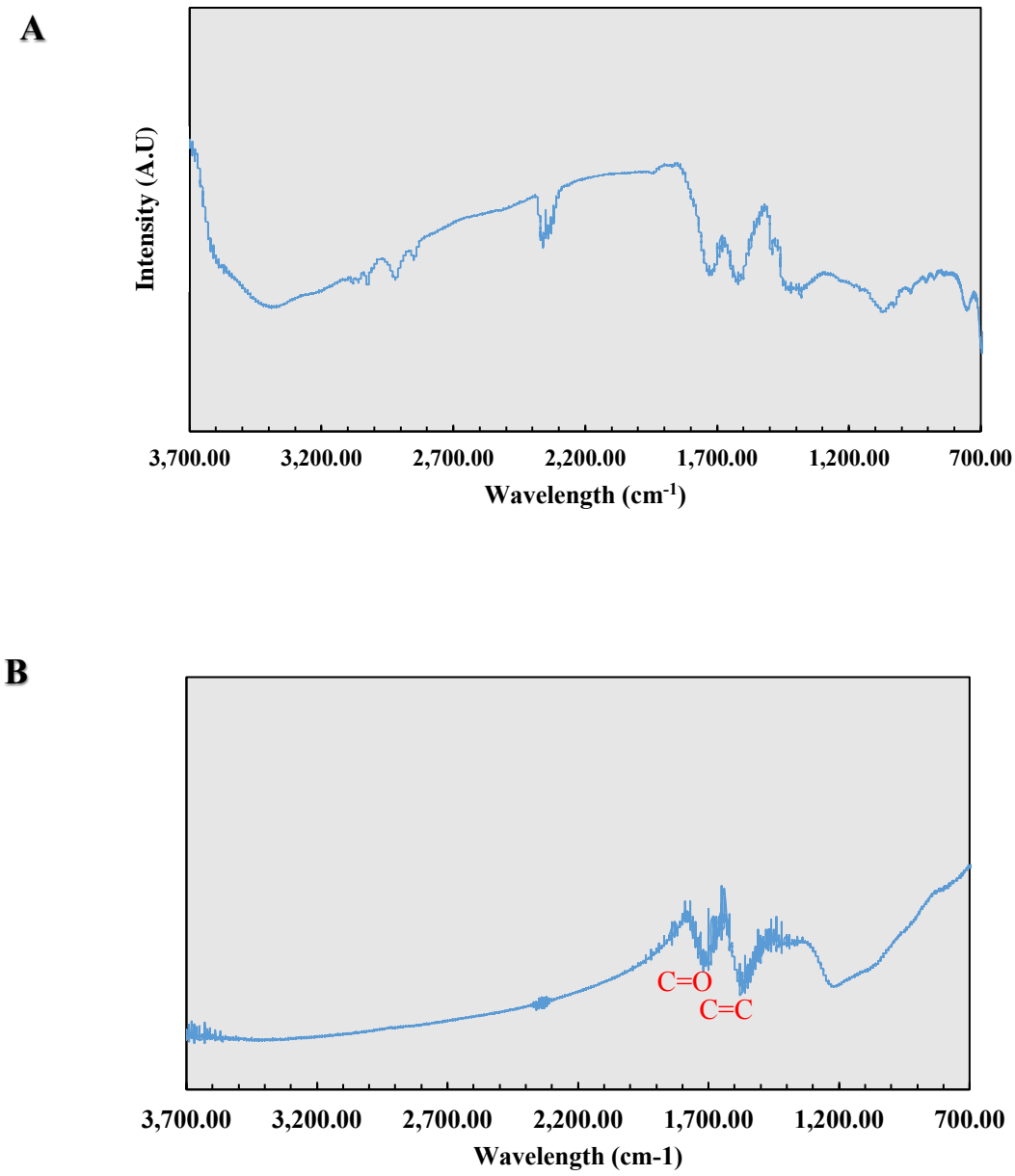

Figure 9. FTIR spectra of A) GO and B) r-GO. **A**) FTIR spectrum of GO shows the functional groups on the surface of GO. The spectrum indicates that the oxidation of graphite led to the formation of hydroxyl, epoxide and carboxyl groups on GO surface. **B**) FTIR spectrum of r-GO shows the disappearance of hydroxyl and epoxy groups absorption peaks alongside the existence of carboxylic and aromatic stretching. FTIR spectra confirms the effective elimination of oxygen functional groups after the thermal reduction of GO.

X-ray photoelectron spectroscopy (XPS) analysis was used to measure the carbon to oxygen ratio (C:O), which was at 2:1 for GO (**Figure 10A**) and 4:1 for r-GO (**Figure 10B**). Both results are in agreement with the literature (Bianco, 2013, Wick et al., 2014, Chen et al., 2012) and the ratio obtained for GO is as expected from Hummer's method (Hummers and Offeman, 1958).

High-resolution C1s spectra showed a well-defined double peak formation which is a signature of GO oxidation (**Figure 11A**). Gaussian lines were fitted to the C1s spectra of GO which presented three peaks, corresponding to the **C-C**/**C=C** in aromatic rings (284.5 eV), epoxy **C-O** (286.8 eV), carbonyl **C=O** and carboxyl group HO-**C=O** (289.0 eV). For r-GO, the intensity of peaks fitted to oxygen functional groups were decreased compared to the intensity of GO peaks (**Figure 11B**), as observed by FTIR. XPS data were consistent with the literature in terms of oxygen functional groups present on the GO and r-GO surface (Russier et al., 2013, Yang et al., 2013a, Díez et al., 2015, Mittal et al., 2016, Jasim et al., 2016, Drewniak et al., 2016, Wang et al., 2017b).

The collected XPS spectra confirms the presence of oxygen atoms on the surface of graphene due to a considerable degree of oxidation *via* Hummer's reaction. The weak peak intensities present in the C1s XPS spectrum of r-GO indicates thermal reduction of some oxygen functional groups on GO's surface.

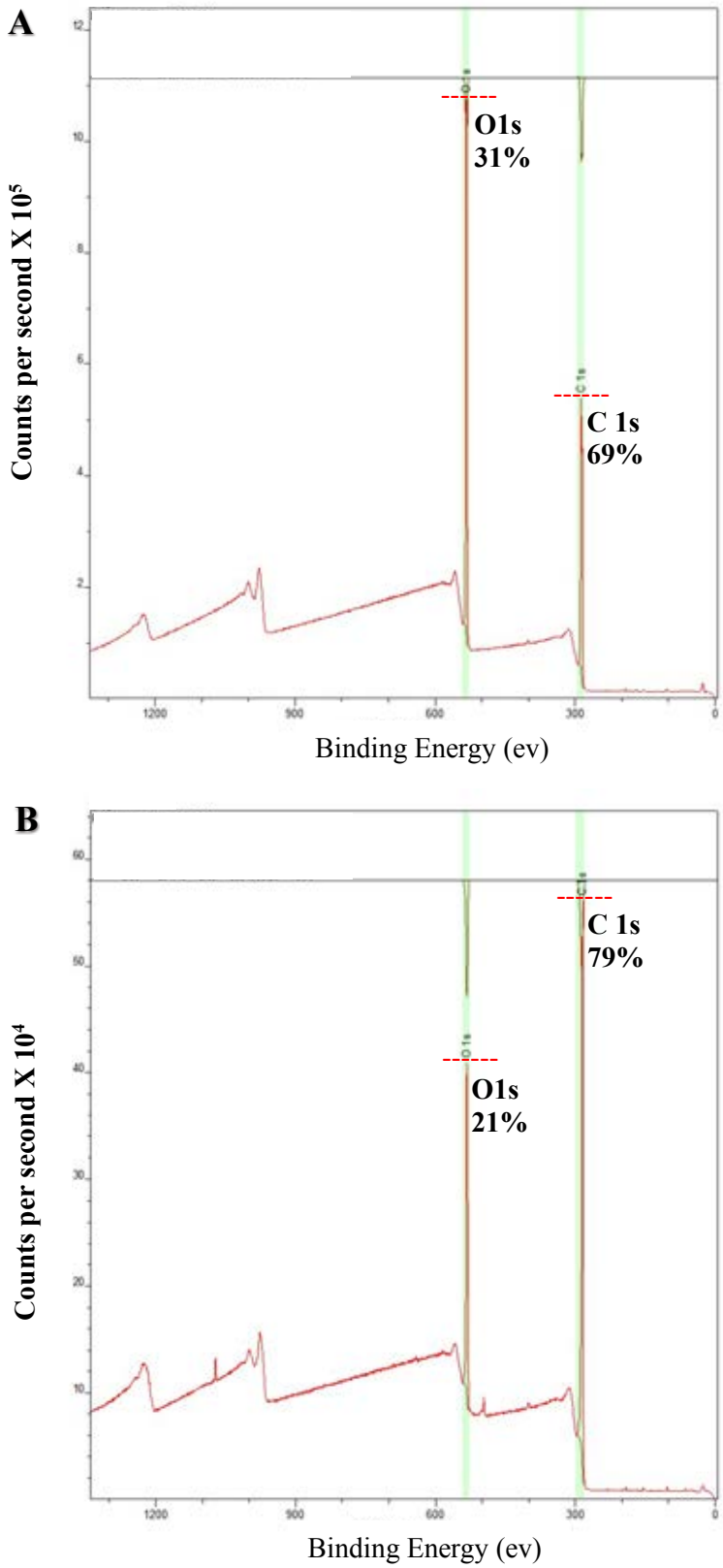

Figure 10. XPS survey spectra of GO and r-GO. A) C1s and O1s XPS spectra of GO **B**) C1s and O1s XPS spectra of r-GO. The oxygen content decreased from 31% to 21% after hydrothermal reduction of GO. The C:O ratio of GO was 2:1 while the C:O ratio of r-GO was 4:1 . XPS spectrum were obtained using CasaXPS software.

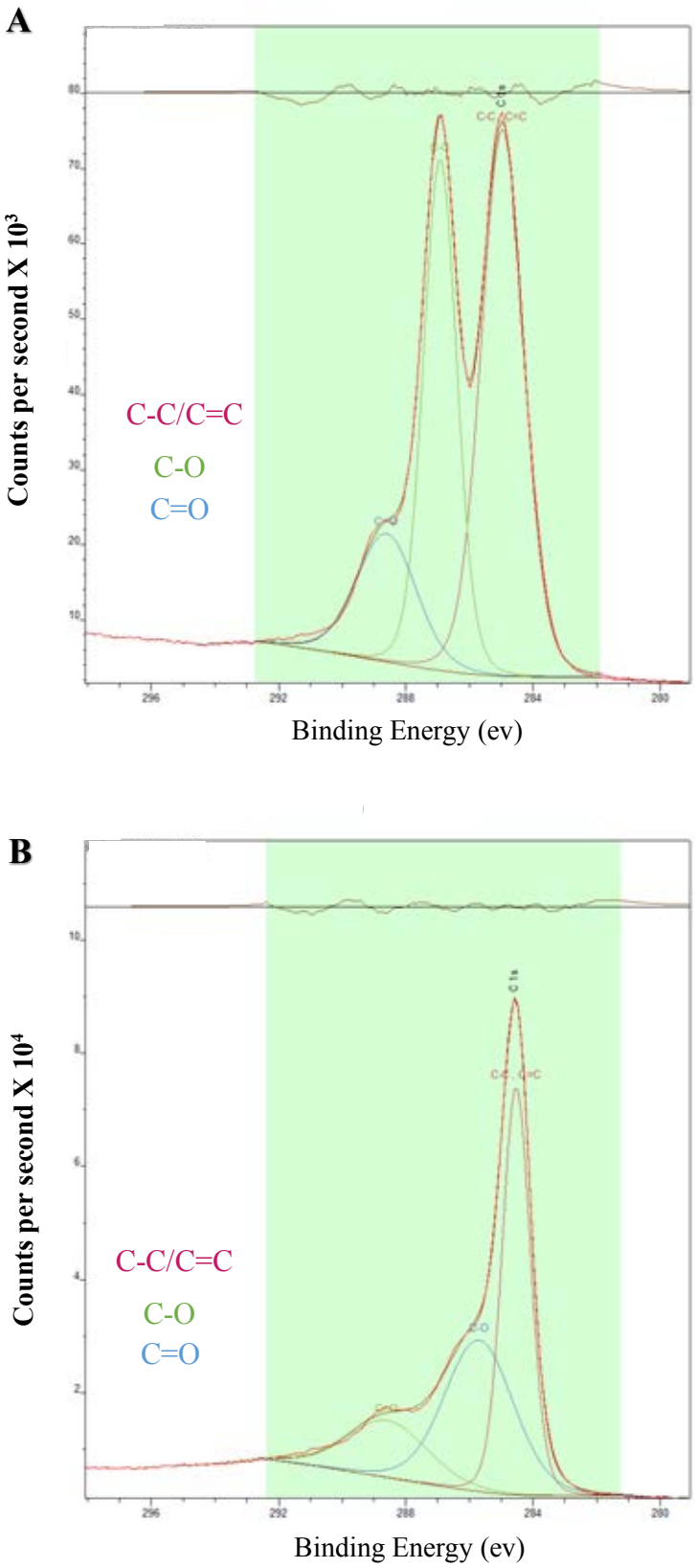

Figure 11. High-resolution C1s XPS spectra of GO and r-GO. A) Gaussian line fitted C1s spectra of GO **B**) Gaussian line fitted C1s spectra of r-GO. The XPS data indicates considerable removal of oxygen containing groups present on the GO surface following hydrothermal reduction to form r-GO. XPS spectrum were obtained using CasaXPS software.

Differences in the chemistries of GO and r-GO were further evidenced *via* thermal gravimetric analysis (TGA) analysis, whereby weight loss over a specific temperature range can be related to chemical composition (**Figure 12**). For graphite, there was no change in mass, even at high temperatures. As expected, GO showed the highest degree of functionalization. GO incurred a mass reduction (10%) between 100 and 200 ºC, due to removal of water and decomposition of the carboxylic and aldehyde groups yielding CO, CO_2 and steam (Shen et al., 2011, Chang et al., 2012, Jasim et al., 2016, Drewniak et al., 2016). The thermal decomposition of GO was accompanied by strong release of gas which led to the rapid expansion of the material, causing GO debris to disperse. This has been reported (Stankovich et al., 2007) and is the reason for limiting the amount of GO used in TGA analysis (≤ 2 mg). A second mass loss was observed at 260 ºC with GO (25%) and r-GO (7%). This relates to the pyrolysis of stable oxygen groups such as epoxides. A smaller mass loss was incurred by r-GO between 100 ºC and 270 ºC, compared to GO. This relates to the loss of the most liable oxygen functional groups during the thermal reduction of GO, whereby r-GO has increased thermal stability. A gradual mass loss was also observed for GO and r-GO from 270 ºC to 1000 ºC, which might be attributed to the pyrolysis of more stable oxygen groups such as phenols (GO) and carbonyls (GO and r-GO) or to the decomposition of the carbon skeleton (Shen et al., 2011, Chang et al., 2012, Namvari and Namazi, 2014).

Finally, the surface charges of GO and r-GO samples were measured by ζ-potential analysis. GO and r-GO were found to be negatively charged, with ζ-potential values of (- 42.4 ± 0.84 mV) and (- 30.0 ± 1.91mV), respectively. Since graphene derivatives are non-spherical, caution is advised in using ζ-potential values obtained by electrophoretic mobility measurements as calculations are based on the Henry equation which assumes spherical particles (Jacobasch et al., 1985, Jasim et al., 2016).

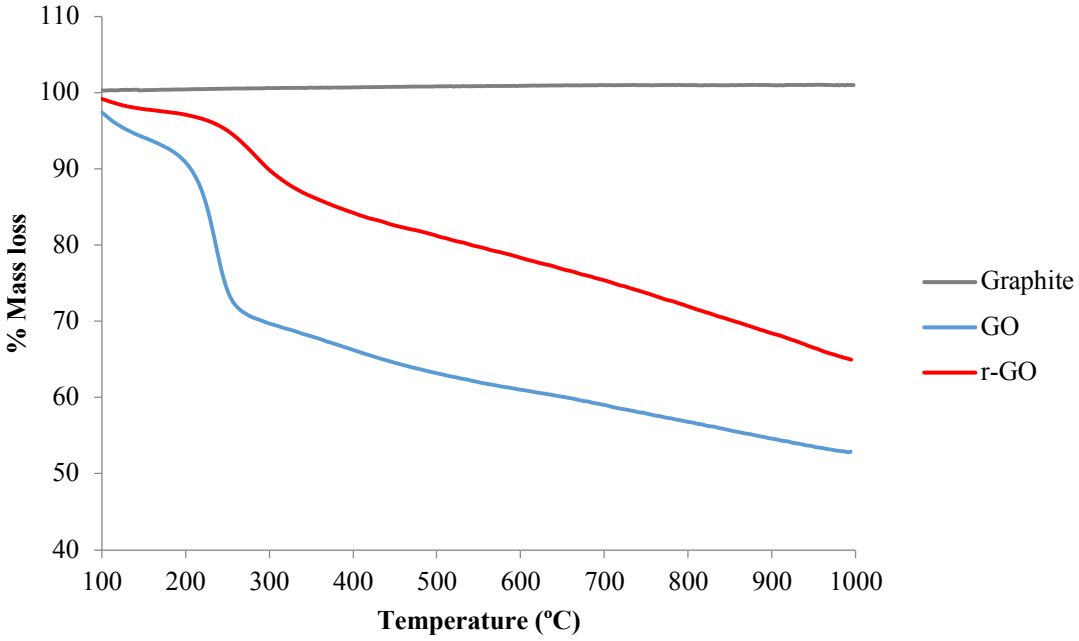

Figure 12. TGA curves of GO, r-GO and graphite. Degree of surface functionalisation of graphite, GO and r-GO by TGA. Graphite does not incur any mass loss. GO and r-GO showed first mass losses between 100 and 200 ºC due to removal of water and decomposition of carboxylic and aldehyde groups. The second mass loss occured at 260 ºC and relates to the pyrolysis of stable oxygen group such as epoxides.

3.2.3 **Size analysis**

The morphology and size of GO and r-GO particles were characterized using transmission electron microscopy (TEM). TEM analyses were performed on non-sonicated (**Figure 13A**) and water sonicated (30 minutes) (**Figure 13B**) samples.

TEM data obtained in this study showed that GO sheets were transparent and entangled with one another with irregular shapes. The non-sonicated GO sheets were mostly of micron size. The images in Figure 13A were possibly the smallest sheets in the non-sonicated sample and presented to show a clear view of GO's shape. In the case of sonicated GO sample, sheets were found to be mostly in the nano size range. Further analysis of the TEM data, by the use of image J software for 100 GO sheets, showed that the lateral dimensions in sonicated samples predominantly ranging from 11 to 30 nm (**Figure 13D**).

On the other hand, TEM images of r-GO showed black clusters of r-GO nanoparticles with sizes <200 nm (**Figure 13E**). The clustering of r-GO crumbled nanoparticles made it difficult to determine the size of individual particles, though these appeared smaller than the GO nano-sheets. This could relate to the fact that the black dry product obtained after thermal reduction of GO was re-dispersed in water and subjected for 1-hour sonication prior to TEM analysis.

Data indicated significant transformation of shape from a transparent flat GO sheet to an aggregated crumbled r-GO nanoparticle due to hydrothermal reduction of GO. This has been reported in the literature (Stankovich et al., 2007, Nethravathi and Rajamathi, 2008, Díez et al., 2015).

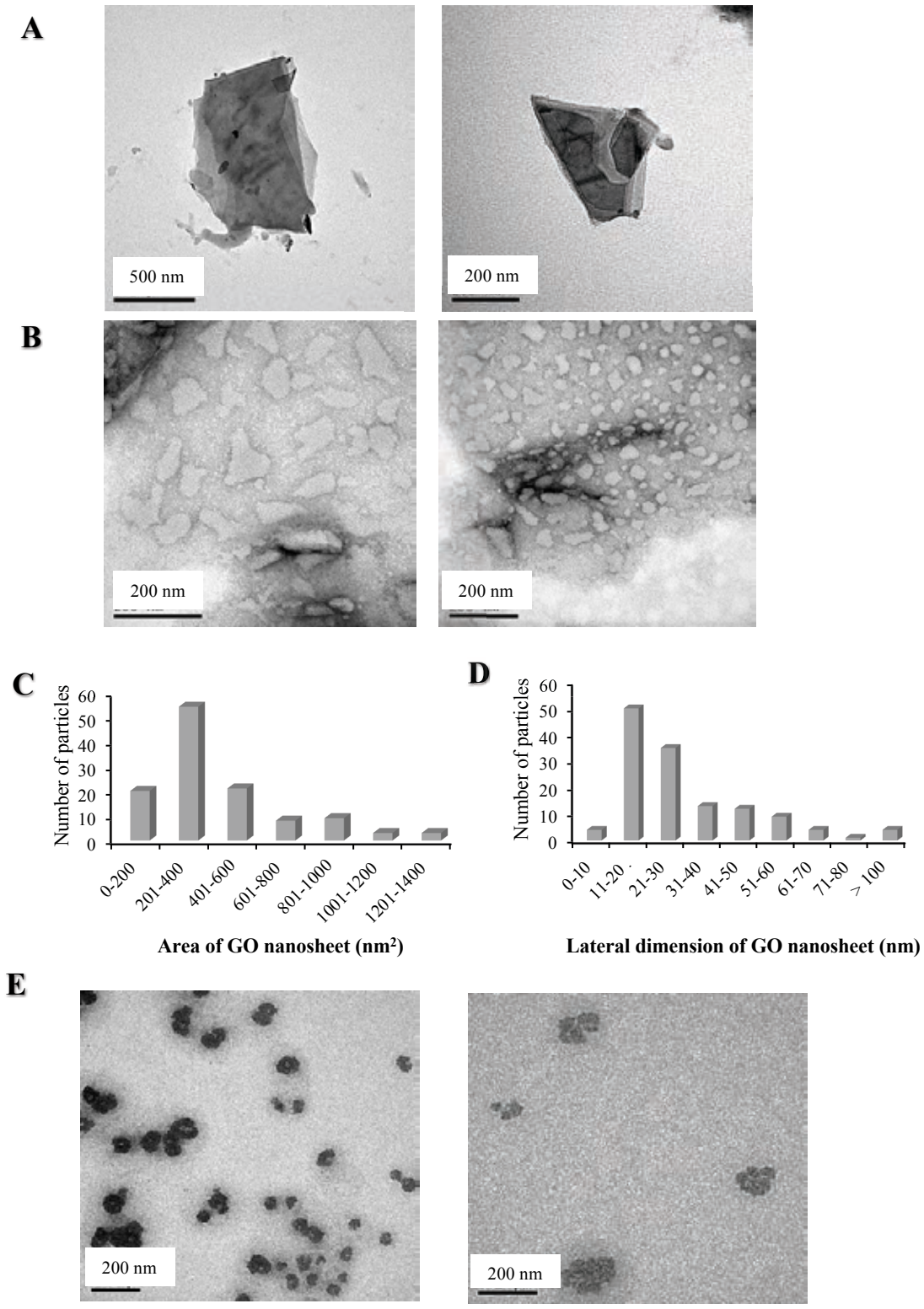

Figure 13. TEM photomicrographs of A) non-sonicated GO B) sonicated GO and E) r-GO. **A &B**) Photomicrographs showing the shape of the GO nano-sheet **C**) Size distribution of the sonicated GO nano-sheets area (nm^2) **D**) Size distribution of the sonicated GO nano-sheets lateral dimension (nm) (Image J software for 100 GO sheets, n=100). **E)** Photomicrographs showing the aggregates of r-GO nanoparticles. The aggregates of adhered r-GO nanoparticles are less than 200 nm.

Additional information on GO sheets height profile was obtained by atomic force microscopy (AFM). It has been reported that an individual GO nano-sheet is 1 nm thick (Novoselov et al., 2012). Here, AFM analysis showed that GO nano-sheets had few layers and were about 1 to 3 nm thickness. AFM was performed on GO samples before and after sonication (5 or 30 minutes) (**Figure 14**). AFM images showed that non-sonicated GO sheets were of micron size (>1 μm). The AFM images after sonication showed extensive reduction in the size of GO sheets, from micron-sized to less than 50 nm.

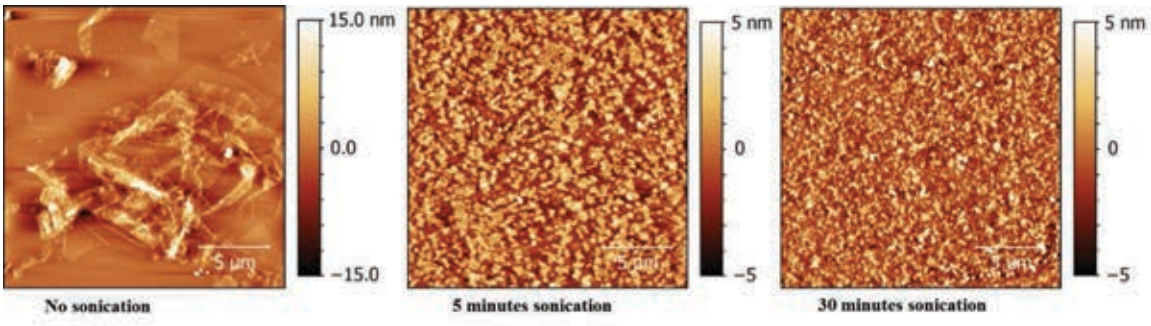

Figure 14. AFM images of GO samples. AFM analysis indicate that water sonication of GO sheets led to a pronounced size reduction of GO nanoparticles.

3.2.4 **Optical properties**

The optical properties of GO and r-GO, such as ultraviolet-visible (UV-Vis) absorbance and fluorescence, were investigated. These optical properties are beneficial to bio-imaging and predicting applications of graphene derivatives (Qian et al., 2012). The UV spectrum of GO sample showed an absorption peak at 230 nm with a shoulder around 300 nm (**Figure 15A**). The peak at 230 nm is due to the delocalisation of π-electrons resulting from oxidation of graphene, while the shoulder at 300 nm arises from C=O transitions, which is in agreement with the literature for GO (Ali-Boucetta et al., 2013a, Jasim et al., 2016).

The GO absorbance was found to be concentration-dependent and linear (R^2: 0.9986) within a 10-50 μg/ml range. Compared to GO, a peak at 230 nm was not observed for r-GO (**Figure 15B**). This most likely relates to the changes in the electronic configuration by reduction of GO (Thema et al., 2013). The UV spectra of r-GO also showed a base line shift, possibly due to the aggregation of r-GO particles. GO, but not r-GO, was also shown to emit light over the visible region when excited at a wavelength of 525 nm (**Figure 15C**). The fluorescence properties of GO are possibly due to the electron transitions between the non-oxidised carbon atoms and the oxidised carbon regions (Qian et al., 2012, Thomas et al., 2013, Jasim et al., 2016).

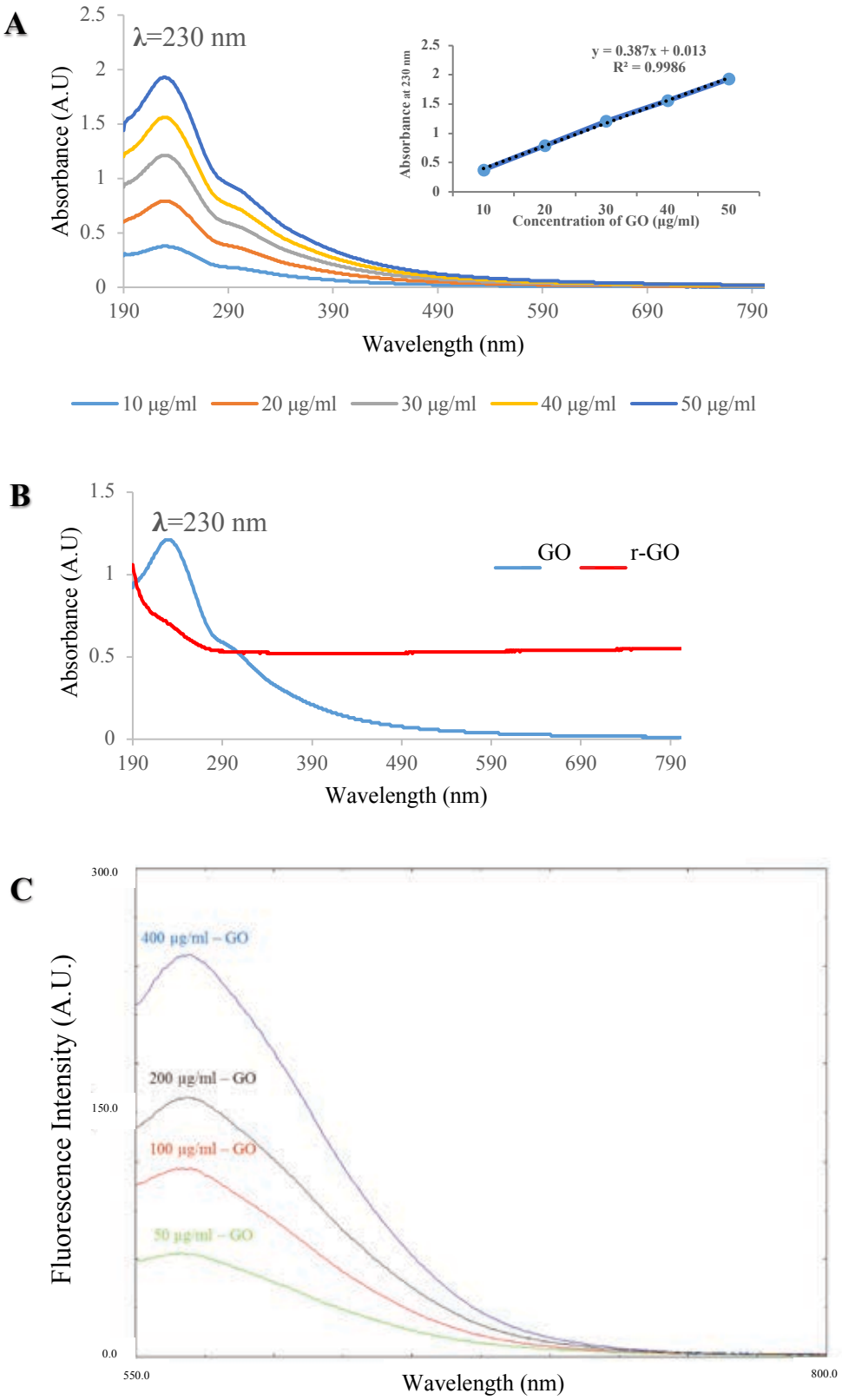

Figure 15. Optical properties of GO and r-GO. A) The UV-Vis spectrum of different concentrations of the GO sample with maximum absorption peak at 230 nm. The inset graphs display the absorbance calibration curves at 230 nm. **B)** The UV-Vis spectrum r-GO showed no maximum absorption peak, as for GO, and a base line shift due to the aggregation of r-GO particles. **C)** Fluorescence emission spectra of GO (550 -600 nm) at the excitation wavelength of 525 nm, and for different GO concentrations (50-200 µg/ml).

3.2.5 **GO and r-GO in physiologically-relevant media**

The stabilities of GO and r-GO in cell culture medium were studied. GO showed great colloidal stability in water, but the ability to remain suspended in solution depends on the chemical composition of the suspending medium (McCallion et al., 2016). This point is vital regarding cell culture medium, whereby biomolecules, salts and ions may all interact with the GO/r-GO surface resulting in aggregation of the suspended particles. GO and r-GO were dispersed in EMEM medium supplemented with 10% FBS. The sonicated GO sample dispersed better and showed colloidal stability in cell culture medium (**Figure 16B**). Non-sonicated GO dispersed poorly in cell culture medium and the GO nano-sheets were precipitated and separated from the aqueous media solution within 2 hours after dispersion (**Figure 16A**). Similar results were observed using F-12 HAM's medium supplemented with 10% FBS (data not shown). It was therefore decided to sonicate GO sample for 30 minutes before dispersing in biological medium for the cell culture experiments.

Physical factors, for instance, lateral size and thickness play a major role in the stability of graphene nanoparticles (McCallion et al., 2016). It has been found that smaller graphene sheets have a lower tendency of inter-sheet interaction and, therefore, aggregate less frequently (Khan et al., 2010). Here, it was confirmed by AFM and TEM measurements that water bath sonication of GO has led to an extensive reduction in GO sheets size from microns to nano-sheets (<100 nm). Therefore, the stability observed with sonicated GO samples in cell culture medium could be related to the smaller size of the sonicated GO than non-sonicated sample (Xu et al., 2015). r-GO dispersed poorly in both water and cell culture medium, possibly due to its high hydrophobicity (Fu and Yang, 2013, Bianco, 2013, Wick et al., 2014).

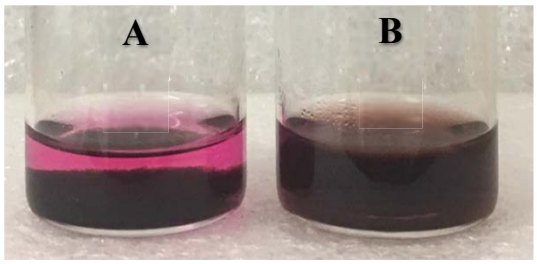

Figure 16. Static experiment of GO in EMEM cell culture media. **A**) 300 μg/ml of non-sonicated GO sample in cell culture media **B**) 300 μg/ml of sonicated GO sample in cell culture media. Non-sonicated GO samples showed poor dispersion in cell culture medium supplemented with 10% FBS. Sonicated GO samples showed stable aqueous dispersion in cell culture medium supplemented with 10% FBS, as revealed by macroscopic monitoring over than 4 weeks. Images presented are for 4 weeks of static conditions.

In conclusion, highly purified GO nano-sheets have been synthesised, by following a modification of the Hummer's method. Furthermore, r-GO was synthesised through thermal reduction of GO. Surface characterisation tools have confirmed the successful oxidation of graphite to GO, following the modified Hummer's protocol, and also the loss of some oxygen functional groups during the thermal reduction of GO. Polar groups such as hydroxyl groups that are present on the GO surface contribute to its good dispersion in water and stability while the reduction of oxygen polar groups on r-GO surface led to poor aqueous dispersion. Both nanomaterials have different physicochemical properties (surface chemistry and morphology), which can have a significant influence on how the materials interact with biological systems. Functionalisation of graphene-based materials can improve their stability in biological solutions. The most commonly utilised substances to stabilize graphene are polyethylene glycol (PEG) (Yang et al., 2012b, Yang et al., 2013a, Zhou et al., 2014), dextran (Chu et al., 2013, Chowdhury et al., 2013), chitosan (Yang et al., 2012a, Hu et al., 2014) and serum proteins (Jokar et al., 2014). However, the research interest of this study was to investigate the impact of the unmodified structure of graphene derivatives with different surface chemistry on biological milieu. The following Chapter 4 presents and discusses findings.

Chapter 4

Toxicological assessment of GO and r-GO *in vitro*

4.1 Introduction

This chapter focuses on the assessment of the interaction between graphene derivatives with biological milieu in a cell culture model. Two immortalised cells lines were selected to test the behaviour of GO and r-GO, one established from a 58 years old Caucasian male lung cancer patient (A549) and one established from the lung tissue of a 14 weeks' old aborted Caucasian male foetus (MRC-5). The cells lines are generally highly proliferative, easier to culture and are well adapted to the two-dimensional culture environment, and as a result, often differ genetically and phenotypically from their tissue origin and show altered morphology. In contrast to cell lines, primary cells which are isolated directly from tissues, have a finite lifespan and limited expansion capacity. On the positive side, primary cells have normal cell morphology and maintain many of the important markers and functions seen in vivo (Pan et al., 2009). A549 cells are cancerous alveolar epithelial cells and are a commonly used model to assess the pulmonary toxicity of nanomaterials, following occupational or environmental exposure and also used as a model for the development of drug therapies against lung cancer (Carero et al., 2001, Chang et al., 2011, Zhang et al., 2010). MRC-5 cells were included in this study to gain insight to how non-cancerous cells interact with graphene derivatives as such information will be of particular interest for their safety profile.

Firstly, experiments were performed to establish the cytotoxicity profiles of both materials and highlight any differences between healthy and cancerous cells. Then, studies probed possible mechanism of toxicity, including oxidative stress, genotoxicity and impact on the expression of proteins that are crucial for normal cell development.

4.2 Results and discussion

4.2.1 Cytotoxicity assessment of graphene-based nanomaterials (GO and r-GO)

Initial assessment of GO and r-GO cytotoxicity was performed using a modified-version of the lactate dehydrogenase (LDH) assay, which is based on the quantification of intracellular LDH levels, rather than LDH release (Ali-Boucetta et al., 2011). LDH release gives an indication of cell membrane damage, which is a hallmark of necrosis (Decker t. and J., 1988). The modified-LDH (m-LDH) assay gives information only about the number of viable cells in the sample but does not act as an indicator of necrosis. However, the modification allows the removal of excess nanoparticles prior to analysis, which limits the risk of interference from carbon-based nanomaterials. As such, the m-LDH assay is considered to be the most reliable method available to date to assess the cytotoxicity of this type of material (Ali-Boucetta et al., 2013a, Vranic and kostarelos, 2017) and was used here for this reason.

The results obtained from the assessment of GO and r-GO revealed toxicity to be time- and concentration-dependent and to be related to cell type and physicochemical properties. Short exposure times (3 hours) did not lead to significant toxicity, regardless of material and cell-type. However, from 24 hours, differences between materials could be observed.

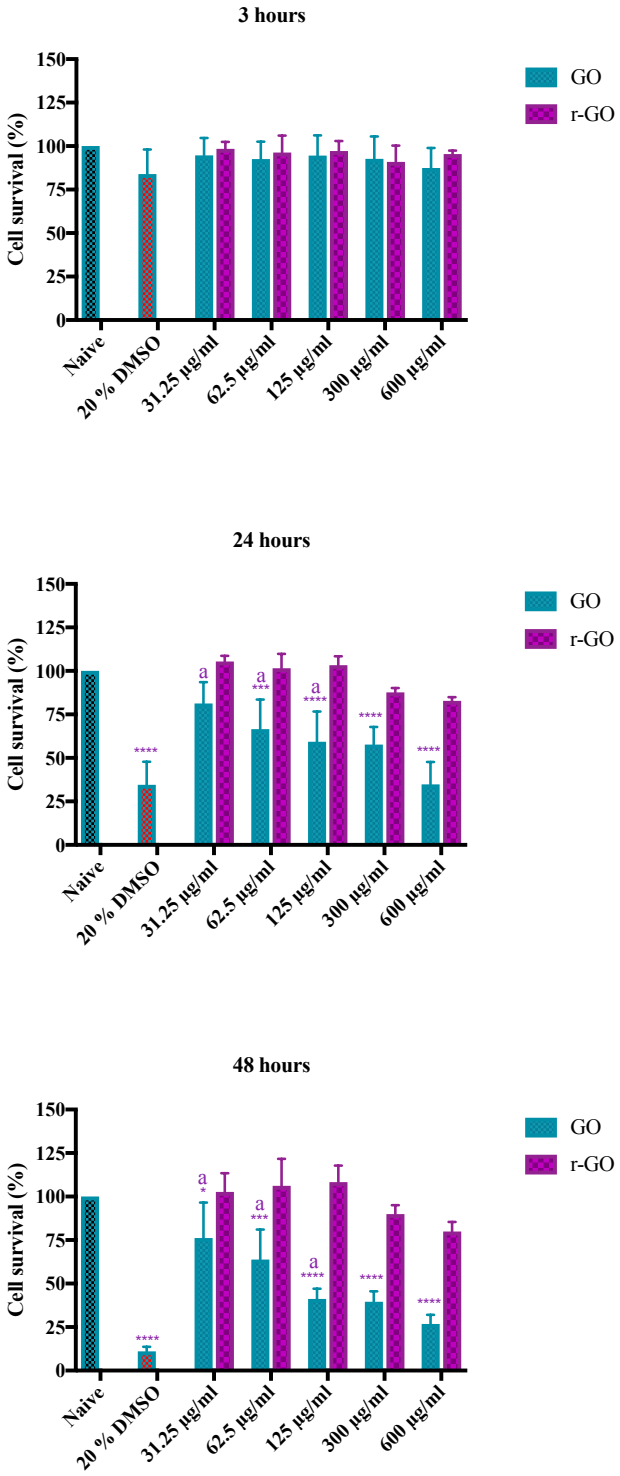

Figure 17. Cytotoxicity assessment of GO and r-GO on MRC-5 cells by uses of the m-LDH assay. Cells were incubated with GO and r-GO at different concentration (31.25-600 µg/ml) for 3, 24, and 48 hours. No toxicity was observed at 3 hours. GO decreased cell viability in a concentration and time dependent manner after 24 and 48 hours of treatment. No effect on cell viability was observed after treatment with r-GO at all tested time points. Bars represent the mean ± SD (n=4). (*$p < 0.05$, **$p < 0.002$, ***$p < 0.0002$ and ****$p < 0.0001$ versus naïve by ANOVA) and (a = $p < 0.05$ versus cells incubated with 600 µg/ml of GO by ANOVA).

For MRC-5, cell survival decreased with time and GO concentration to reach 12.9 ± 35% and 5.2 ± 27% cell survival after 24 and 48 hours, respectively, for the highest concentration tested (**Figure 17**). Exposing cells to GO concentrations up to 300 µg/ml for 24 hours resulted in a similar effect for all treatment (ca. 70-60% cell survival). However, after 48 hours, all but the lowest two concentrations tested were above the LD50. In contrast, exposure to r-GO did not significantly affect cell viability, with values remaining around the 80% toxicity threshold for all of the concentration and times tested (**Figure 17**).

For A549 cells, very similar cytotoxicity profiles were observed for GO and r-GO. For both materials, cytotoxicity increased incrementally with concentration and time (**Figure 18**). Although the toxicity of r-GO almost mirrors the results obtained in MRC-5, GO had a weaker effect on the cancer cells compared to the healthy ones. Indeed, cell survival at 600 µg/ml was twice as high in A549, compared to MRC-5 cells after 24 and 48 hours.

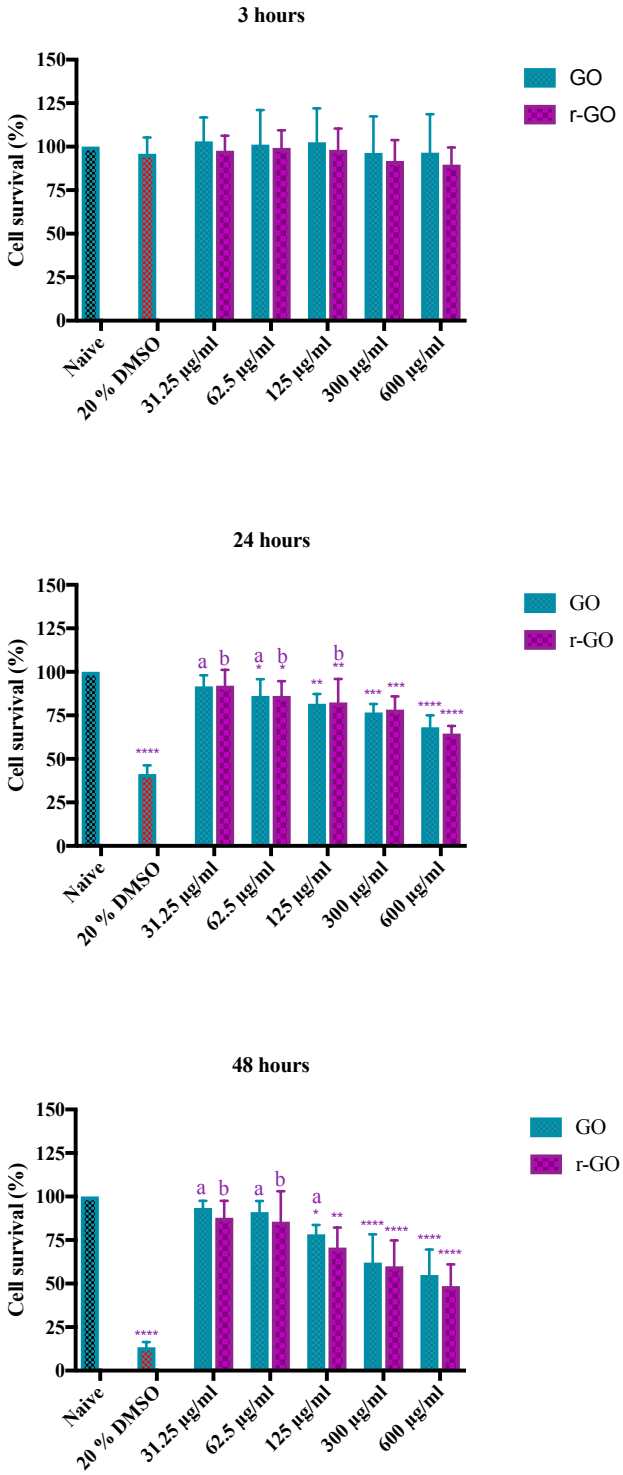

Figure 18. Cytotoxicity assessment of GO and r-GO on A549 cells by use of the m-LDH assay. Cells were incubated with GO and r-GO at different concentration (31.25-600 µg/ml) for 3, 24, and 48 hours. Both GO and r-GO decreased cell viability in a concentration and time dependent manner after 24 and 48 hours. No toxicity was observed at 3 hours. Bars represent means ± SD (n=4). (*$p < 0.05$, **$p < 0.002$, ***$p < 0.0002$ and ****$p < 0.0001$ versus naïve by ANOVA), (a = $p < 0.05$ versus cells incubated with 600 µg/ml of GO by ANOVA) and (b = $p < 0.05$ versus cells incubated with 600 µg/ml of r-GO by ANOVA).

.

There are limitations of the most common used cytotoxicity assay, and therefore alternatives to the m-LDH assay were sought, in an attempt to confirm the cytotoxicity data. Of all detection methods used to study cell survival, luminescence-based assays are the only ones not reported to interfere with carbon-based materials. However, reports of interference with metallic nanoparticles suggest that the use of such assays may be problematic (Kakinen et al., 2013, Lehmann et al., 2016). Moreover, interference with light is not the only factor to consider. Indeed, metabolic assay (e.g MTT) can result in false negatives (low toxicity) due to the interaction of carbon-based materials with the insoluble formazan crystals (Monteiro-Riviere and Inman, 2006, Liao et al., 2011, Ali-Boucetta et al., 2011).

Taking all of this into account, a new luminescence assay, RealTime-Glo™ MT, was examined regarding its suitability for the study of graphene nanomaterials. This particular viability assay measures the reducing potential of living cells and therefore, does not allow removal of the nanomaterial; this makes the test particularly suited to the study of interference. In the assay, the signal is produced following the diffusion of the reduced MT substrate from cells into the surrounding medium, where it binds to luciferase; this luminescent signal correlates to the number of viable cells. In the first instance, only GO was used due to its superior dispersibility *vs*. r-GO.

The cell viability results obtained after 3 hours of exposure already suggested possible interference, even when differences in end-point, sensitivity and toxicity mechanism were accounted for (**Figure 19**) as this short exposure time was not linked to significant GO toxicity (**Figure 18**). In comparison, results from the RealTime-Glo™ MT viability suggested a 50% reduction in cell viability, even following exposure to a low GO concentration (31.25 μg/ml). It should be noted that such levels of toxicity were not observed even at higher concentrations and 48 hours treatment when cytotoxicity was assessed using the modified-LDH assay.

It has been known that metabolic based assays may overestimate the effect of a substance that alters cell metabolism but not cell viability because of the fact that these assays analyse metabolic activity as indirect readout for cell viability (MV et al., 2005, Smith et al., 2011). However, the pronounced cytotoxicity exhibited by GO towards A549 cells at concentrations ranging from 31.25 to 125 μg/ml at all of the time points observed with RealTime-Glo™ MT assay compared to the m-LDH assay data was beyond the expected high sensitivity of RealTime-Glo™ MT assay.

In order to clarify the discrepancy with the m-LDH assay data, another experiment was performed. In this experiment, cells were plated with the assay reagent and luminescence was measured after 24 hours. Once the baseline was quantified, different concentrations of GO were added to the wells and the luminescence was measured immediately. The results showed a significant drop in luminescence after the addition of GO (**Figure 20A**), with a 25% and 95% decrease in the average signal at concentrations of 15.6 and 125 μg/ml, respectively. Taken together, all these results pointed to a likely interference between GO and the assay based on luminescence. Although never reported, this was somewhat expected since carbon nanomaterials interfere with fluorescence, a closely related phenomenon (Xie et al., 2009, Wu et al., 2018). Furthermore, interaction between GO and reagents in the assay cannot be overlooked. In all likelihood, luminescence assays will need to be modified to introduce an extra step to remove the nanoparticles, similar to what was required for the LDH assay. As this cannot be done for the RealTime-Glo™ assay, a different luminescence assay (Celltiter Glo) was selected for further tests.

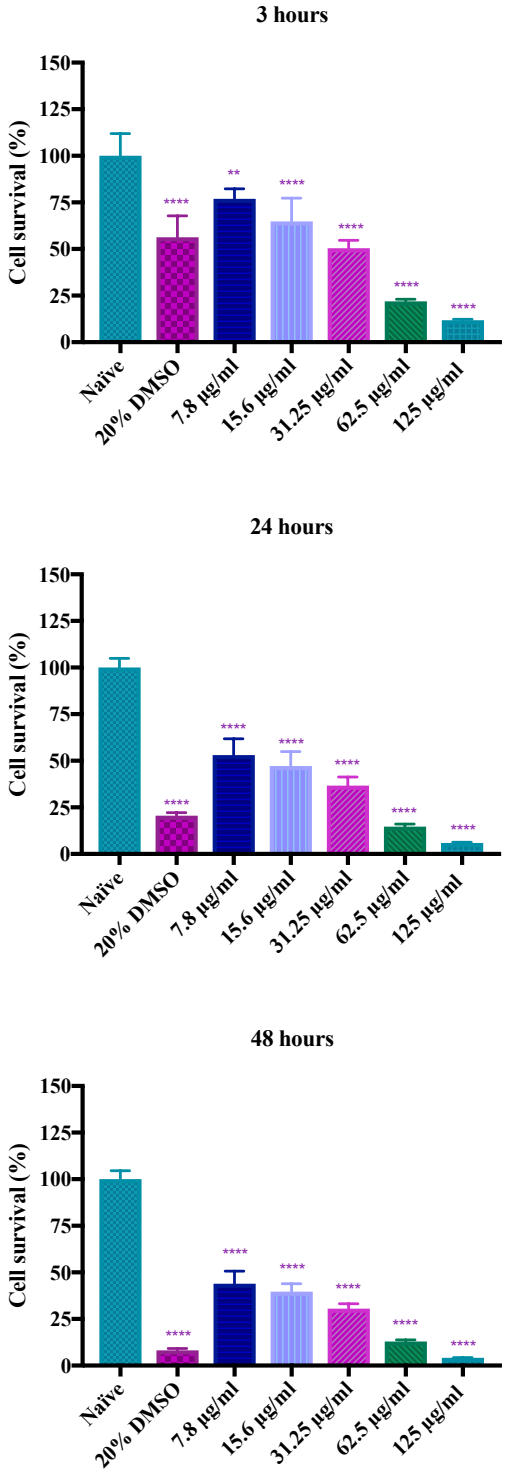

Figure 19. RealTime-GloTM MT viability assay of GO treatment in A549 cells. The figure shows the percentage cell survival of cells treated with GO in comparison with untreated cells and the positive control after 3, 24 and 48 hours. Results showed a significant dose dependent cytotoxicity of GO in A549 cells at all tested time points, which indicated possible interference of GO with the assay. Bars represent means ± SD (n=4). (*$p < 0.05$, **$p < 0.002$, ***$p < 0.0002$ and ****$p < 0.0001$ versus naïve by ANOVA).

In the CelltiterGlo assay, the number of metabolically active cells is measured through the quantification of ATP levels. Since the method requires cell lysis, a washing step can be introduced. In the absence of this extra step, GO once more appeared to be highly toxic. Indeed, for MRC-5, cell survival remained at 48% and 3%, respectively for cells incubated with 31.25 and 600 µg/ml of GO, while those values increased to 90% and 42% if the GO was washed-out (**Figure 20B**). Viability data obtained after introducing the washing step were comparable with the modified LDH assay results. These findings confirm that the washing step was successful in removing most of the interfering GO and that luminescence-based assays suffer from the same limitations as colorimetric and fluorescent ones.

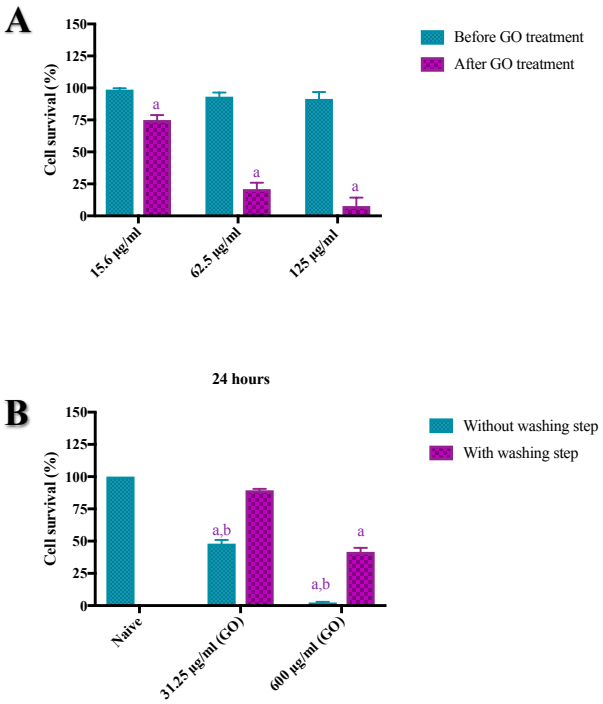

Figure 20. Assessment of interference of GO with luminescence in A) RealTime-GloTM MT and B) CellTiter-Glo viability assay. Both assays confirmed the interference with luminescence. The washing step in CellTiter-Glo assay was efficient to overcome interference with luminescent signals. Bars represent means ± SD (n=4). In figure A (a = $P < 0.001$ versus before addition of GO by ANOVA). In figure B (a = $P < 0.001$ versus naïve and b= $P < 0.001$ versus with washing step of GO by ANOVA).

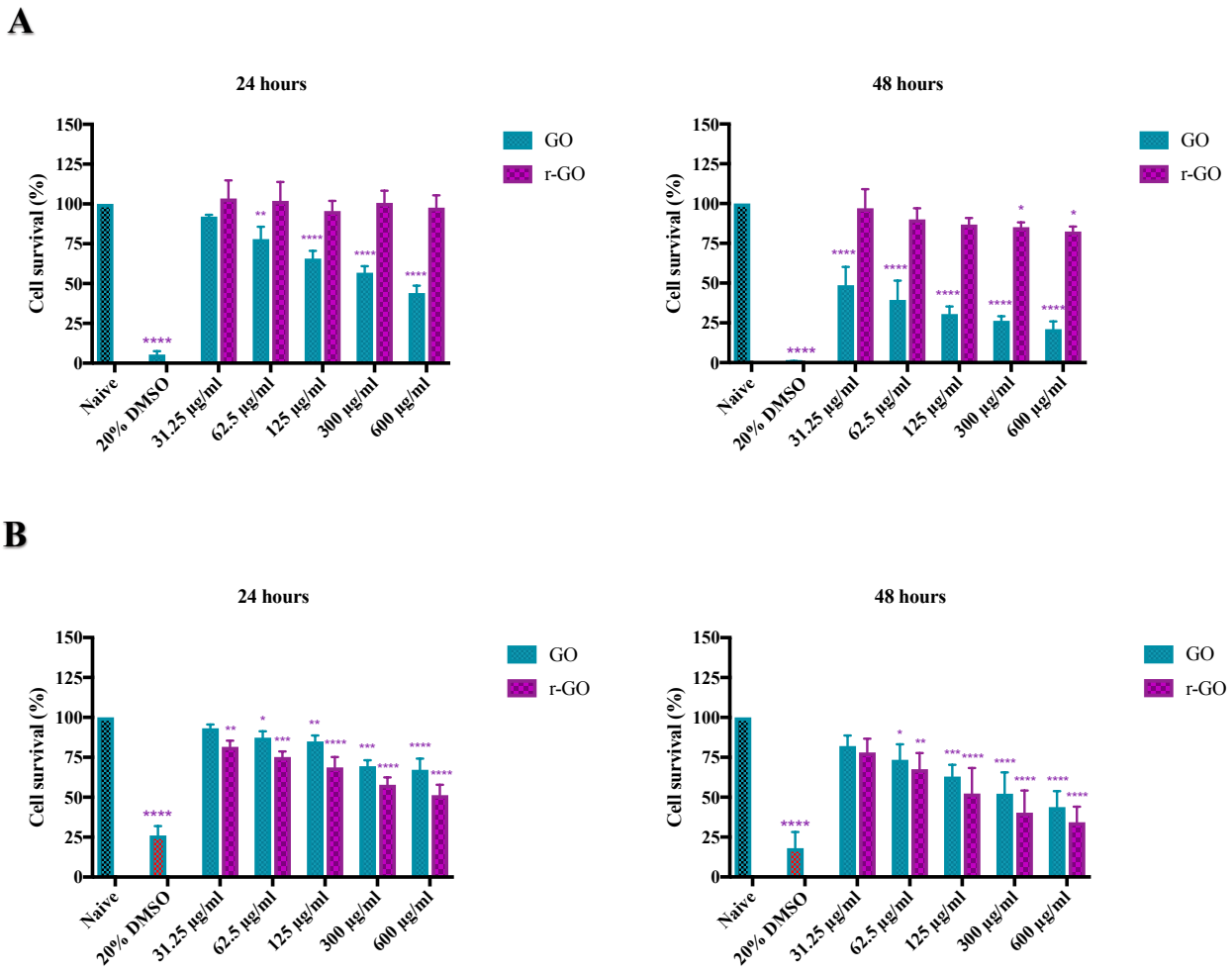

Figure 21. Cytotoxicity assessment by use of the CellTiter-Glo assay in A) MRC-5 and B) A549 cells. Cells were incubated with GO and r-GO at different concentrations (31.25-600 µg/ml) for 24 and 48 hours. GO decreased MRC-5 cell viability in a concentration and time dependent after 24 and 48 hours. A decrease in MRC-5 cell viability was only observed at the highest tested concentrations of r-GO (300-600 µg/ml) after 48 hours. For A549 cells, GO and r-GO decreased cell viability in a concentration and time dependent manner after 24 and 48 hours exposure. Bars represent means ± SD (n=3). (*$p < 0.05$, **$p < 0.002$, ***$p < 0.0002$ and ****$p < 0.0001$ versus naïve by ANOVA).

Table 7. Cytotoxicity data of modified LDH and CellTiter-Glo assays in MRC-5 and A549 cells. Values are means ± SD.

Sample	Concentration (µg/ml)	Time (hours)	MRC-5 cells		A549 cells	
			Cell survival data		Cell survival data	
			Modified-LDH (n=4)	CellTiter-Glo (n=3)	Modified-LDH (n=4)	CellTiter-Glo (n=3)
GO	**125**	**24**	60% ± 17.3	65% ± 4.9	80% ± 5.5	85% ± 3.7
		48	40% ± 5.9	31% ± 4.7	78% ± 5.3	62% ± 7.4
	300	**24**	57% ± 10.1	56% ± 4.1	78% ± 4.8	69% ± 3.7
		48	40% ± 6.0	26% ± 2.8	62% ± 16.1	52% ± 13.3
	600	**24**	35% ± 12.9	44% ± 4.6	68% ± 6.8	67% ± 6.8
		48	27% ± 5.2	20% ± 4.8	55% ± 14.6	44% ± 10.0
r-GO	**125**	**24**	100% ± 5.1	95% ± 6.3	82% ± 13.5	69% ± 6.4
		48	100% ± 9.4	87% ± 4.0	70% ± 11.5	53% ± 15.9
	300	**24**	88% ± 2.4	100% ± 7.5	78% ± 7.6	57% ± 4.6
		48	89% ± 5.0	85% ± 3.0	60% ± 14.8	40% ± 13.8
	600	**24**	83% ± 2.2	97% ± 7.7	65% ± 4.4	51% ± 6.5
		48	80% ± 5.6	82% ± 3.1	49% ± 12.6	35% ± 9.7

Using the CellTiter-Glo, the toxicity of GO was confirmed to be time- and concentration-dependent for both cell lines (**Figure 21**). r-GO showed a similar cytotoxicity profile to GO in A549 cells. The modified-CellTiter-Glo assay data were then compared to the modified-LDH assay (**Table 7**). The results from both assays shown the same trend, and values were mostly in agreement, generally revealing a higher sensitivity of MRC-5 to GO, but not r-GO, compared to A549 cells.

There are limited number of investigations of the biocompatibility of graphene derivatives on MRC-5 cells. However, the few studies published reflect the results obtained here, where the GO's LD50 was around 130 µg/ml after 48 hours and r-GO showed no cytotoxicity (Muthoosamy et al., 2015, Geetha Bai et al., 2017). Cytotoxicity of GO has also been reported from studies using normal human lung fibroblast (HLF) (Wang et al., 2013) and

human dermal fibroblasts (HDF)(Wang et al., 2011). These studies used concentrations beyond 50 μg/ml and examined effects after 24 hours. Taken together, data indicate cytotoxicity of GO towards healthy normal fibroblasts. Thereby, GO's biocompatibility must be considered before its biomedical *in vivo* applications. The observed cytotoxicity profile for MRC-5 reveals the impact of the different physiochemical properties between GO and r-GO on cellular interaction. It has been reported that the higher level of oxidation of GO compared to r-GO contributes to the increased cytotoxicity of GO against human endothelial cells and keratinocytes (Das et al., 2013). Therefore, the high GO cytotoxicity against MRC-5 could be related to its higher oxidation level than r-GO. In contrast, Bengtsen and colleagues recently reported that the oxidation level has no effect on GO and r-GO nanomaterials cytotoxicity in the case of a lung epithelial cell line FE1 (Bengtson et al., 2016). However, in the latter study both GO and r-GO were reported as non-cytotoxic and the lateral dimension of the nanoparticles was larger (>500 nm) than the size of nanoparticles used in the current study (<200 nm). Thus, size could be a major factor in the cytotoxicity data. Indeed, it has been reported that GO cytotoxicity is concentration (50-200 μg/ml) and size (160-780 nm) dependent and GO with a smaller size exhibits the most cytotoxic effect (Chang et al., 2011).

Exposure of A549 cells to graphene derivatives at concentrations ranging from 31.25 to125 μg/ml) indicated subtle impacts on cell viability up to 48 hours and the oxidation level had no effect on cytotoxicity. The cytotoxicity profile seen for A549 is in agreement with other studies in which GO had similar physiochemical properties to the GO used in this research (Ali-Boucetta et al., 2013a, Jasim et al., 2016). In these other studies, GO was synthesised following the same methodology as the present work and the cytotoxicity was assessed using the modified LDH assay, which is considered most reliable method to screen carbon-based nanomaterials (Vranic and kostarelos, 2017). The results collectively indicate that

graphene derivatives are biocompatible to A549 cells which is in agreement with GO drug delivery studies (Zhang et al., 2010, Zhang et al., 2017a).

In contrast, other studies have reported a significant damaging effect on A549 by exposure to GO at lower concentrations (Hu et al., 2011, Mittal et al., 2016). For example, Mittal et al reported concentration- and time-dependent cytotoxicity for A549 cells exposed to 1-100 μg/ml of GO and r-GO (Mittal et al., 2016). However, in Mittal et al and Hu et al work, the MTT assay was used to screen cytotoxicity, and has been reported to be unreliable for carbon-based nanomaterials (Liao et al., 2011, Ali-Boucetta et al., 2011). Therefore, comparisons between the literature should be drawn cautiously as various assays as well as different physiochemical properties of graphene derivatives can give different conclusions regarding biocompatibility.

In drug delivery, nanoparticles can deliver antineoplastic drugs into cancer cells with minimum drug exposure to healthy cells (Bahrami et al., 2017). Therefore, the safety profile of nanoparticles proposed for drug delivery application should be carefully addressed using healthy cells. Here, the high sensitivity of healthy lung cells toward GO cytotoxicity calls for further thorough systemic investigation before drawing any solid conclusion on the safety of graphene nano-sheets of certain size and surface chemistry. However, the preliminary data obtained here indicate that GO could be used safely at concentrations up to 31.25 μg/ml. With regards to r-GO, although no toxicity could be observed in healthy cells, data from cancer cells indicate that safe concentrations of r-GO are up to 125 μg/ml. Despite the better cytotoxicity profile of r-GO than GO, the surface chemistry of GO in the present work render it a favourite candidate for drug delivery than its reduced form. For instance, GO has a several functional groups on its surface that allow the possibility of different bio-conjugation to improve its biocompatibility (Bitounis et al., 2013).

In summary, the cytotoxicity of graphene derivatives was concentration-, time- and cell-dependent. More interestingly, toxicity varied with the material used. These data indicate that the surface chemistry of graphene nanoparticles has a crucial influence on biocompatibility of graphene derivatives. The next step will examine nanomaterial-cell interactions and the mechanisms responsible for the toxicity observed.

4.2.2 **Cellular interaction of graphene nanomaterials**

Following identification of the potential cytotoxic effect of graphene derivatives in lung cells, the question addressed was whether cytotoxicity is due to internalisation or interaction with the plasma membrane. Some studies have shown that the entry of graphene nanoparticles is responsible for their observed cytotoxicity, whereas other studies have showed that graphene translocation into cells can transport therapeutic drugs without causing injury to cells (Zhang et al., 2016).

Different energy dependent endocytosis processes are required for the entry of nanoparticles into cells. There are various types of endocytotic pathways, including phagocytosis that can actively internalize large particles (>500 nm) into phagocytes (Sahay et al., 2010, Zhang et al., 2016). Moreover, endocytosis is classified into multiple mechanisms depending on the size of nanoparticles, namely, micropinocytosis (< 500 nm), clathrin-dependent endocytosis (~120 nm), caveolin-dependent endocytosis (~ 60 nm), and clathrin and caveolin-independent endocytosis (~ 60 nm) (Sahay et al., 2010, Conner and Schmid, 2003, Kinnear et al., 2017). Non-phagocytic cells such as A549 and MRC-5 cells are able to uptake small nanoparticles (He et al., 2010, Vila et al., 2012). As the average size of graphene derivatives in the present study was found to be predominantly less than 200 nm, it was expected that their internalization will be *via* a non-phagocytic endocytosis mechanism in MRC-5 and A549 cells. In addition, some nanoparticles have the potential to gain entry through passive

diffusion across the plasma membrane (Shang et al., 2014). For example, carbon nanotubes are reported to gain entry to cells *via* piercing the plasma membrane (Lacerda et al., 2007). Fluorescence staining is commonly used as a method to study nanoparticle uptake by cells (Sadik et al., 2009). However, as stated in the previous section, quenching of the signal makes this method unsuitable for graphene nanomaterials (Xie et al., 2009, Wu et al., 2018). Al-Jamal and Kostarelos (2010) have proposed an alternative approach based on the qualitative assessment of changes in light scattering by flow cytometry. Specifically, the method is based on the binding of carbon-based nanomaterials to cells leading to an increased granularity which translates into changes to the side scatter profile (Al-Jamal and Kostarelos, 2010, Suzuki et al., 2007). Although, side scattering method is unable to differentiate between cell adsorption and internalization of nanoparticles by cells, this method was successfully used for the study of the uptake of carbon nanotubes (Al-Jamal and Kostarelos, 2010, Ali-Boucetta et al., 2011), zinc oxide, titanium dioxide and silver nanoparticles (Toduka et al., 2012) and was expected to provide useful information on the interaction of graphene nanomaterials with cells (Ma et al., 2015). For this experiment, cells were exposed to a maximum concentration of 125 μg/ml because of the high cytotoxicity exhibited by graphene derivatives at higher levels that could lead to a low cell count.

In the present study, the interaction was analysed for MRC-5 and A549 cells after incubation with GO and r-GO at different concentration ranges (15.6-125 μg/ml) for 24 and 48 hours. Here, the lack of change in the side scatter profiles suggest a negligible interaction between nanomaterial and MRC-5 (**Figure 22**) and A549 cells (**Figure 23**). This somewhat challenges the cytotoxicity data, especially in the case of MRC-5 cells where the low cell survival observed after 48 hours treatment with 125 μg/ml of GO would imply some interaction between the cells and nanomaterials.

It is possible that the shape and the 2D structure of the GO and r-GO nanoparticles had restricted their capacity to translocate into cells (Verma and Stellacci, 2010, Li et al., 2016, Zhao et al., 2017, He and Park, 2016, Xie et al., 2017). The study of the interaction of 2D nanomaterials is still in early stages, especially as this shape is less common compared to cylindrical and spherical shapes (Chimene et al., 2015, Kinnear et al., 2017). So far, the side scatter method has been applied successfully to a range of material of varying composition and shape, but different tools were required to arrive at conclusions about the cellular uptake of graphene derivatives in this work.

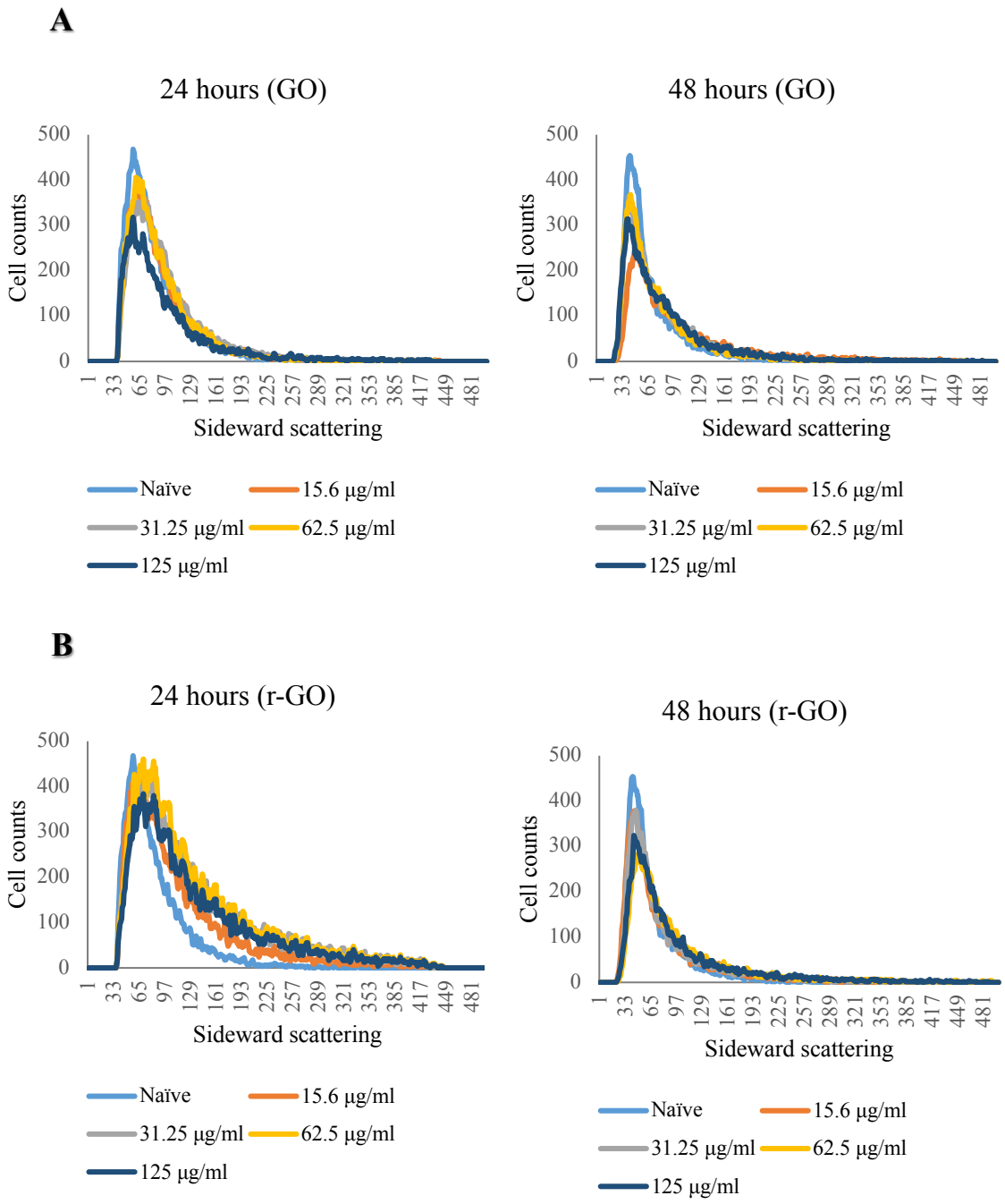

Figure 22. Analysis of cellular uptake of GO and r-GO using flow cytometry in MRC-5 cells. Univariate scatter histograms were recorded by flow cytometry showing the cell number versus sideward scattering for the non-cancerous human lung MRC-5 cells incubated with varying concentrations of GO **(A)** and r-GO **(B)** (15.6-125 µg/ml) for 24 and 48 hours (n=3). No change in the cellular granularity (side scattering) was detected in cells incubated with GO or r-GO as compared to the untreated cells (naïve) at both time points.

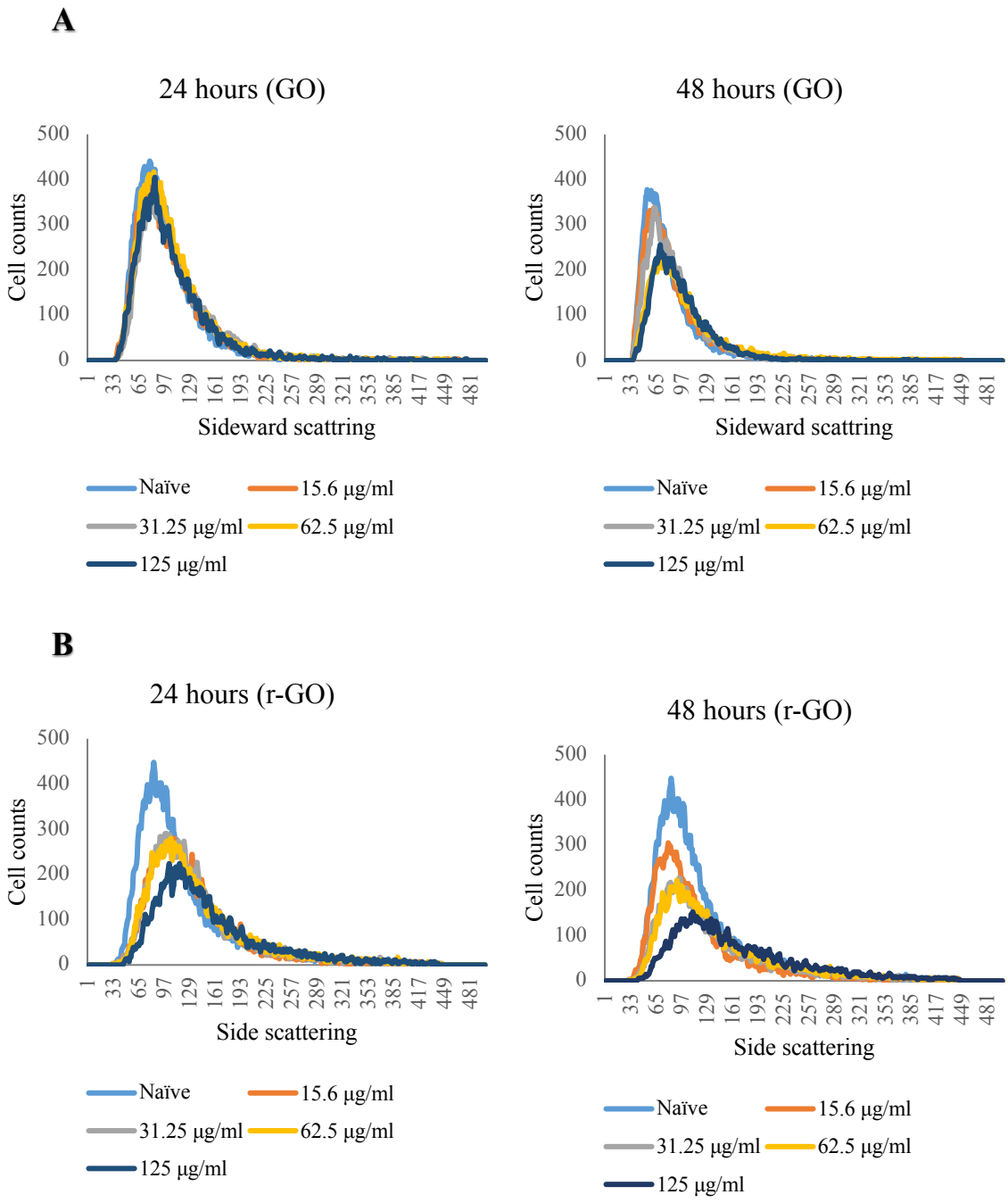

Figure 23. Analysis of cellular uptake of GO and r-GO using flow cytometry in A549 cells. Univariate scatter histograms were recorded by flow cytometry showing the cell number versus sideward scattering for the human lung carcinoma A549 cells incubated with varying concentrations of GO **(A)** and r-GO **(B)** (15.6-125 µg/ml) for 24 and 48 hours (n=3). The change in the cellular granularity (side scattering) was minimal after 24 and 48 hours incubation with GO and r-GO versus naïve cells.

The cellular uptake of graphene derivatives in the present study was further investigated indirectly by assessing the cytotoxicity of GO and r-GO after blocking cellular uptake *via* an endocytosis inhibitor. MRC-5 and A549 cells were pre-incubated with sodium azide to block endocytotic uptake. In this experiment, the findings at the 48-hour time-point were excluded because the inhibitory effect of sodium azide will have subsided by this time.

For MRC-5 cells, there was a significant decrease in the cytotoxicity of GO when cellular uptake was inhibited by sodium azide. Cell viability was 67% compared to 52% when cellular uptake was not blocked and for the highest GO concentration (**Figure 24A**). This small increase in cell survival indicates that only a very small proportion of GO is taken up by the cells through an active process, if at all. The flow cytometry results and these findings indicate that uptake is unlikely to be the main mechanism that is responsible for GO toxicity. However, the induced cytotoxicity observed at high GO concentrations might relate to plasma membrane damage or possibly passive internalization of graphene nanoparticles into cells.

In case of A549 cells, there was not any significant decrease in the cytotoxicity provoked by GO or r-GO after blocking the cellular uptake process other than the trend was that sodium azide rescued the viability of cells exposed to GO but not r-GO (**Figure 24B**). However, as the cytotoxicity of graphene derivatives toward A549 cells after 24 hours was slightly low, it was difficult to arrive at a firm conclusion regarding the effect of sodium azide.

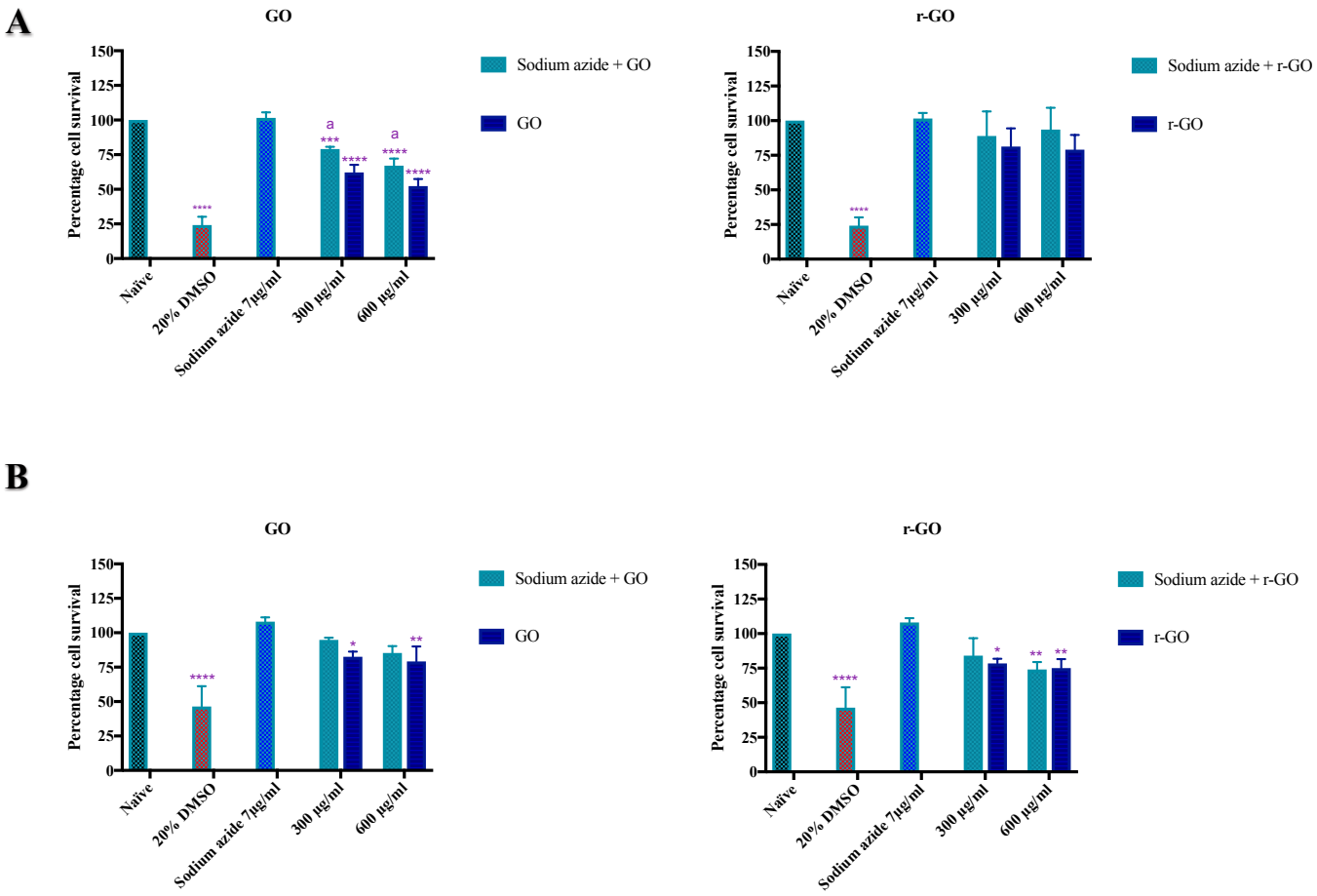

Figure 24. Cytotoxicity assessment after blocking endocytosis cellular uptake in A) MRC-5 and B) A549 cells and by means of the m-LDH assay. Cells were pre-treated with the endocytosis inhibitor (7 µg/ml of sodium azide for 1 hour) before treatment with GO or r-GO at cytotoxic concentrations (300-600 µg/ml) for 24 hours. **A)** Shows the m-LDH data obtained for MRC-5 cells. **B)** Shows the m-LDH data obtained for A549 cells. A significant decrease in GO toxicity in MRC-5 cells was observed after blocking endocytosis versus GO toxicity without blocking endocytosis. In A549 cells, there was no significant change in the GO or r-GO toxicity after blocking the endocytosis process versus toxicity without endocytosis inhibitors. Bars represent means ± SD (n=3). (*$p < 0.05$, **$p < 0.002$, ***$p < 0.0002$ and ****$p < 0.0001$ versus naïve by ANOVA) and (a = $p < 0.05$ versus equivalent concentration of GO without endocytosis inhibitors by ANOVA).

Collectively, the findings presented so far indicate there is negligible cellular uptake of GO and r-GO nanoparticles by MRC-5 and A549 cells. However, both of the techniques used to assess cellular uptake are indirect and qualitative tools. For these reasons, further investigation regarding cellular uptake of GO and r-GO is required with more advanced techniques to be sure about the capacity of graphene derivatives to translocate into cells.

The inability of GO to be up taken by MRC-5 and A549 cells is in agreement with other studies, which have shown that only phagocytes such as macrophages can uptake GO nanoparticles (Yue et al., 2012, Ma et al., 2015). Reshma and colleagues reported the inability of A549 cells to uptake r-GO nanoparticles by using side scattering measurement as in this work (Reshma et al., 2016). r-GO was expected to have a very weak cellular uptake because of its poor dispersion in water as result of its high hydrophobicity which can minimize its cellular interaction (Chatterjee et al., 2014). As presented in chapter 3, both GO and r-GO are negatively charged with a ζ-potential value of (- 42.4 ± 0.84 mV) and (- 30.0 ± 1.91mV), respectively. Therefore, this weak capability of cells to uptake both GO and r-GO could be related to the strong electrostatic repulsions between the negatively charged cell surface and the negatively charged graphene surface (Verma and Stellacci, 2010, Yue et al., 2011, Yue et al., 2012). Macrophages may overcome the strong electrostatic repulsions between graphene surface and the negatively charged cell membrane through the FCγ receptor mediated phagocytosis pathway (Yue et al., 2012). Zhang and colleagues showed that changing 3D polystyrene nanoparticles to 2D polystyrene nanoparticles rendered them unable to translocate into mammalian cells (Zhang et al., 2012b). Therefore, besides the negatively charged surface of GO, its 2D shape might plays a major role in weak cellular uptake. To investigate further the interaction of graphene derivative with the cellular membrane, their capacity to lyse RBCs was evaluated.

Hemolysis assessment is one of the most common assays used to screen for the interaction of nanomaterials with RBCs (Dobrovolskaia and McNeil, 2013). Hemolysis is the damage to RBCs that may lead to life threatening conditions. In the present study, sheep RBCs were used to assess the hemolysis potential of GO or r-GO at 25 °C or 37 °C. No reports have showed significant differences within the hemolysis assay using species of different origins (Dobrovolskaia and McNeil, 2013).

At 25 °C, GO induced lysis up to 7% at 600 μg/ml while r-GO induced lysis up to 4 and 28% at 300 and 600 μg/ml, respectively (**Figure 25**). Lysis of RBCs by GO and r-GO was concentration dependent and only observed at concentrations higher than 62.5 μg/ml at 37 °C. Both GO and r-GO led to more than 20% RBCs lysis at 600 μg/ml at 37 °C. GO cytotoxicity towards RBCs was more pronounced at 37 °C, inducing about 13% lysis at 300 μg/ml (**Figure 25**).

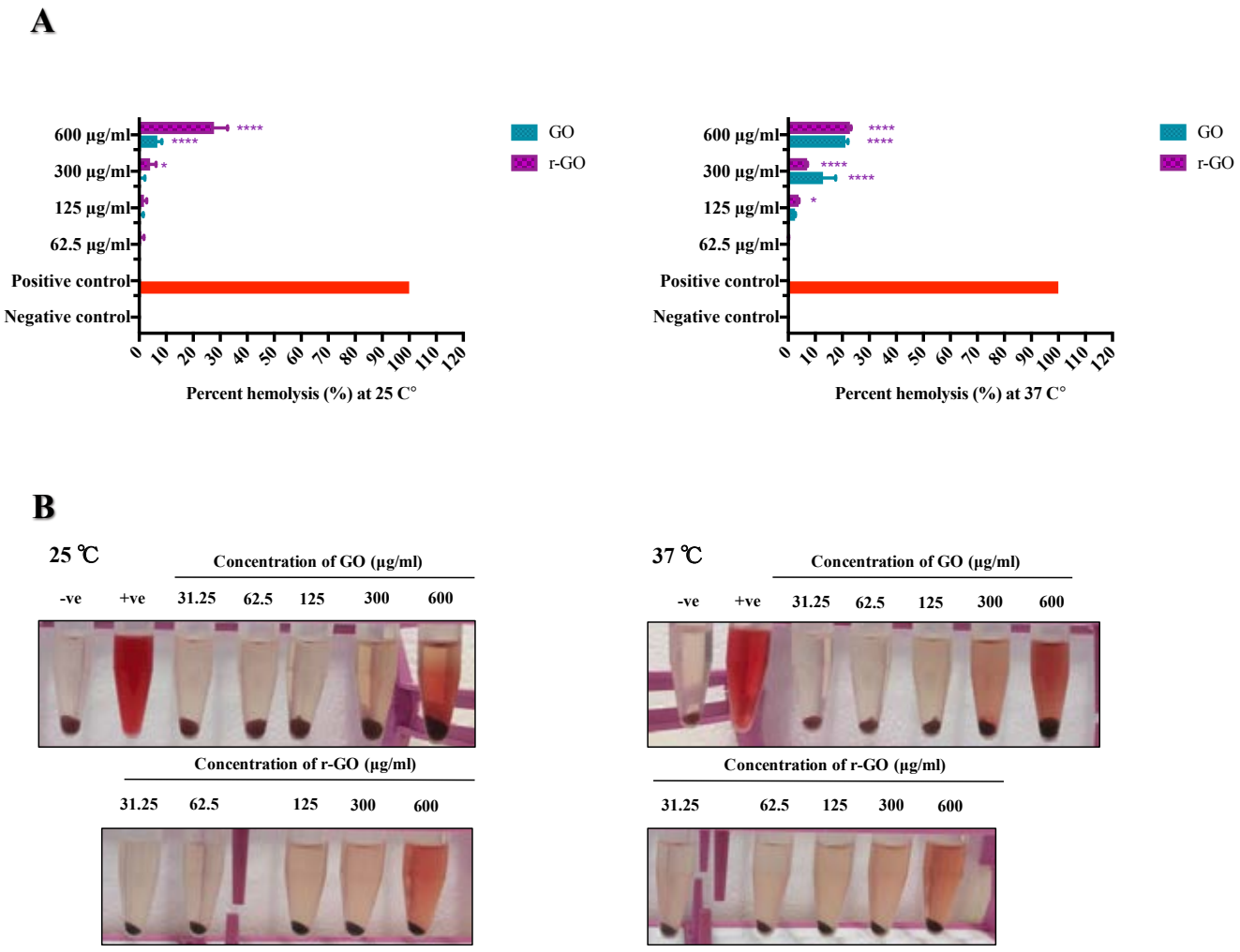

Figure 25. RBCs hemolysis. **A)** Percentage of hemolysis of sheep RBCs incubated with GO or r-GO at different concentrations ranging from 62.5 to 600 µg/ml for 3 hours. Data represent the means ± SD from 3 independent experiment. *p < 0.05, **p < 0.002, ***p < 0.0002 and ****p < 0.0001 versus naïve by one-way ANOVA analysis. **B)** Photographs of hemolysis of sheep RBCs incubated with GO or r-GO. The appearance of red haemoglobin in the supernatant is related to damage of RBCs. Phosphate buffered saline and deionised water are used as negative and positive controls, respectively.

According to the ASTM international E2524-08 protocol, the threshold for *in vitro* hemolysis is 2%. As such, if the hemolysis assay results for a test nanomaterial falls below 2%, the agent is viewed as non-hemolytic. Agents that result in hemolysis values between 2 and 5% are considered as moderate hemolytics and values above 5% certify the test nanomaterial as hemolytic. Hemolysis of graphene derivatives in the current research was more pronounced at 37 °C than 25 °C. Also, the hemolysis data revealed that GO and r-GO are moderately hemolytic at a concentration of 125 µg/ml and highly hemolytic at concentrations ≥ 300 µg/ml at 37 °C. Although both GO and r-GO nanoparticles showed concentration dependent hemolysis toward sheep RBCs, differences were seen in the extent of the hemolytic activity between GO and r-GO. The observed hemolysis was possibly due to the irregular edges of GO and r-GO nanoparticles, which upon contact with RBCs may result in mechanical disruption of the plasma membrane and therefore cause lysis. This could also explain the cytotoxicity observed for MRC-5 and A549 cells after exposure to high concentrations of graphene derivatives. The physical interaction of graphene nanomaterials with the cell surface is considered one of the major causes of cytotoxicity due to its sharp edges (Seabra et al., 2014, Gurunathan et al., 2014).

It has been reported that GO induces severe hemolytic activity at 25 µg/ml (Liao et al., 2011). The findings by Jaworski and colleagues are similar to what has been found in this study in relation to the hemolytic activity of GO and r-GO (Jaworski et al., 2017). In contrast, another study observed that graphene and its derivatives have no hemolytic activity (Strojny et al., 2015). This finding of *in vitro* RBC compatibility of graphene nanoparticles is vitally important as accidental exposure to graphene nanoparticles by inhalation, ingestion or by skin contact, can potentially result in the transportation of graphene nanoparticles into the bloodstream. Also, many of the proposed graphene biomedical applications requires intravenous injection (IV), which will mostly lead to the interaction of graphene

nanoparticles with blood components (Chen et al., 2015b, Monasterio et al., 2017). RBCs are one of the initial sites of contact upon IV injection; for this reason, hemo-compatibility assessment for graphene nanoparticles to be used in biomedical applications is essential (Kiew et al., 2016). The hemo-compatibility of graphene derivatives should be carefully reviewed before therapeutic application and surface modification of graphene can improve hemo-compatibility. For instance, coating with chitosan (Liao et al., 2011), heparin (Cheng et al., 2013) and liposome (Monasterio et al., 2017) almost demolished the hemolytic activity of GO.

Cytotoxicity of GO was evident in this project when MRC-5 and A549 cells were treated with concentrations ranging from 125 to 600 µg/ml and after 24 and 48 hours exposure. r-GO cytotoxicity was also evident at similar concentrations of GO but only in the case of A549 cells. In summary, many researchers have studied the cytotoxicity of graphene nanomaterials, but the exact mechanisms that underlie the cytotoxicity are still unclear (Ou et al., 2016). Therefore, the assessments described in the next section were performed to identify the possible mechanism(s) of graphene nanoparticle cytotoxicity.

4.2.3 **Mechanistic assessment of GO and r-GO cytotoxicity**

Exposing cells to cytotoxic materials can lead to different types of cell death. One example is the accidental cell death which is termed necrosis. The necrosis process is characterised by rapid cell swelling and a loss of membrane integrity, resulting in the release of cellular content into the surrounding environment. Necrosis cell death is not the only way cells can die, the cells may also undergo apoptosis, which is a type of highly regulated cell suicide. Apoptosis is characterized by cytoplasmic shrinkage, membrane budding, nuclear condensation and explicit fragmentation (Klaassen and Watkins, 2008). In addition to apoptosis and necrosis, autophagy is another mechanism of cell death. Autophagy is a recycling system that breaks down abnormal protein mass, cytoplasmic contents and damaged organelles (Codogno et al., 2012). However, unrestrained autophagy can leads to a non-apoptotic cell death (Pecorino, 2008). It has been reported that disruption of autophagy function leads to cell injury that can cause cell death, and this disruption is postulated to be a potential mechanism of nanomaterials toxicity (Mishra et al., 2016, Wang et al., 2017a). The mechanisms of nanoparticle toxicity have been extensively investigated. Different types of nanomaterials have been reported to induce toxicity through the formation of reactive oxygen species (ROS) in many biological systems. Overproduction of ROS leads to oxidative stress, a condition that gives rise to different toxicity ends point such as unregulated cell signalling, changes in cell motility, genotoxicity, carcinogenesis, autophagy and apoptosis (Gonzalez et al., 2009, Fu et al., 2014). Therefore, in this section the possible mechanism of cell death, oxidative stress and genotoxicity of GO and r-GO were investigated.

4.2.3.1 Apoptosis

Apoptosis is divided into two pathways, the death receptor pathway (extrinsic) and mitochondrial pathway (intrinsic). The extrinsic pathway is induced by TNF family receptors and their ligands, while the intrinsic apoptosis pathway is regulated by the mitochondrial Bcl-2 family proteins. (Dickens et al., 2012, Shamas-Din et al., 2013, Ou et al., 2017). In both cases, apoptosis will ultimately result in the activation of caspase 3 which initiates the apoptotic process (**Figure 26**).

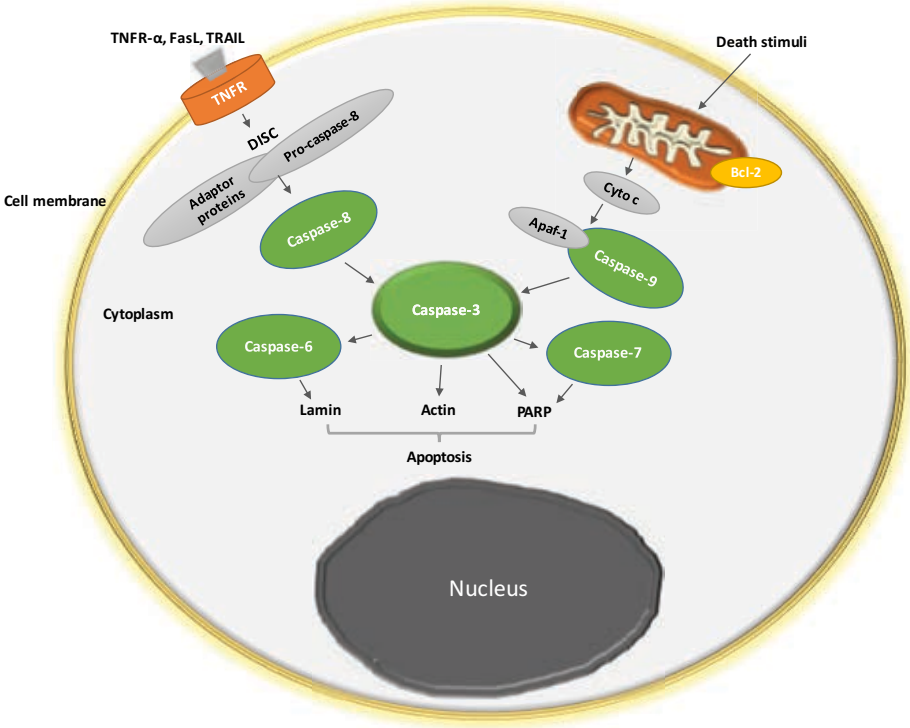

Figure 26. Extrinsic and intrinsic apoptosis pathways. The extrinsic pathway is induced by death receptors (TNF) which, once activated, induces adaptor proteins and pro-caspase-8 to form a death inducing signalling complex (DISC). The DISC activates caspase-8 and the latter leads to the cleavage of pro-caspase-3 into active caspase-3 and initiates the apoptotic process. The intrinsic apoptosis pathway is regulated by mitochondrial Bcl-2 family proteins. Stimulation of mitochondria by extracellular or intracellular signals leads to release of cytochrome c into the cytosol by Bcl-2 protein action. Cytochrome c recruits Apaf-1 to form the apoptosome that binds and trigger caspase-9 which results in caspase-3 cleavage and consequently in apoptosis (Dickens et al., 2012, Shamas-Din et al., 2013, Ou et al., 2017).

In the initial stages of apoptosis, phosphatidylserine is translocated from the internal surface of the plasma membrane to its external surface (Vermes et al., 1995). This change to the cell make-up can be detected using an Annexin-V/PI flow cytometry-based assay. Annexin-V stain binds to phosphatidylserine upon the outer surface of the apoptotic cell membrane; as necrotic cells may also go through membrane flip-flop, propidium iodide (PI) stain is added to differentiate between apoptotic cells and necrotic cells. During necrosis, the membrane impermeable PI stain passes through damaged plasma membranes and stains DNA within the nucleus, giving rise to red fluorescence.

The ability of GO and r-GO (125 and 300 μg/ml) to trigger apoptosis was tested on MRC-5 and A549 cells. This concentration range (125 and 300 μg/ml) was selected as it has induced cell death based on the aforementioned cytotoxicity data. Cell populations using Annexin V/PI assay can be classified into one of four categories: healthy cells (bottom left quadrant [AnnexinV-/PI-]), apoptotic cells (bottom right quadrant [AnnexinV+/PI-]), necrotic cells (top right quadrant [AnnexinV+/PI+]), and cell debris (top left quadrant [AnnexinV-/PI+]).

The results showed that there was no substantial induction of apoptosis or necrosis of MRC-5 cells after 24 hours of incubation with GO or r-GO (**Figure 27**). The percentage of healthy cells after incubation with GO was only 20% lower compared to the negative control. The highest degree of apoptosis was detected after incubation with GO (300 μg/ml) for 48 hours, although only 17% of cells were apoptotic compared to 85% for staurosporine (positive control). Results obtained for A549 cells showed a similar trend where induction of neither necrosis nor apoptosis could be observed (**Figure 28**).

Unexpectedly neither cell line showed signs of toxicity, even when exposed to GO at a concentration of 300 μg/ml (ca. 55% and 75% cell survival in MRC-5 and A549 cells, respectively [**Table 7**]). Similar inconsistencies were reported by other researchers and are

attributed to quenching of the fluorescent-probes by nanoparticles (Zhu et al., 2010c, Ali-Boucetta et al., 2011, Wu et al., 2018). However, this is unlikely to be the case here since the nanomaterials were gently removed to limit interference. Still, dead cells could become detached during the procedure, leading to an underestimation of cell death. The latter issue is the most likely reason for the inconsistent cytotoxicity data obtained by using the Annexin V/PI assay.

In addition, as graphene nanoparticles tend to agglomerate, this maybe another potential issue in assessing carbon-based nanomaterials by the use of flow cytometry techniques. These agglomerates possibly resemble the size of a cell and hence can be counted as unstained event on the Annexin V/PI bivariate dot plot. The latter issue results in an overestimate of populations of healthy cells in the sample, which can give rise to a false conclusion about the toxicity of the nanomaterial (Vranic and kostarelos, 2017). Nevertheless, results so far indicate that neither GO nor r-GO trigger apoptosis at the concentrations tested.

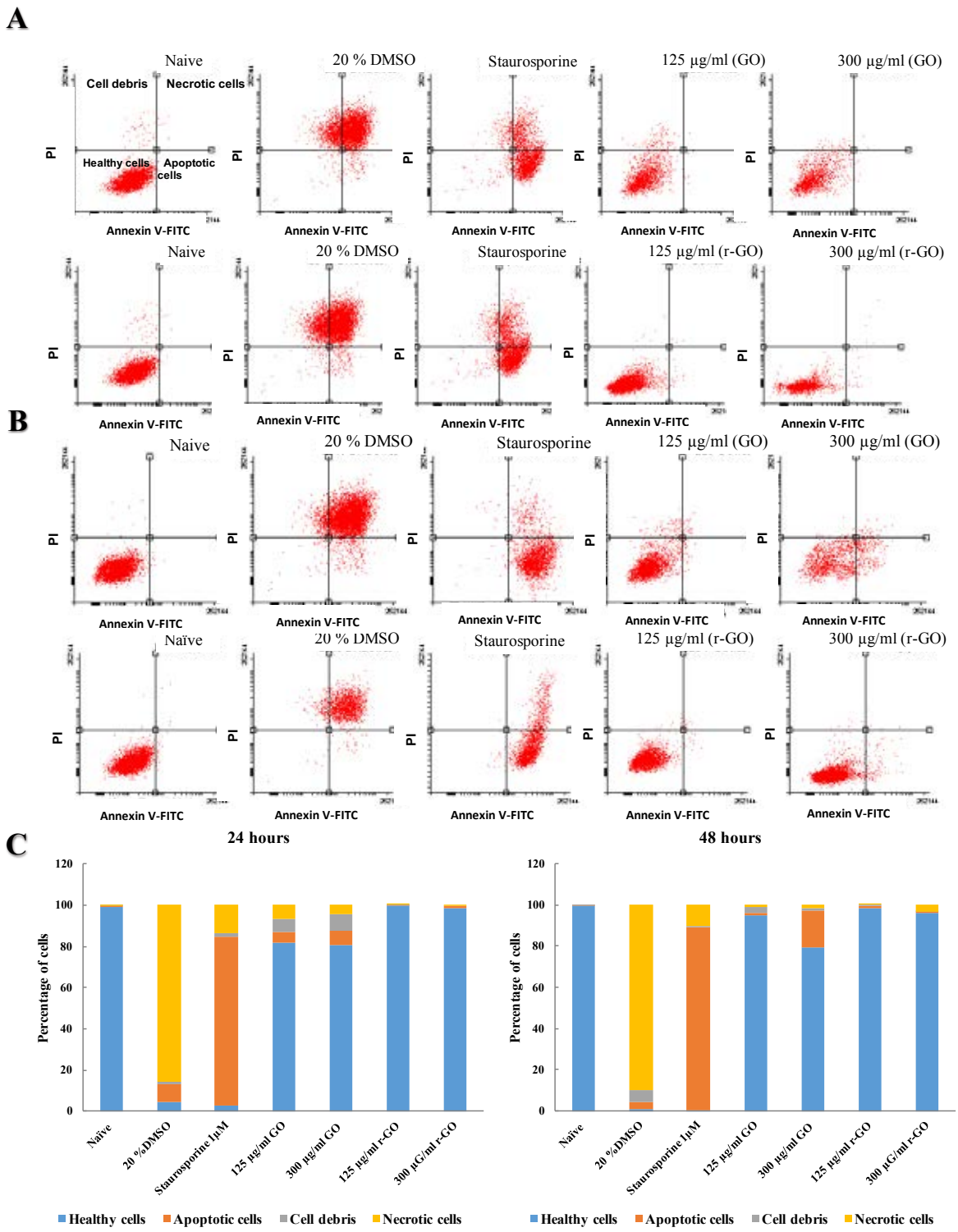

Figure 27. Investigation of apoptotic cell death in MRC-5 cells by flow cytometry. **A** and **B** represent flow cytometry dot-plots for cells incubated with GO and r-GO for 24 and 48 hours, respectively, indicating: the healthy cells (bottom left quadrant), apoptotic cells (bottom right quadrant), necrotic cells (top right quadrant), and cell debris (top left quadrant) (n=3). **C)** Frequency of cells in each quadrant in every treatment group for the 24 and 48-time points. DMSO was used as a positive control for necrosis while staurosporine (1µM, 24 hour) was used as a positive control for apoptosis.

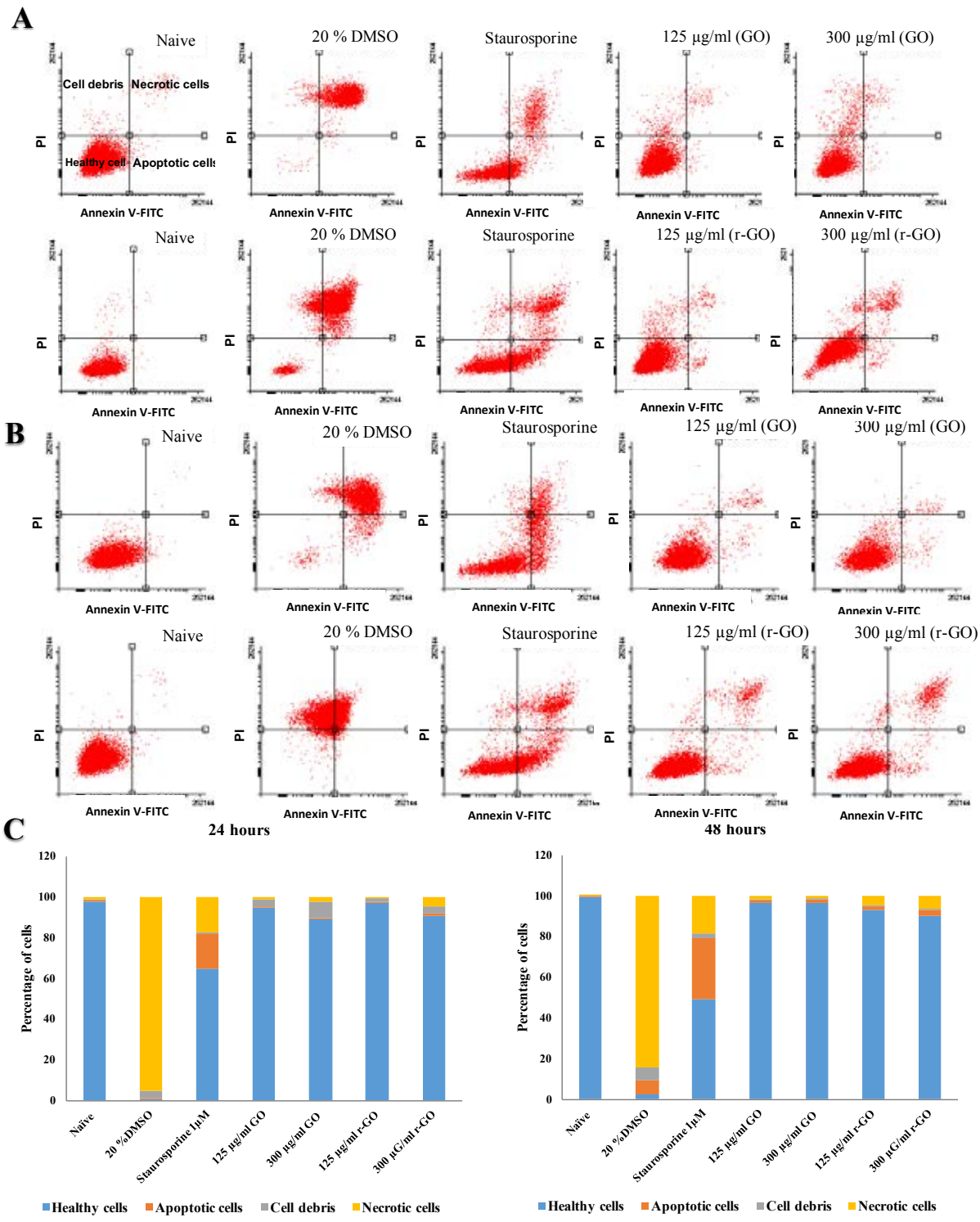

Figure 28. Investigation of apoptotic cell death in A549 cells by flow cytometry. **A** and **B** represent flow cytometry dot-plots for cells incubated with GO and r-GO for 24 and 48 hours, respectively, indicating: the healthy cells (bottom left quadrant), apoptotic cells (bottom right quadrant), necrotic cells (top right quadrant), and cell debris (top left quadrant) (n=3). **C** represents percentage of cells in each quadrant in every treatment group for 24 and 48 time-points. DMSO was used as a a positive control for necrosis while staurosporine (1µM, 24 hour) was used as a positive control for apoptosis.

Analysis of caspase expression can provide further insight into the mechanism of cell death. Caspases fall into two categories including initiators and executioners (Favaloro et al., 2012). The initiator caspases-2, caspases-8, caspases-9, caspases-10, and caspases-12 are linked to upstream pro-apoptotic signals and function by cleaving and stimulating the downstream executioner caspases. The executioner caspases-3, caspase-6 and caspase-7 modify proteins that are responsible for apoptotic process. Executioner caspases cleave many targets such as Poly (ADP-ribose) polymerase (PARP) and lamin A/C (McIlwain et al., 2013). Here, caspase expression, specifically caspases-3 and -7, was first determined by Caspase-Glo 3/7 assay (**Figure 29**). Results showed neither executioner caspases were induced after incubation with GO and r-GO in both cell lines.

To further confirm data, the intracellular levels of cleaved-caspase-3 and its target cleaved-PARP were analysed by flow cytometry. In the case of MRC-5 cells, analysis indicated that there was no induction of cleaved-caspase-3 or cleaved-PARP proteins after incubation with both graphene derivatives compared to positive control (**Figure 30**). However, results in A549 cells hint that apoptosis may be involved in GO-triggered cytotoxicity after 24 hours, but not 48 hours (**Figure 31**); no change in the levels of cleaved-caspase was seen when cells were exposed to r-GO, independently of exposure time. Cleaved-PARP measurement in A549 cells incubated with graphene derivatives indicated no signs of activation of PARP protein. This finding shows that GO and r-GO do not induce apoptosis in MRC-5 and A549 cells.

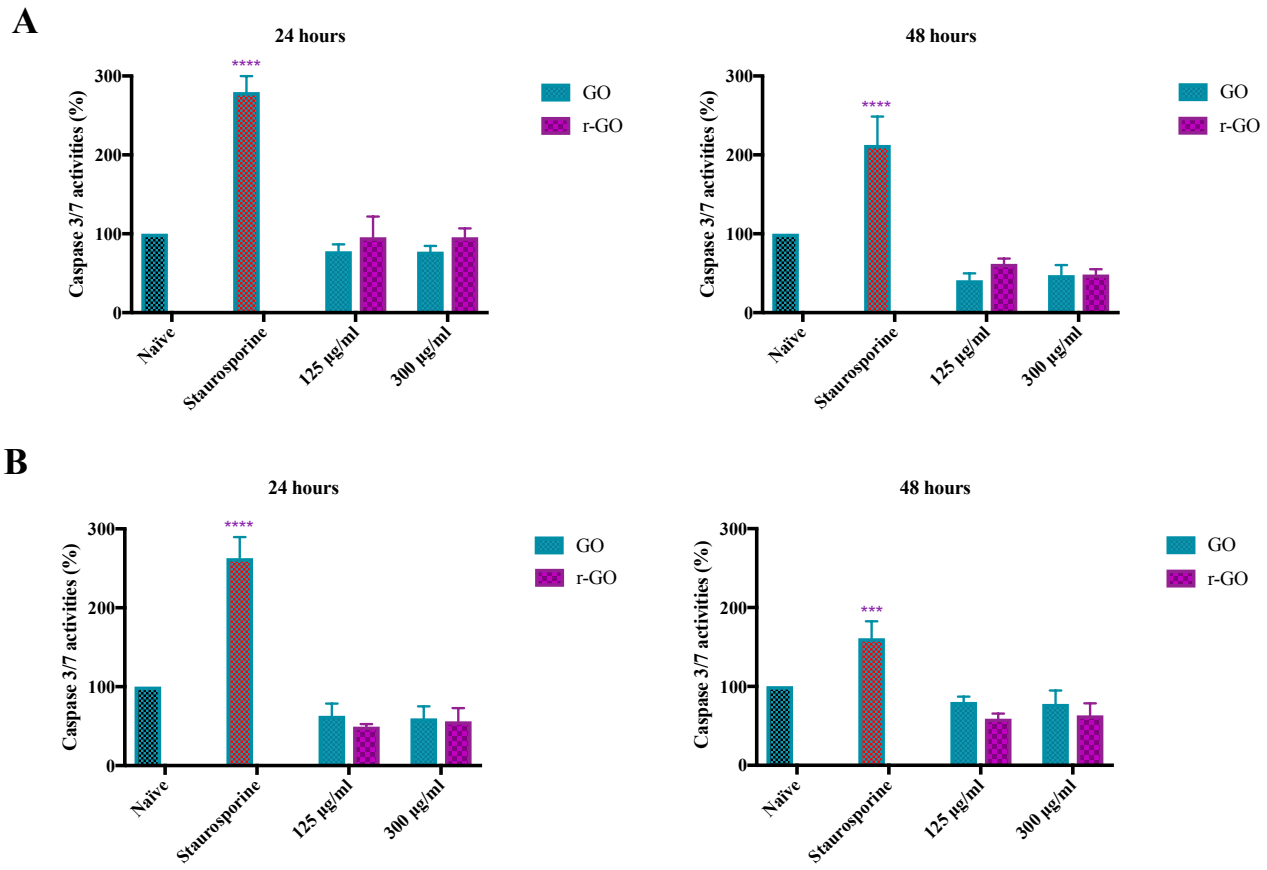

Figure 29. Caspase-Glo 3/7 assay in A) MRC-5 and B) A549 cells. Percentage of caspase 3/7 activities in MRC-5 **(A)** and A549 cells **(B)** incubated with GO and r-GO at cytotoxic concentrations (125-300 µg/ml) for 24 and 48 hours in comparison to untreated (naïve) and staurosporine for 6 hours (10 µM; positive control). There were no increases in caspase 3/7 activities in GO/r-GO treated group compared to naïve. Bars represent means ± SD (n=3). (*$p < 0.05$, **$p < 0.002$, ***$p < 0.0002$ and ****$p < 0.0001$ versus naïve by ANOVA).

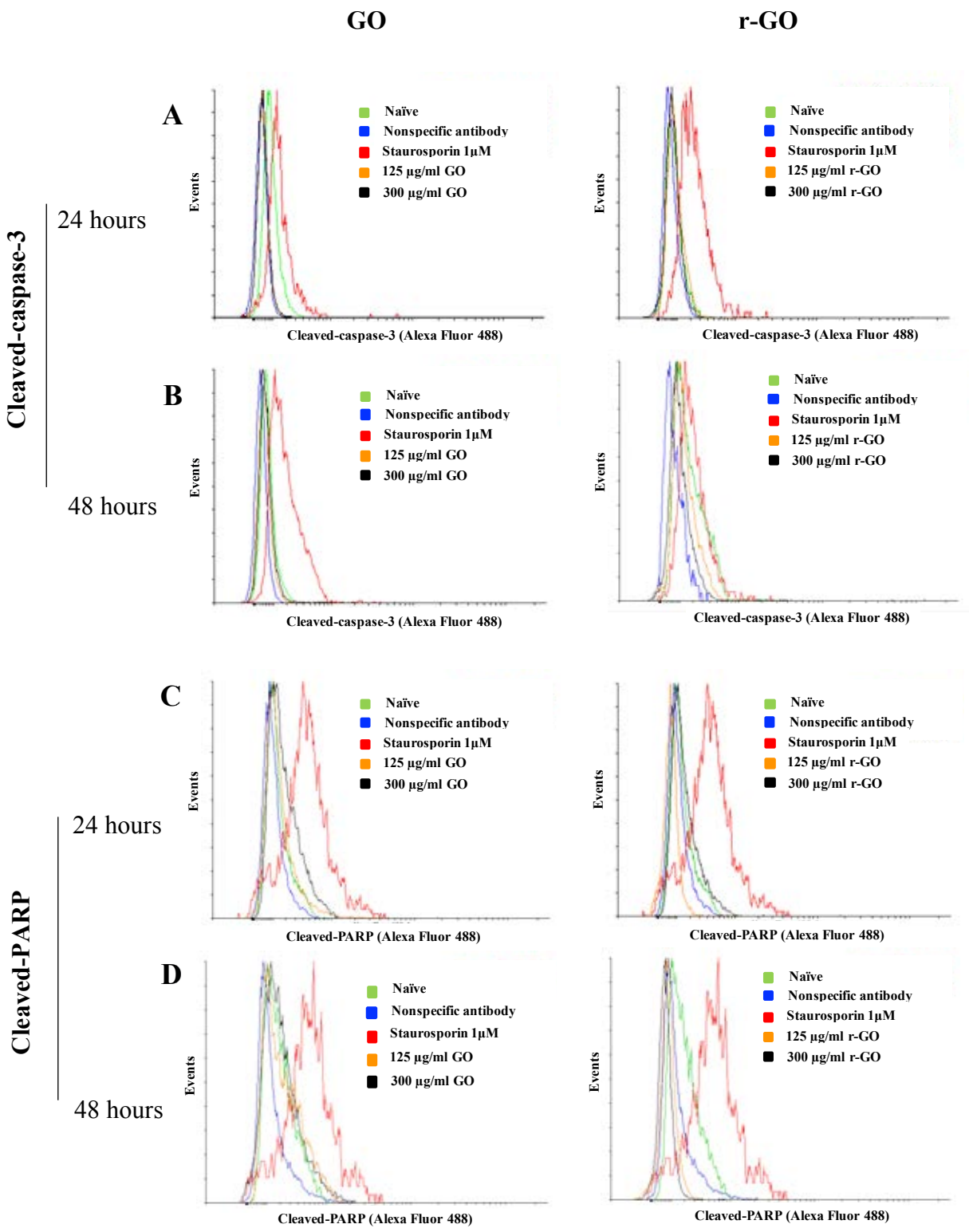

Figure 30. Flow cytometric analysis of cleaved-caspase-3 and cleaved-PARP in MRC-5 cells. Flow cytometric analysis using cleaved-caspase-3 antibody: cells exposed to GO and r-GO for 24 hours (**A**), cells exposed to GO and r-GO for 48 hours (**B**) (n=3). Flow cytometric analysis using cleaved-PARP antibody: cells exposed to GO and r-GO for 24 hours (**C**), cells exposed to GO and r-GO for 48 hours (**D**) (n=3). Graphene derivatives treated samples were compared to non-specific negative control antibody (blue), naïve (green peak) and to the positive control (staurosporin1µM, red peak). GO and r-GO do not induce apoptosis.

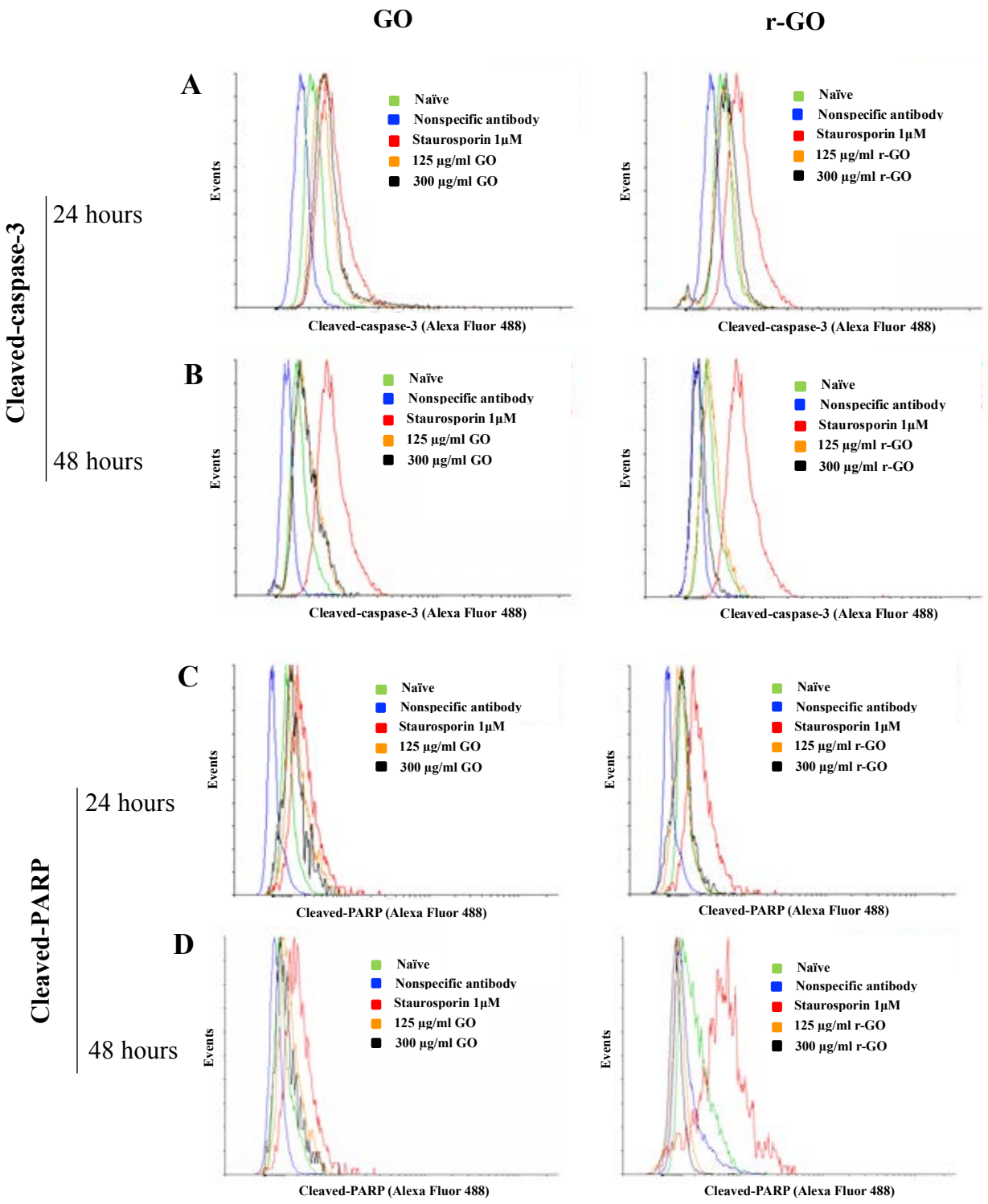

Figure 31. Flow cytometric analysis of cleaved-caspase-3 and cleaved-PARP in A549 cells. Flow cytometric analysis of cleaved-caspase-3: cells exposed to GO and r-GO for 24 hours (**A**), cells exposed to GO and r-GO for 48 hours (**B**) (n=3). Flow cytometric analysis using cleaved-PARP antibody: cells exposed to GO and r-GO for 24 hours (**C**), cells exposed to GO and r-GO for 48 hours (**D**) (n=3). Graphene derivatives treated samples were compared to nonspecific negative control antibody (blue), naïve (green peak) and to a positive control (staurosporin1µM, red peak). Cleaved-caspase-3 intensity in cells incubated with GO for 24 hours was similar to intensity seen with the positive control, but after 48 hours the intensity was comparable to the negative control. Analysis of cleaved-PARP indicated no induced apoptosis.

In addition, both intracellular proteins, cleaved-caspase-3 and cleaved-PARP, as well as pro-caspase-3 protein were analysed for both cell lines using the Western blot technique. Western blot analysis in MRC-5 and A549 cells confirmed that neither cleaved-caspase-3 nor cleaved PARP were activated after incubating cells with cytotoxic concentrations (300 µg/ml) of GO and r-GO for 24 hours (**Figure 32**). Activated caspase and PARP were only detected in cells incubated with staurosporine. These findings support the viewpoint that GO and r-GO do not induce apoptosis in MRC-5 and A549 cells. The next mechanistic investigation was of autophagy, as the disruption of this process can be a potential mechanism of nanomaterials toxicity (Mishra et al., 2016, Wang et al., 2017a).

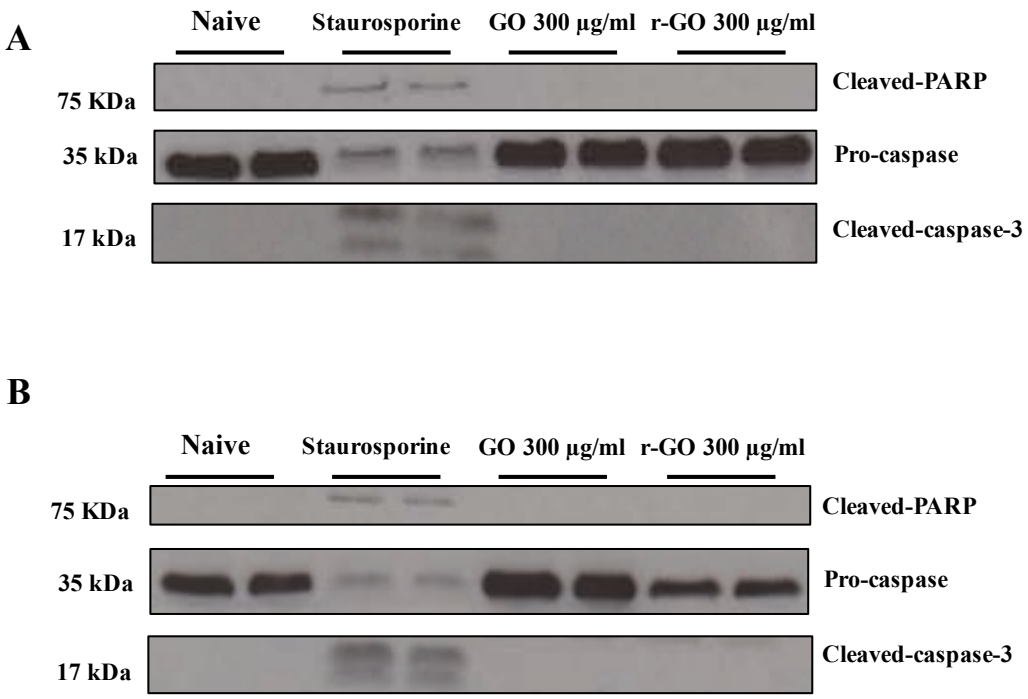

Figure 32. Western blot analysis for the pro-caspase 3, cleaved-caspase-3 and cleaved-PARP in A) MRC-5 and B) A549 cells. The cleaved-caspase-3 and cleaved-PARP were not detected in MRC-5 **(A)** and A549 **(B)** cells incubated with 300 µg/ml of GO or r-GO. Results indicated that GO or its reduced form do not induce apoptosis. Bands of the cleaved-caspase and cleaved PARP were only detected for cells incubated with10 µM staurosporine for 6 hours (positive control).

4.2.3.2 Autophagy analysis

Autophagy is an evolutionary catabolic process; described as self-eating or type-II programmed cell death that is essential for the homeostasis of cells (Rautou et al., 2010). Autophagy under cellular stressful conditions permits the degradation of extra proteins and recycling of amino acids for the formation of proteins that are crucial for cell survival (Klionsky and Emr, 2009). Autophagy is a multistage and highly dynamic process. As for other cellular pathways, autophagy can be regulated positively or negatively at different stages (Jin and Klionsky, 2014, Klionsky et al., 2016). Therefore, understanding autophagic flux is critical.

During autophagy, protein aggregates and damaged organelles are engulfed by a newly formed membrane called a phagophore to form a double membraned structure called an autophagosome (**Figure 33**). The autophagosome is then targeted to fuse with the lysosomes forming an autolysosome. The autolysosome then degrades cellular components by lysosomal enzyme (Jin and Klionsky, 2014). The induction of autophagy is controlled by different kinases but the mammalian target of rapamycin kinase (mTOR) is the critical regulator in autophagy cell signalling. mTOR is a negative regulator of autophagy and acts as a checkpoint at the start stage integrating nutrient, growth factors and energy signals.

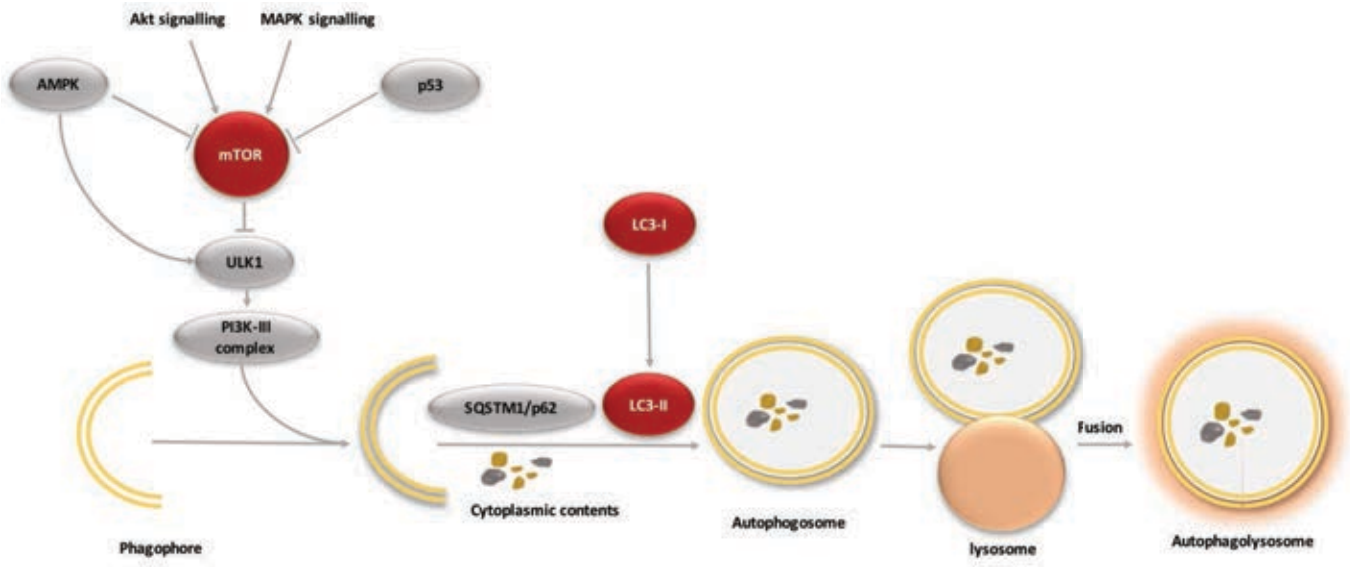

Figure 33. Autophagy signalling. mTOR is a negative regulator of autophagy and its activation through Akt and MAPK signalling results in autophagy suppression while negative regulation of mTOR through AMPK and p53 signalling leads to autophagy induction. The serine/threonine kinase ULK1 acts downstream the mTOR and can be directly activated by AMPK. ULK1 triggers PI3K-III and forms a complex with associated proteins. PI3K-III complex interacts with phagophore and start the formation of autophagosome. During the autophagosome formation, the microtubule associated protein LC3-I is converted to LC3-II to be attached to the autophagosome membrane. During autophagy, SQSTM1/p62 binds to LC3 and delivers protein aggregates to the autophagosome. The autophagosome is then targeted to fuse with the lysosomes forming an autolysosome for autophagic degradation.

As shown in Figure 33, mTOR activation through Akt and MAPK signalling results in autophagy suppression while negative regulation of mTOR through AMPK and p53 signalling leads to autophagy induction (Alers et al., 2012). The mammalian serine/threonine kinases ULK, such as ULK1, play a vital role in autophagy induction signalling and act downstream the mTOR complex. ULK also can be phosphorylated and activated by AMPK directly. Activation of ULK1 triggers phosphoinositide-3 kinase III (PI3K class III) and forms a complex with associated proteins. PI3K class III complex interacts with phagophore forming binding sites for autophagic proteins and start the formation of autophagosome (Papinski and Kraft, 2014, Klionsky et al., 2016).

During the autophagosome formation, the light chain 3 (LC3-I) protein in the cytoplasm is converted to its lipidated form LC3-II, and attached to the autophagosome membrane; LC3-

II protein level is commonly used as an index of autophagosome formation (Wu et al., 2006). Throughout autophagy process, sequestosome 1 (SQSTM1/p62) binds to LC3 and delivers SQSTM1-bound protein aggregates to the autophagosome for degradation (Trocoli et al., 2014). SQSTM1/p62 proteins are used as a marker for autophagic degradation (Klionsky et al., 2016). Proteins including LC3, SQSTM1/p62 and mTOR were analysed in this research to assess autophagy process in cells exposed to graphene nanomaterials.

First, the protein level of LC3 protein was measured in extracts of MRC-5 and A549 cells exposed to GO and r-GO for 24 hours at concentration of 300 µg/ml. Chloroquine was used as a positive control for LC3-II, as it inhibits the autophagic flux by increasing the lysosomal pH, thus preventing the fusion of autophagosome with lysosomes and inhibiting autophagic degradation (Takahiro Shintani, 2004). Blocking autophagy degradation by chloroquine leads to the accumulation of LC3-II protein. Here, the conversion of LC3-I to LC3-II was measured by Western blot analysis. After incubation with GO, the levels of LC3-I/II were significantly decreased in both cell lines, compared to the untreated control (**Figure 34**), with LC3-I depletion being more pronounced in MRC-5 cells. In comparison, LC3-I/II levels remained mostly unchanged when cells were treated with r-GO with the exception of LC3-II in A549 (**Figure 34F**). These findings indicate that r-GO may have induced autophagy or partly mimicked chloroquine in those cells.

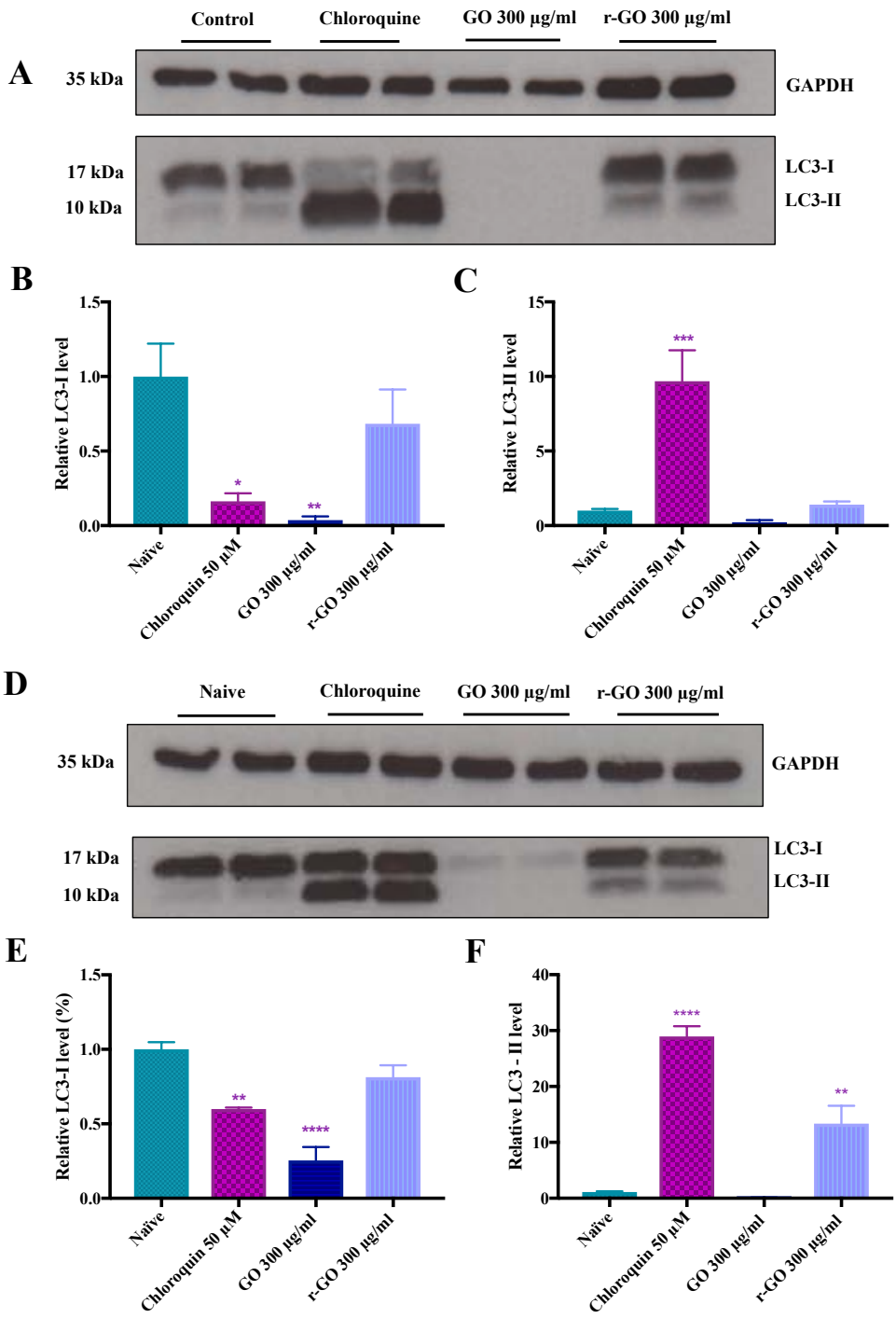

Figure 34. Expression of LC3-I to LC3-II in MRC-5 (A-C) and A549 (D-F) cells. Representative Western blot analysis of LC3 expression in MRC-5 (**A**) and A549 cells (**D**) including untreated control and cells treated with 50 µM of chloroquine, 300 µg/ml of GO and r-GO for 24 hours. **B** and **E** show densitometry analysis of LC3-I in MRC-5 and A549 cells, respectively. **C** and **F** show densitometry analysis of LC3-II in MRC-5 and A549 cells, respectively. LC3 protein was significantly decreased by GO in both cell lines compared to naïve cells. r-GO significantly increased the level of LC3-II only in A549 cells compared to naïve cells. The protein expression was normalized to GAPDH (loading control) relative to untreated group. Bars represent mean ± SEM (n=4). * = $p < 0.05$, ** = $p < 0.002$, *** = $p < 0.0002$ and **** = $p < 0.0001$ versus naive by ANOVA.

Data obtained from LC3 expression indicated that GO has an effect on the autophagy process, but the nature of this effect was obscure as GO decreased protein expression of both LC3-I and LC3-II. To gain further insight into how GO impacts on autophagy, the effect of a mixture of GO and chloroquine on LC3 protein was investigated. Two other treatments in this test were included, a treatment whereby cells were pre-treated with chloroquine overnight and then were exposed to fresh media for 24 hours, in order to test potential recovery from the inhibitory chloroquine effect. In the second treatment, cells were pre-treated with chloroquine overnight and then were exposed to GO (300 μg/ml) for 24 hours, to check if GO has any effect on the accumulation of LC3-II and thus, autophagosome formation.

For MRC-5 and A549 cells pre-incubated with chloroquine followed by incubation with fresh media, the level of LC3-II protein was less than for the chloroquine control (**Figure 35**). However, results indicated that recovery was partial after 24 hours as the LC3-II levels were still relatively high. In all cases, the addition of GO suppressed LC3-I/II expression to barely detectable levels, independently of the order of addition. These data indicate that GO has the ability to overcome the inhibitory effect of chloroquine on the autophagy process. However, it was still unclear whether GO had inhibitory or stimulatory effect on autophagy.

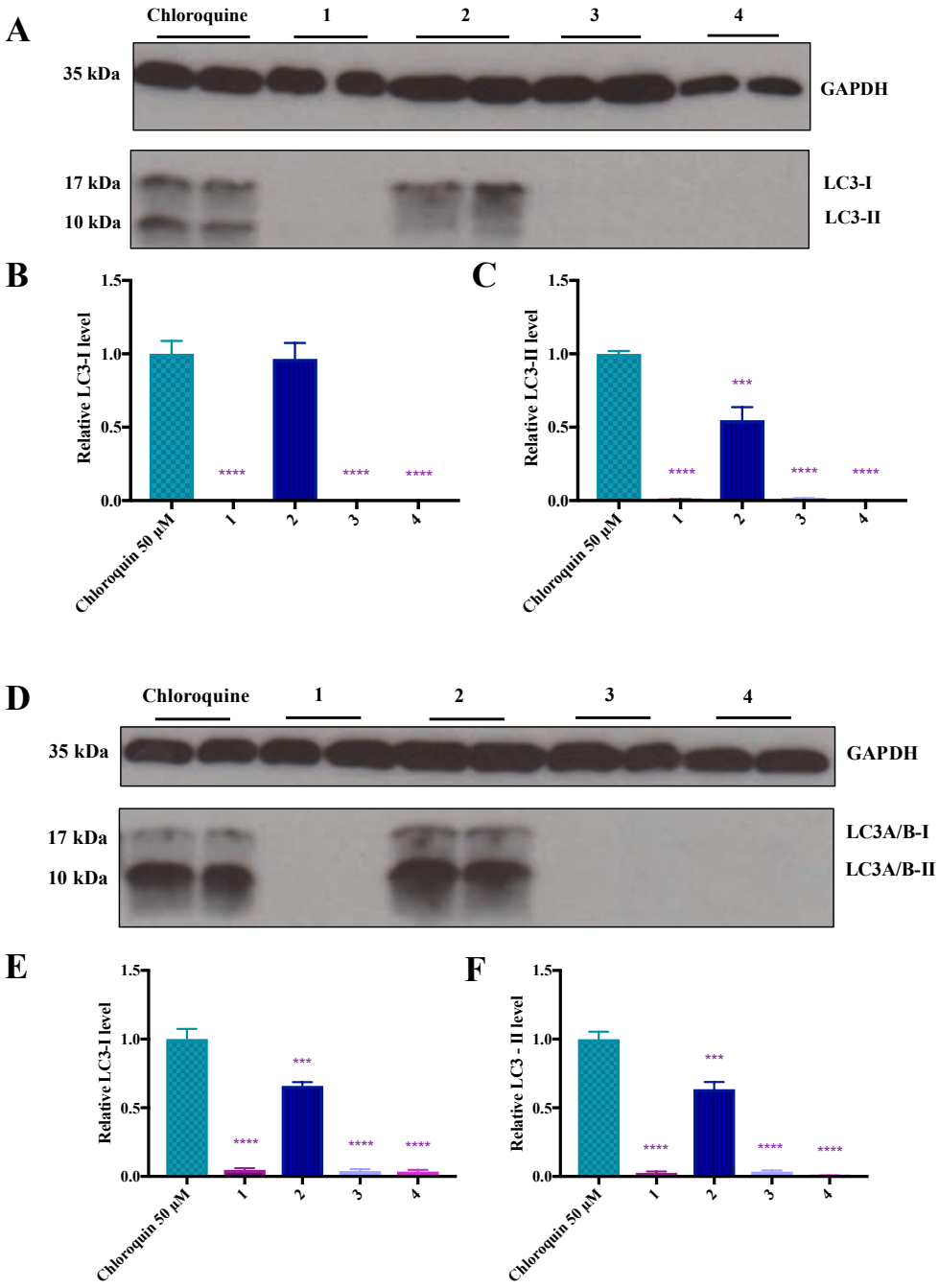

Figure 35. The impacts of GO on chloroquine inhibitory effect on autophagic flux in A-C) MRC-5 and D-F) A549 cells. Representative western blot analysis of LC3 expression in MRC-5 (**A**) and A549 cells (**D**) including chloroquine control (50 µM, overnight), (1) Chloroquine (50 µM) and GO (300 µg/ml) for 24 hours, (2) Chloroquine (50 µM, overnight) followed by incubation with fresh media for 24 hours, (3) Chloroquine (50 µM, overnight) followed by treatment with GO for 24 hours and (4) 300 µg/ml GO for 24 hours. **B** and **E** show densitometry analysis of LC3-I in MRC-5 and A549 cells, respectively. **C** and **F** show densitometry analysis of LC3-II in MRC-5 and A549 cells, respectively. GO caused statistical decrease in both LC3 proteins, after cells were exposed to a mixture of GO and chloroquine or after exposing chloroquine pre-treated cells to GO, in comparison to chloroquine treated cells (control). The protein expression was normalized to GAPDH (loading control) relative to chloroquine control group. Bars represent mean ± SEM (n=3). * = $p < 0.05$, ** = $p < 0.002$, *** = $p < 0.0002$ and **** = $p < 0.0001$ versus chloroquine by ANOVA.

The autophagy process is initiated by different kinases and comprises the association of cargo (protein aggregates) within the autophagosome, fusion of the autophagosome with lysosomes and its subsequent turnover (Klionsky et al., 2016). During this process LC3-I is expected to decrease as the protein is converted to LC3-II. If the autophagy process continues unhindered, the expectation is that LC3-II decreases after an initial rise as the autophagosome are depleted (Cai et al., 2010, Klionsky et al., 2016). Low levels of LC3-I accompanied by high levels of LC3-II, as seen with chloroquine, generally indicate accumulation of autophagosomes, likely through a reduction in their clearance rate (Takahiro Shintani, 2004, Yoon et al., 2010). In comparison, depletion of both LC3-I/II, as seen with GO, is more likely indicative of triggering of the autophagic process, which is then allowed to proceed to completion. Therefore, in order to confirm that GO induced autophagy in MRC-5 and A549 cells, a second protein marker SQSTM1/p62 was investigated.

During autophagy, SQSTM1/p62 becomes associated with the completed autophagosome and is subsequently degraded in autolysosomes to complete the autophagic process. Thus, the decrease in SQSTM1/p62 protein level within the cells serves as an index of autophagic degradation. For this experiment, a wider range of GO concentrations (31.25 to 300 µg/ml) were studied in an attempt to examine the concentration-dependence of the induction of autophagy (**Figure 36**).

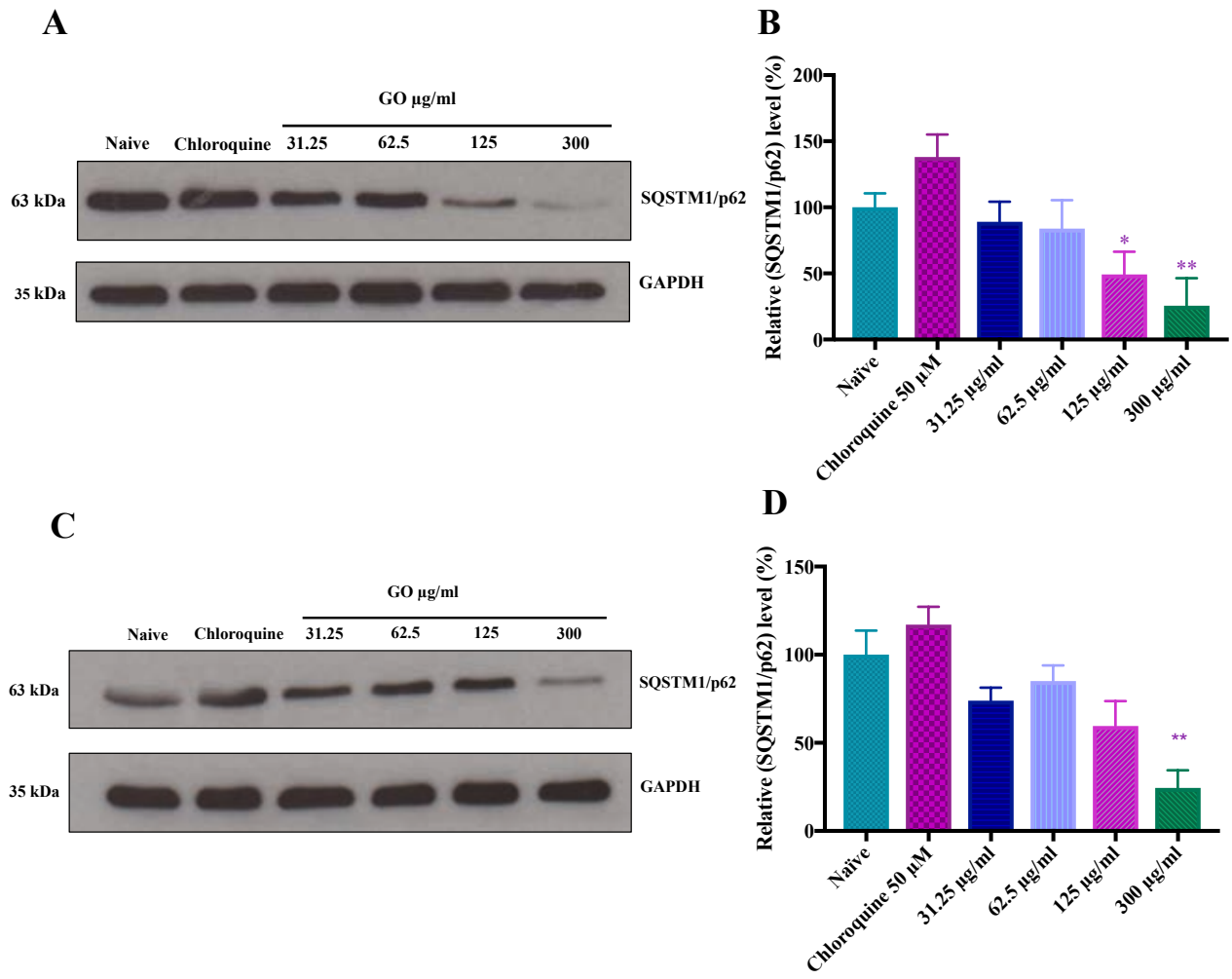

Figure 36. Analysis of autophagic degradation by GO in MRC-5 (A-B) and A549 cells (C-D). Analysis include untreated cells (naïve), cells treated with 50 µM of chloroquine, and cells incubated with different concentrations of GO (31.25,62.5,125 and 300 µg/ml) for 24 hours. **B** and **D** are the densitometry analysis of SQSTM1/p62 in MRC-5 and A549 cells, respectively. Concentration dependent decrease in the in SQSTM1/p62 level was observed in cells incubated with GO compared to untreated control. The protein expression was normalized to GAPDH (loading control) relative to the untreated group. Results are represented as % versus untreated group. Bars represent mean ± SEM (n=3). * = $p < 0.05$, ** = $p < 0.002$ versus naive by ANOVA.

Chloroquine-treated cells expressed a higher level of SQSTM1/p62 than naive cells as autophagic degradation was inhibited by blocking fusion of the autophagosome with lysosome. On the other hand, GO induced a significant reduction in SQSTM1/p62 expression at concentrations ranging from 125 to 300 μg/ml in MRC-5 and at concentration of 300 μg/ml in A549 cells compared to the untreated control. These results indicated that GO induces an unrestrained autophagic flux that has led to the extensive conversion of LC3-I to LC3-II to be associated with the autophagosome structure.

To further evaluate the effect of graphene derivatives on the autophagy pathway, total mTOR protein expression was studied following exposure to GO or r-GO (300 μg/ml) for 24 hours. mTOR is a negative regulator in the classical pathway of autophagy, so suppression of mTOR activity can lead to uncontrolled autophagic flux (Klionsky et al., 2016). A significant downregulation of mTOR protein was observed for both cell lines after exposure to GO which confirms the assumption in this work that GO, but not r-GO, may lead to unrestrained autophagic flux resulting in cell death (**Figure 37**). A wider range of GO concentrations (31.25 to 125 μg/ml) were studied and results showed a significant reduction in mTOR level in cells incubated with GO at a concentration of 125 μg/ml compared to the untreated group in MRC-5 cells. However, no reduction was observed in A549 cells (**Figure 38**). These findings support the cytotoxicity data where GO showed more impact at lower concentrations on healthy MRC-5 cells than the cancerous A549 cells.

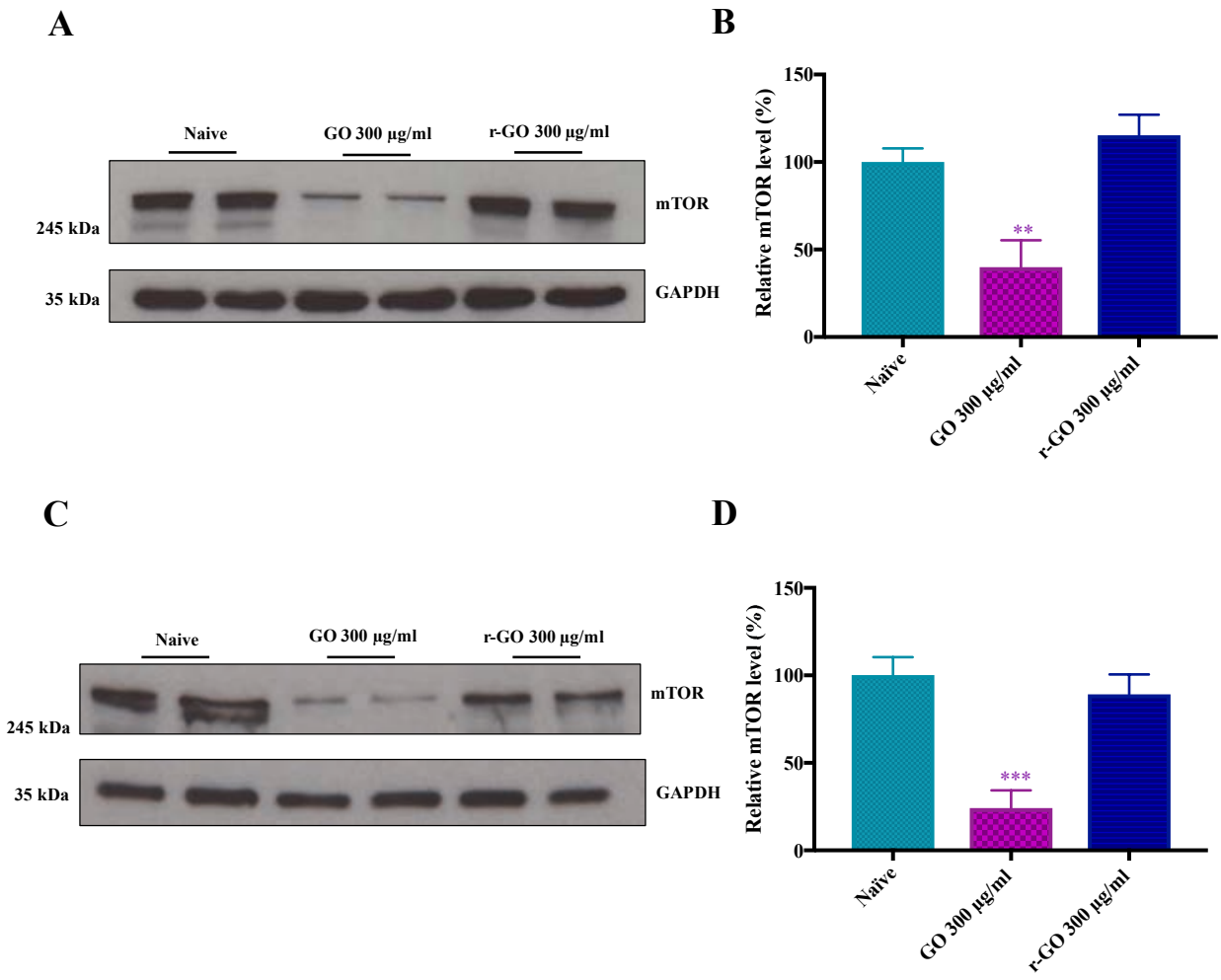

Figure 37. Impacts of GO and r-GO on the negative regulator of autophagy in A) MRC-5 and C) A549 cells. A and **C** represent western blot analysis of mTOR in extracts from MRC-5 and A549 cells, respectively. The measurement includes untreated (naïve) and cells exposed to 300 µg/ml of GO and r-GO for 24 hours. **B** and **D** represent densitometry analysis of mTOR protein expression in MRC-5 and A549 cells, respectively. mTOR was significantly decreased in cells treated with GO in comparison to naïve while r-GO has no effect on mTOR expression. The protein expression was normalized to GAPDH (loading control) relative to the untreated group (naïve). Results are represented as % compared to untreated group. Bars represent mean ± SEM (n=6). *$p < 0.05$, **$p < 0.002$, ***$p < 0.0002$ and ****$p < 0.0001$ versus naïve by ANOVA analysis.

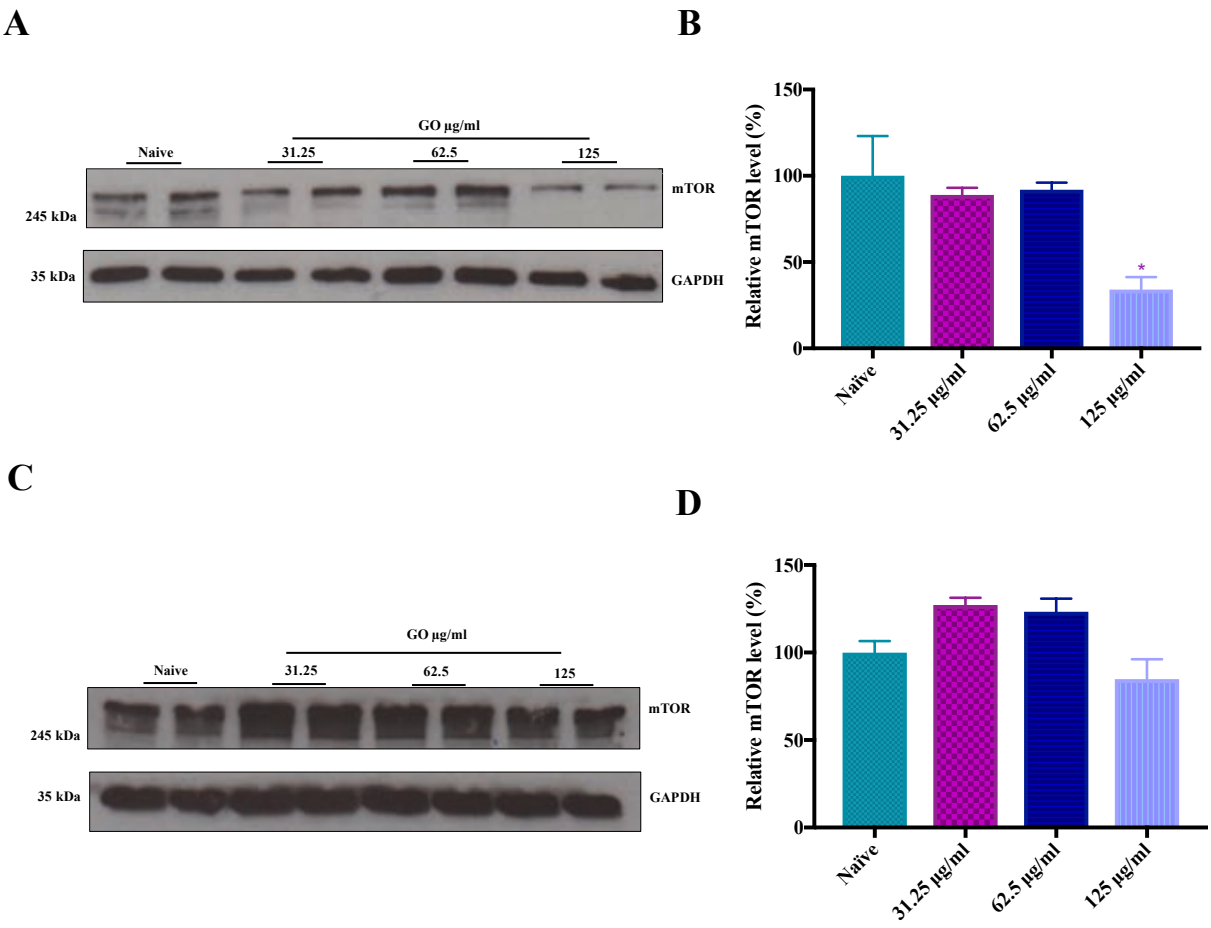

Figure 38. Impacts of different concentrations of GO on the negative regulator of autophagy (mTOR) in A-B) MRC-5 and C-D) A549 cells. A and **C** represent Western blot analysis of mTOR in extracts from MRC-5 and A549 cells, respectively. Analysis includes untreated (naïve) and cells exposed to GO at concentrations ranging from 31.25 to 125 µg/ml for 24 hours. **B** and **D** represent densitometry analysis of mTOR protein expression in MRC-5 and A549 cells, respectively. mTOR was significantly decreased in MRC-5 cells incubated with GO at concentration of 125 µg/ml in comparison to naïve. In A549 cells, no changes in mTOR levels were observed compared to naive. The protein expression was normalized to GAPDH (loading control) relative to the untreated group (naïve). Results are represented as % compared to untreated group. Bars represent mean ± SEM (n=4). *$p < 0.05$ versus naïve by ANOVA analysis.

Collectively, based on the autophagy analysis presented, the conclusion is that GO causes an unrestrained autophagy leading to a non-apoptotic cell death. Several studies support this conclusion as they have shown that graphene nanomaterials induced autophagy, particularly GO in different healthy and cancerous cell lines. However, there was a lack of information regarding distinguishing between autophagy and autophagic cell death. For example, GO induces autophagy in RAW264.7 macrophages in a concentration dependent manner (5-100 μg/ml) and after 24 hours (Chen et al., 2012). As macrophages can uptake graphene nanoparticles, autophagy might have been triggered in an attempt to rid the cells of GO. Investigators have reported that graphene nano-sheets induce both apoptosis and autophagy at a low concentration (20 μg/ml; 24 hours) in BEAS-2B, a human bronchial epithelial cell line (Park et al., 2015a). Autophagy was also induced in human hamster hybrid AL cells by GO at 10 μg/ml after 4 hours without being cytotoxic (Liu et al., 2016). In these other studies, autophagy was evident regarding an increase in the level of LC3-II, indicating autophagosome formation. In this project, Western blot data showed complete downregulation of LC3-I/II proteins in both cell lines when exposed to a cytotoxic concentration (300 μg/ml) indicating dysregulation of the process and autophagosome degradation was confirmed by the decreased level of SQSTM1/p62.

Moreover, GO stimulates autophagy and induces cytotoxicity in different cancer cell lines, such as colon carcinoma cells (CT26) (Chen et al., 2014), human neuroblastoma cells (Jeong et al., 2017) and the osteosarcoma MG63 cell line (Tang et al., 2018). As GO has been explored in a wide range of therapeutic applications including anticancer therapy (Chen et al., 2016b), autophagy possibly provides a novel mechanism that underlies the anticancer effect of GO (Tang et al., 2018). Additionally, most human cancers require hyper activation of the mTOR pathway, thus mTOR inhibitors are expected to have powerful anticancer effect (Meric-Bernstam and Gonzalez-Angulo, 2009, Watanabe et al., 2011,

Dong et al., 2010). Here, GO exhibited an inhibitory effect on mTOR protein in MRC-5 cells at 125 μg/ml and in A549 cells at 300 μg/ml, thereby such effect can be implied for cancer treatment. However, as the cytotoxic effect of GO was more pronounced in healthy cells, further work to improve selectivity of the effect of GO is required to reduce any adverse effect on normal tissue. The r-GO nanoparticles in this study was found to be biocompatible with healthy MRC-5 cells while in cancerous A549 cells showed subtle cytotoxicity and autophagosome formation after 24 hours exposure at 300 μg/ml. The good biocompatibility profile of r-GO over GO on healthy cells could pave the way for development of r-GO nanomaterials for biomedical applications. However, and as described previously, the physiochemical properties of r-GO can be an obstacle to its medical application.

With autophagy confirmed as the most likely mechanism of GO cytotoxicity, the following sections will focus on understanding the mechanisms leading to cell death *via* autophagy, starting with oxidative stress. Oxidative stress was recognized as one of the most significant mechanisms of cell damage due to the generation of ROS by nanomaterials (Gonzalez et al., 2009, Fu et al., 2014, Seabra et al., 2014, Chen et al., 2016a). Also, ROS levels play a major role in regulating the induction of autophagy (Poillet-Perez et al., 2015).

4.2.3.3 Oxidative stress assessment

Recent studies have suggested that ROS play a major role in mediating the cytotoxicity of graphene derivatives (Seabra et al., 2014, Chen et al., 2016a, Tabish et al., 2018). ROS are small, highly reactive and short lived chemical species that are produced by flawed one electron reduction of oxygen. Oxygen anions, superoxide and hydroxyl radicles, and hydrogen peroxide are examples of ROS. Overproduction of ROS leads to oxidative stress, a state in which cell constituents such as proteins, lipids and DNA are oxidized. Consequently, oxidative stress leads to different toxicity ends point such as unregulated cell signalling, changes in cell motility, genotoxicity, carcinogenesis, autophagy and apoptosis (Shibata and Niki, 2001, Batandier et al., 2002).

Antioxidant inside the cells plays a vital role in detoxifying ROS and limits oxidative stress. Normal cellular conditions reflect a balance between the level of ROS formation and ROS elimination by antioxidants. There are several non-enzymatic and enzymatic antioxidants including glutathione, thioredoxin, catalas, peroxidases and superoxide dismutase. High levels of ROS can overwhelm the activity of cellular antioxidants (Finkel, 2003, Scherz-Shouval and Elazar, 2011).

In this study, oxidative stress was measured by analysing the levels of ROS and glutathione inside the cells. To further evaluate the potential stress caused by graphene nanomaterials, phospho-p38 MAP kinase was investigated. Phospho-p38 MAP kinase is involved in a signalling that directs cellular responses to stress. p38 MAP kinase is activated by different cellular stresses. In addition, heat shock protein 27 (HSP27) was also analysed as its expression increases in response to stress. HSP27 is phosphorylated as response to the activation of the p38 MAP kinase (Rouse et al., 1994, landry et al., 1992, raingeaud et al., 1995).

In the present study, oxidative stress was initially studied by flow cytometry for cells incubated with GO and r-GO (60 and 300 μg/ml) for 24 and 48 hours. These concentrations were chosen to mimic low and high cytotoxicity. As with previous tests, a washing step was introduced to limit the risk of interference. Tert-butyl hydroperoxide (TBHP) (300 μM, for 1 hr) and the antioxidant N-acetylcysteine (NAC) (2000 μM, for 1 hr before treatment with TBHP) were used as positive and negative controls, respectively.

Increased ROS production was detected in MRC-5 cells incubated with GO and r-GO compared to naïve cells and was concentration dependent (**Figure 39**). For A549 cells, GO caused a slight, concentration-dependent increase in ROS levels after 24 hours. After 48 hours, the effect of GO was pronounced, with the highest concentration tested inducing ROS to a similar level to the positive control (**Figure 40**). A549 cells incubated with only the lowest concentration (62.5 μg/ml) of r-GO showed an increase in ROS level in comparison to naïve cells and the negative control after 24 hours. However, both concentrations (62.5 and 300 μg/ml) of r-GO increased ROS level to a similar extent after 48 hours. Data obtained in this study indicates that GO and r-GO altered ROS production in both cell lines. As ROS generation can have deleterious effects on cellular antioxidants, the impact of both nanomaterials on glutathione levels was investigated. Glutathione, is a ubiquitous antioxidant which exists mostly in its reduced form (GSH) with only a small percentage present as oxidised glutathione (GSSG) under normal cellular conditions. Oxidative stress may result in changes to the GSH/GSSG ratio, leading to cell signalling events that often ends in cell death (Ballatori et al., 2009, Rebrin and Sohal, 2008). Here, the GSH/GSSG ratio was measured in MRC-5 and A549 cells after incubation with GO and r-GO at concentrations ranging from 31.25 to 300 μg/ml for 24 and 48 hours; menadione was used as the positive control.

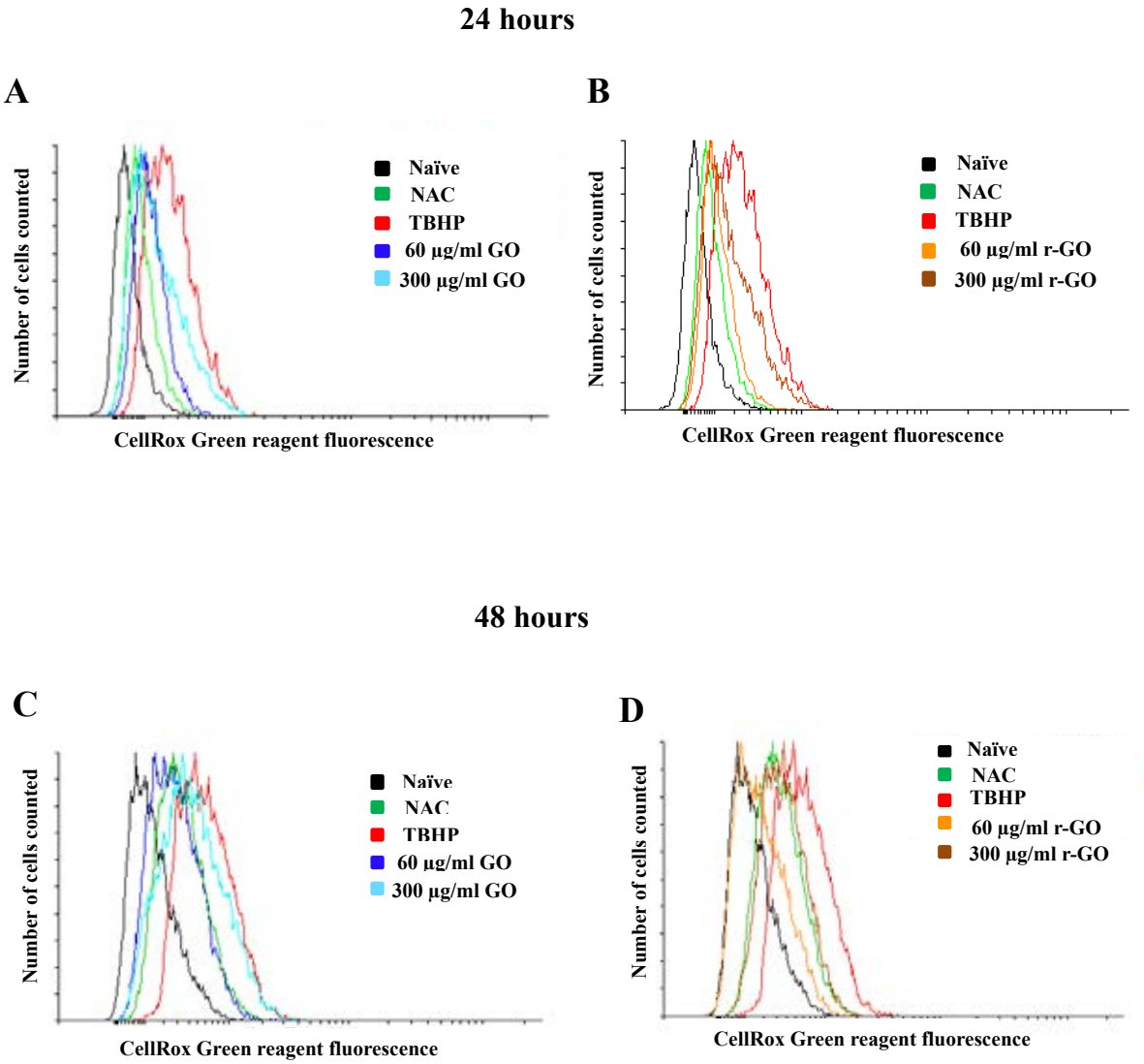

Figure 39. CellROX flow cytometry assay in MRC-5 cells. **A** and **B** represent flow cytometric analysis of ROS in MRC-5 cells incubated for 24 hours with GO and r-GO, respectively. **C** and **D** show flow cytometric analysis of ROS in cells incubated for 48 hours with GO and r-GO, respectively. Two concentrations of graphene derivatives were used including 60 and 300 µg/ml (n=3). Cells incubated with TBHP (red), positive control, have increased staining with CellROX label compared to cells pretreated with NAC (green), negative control, and naïve (black). As the stain intensity increases, the peak shifts to the right side of the chart. An increase in the stain intensity is correlated to the increase in the ROS. An increase in the ROS level was observed in cells incubated with GO and r-GO compared to naïve cells and negative control after 24 and 48 hours.

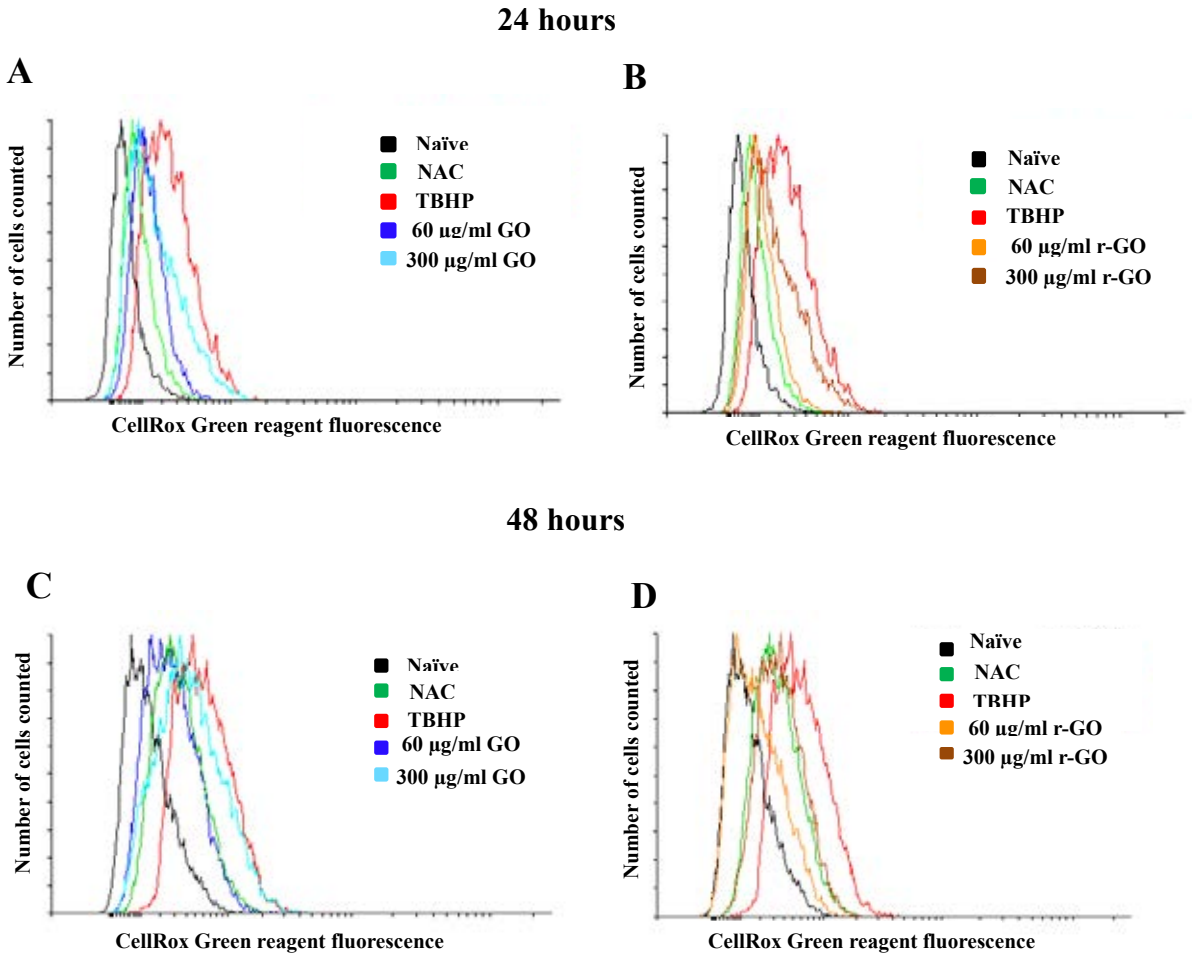

Figure 40. CellROX flow cytometry assay in A549 cells. **A** and **B** represent flow cytometric analysis of ROS in A549 cells incubated for 24 hours with GO and r-GO, respectively. **C** and **D** show flow cytometric analysis of ROS in cells treated for 48 hours with GO and r-GO, respectively. Two concentrations of GO and r-GO were used including 60 and 300 µg/ml (n=3). Cells incubated with TBHP (red), positive control, have increased staining with CellROX label compared to cells pretreated with NAC (green), negative control, and naïve (black). As the stain intensity increases, the peak shifts to the right side of the chart. An increase in the stain intensity is correlated to the increase in the ROS. An increase in the ROS level was observed in cells incubated with GO and r-GO compared to naïve cells and negative control after 24 and 48 hours.

GSH/GSSG ratio was significantly decreased in MRC5 cells incubated with GO at concentrations range from 62.5 to 300 μg/ml for 24 hours versus naïve cells (**Figure 41A**). The ratio of GSH/GSSG was significantly reduced in MRC-5 cells by r-GO at concentrations range from 125 to 300 μg/ml for 24 hours compared to the untreated group. After 48 hours, all tested GO concentrations showed a significant decrease in the GSH/GSSG ratio in comparison to naïve cells. Concentrations ranging from 62.5 to 300 μg/ml of r-GO induced a significant reduction of the GSH/GSSG ratio versus naïve cells after 48 hours incubation.

For A549 cells, no change in the GSH/GSSG ratio observed after 24 hours exposure to GO and r-GO compared to naïve cells. After 48 hours, both GO and r-GO induced significant reductions in the GSH/GSSG ratio versus naïve cells at concentrations ranging from 125 to 300 μg/ml (**Figure 41B**). The observed decrease in GSH/GSSG ratio was an indication of induction of oxidative stress in cells exposed to graphene derivatives.

The observed decrease in GSH/GSSG ratio reflects the oxidation of sulfhydryl group of GSH by ROS to form the oxidised disulphide complex (GSSG) (Ballatori et al., 2009). To further evaluate the potential stress caused by graphene derivatives, proteins that are activated by cellular stress including phospho-p38 MAP kinase and downstream phospho-HSP27 were analysed (Rouse et al., 1994, landry et al., 1992, raingeaud et al., 1995).

In this work, it was hypothesised that there will be an increase in the expression of both phospho-p38 MAP kinase and phospho-HSP27 proteins in response to the increased oxidative stress resulting from exposure to graphene-based nanomaterials (300 μg/ml of GO or r-GO; 24 hours). Anisomycin was used as a positive control (25 μg/ml, 30 minutes). The results indicated a significant increase in the phospho-p38 MAPK (9-folds) and Phospho-HSP27 (3-folds) protein expression in MRC-5 cells after incubation with GO or r-GO for

24 hours compared to naïve cells (**Figure 42A**). In the case of A549 cells incubated with GO or r-GO, there was no observed change to either phospho-p38 MAPK or phospho-HSP27 in comparison to naïve cells (**Figure 42D**).

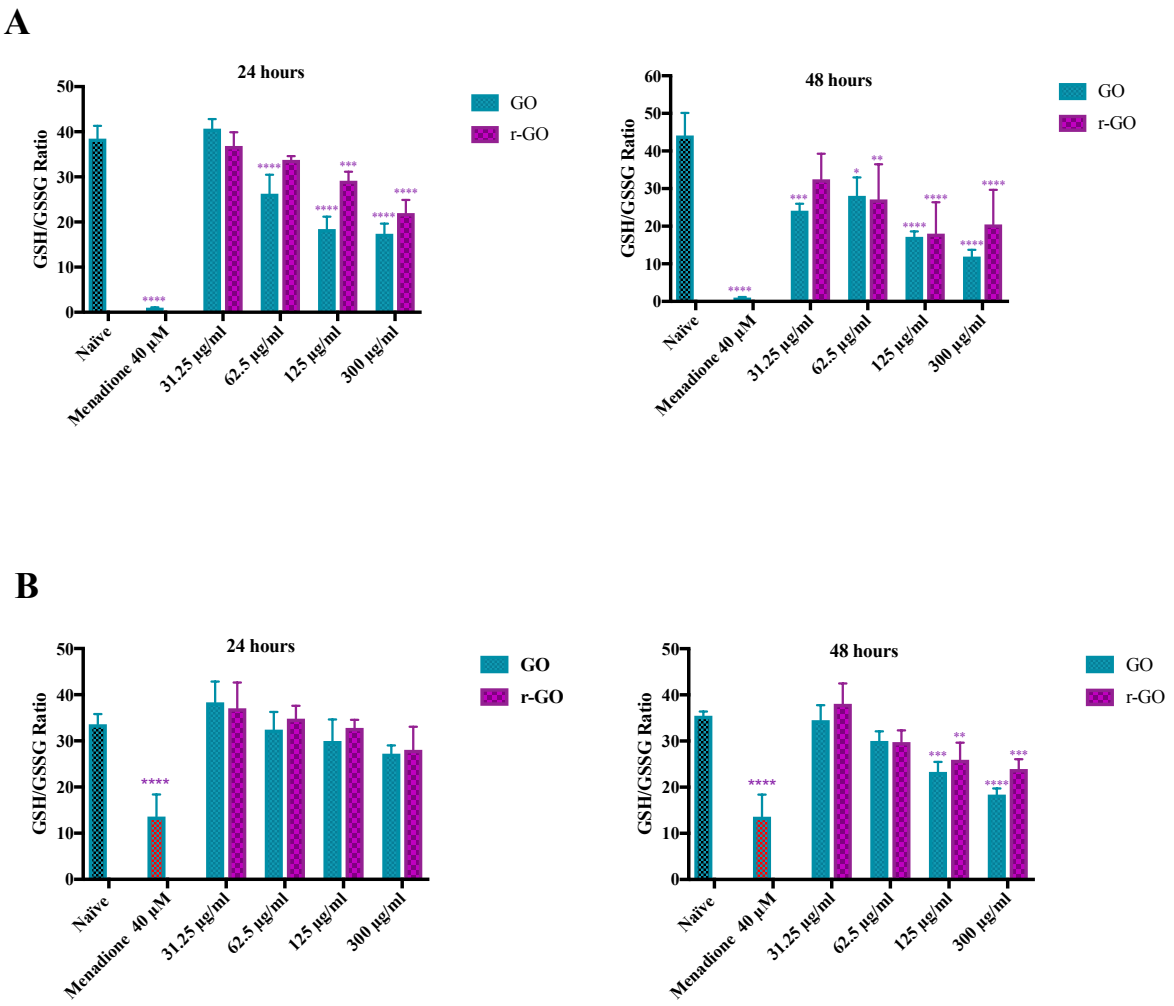

Figure 41. GSH/GSSG ratio assessment in A) MRC-5 and B) A549 cells by means of GSH/GSSG-GloTM Assay. Cells were incubated with GO and r-GO at different concentrations (31.25-300 µg/ml) for 24 and 48 hours. **A)** A significant decrease in GSH/GSSG ratio was observed in MRC-5 cells after 24 and 48 hours exposure to GO and r-GO versus naïve. **B)** After 24 hours, there was an insignificant change on the GSH/GSSG ratio between cells exposed to GO and r-GO compared to naïve. A significant decrease in GSH/GSSG ratio in A549 cells was observed after 48 hours incubation with GO and r-GO at concentrations ranging from 125 to 300 µg/ml versus naïve. Bars represent mean ± SD (n=4). *p < 0.05, **p < 0.002, ***p < 0.0002 and ****p < 0.0001 versus naïve by ANOVA analysis.

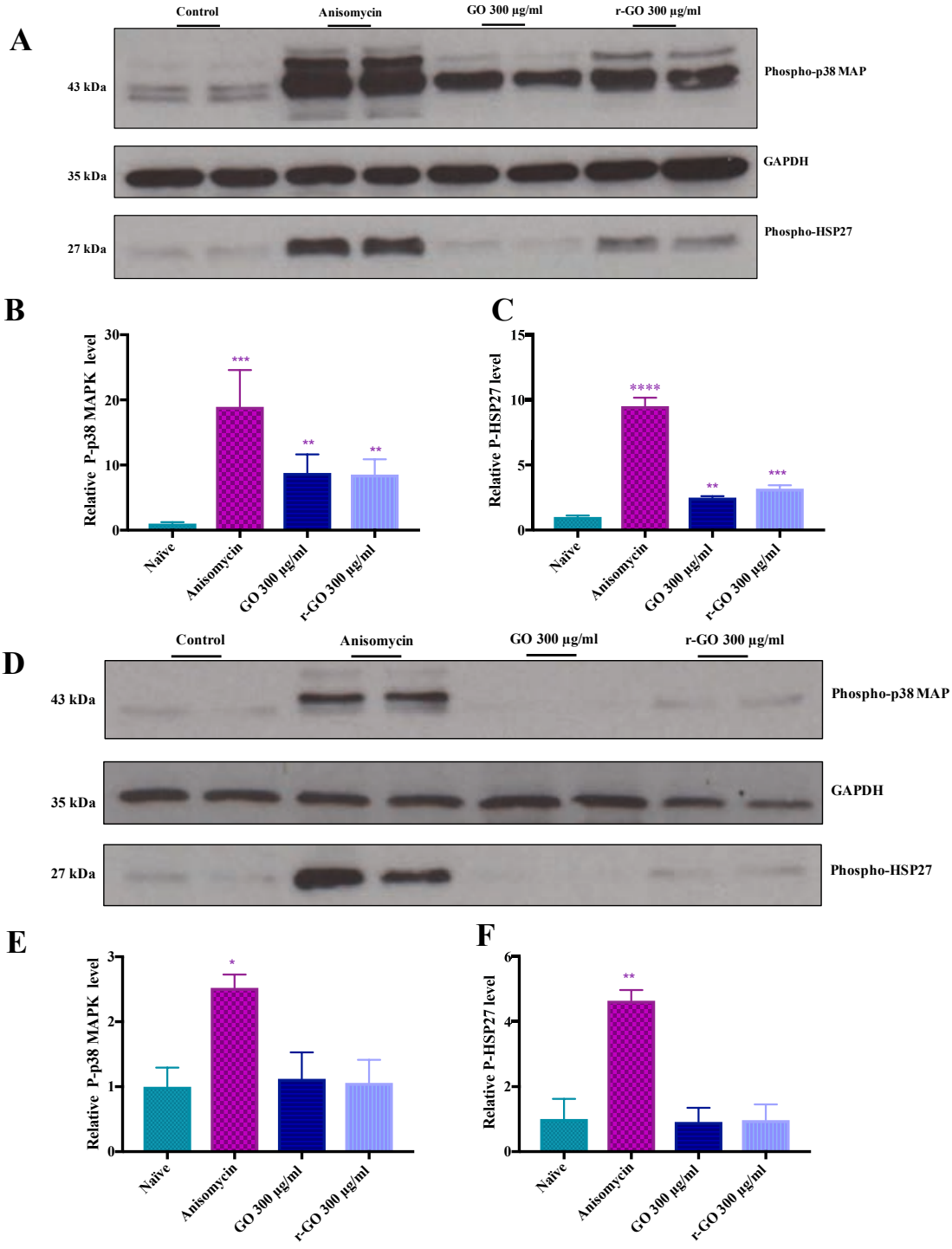

Figure 42. The analysis of phosphor-p38 MAPK and phosphor-HSP27 in A-C) MRC-5 and D-F) A549 cells. Western blot films represent analysis of P-p38 MAPK and P-HSP27 expression in MRC-5 (**A**) and A549 cells (**D**). Analysis included untreated cells (naïve), cells incubated with 25 µg/ml of anisomycin for 30 minutes, and cells incubated with GO and r-GO at concentration of 300 µg/ml for 24 hours. **B** and **E** show densitometry analysis of P-p38 MAPK in MRC-5 and A549 cells, respectively. **C** and **F** show densitometry analysis of P-HSP27 in MRC-5 and A549 cells, respectively. There was a significant increase in P-p38 MAPK and P-HSP27 protein expression in MRC-5 cells, but not in A549 cells, incubated with graphene derivatives compared to naïve. The protein expression was normalized to GAPDH (loading control) relative to naive. Bars represent mean ± SEM (n=3). * = $p < 0.05$, ** = $p < 0.002$, *** = $p < 0.0002$ and **** = $p < 0.0001$ versus naïve by ANOVA.

In summary, both graphene derivatives induced oxidative stress that was evident by an increased ROS level as well as a reduction in GSH/GSSG ratio. Accordingly, both phospho-p38 MAP kinase and phospho-HSP27 proteins were increased in MRC-5 cells, but not A549 cells, after 24 hours. The latter observation could be explained by the fact that significant oxidative stress was observed only after 48 hours in A549 cells.

Investigators have reported that pristine graphene increases ROS levels in the murine RAW 264.7 macrophage cell line at concentrations ranging from 5 to 20 μg/ml that triggered apoptosis through mitochondrial signalling (Li et al., 2012). R-GO is expected to mimics pristine graphene effect but in this work r-GO significantly induced ROS levels only at the higher concentration range (125-300 μg/ml), and apoptosis was not evident. The different finding could be attributed to the fact that in the Li and colleagues study RAW 264.7 macrophages were used which are able to uptake pristine graphene whereas in the current work non-phagocytic cells were used and cell uptake data showed negligible uptake of r-GO. GO moderately increased ROS in dose dependent manner in A549 (Chang et al., 2011), which is consistent with this work. Also, GO was shown to cause oxidative stress in a human lung fibroblast (HLF) cell line, leading to cytotoxicity and genotoxicity (Wang et al., 2013). GO and r-GO were observed to decrease the GSH/GSSG ratio in human liver carcinoma cells (HepG2). Also, graphene quantum dots at concentration ranges from 10 to 200 μg/ml for 24 hours, were shown to induce an inflammatory response and autophagy through induction of phospho-p38 MAP kinase in THP-1 macrophages (Qin et al., 2015). This finding is similar to what has been observed for MRC-5 cells incubated with GO in this study. Data from the literature and findings from this study support the view point that oxidative stress has a critical role in graphene-based nanomaterial's cytotoxicity.

The significant GO cytotoxicity seen in MRC-5 cells is presumably a consequence of oxidative stress. On the other hand, the data here demonstrated that r-GO induced oxidative

stress in MRC-5 cells, but r-GO cytotoxicity was not evident in MRC-5 cells. However, the effect GO has on GSG/GSSG in MRC-5 cells was more pronounced than r-GO after 24 hours exposure. For A549 cells, the data obtained for cell viability showed that cytotoxicity was more evident after 48 hours than 24 hours post-exposure to both GO and r-GO, and this was consistent with GSH/GSSG measurements as the decrease in the ratio was only significant after 48 hours. These findings indicate that a component of the cytotoxicity mechanisms of GO and r-GO is the induction of oxidative stress but there are possibly other causes of cell death.

Furthermore, ROS levels can regulate autophagy induction (Poillet-Perez et al., 2015). The induction of autophagy requires the formation of hydrogen peroxide (H_2O_2) to oxidise and inactivate ATG4 enzyme. Inactivation of ATG4 is responsible for the formation of the LC3-II protein that associates with the autophagosome (Ruth Scherz-Shouval et al., 2007). Also, ROS can activate the AMPK pathway leading to the inhibition of mTOR and autophagy induction (Poillet-Perez et al., 2015). Additionally, AMPK can directly activate ULK1 that triggers PI3K-III and forms a complex with the associated proteins to start autophagy (Papinski and Kraft, 2014, Klionsky et al., 2016). All of the above suggest that one of the reasons for GO- induced autophagic cell death is *via* induction of ROS.

4.2.3.4 Genotoxicity assessment

Excessive ROS formation could be the initial step in the mechanism of genetic damage by nanomaterial (Ou et al., 2016). Here, it might be the main mechanism as neither nanomaterial was taken-up by cells. The genotoxicity effect of nanomaterials can relate to their physiochemical properties. For instance, ROS generation and genotoxicity are reported to be size dependent. As the size of nanoparticles decrease, the surface area per unit mass increases and thus a higher surface area could be an important factor in genotoxicity (Gonzalez et al., 2009, Magdolenova et al., 2014), particularly that a direct relationship between the surface area of nanoparticles and ROS formation has been reported (Li et al., 2011). In addition to the size, the surface properties of nanoparticles are another factor that can affect their cytotoxicity and genotoxicity profile (Ahamed et al., 2008, Gonzalez et al., 2009, Wang et al., 2015a).

Genotoxicity assessment is essential, since there is a close correlation between genetic damage and cancer (Klaassen and Watkins, 2008). Due to the direct relation between the generation of ROS and DNA damage it was essential to assess genotoxicity of GO and r-GO particularly both were found to induce ROS in this work. Here the level of DNA strand breaks in cells incubated with GO and r-GO (125 and 300 μg/ml) for 3 and 24 hours was assessed by comet assay (single cell gel electrophoresis) and presented as tail length intensity. A three-hour time point was added to detect possible transient genotoxicity.

Figure 43, shows the images after staining with SYBR-GOLD solution for DNA migration through gel electrophoresis, which is referred to as comets in both the negative control (Naïve) and positive control (0.2 µg/ml, 4-Nitroquinoline N-Oxide). Comets obtained from negative control cells showed an intact nucleus, without any DNA damage, whereas 4-Nitroquinoline N-Oxide treated cells showed a clear comet-like tail which is an indicator of DNA damage. Comet analyses for MRC-5 and A549 cells indicated no signs of genotoxicity, after incubation with GO or r-GO for 3 and 24 hours and in comparison, to negative and positive control (**Figure 44**).

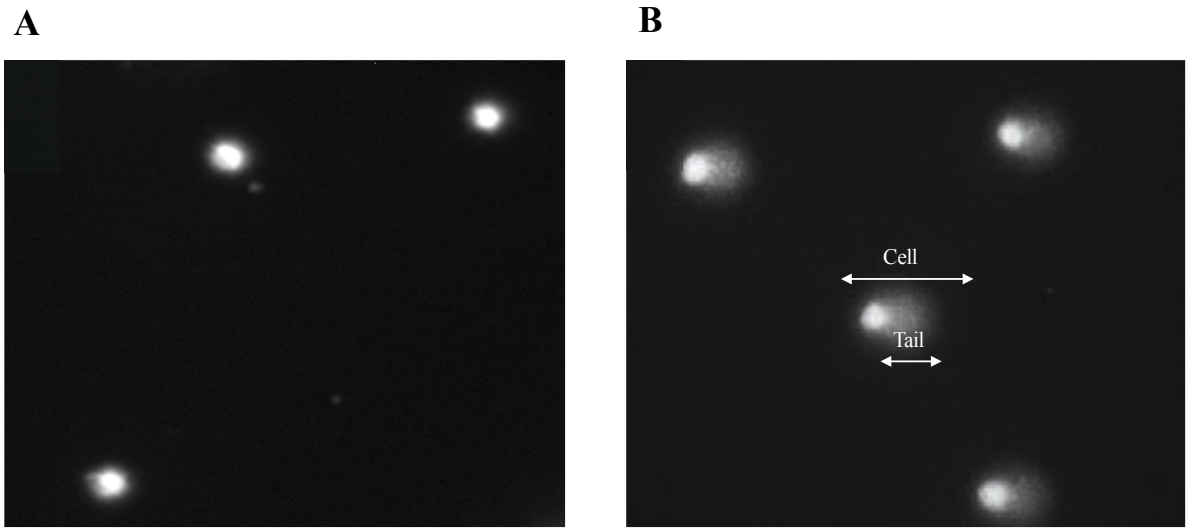

Figure 43. Images of comets from single cell gel electrophoresis stained with SYBR-GOLD solution. A) Shows untreated MRC-5 cells with an intact nucleus. **B)** Cells treated with 0.2 µg/ml of 4-Nitroquinoline N-Oxide for 2 hrs showing increasing tail length which indicates DNA damage. Images were taken using an Axiovert 10 microscope (Zeiss) at 200-fold magnification (n=3).

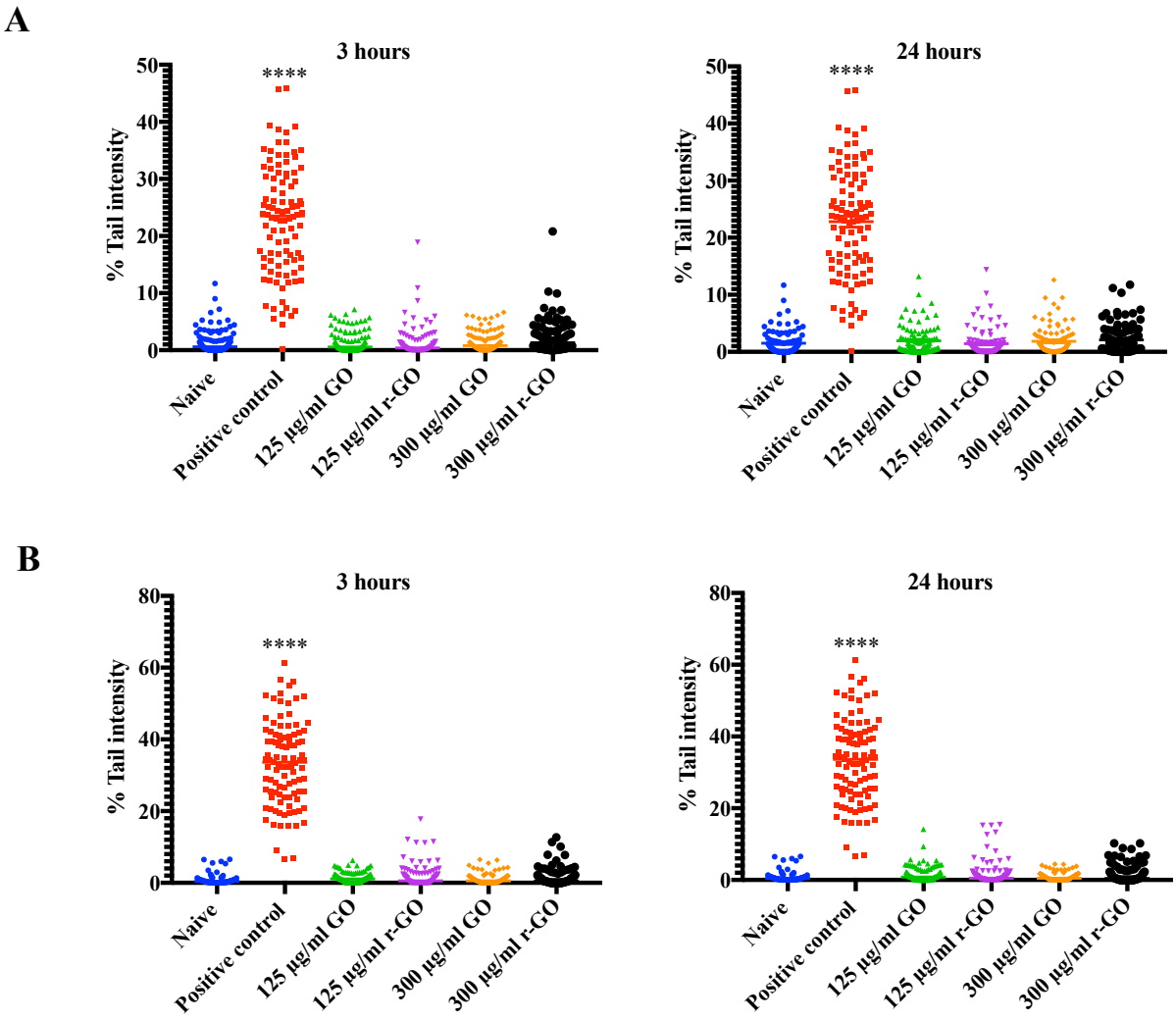

Figure 44. Tail intensity percentage in A) MRC-5 and B) A549 cells. Cells were incubated with 125 or 300 µg/ml of GO and r-GO for 3 and 24 hours. Controls in the comet assay included naïve (negative control) and cells incubated with 0.2 µg/ml of 4-Nitroquinoline N-Oxide for 2 hours (positive control**. A)** Tail intensity in MRC-5 cells **B)** Tail intensity analysis in A549 cells. No signs of genotoxicity were observed for both cell lines after incubation with graphene derivatives at concentrations ranging from 125 to 300 µg/ml for 3 and 24 hours, compared with experimental controls. Data were measured using comet IV software. Data represent median of 100 scores from two independent experiment (50 scores each). * = $p < 0.05$, ** = $p < 0.002$, *** = $p < 0.0002$ and **** = $p < 0.0001$ versus naïve by Kruskal-wallis test.

Genotoxicity data obtained from this study revealed that both GO and r-GO were non-genotoxic which is in agreement with Bengtson and colleagues work who used similar concentrations and time exposure and murine pulmonary epithelial cell line (FE1) (Bengtson et al., 2016). On the other hand, several studies have reported genotoxic effect of GO and r-GO nanomaterials. Wang and colleagues (Wang et al., 2013) found that GO treatment leads to DNA damage in a human lung fibroblast line (HLF) at a dose-range of 1–100 μg/ml and in another study genotoxicity was also evident with GO but not with r-GO for human umbilical vein endothelial cells (HUVEC) (Das et al., 2013). Additionally, Chatterjee and colleagues have reported that both GO and r-GO are genotoxic for human liver carcinoma HepG2 cells (Chatterjee et al., 2014). In all of these studies, ROS generation was the underlying mechanism of DNA damage. However, in the current study the ROS generated by GO and r-GO was not sufficient to induce DNA damage, which was similar to Bengtson and colleagues observations (Bengtson et al., 2016), suggesting that probably higher ROS levels are required to induce genetic damage in MRC-5 and A549 cells.

In addition, different graphene derivatives including graphene, graphite and r-GO were found to induce DNA damage in glioblastoma U87 cells, whereas GO was reported as non-genotoxic for the same cell line (Hinzmann et al., 2014). Moreover, Martinez Paino and colleagues reported that GO was not genotoxic to mouse fibroblast L929 cells but exhibited a genotoxic effect against human cervical carcinoma HeLa and human monocyte cells at 24 μg/ml for 24 hours (Martinez Paino et al., 2017). The data provided from the above studies highlight the influence of the cell type as well as the different surface chemistry of graphene-based nanomaterials on their genotoxic effect. Hence, further studies on the genotoxicity of graphene-based nanomaterials are necessary particularly in healthy non-cancerous cells.

4.2.3.5 Impacts of GO and r-GO on Wnt/β-catenin and Akt cell signalling pathways

Recent studies have shown that cellular responses induced by nanoparticle exposure were due to an effect on certain cell signalling pathways (Kang et al., 2017, Shi et al., 2017, Wierzbicki et al., 2017). One such important signalling pathway is the Wnt signalling pathway which plays a crucial role in embryonic development and carcinogenesis (Goessling et al., 2009, Nusse and Clevers, 2017). The Wnt signalling pathway is divided into two major components, β-catenin dependent and β-catenin independent; the former controls cell proliferation and cell fate during development.

Wnt/β-catenin signalling initiates when Wnt protein binds to a frizzled receptor (Fz) that leads to inactivation of the destruction complex (**Figure 45**). The destruction complex is composed of adenomatosis polypsis coli (APC), axin and glycogen synthase kinase-3 (GSK-3β) and targets β-catenin for degradation. Consequently, the inactivation of the destruction complex leads to the accumulation of β-catenin in the cytosol and then in the nucleus, where it controls gene expression (MacDonald et al., 2009, Rao and Kuhl, 2010). β-catenin is the central signalling molecule that controls cell fate and when dysregulated is a major driver of cancer (Nusse and Clevers, 2017). In addition to its role in the Wnt pathway, GSK-3β is also involved in Akt and AMPK signalling. The inhibition of GSK-3β has been related to a variety of diseases such as diabetes, Alzheimer's disease and cancer (Metcalfe and Bienz, 2011). GSK-3β was also reported to indirectly inhibit the autophagy process (Azoulay-Alfaguter et al., 2015, Weikel et al., 2016, Avrahami et al., 2013, Ark et al., 2014). To assess the impacts of graphene nanomaterials on the Wnt/β-catenin cell signalling pathway, β-catenin and GSK-3β protein expression was analysed for cells exposed to graphene derivatives.

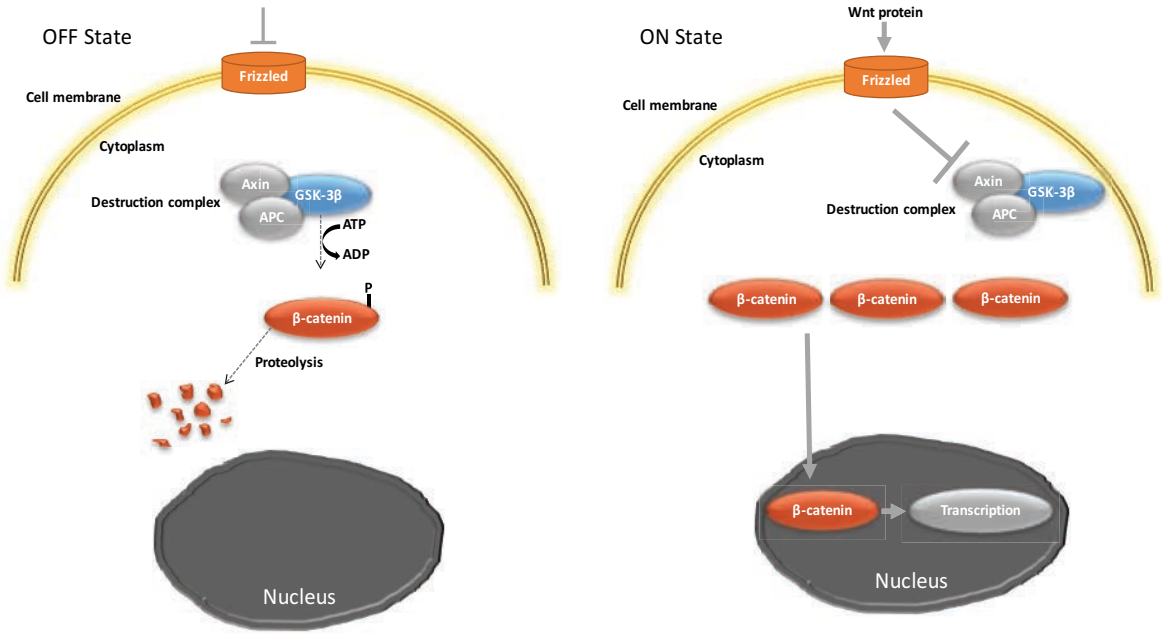

Figure 45. Wnt/β-catenin cell signalling pathway. The Wnt/β-catenin signalling starts when Wnt protein binds to a frizzled receptor that leads to inactivation of the destruction complex. The destruction complex proteins components are adenomatosis polypsis coli (APC), axin and glycogen synthase kinase-3 (GSK-3β). (APC/Axin/GSK-3β)-complex targets β-catenin for degradation. The inactivation of (APC/Axin/GSK-3β)-complex gives rise to accumulation of β-catenin in the cytosol and then its subsequent translocation into the nucleus. Inside the nucleus the β-catenin induces cellular response through gene transcription.

In the present work, the β-catenin level was analysed for MRC-5 and A549 cells after incubation with a cytotoxic concentration of GO or r-GO (300 μg/ml) for 24 hours. Only 2% and 10% of β-catenin protein expression was found in MRC-5 and A549 cells, respectively, after incubation with 300 μg/ml of GO. However, there was not any observed significant change in β-catenin protein expression after incubation with r-GO (**Figure 46**). When lower GO concentrations were tested, a significant reduction (to ca. 4% of the baseline) was seen at a concentration of 125 μg/ml after 24 hours. Conversely, there was not a significant reduction in β-catenin expression in A549 cells (**Figure 47**).

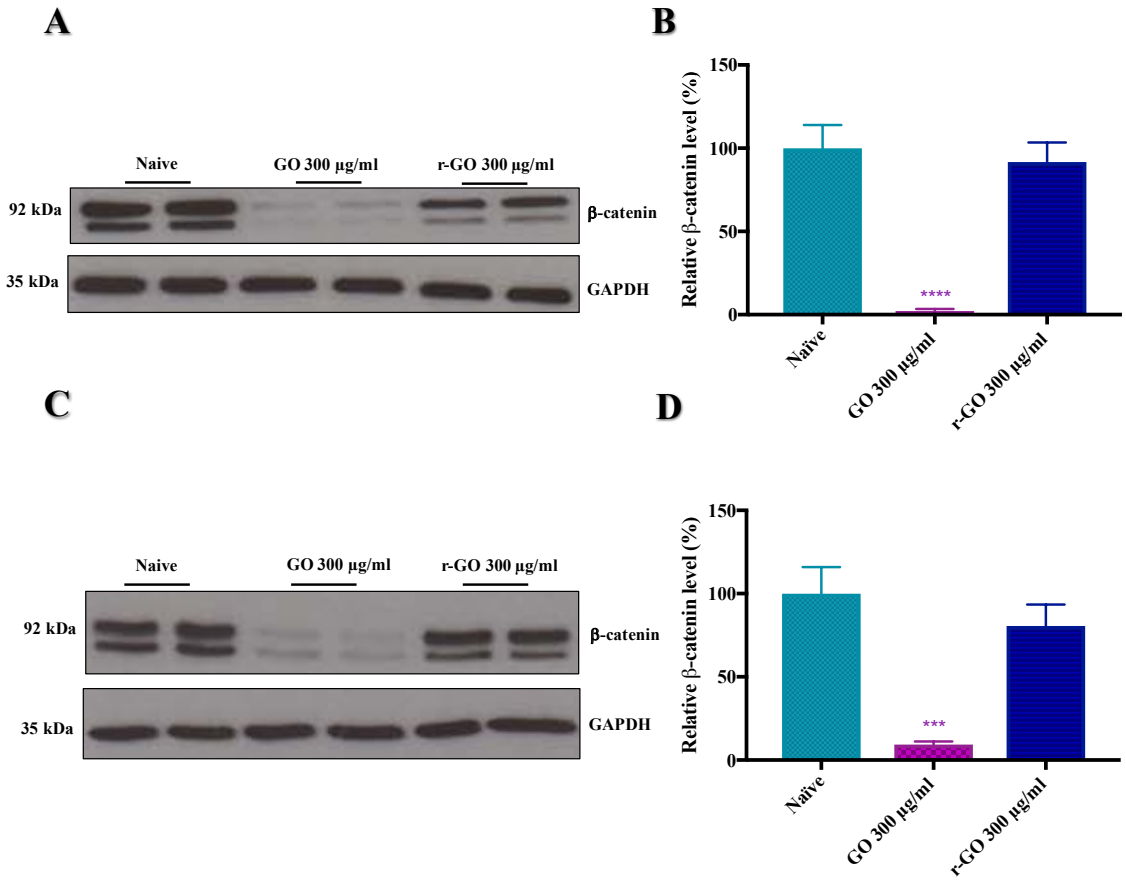

Figure 46. The effect of GO and r-GO on β-catenin protein expression in A-B) MRC-5 and C-D) A549 cells. A and **C** are representative Western blot analysis of β-catenin expression in MRC-5 cells and in A549 cells, respectively. Analysis included untreated cells (naïve) and cells treated with 300 µg/ml of GO or r-GO for 24 hours. Pronounced reduction was observed in both cell lines treated with GO. **B** and **D** are densitometry analysis of β-catenin expression in MRC-5 cells and in A549 cells, respectively. The protein expression was normalized to GAPDH (loading control) relative to the untreated group (naïve). Results are represented as % compared to untreated group. Bars represent mean ± SEM (n=6). *$p < 0.05$, **$p < 0.002$, ***$p < 0.0002$ and ****$p < 0.0001$ versus naïve by ANOVA analysis.

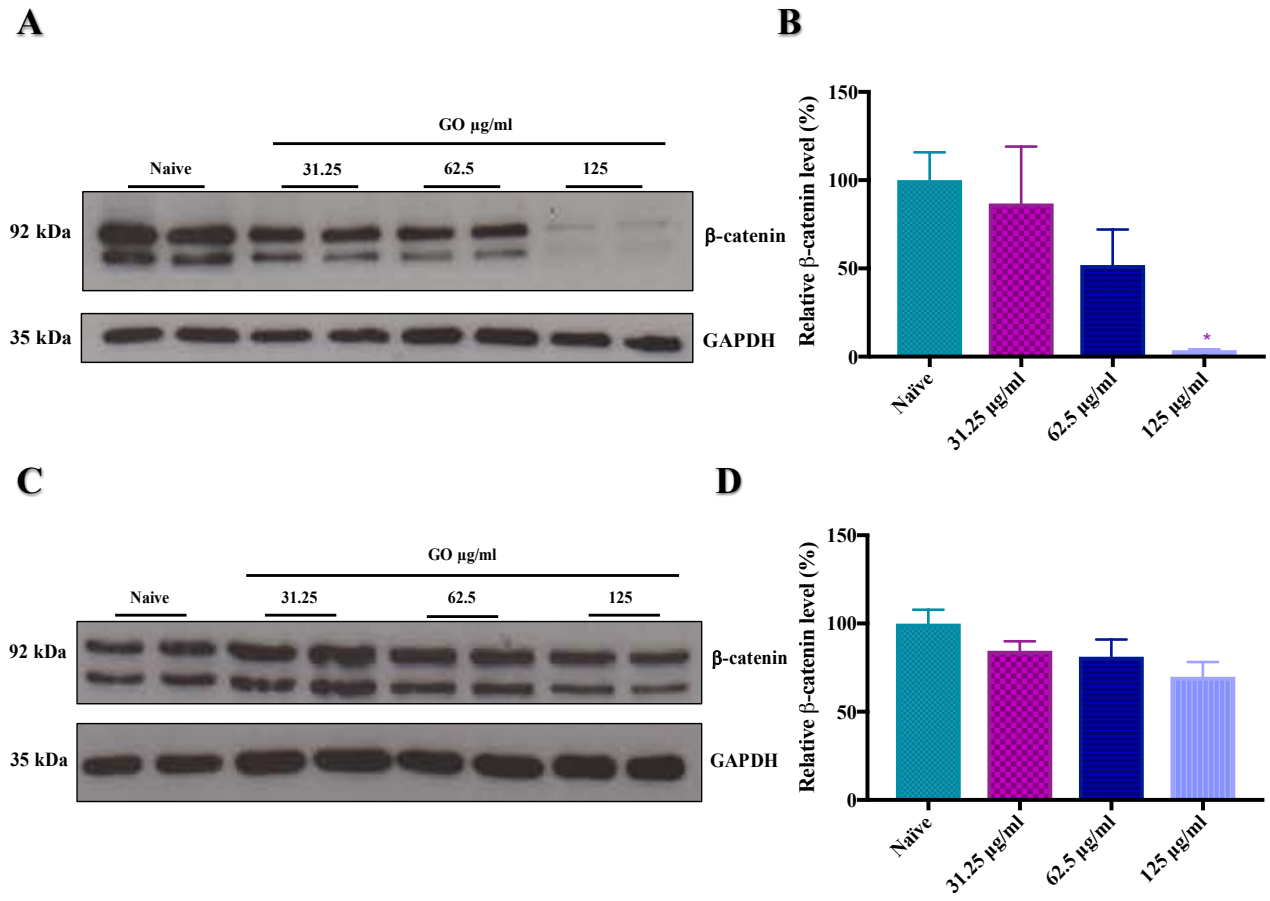

Figure 47. The effect of different concentrations range of GO on β-catenin protein expression in A-B) MRC-5 and C-D) A549 cells. A and **C** are representative Western blot analysis of β-catenin expression in MRC-5 cells and in A549 cells, respectively. Analysis included untreated cells (naïve) and cells treated with GO at concentrations ranging from 31.25 to 125 µg/ml for 24 hours. Significant reduction in β-catenin expression was only seen at concentration of 125 µg/ml in MRC-5. **B** and **D** are densitometry analysis of β-catenin expression in MRC-5 cells and in A549 cells, respectively. The protein expression was normalized to GAPDH (loading control) relative to the untreated group (naïve). Results are represented as % compared to untreated group. Bars represent mean ± SEM (n=6). *$p < 0.05$, **$p < 0.002$, ***$p < 0.0002$ and ****$p < 0.0001$ versus naïve by ANOVA analysis.

Furthermore, a significant decrease was observed in GSK-3β levels (<4% of the baseline) for MRC-5 and A549 cells incubated with 300 μg/ml of GO for 24 hours. In the case of cells incubated with r-GO, there was not a significant change in the level of GSK-3β expression in both cell lines (**Figure 48**). Further tests revealed that GSK-3β levels were significantly reduced following exposure to a low concentration of GO (**Figure 49**). Indeed, a ca. 63% reduction in the GSK-3β expression was observed for MRC-5 cells after exposure to 31.25 μg/ml of GO. For A549 cells, the impact was less visible at this low concentration (ca. 15% decrease), but GSK-3β expression was decreased by half as compared to naïve cells when A549 were exposed to 125 μg/ml of GO.

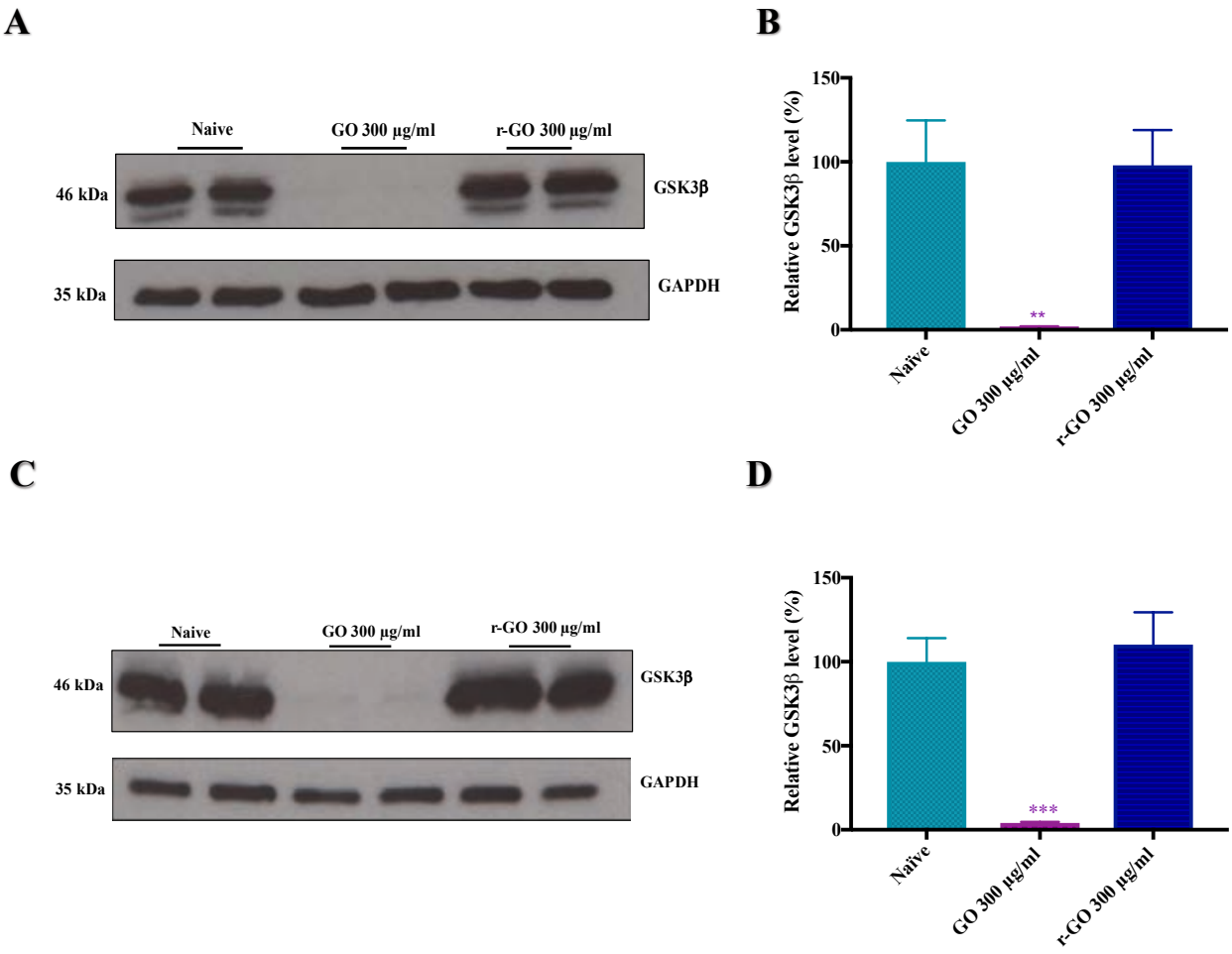

Figure 48. The effect of GO and r-GO on GSK-3β protein expression in A-B) MRC-5 and C-D) A549 cells. A and **C** are representative Western blot analysis of GSK-3β protein expression in MRC-5 cells and in A549 cells, respectively. Analysis included untreated cells and cells treated with 300 µg/ml of GO or r-GO for 24 hours. A significant reduction was seen for both cell lines exposed to GO. r-GO showed no effect on GSK-3β protein expression. **B** and **D** are densitometry analysis of GSK-3β expression in MRC-5 cells and in A549 cells, respectively. The protein expression was normalized to GAPDH (loading control) relative to the untreated group (naïve). Results are represented as % compared to untreated group. Bars represent mean ± SEM (n=6). *$p < 0.05$, **$p < 0.002$, ***$p < 0.0002$ and ****$p < 0.0001$ versus naïve by ANOVA analysis.

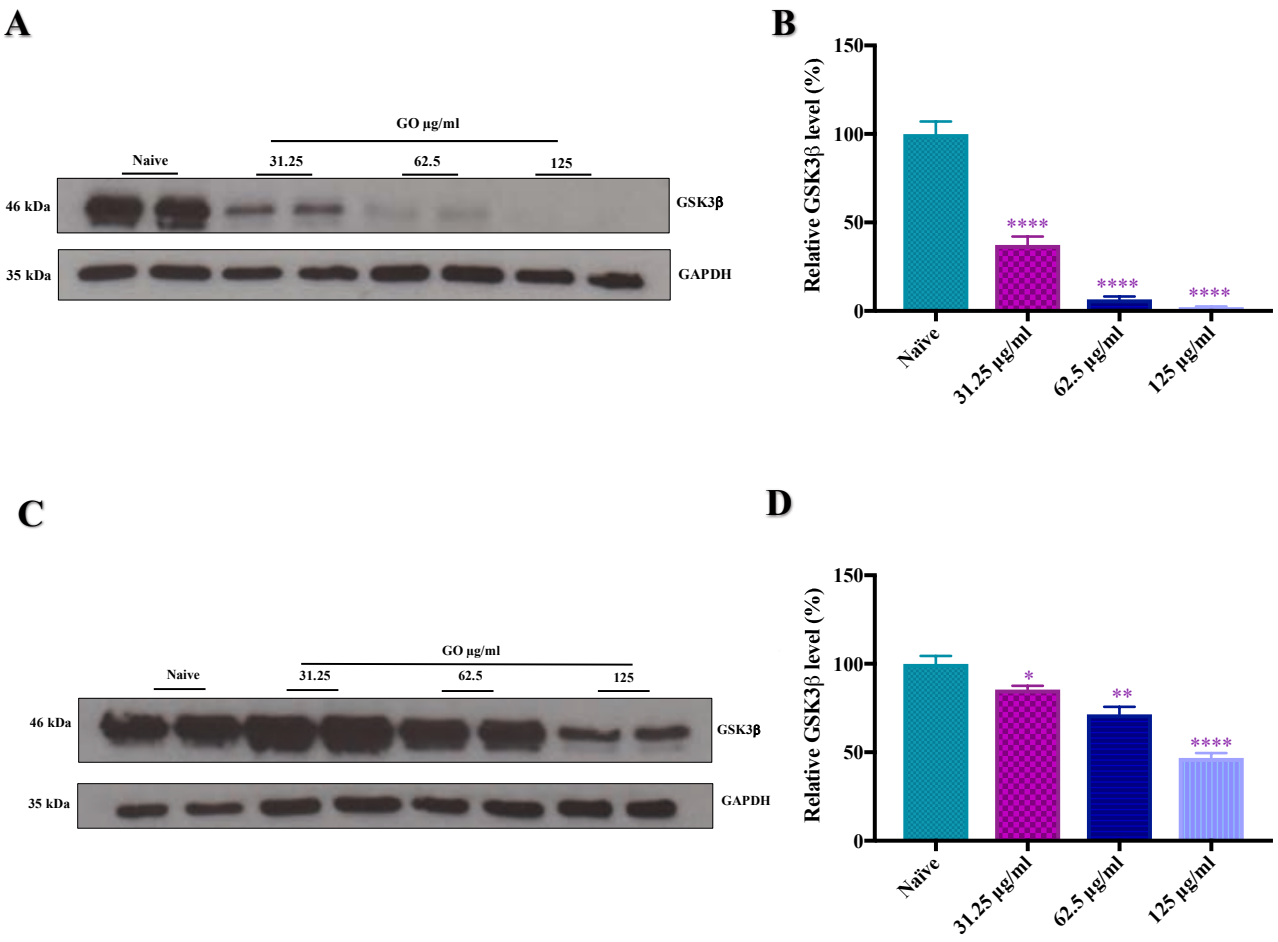

Figure 49. The effect of different concentrations range of GO on GSK-3β protein expression in A-b) MRC-5 and C-D) A549 cells. A and **C** are representative Western blot analysis of GSK-3β expression in MRC-5 cells and in A549 cells, respectively. Analysis included untreated cells (naïve) and cells treated with GO at concentrations ranging from 31.25 to 125 µg/ml for 24 hours. A significant concentration dependent reduction in GSK-3β protein expression was seen for both cell lines exposed to different concentrations of GO. **B** and **D** are densitometry analysis of GSK-3β expression in MRC-5 cells and in A549 cells, respectively. The protein expression was normalized to GAPDH (loading control) relative to the untreated group (naïve). Results are represented as % compared to untreated group. Bars represent mean ± SEM (n=3). *p < 0.05, **p < 0.002, ***p < 0.0002 and ****p < 0.0001 versus naïve by ANOVA analysis.

These results indicated that GO, but not r-GO, has an effect on Wnt/β-catenin signalling pathway, because GO downregulated the expression of β-catenin and GSK-3β proteins that play a major role in this pathway. The dysregulation of Wnt/β-catenin cell signalling observed in this study agrees with the findings by other investigators who reported that GO but not r-GO alter Wnt/β-catenin cell signalling pathways in Caenorhabditis elegans (Chatterjee et al., 2017, Zhi et al., 2017). As the Wnt signalling pathway plays a crucial role in embryonic development, disruption of this cellular pathway can lead to reproductive damage. Indeed, GO was reported to induce high reproductive toxicity in Caenorhabditis elegans through its effect on the Wnt/β-catenin signalling pathway (Chatterjee et al., 2017). The latter study could explain the weak reproductive capacity observed in Caenorhabditis elegans exposed to GO by recent studies (Chatterjee et al., 2015, Chatterjee et al., 2014, Zhao et al., 2016).

GSK-3β was significantly downregulated even at non-cytotoxic concentration of GO (31.25 μg/ml) particularly in MRC-5 cells. These data point to non-lethal cellular responses that are driven by GO and that should be further evaluated. The observed suppression of expression of GSK-3β possibly plays a major role in the toxicity of GO, especially considering that GSK-3β is a vital component of various cell signalling pathways, such as Wnt, Akt and AMPK. Additionally, GSK-3β inhibition has been related to a variety of diseases including cancer (Metcalfe and Bienz, 2011). Therefore, the data obtained using healthy cells in the present work raises concerns regarding the use of GO in biomedical applications.

As mentioned previously, GSK-3β can indirectly inhibit the autophagy process *via* different mechanisms such as decreasing lysosome acidification (Avrahami et al., 2013), inactivation of AMPK (Ark et al., 2014) or activation of mTOR (Azoulay-Alfaguter et al., 2015, Weikel et al., 2016). In the present study, GO was found to induce autophagy and downregulate

mTOR protein, a negative autophagy regulator, that possibly has led to uncontrolled autophagy. Therefore, a conclusion is that the inhibitory effect of GSK-3β on autophagy and the activation of mTOR are possibly prevented by GO mediated downregulation of GSK-3β protein. Though 63% reduction of GSK-3β protein was observed in MRC-5 by 31.25 μg/ml of GO, only a 10% reduction of mTOR was detected post-treating cells with the same concentration of GO for 24 hours.

Akt signalling pathway is another vital signalling cascade that regulates a variety of cellular functions for instance cell metabolism, protein synthesis, proliferation and survival (Osaki M and Oshimura M, 2004). The Akt signalling (**Figure 50**) is initiated by the activation of surface receptors such as receptor tyrosine kinase (RTK), G protein coupled receptor (GPCR) and cytokine receptors leading to the formation of phosphatidylinositol triphosphates (PIP3) at the plasma membrane. The PIP3 recruits Akt to the membrane for activation through phosphorylation, by kinases such as 3-phosphoinositide-dependent protein kinase-1 (PDK1) (Manning and Cantley, 2007).

Akt activity is negatively regulated by the tumour suppressor phosphatase and tension homolog (PTEN), *via* dephosphorylating PIP3 (Carracedo and Pandolfi, 2008). Impairment of Akt cell signalling is a mechanism that underlies many different pathologies (Vasudevan et al., 2004, Salmena et al., 2008). In this study, PDK1 and PTEN protein expression were investigated for cells treated with graphene nanomaterials.

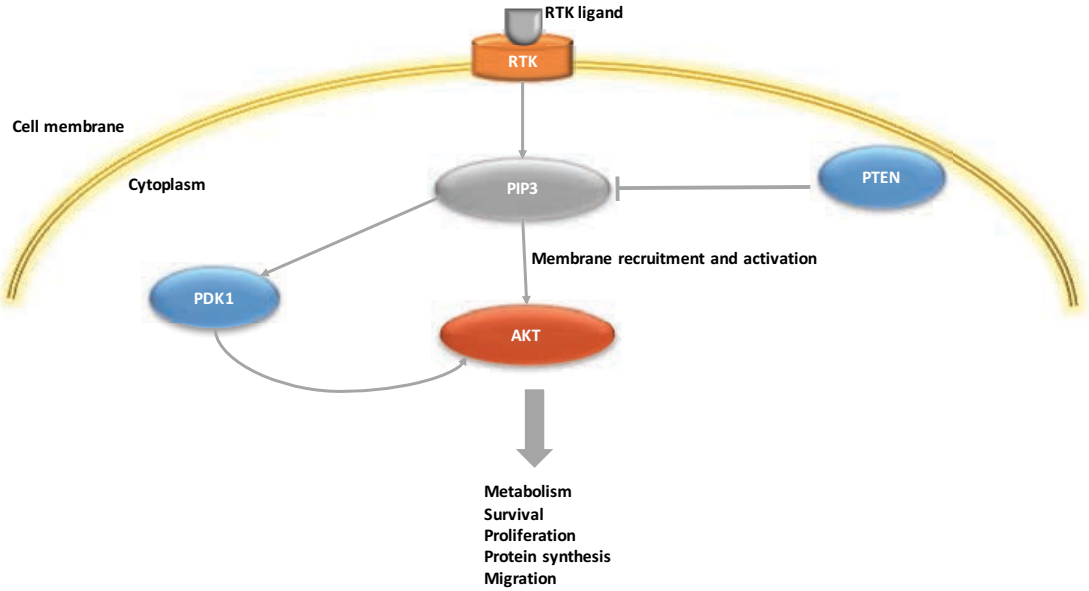

Figure 50. Akt signalling pathway. The Akt signalling is initiated by the activation of surface receptors such as receptor tyrosine kinase (RTK) that induces formation of phosphatidylinositol triphosphates (PIP3) at the plasma membrane. The PIP3, recruits Akt to the membrane to be activated through phosphorylation by kinases such as 3-phosphoinositide-dependent protein kinase-1 (PDK1). Akt activity is negatively regulated by the tumour suppressor phosphatase and tension homolog (PTEN) through dephosphorylating PIP3.

PDK1 protein expression was reduced up to 73% and 41% after incubation of MRC-5 and A549 cells, respectively, with GO but not r-GO at a concentration of 300 μg/ml (**Figure 51**). For MRC-5 cells, there was a significant reduction in PDK1 protein for all tested concentrations, while in A549 cells a significant reduction was only seen at a concentration of 125 μg/ml (**Figure 52**). Moreover, the expression of the tumour suppressor PTEN protein was measured and no significant change was detected for both cell lines incubated with 300 μg/ml of GO or r-GO for 24 hours compared to untreated cells (**Figure 53**).

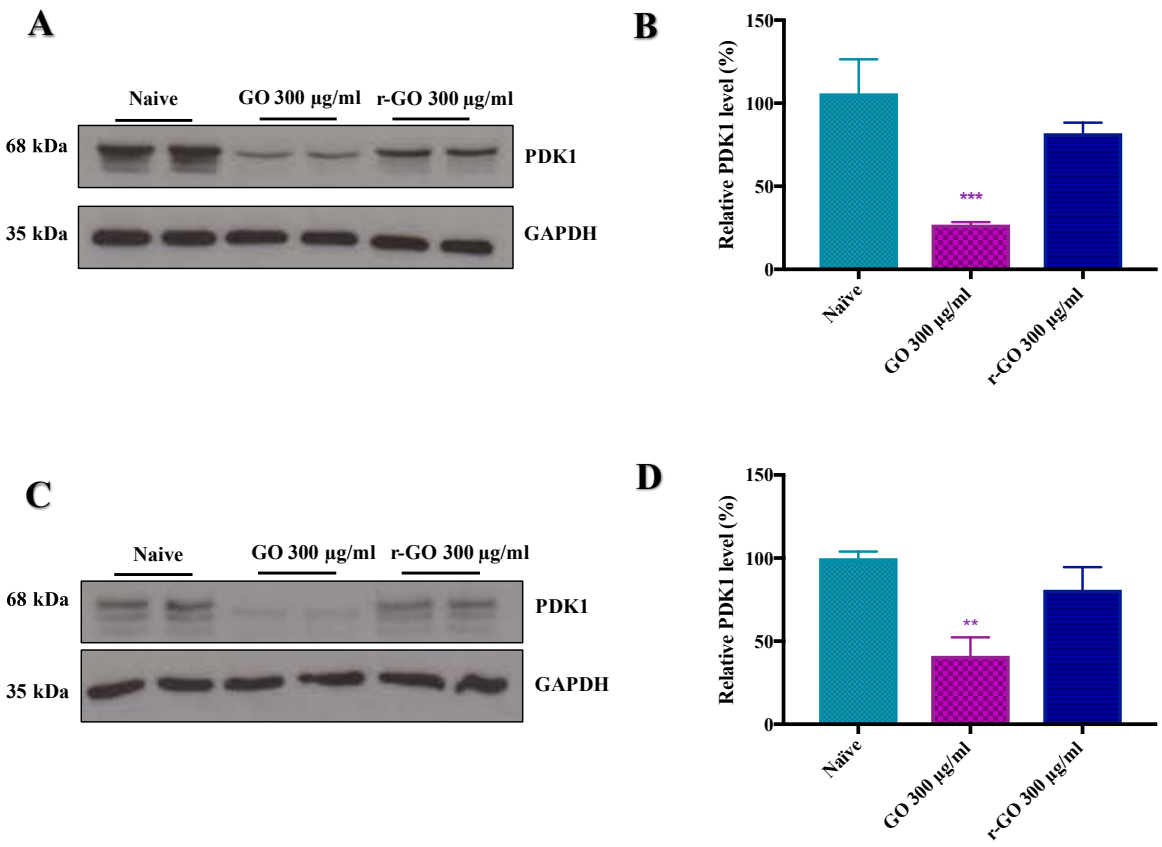

Figure 51. The effect of GO and r-GO on PDK1 protein expression in A-B) MRC-5 and C-D) A549 cells. **A** and **C** are representative Western blot analysis of PDK1protein expression in MRC-5 cells and in A549 cells, respectively. Analysis included untreated cells (naïve) and cells treated with 300 µg/ml of GO or r-GO for 24 hours. A significant reduction in PDK1 protein expression was observed in both cell lines exposed to GO. **B** and **D** are densitometry analysis of PDK1 expression in MRC-5 cells and in A549 cells, respectively. The protein expression was normalized to GAPDH relative to naïve. Results are represented as % compared to untreated group. Bars represent mean ± SEM (n=6). *p < 0.05, **p < 0.002, ***p < 0.0002 and ****p < 0.0001 versus naïve by ANOVA analysis.

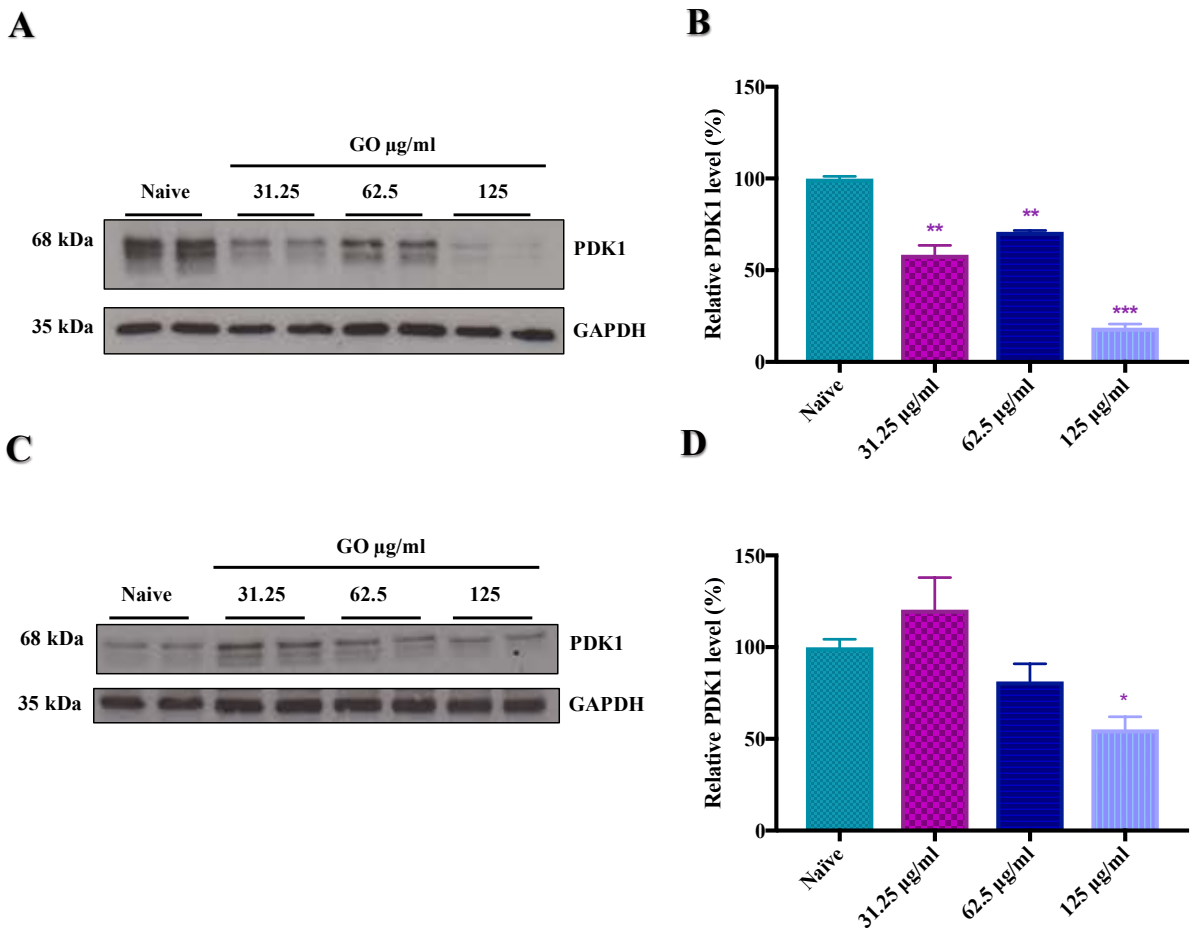

Figure 52. The effect of different concentration ranges of GO on PDK1 protein expression in A-B) MRC-5 and C-D) A549 cells. A and **C** are representative Western blot analysis of PDK1 protein expression in MRC-5 cells and in A549 cells, respectively. Analysis included untreated cells (naïve) and cells treated with GO at concentrations ranging from 31.25 to 125 µg/ml for 24 hours. A significant reduction in PDK1 protein expression was seen at all tested concentration in MRC-5. GO significantly decreased PDKI protein expression in A549 cells at a concentration of 125µg/ml. **B** and **D** are densitometry analysis of PDK1 protein expression in MRC-5 cells and in A549 cells, respectively. The protein expression was normalized to GAPDH (loading control) relative to the untreated group (naïve). Results are represented as % compared to untreated group. Bars represent mean ± SEM (n=3). *p < 0.05, **p < 0.002, ***p < 0.0002 and ****p < 0.0001 versus naïve by ANOVA analysis.

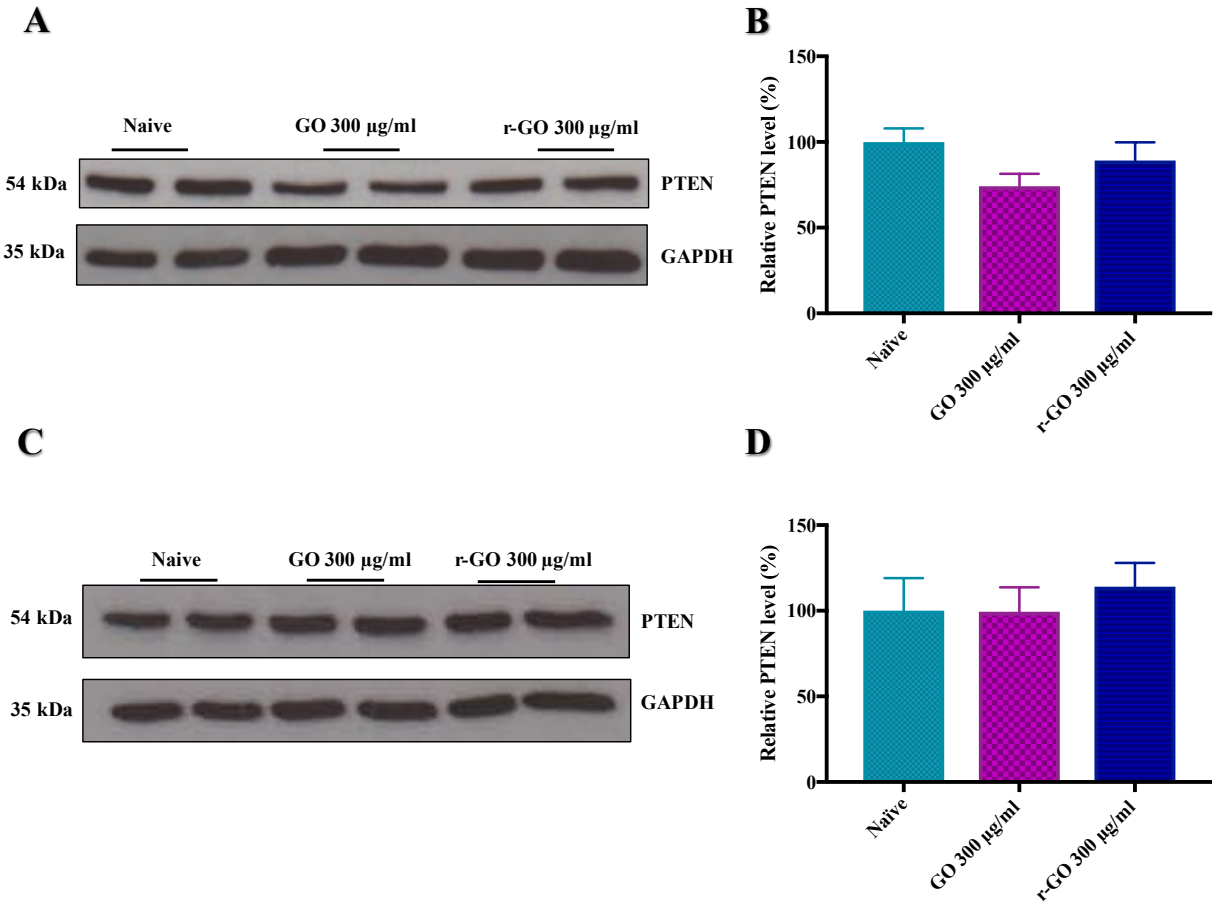

Figure 53. The effect of GO and r-GO on PTEN protein expression in A-B) MRC-5 and C-D) A549 cells. **A** and **C** are representative Western blot analysis of PTEN protein expression in MRC-5 cells and in A549 cells, respectively. Analysis included untreated cells (naïve) and cells treated with 300 µg/ml of GO or r-GO for 24 hours. No significant change in PTEN protein expression was observed in both cell lines exposed to GO or r-GO. **B** and **D** are densitometry analysis of PTEN expression in MRC-5 cells and in A549 cells, respectively. The protein expression was normalized to GAPDH (loading control) relative to the untreated group (naïve). Results are represented as % compared to untreated group. Bars represent mean ± SEM (n=6). *$p < 0.05$, **$p < 0.002$, ***$p < 0.0002$ and ****$p < 0.0001$ versus naïve by ANOVA analysis.

PDK1 is a primary regulator of the activation of Akt signalling. In this study, GO, but not r-GO, was found to inhibit the Akt cell signalling pathway *via* downregulation of PDK1 protein. GO showed no effect on the level of PTEN. In addition, mTOR is downstream of Akt cell signalling in autophagy and therfore Akt inhibition can lead to inactivation of mTOR which is in agreement with the current research findings.

In cancer, Akt is most often constitutively active and this can lead to unregulated cell proliferation (Hers et al., 2011). Also, overexpression of Akt is associated with resistance to chemotherapy (West et al., 2002). Therefore, Akt signalling has been an attractive target for new cancer treatments and other targets includes PIP3, PDK1and mTOR as a focus of research (Nitulescu et al., 2016, Cheng et al., 2005, Yang et al., 2017a). Here, GO exhibited an inhibitory effect on PDK1, mTOR and GSK-3β protein expression. Together, these findings may suggest that GO may present a novel strategy for targeting cancer cells. However, further studies are still required to probe upstream and downstream signalling cascades to understand the underlying molecular mechanisms of the action of GO in dysregulating signalling pathways. In addition, specific targeting of GO nano-sheets to cancer cells is also essential to eliminate any deleterious effect on healthy cells.

On the other hand, r-GO nanoparticles did not have an effect on Wnt/β-catenin or Akt cell signalling pathways in the case of both cell lines. This finding might indicate limited interaction between r-GO nanoparticles and cells as compared to GO nano-sheets, although data showed negligible cellular uptake of both graphene derivatives. However, cell uptake was not quantified in the current work and further investigation is required. The RBCs hemolysis data indicated that both GO and r-GO can physically interact with cell membrane, as evidenced by provoked cell lysis. Indeed, this could explain the subtle cytotoxic effect induced by r-GO in A549 cells and ROS generation in both cell lines after 48 hours. These effects may be a result of physical damage upon contact of cells with the nanoparticles. In

the case of GO, physical interaction with cells seemed to be more pronounced than r-GO which is reflected by a significant effect on cell signalling proteins for both cell lines. Nanoparticles have the ability to interact with membrane receptors and can, therefore, modulate signal transduction pathways (Marano et al., 2011, Rauch et al., 2013). Therefore, the dysregulation of signalling events by GO nano-sheets might be attributed to their association with the cell membrane receptors. The passive capacity of GO to translocate inside cells is a possible trigger to the observed cellular events, but further work is needed to confirm this. Chang and colleagues have suggested that the shape of GO (sheet-like structure) possibly blocks tunnels at the cell surface, thereby interfering with substance exchange by A549 cells (Chang et al., 2011). The latter study also showed that GO has a poor capacity to enter A549 cells. Therefore, blockade of substance exchange by the cell membrane might be an indirect effect of GO leading to dysregulation of different cell signalling pathways. Another possibility regarding indirect actions of GO nano-sheets is that they absorb nutrients from the culture medium, causing oxidative stress and cellular starvation which can induce autophagy. This phenomenon has been reported by many investigators (Martinez Paino et al., 2017, Fatisson et al., 2012, Qin et al., 2010).

The different cellular response exhibited by GO in comparison to r-GO is definitely attributed to the different physicochemical properties including surface chemistry, shape and size (as described in chapter 3). The surface chemistry influences the dispersion of GO and r-GO in culture media, though both particles are negatively charged, r-GO was aggregated and precipitated. Aggregation of nanoparticles have an impact on their physicochemical properties which then can further influence their biological properties (Sanchez et al., 2012, Liu et al., 2011, Liao et al., 2011, Chatterjee et al., 2014). TEM analysis has shown that r-GO nanoparticles are in aggregates less than 200 nm, but r-GO particles incubated with cells in tissue culture medium is expected to form larger aggregates

possibly of a micron size. Accordingly, the biocompatibility of r-GO nanoparticle is possibly related to its high tendency to aggregate and the formation of larger particles than those formed by GO. In addition to size, the shape of r-GO was that of aggregated crumbled nanoparticles and differed from the 2D nano-sheet structure of GO. This is possibly another factor that leads to different biological responses for r-GO and GO.

Taken together, findings have revealed that GO but not r-GO can dysregulate cell signalling pathways in pulmonary cell lines. This ability maybe of clinical interest as well as may shine the light on the mechanisms related to the toxicological effects of GO.

Chapter 5

Conclusion and future work

5.1 Conclusion

Graphene-based nanomaterials have many potential biomedical applications. As investigators identify more applications of GBNs, the demand for different forms of graphene will increase. To ensure the safe use of GBNs, assessment of the potential risks is mandatory. There has been increasing number of reports regarding the safety profile of GBNs, especially for GO. However, the data are contradictory and this is most likely due to the differences in the methods used to produce the GBNs and insufficient characterisation of the material.

In this research:

- **Highly purified GO and its reduced form (r-GO) were synthesized and their surface chemistry and size were characterised.**

In this study, highly purified few-layered GO nano-sheets, with an average lateral dimension of less than 50 nm (1-3 nm thick), were synthesised and this material exhibited good colloidal stability. R-GO nanoparticles were obtained following non-toxic hydrothermal reduction of GO. R-GO nanoparticles were highly hydrophobic with poor aqueous dispersion and they aggregate into clusters (<200 nm). GO and r-GO have distinct surface chemistry and morphology of, which significantly influence their interaction with biological systems.

- **GO is more toxic towards normal lung fibroblasts than cancerous epithelial lung cells and both GO and r-GO are hemolytic.**

Graphene nanoparticles interfere with the techniques that investigators use commonly to investigate cell toxicity, which limits investigations. Findings from this study indicate interference between GBNs and luminescence-based assays. In this regard, some assays required modification to overcome any possible interference by graphene nanoparticles and gain reliable data. Findings revealed that the cytotoxicity of graphene is dependent on its

surface chemistry. The cell type, concentration used and time of exposure are also important. GO had little effect on the cancerous epithelial lung cells, compared to healthy lung fibroblast. Cytotoxicity data obtained for A549 cells in this work agrees with other studies that showed that these cells are resistant to GO toxicity, at concentrations up to 125 μg/ml.

R-GO was biocompatible to healthy MRC-5 cells, rendering it a potential candidate for biomedical application such as tissue engineering. However, there is the need to improve the stability of r-GO in aqueous solution, particularly if the potential use is in drug delivery. Moreover, both nanoparticles were moderately hemolytic at a concentration of 125 μg/ml and highly hemolytic at a concentration of 300 μg/ml at 37 C°. Poor cellular uptake, cytotoxicity and the hemolytic properties of graphene derivatives will limit their potential use in biomedical applications. Despite these undesirable effects, the unique properties of GBNs still warrant further development to progress their use in biomedical applications. A focus on the chemistry to introduce effective modifications to the graphene sheet, to achieve minimum side effects, should lead to successful biomedical applications.

- **GO, but not r-GO, induced autophagy of both cell lines and ROS was generated post exposure of cells to graphene derivatives with no genotoxicity.**

Investigations of the mode(s) of action of GO in inducing cell death have revealed this is most likely through unrestrained autophagy in both cell lines. However, to confirm that autophagy is stimulating rather than inhibiting cell death, further investigations are required. GO-induced autophagy is possible *via* inhibition of the PIP3-Akt/mTOR pathway and possibly activation of the AMPK cascade in MRC-5 and A549 cells. Oxidative stress was also involved in the toxicity of GO and r-GO. Despite the generation of ROS by GO and r-GO, genotoxicity in MRC-5 and A549 cells was not observed.

- **GO, but not r-GO, dysregulated the Wnt/β-catenin and Akt cell signalling pathways in MRC-5 and A549 cells.**

GO at non-cytotoxic concentrations downregulated expression of GSK-3β protein for both cell lines. Inhibition of GSK-3β protein is known to be associated with a variety of diseases, and therefore the effect on GSK-3β protein requires further investigation to shine further light on the mechanisms that underly the toxicological effects of GO. The dysregulation of critical proteins in Wnt/β-catenin and Akt cellular signalling pathways by GO suggests a potential applicability in cancer therapy. However, caution is required regarding the undesired effects on healthy cells.

5.2 Future works

Further studies are required to determine the precise influence of the size of GO nano-sheets on its cytotoxicity profile. In this research, sonication had a major influence on the average size of GO, and different size ranges of GO nano-sheet are achievable by applying different sonication times or strengths. In this case, the surface chemistry will remain the same. The surface chemistry of graphene derivatives influenced the response of cells to this agent. Worthwhile modifications would include the surface coating of both GO and r-GO, to improve the interaction with cancerous cell lines and minimise the impact on RBCs. More detailed investigation is required to understand how GO alters the Wnt/β-catenin and Akt cell signalling pathways. In this case, investigation of upstream and downstream proteins involved in these cellular cascades is necessary.

Taking all of the findings from this study into consideration, pristine GO and r-GO both have displayed cytotoxicity in cell culture models and further studies are needed before these materials can be safely introduced into the clinic. A better understanding of their mode(s) of interaction with cells, and the events provoked is still of critical importance to any potential biomedical applications.

6 References

ABARRATEGI, A., GUTIERREZ, M. C., MORENO-VICENTE, C., HORTIGUELA, M. J., RAMOS, V., LOPEZ-LACOMBA, J. L., FERRER, M. L. & DEL MONTE, F. 2008. Multiwall carbon nanotube scaffolds for tissue engineering purposes. *Biomaterials,* 29**,** 94-102.

ACCOMASSO, L., CRISTALLINI, C. & GIACHINO, C. 2018. Risk Assessment and Risk Minimization in Nanomedicine: A Need for Predictive, Alternative, and 3Rs Strategies. *Frontiers in Pharmacology,* 9: 228.

AGGARWAL, P., HALL, J. B., MCLELAND, C. B., DOBROVOLSKAIA, M. A. & MCNEIL, S. E. 2009. Nanoparticle interaction with plasma proteins as it relates to particle biodistribution, biocompatibility and therapeutic efficacy. *Advanced Drug Delivery Reviews,* 61**,** 428-4237.

AHAMED, M., KARNS, M., GOODSON, M., ROWE, J., HUSSAIN, S. M., SCHLAGER, J. J. & HONG, Y. 2008. DNA damage response to different surface chemistry of silver nanoparticles in mammalian cells. *Toxicology and Applied Pharmacology,* 233**,** 404-410.

AI, J., BIAZAR, E., JAFARPOUR, M., MONTAZERI, M., MAJDI, A., AMINIFARD, S., ZAFARI, M., AKBARI, H. R. & RAD, H. G. 2011. Nanotoxicology and nanoparticle safety in biomedical designs. *International Journal of Nanomedicine,* 6**,** 1117-11127.

AKHAVAN, O., GHADERI, E. & AKHAVAN, A. 2012. Size-dependent genotoxicity of graphene nanoplatelets in human stem cells. *Biomaterials,* 33**,** 8017-8025.

AL-JAMAL, K. T. & KOSTARELOS, K. 2010. Assessment of cellular uptake and cytotoxicity of carbon nanotubes using flow cytometry. *Methods in Molecular Biology,* 625**,** 123-134.

ALERS, S., LOFFLER, A. S., WESSELBORG, S. & STORK, B. 2012. Role of AMPK-mTOR-Ulk1/2 in the regulation of autophagy: cross talk, shortcuts, and feedbacks. *Molecular and Cellular Biology,* 32**,** 2-11.

ALEXANDER GERBER, M. B., DORIS KLINGELHOFER, DAVID A GRONEBERG 2013. Gold nanoparticles: recent aspects for human toxicology. *Journal of Occupational Medicine and Toxicology,* 8**,** 32-37.

ALI-BOUCETTA, D, B., R, R.-N., A, S., J, V. D. B., K, K. & 2013a. Purified graphene oxide dispersions lack in vitro cytotoxicity and in vivo pathogenicity. *Advanced Healthcare Materials* 2**,** 433-441.

ALI-BOUCETTA, H., AL-JAMAL, K. T., MULLER, K. H., LI, S., PORTER, A. E., EDDAOUDI, A., PRATO, M., BIANCO, A. & KOSTARELOS, K. 2011. Cellular uptake and cytotoxic impact of chemically functionalized and polymer-coated carbon nanotubes. *Small,* 7**,** 3230-3238.

ALI-BOUCETTA, H., BITOUNIS, D., RAVEENDRAN-NAIR, R., SERVANT, A., VAN DEN BOSSCHE, J. & KOSTARELOS, K. 2013b. Purified graphene oxide dispersions lack in vitro cytotoxicity and in vivo pathogenicity. *Advanced Healthcare Materials,* 2**,** 433-441.

ALI-BOUCETTA, H., NUNES, A., SAINZ, R., HERRERO, M. A., TIAN, B., PRATO, M., BIANCO, A. & KOSTARELOS, K. 2013c. Asbestos-like pathogenicity of long carbon nanotubes alleviated by chemical functionalization. *Angewandte Chemie International Edition in English,* 52**,** 2274-2278.

ARK, D. W., JIANG, S., LIU, Y., SIEGAL, G. P., INOKI, K., ABRAHAM, E. & ZMIJEWSKI, J. W. 2014. GSK3beta-dependent inhibition of AMPK potentiates activation of neutrophils and macrophages and enhances severity of acute lung injury. *American Journal of Physiology-Lung Cellular and Molecular Physiology,* 307**,** 735–745.

AVRAHAMI, L., FARFARA, D., SHAHAM-KOL, M., VASSAR, R., FRENKEL, D. & ELDAR-FINKELMAN, H. 2013. Inhibition of glycogen synthase kinase-3 ameliorates beta-amyloid pathology and restores lysosomal acidification and mammalian target of rapamycin activity in the Alzheimer disease mouse model: in vivo and in vitro studies. *Journal of Biological Chemistry,* 288**,** 1295-1306.

AZOULAY-ALFAGUTER, I., ELYA, R., AVRAHAMI, L., KATZ, A. & ELDAR-FINKELMAN, H. 2015. Combined regulation of mTORC1 and lysosomal acidification by GSK-3 suppresses autophagy and contributes to cancer cell growth. *Oncogene,* 34**,** 4613-4623.

BAHRAMI, B., HOJJAT-FARSANGI, M., MOHAMMADI, H., ANVARI, E., GHALAMFARSA, G., YOUSEFI, M. & JADIDI-NIARAGH, F. 2017. Nanoparticles and targeted drug delivery in cancer therapy. *Immunology Letters,* 190**,** 64-83.

BALLATORI, N., KRANCE, S. M., NOTENBOOM, S., SHI, S., TIEU, K. & HAMMOND, C. L. 2009. Glutathione dysregulation and the etiology and progression of human diseases. *Journal of Biological Chemistry,* 390**,** 191-214.

BARROW, M., TAYLOR, A., FUENTES-CAPARROS, A. M., SHARKEY, J., DANIELS, L. M., MANDAL, P., PARK, B. K., MURRAY, P., ROSSEINSKY, M. J. & ADAMS, D. J. 2017. SPIONs for cell labelling and tracking using MRI: magnetite or maghemite? *Biomaterials Science,* 6**,** 101-106.

BATANDIER, C. C., FONTAINE, E., KÉRIEL, C. & LEVERVE, X. M. 2002. Determination of mitochondrial reactive oxygen species: methodological aspects. *cellular and molecular medicine* 6**,** 175-187.

BENGTSON, S., KLING, K., MADSEN, A. M., NOERGAARD, A. W., JACOBSEN, N. R., CLAUSEN, P. A., ALONSO, B., PESQUERA, A., ZURUTUZA, A., RAMOS, R., OKUNO, H., DIJON, J., WALLIN, H. & VOGEL, U. 2016. No cytotoxicity or genotoxicity of graphene and graphene oxide in murine lung epithelial FE1 cells in vitro. *Environmental and Molecular in Mutagenesis,* 57**,** 469-482.

BHATTACHARYA, K., MUKHERJEE, S. P., GALLUD, A., BURKERT, S. C., BISTARELLI, S., BELLUCCI, S., BOTTINI, M., STAR, A. & FADEEL, B. 2016. Biological interactions of carbon-based nanomaterials: From coronation to degradation. *Nanomedicine,* 12**,** 333-351.

BIANCO, A. 2013. Graphene: safe or toxic? The two faces of the medal. *Angewandte Chemie International Edition in English,* 52**,** 4986-4997.

BITOUNIS, D., ALI-BOUCETTA, H., HONG, B. H., MIN, D. H. & KOSTARELOS, K. 2013. Prospects and challenges of graphene in biomedical applications. *Advanced Materials,* 25**,** 2258-2268.

BOSCH-NAVARRO, C., CORONADO, E., MARTI-GASTALDO, C., SANCHEZ-ROYO, J. F. & GOMEZ, M. G. 2012. Influence of the pH on the synthesis of reduced graphene oxide under hydrothermal conditions. *Nanoscale,* 4**,** 3977-3982.

BUSSY, C., ALI-BOUCETTA, H. & KOSTARELOS, K. 2013. Safety Considerations for Graphene- Lessons Learnt from Carbon Nanotubes. *Accounts of chemical research,* 46**,** 692–701.

BUSSY, C., JASIM, D., LOZANO, N., TERRY, D. & KOSTARELOS, K. 2015. The current graphene safety landscape – a literature mining exercise. *Nanoscale,* 7**,** 6432-6435.

BUZEA, C., PACHECO, I. I. & ROBBIE, K. 2007. Nanomaterials and nanoparticles: Sources and toxicity. *Biointerphases,* 2**,** 17-71.

CAI, Q., LU, L., TIAN, J. H., ZHU, Y. B., QIAO, H. & SHENG, Z. H. 2010. Snapin-regulated late endosomal transport is critical for efficient autophagy-lysosomal function in neurons. *Neuron,* 68**,** 73-86.

CARERO, A. D. P., HOET, P. H. M., VERSCHAEVE, L., SCHOETERS, G. & NEMERY, B. 2001. Genotoxic Effects of Carbon Black Particles, Diesel Exhaust Particles, and Urban Air Particulates and Their Extracts on a Human Alveolar Epithelial Cell Line (A549) and a Human Monocytic Cell Line (THP-1). *Environmental and Molecular Mutagenesis,* 37**,** 155–163.

CARRACEDO, A. & PANDOLFI, P. P. 2008. The PTEN-PI3K pathway: of feedbacks and cross-talks. *Oncogene,* 27**,** 5527-5541.

CASIRAGHI, C., HARTSCHUH, A., QIAN, H., PISCANEC, S., GEORGI, C., FASOLI, A., NOVOSELOV, K. S., BASKO, D. M. & FERRARI, A. C. 2009. Raman Spectroscopy of Graphene Edges. *Nano letters,* 9**,** 1433-1441.

CHANG, B. Y., HUANG, N. M., AN'AMT, M. N., MARLINDA, A. R., NORAZRIENA, Y., MUHAMAD, M. R., HARRISON, I., LIM, H. N. & CHIA, C. H. 2012. Facile hydrothermal preparation of titanium dioxide decorated reduced graphene oxide nanocomposite. *International Journal of Nanomedicine,* 7**,** 3379-3387.

CHANG, H., TANG, L., WANG, Y., JIANG, J. & LI, J. 2010. Graphene Fluorescence Resonance Energy Transfer Aptasensor for the Thrombin Detection. *Analytical chemistry,* 82**,** 2341–2346.

CHANG, Y., YANG, S. T., LIU, J. H., DONG, E., WANG, Y., CAO, A., LIU, Y. & WANG, H. 2011. In vitro toxicity evaluation of graphene oxide on A549 cells. *Toxicology Letters,* 200**,** 201-210.

CHATTERJEE, N., EOM, H. J. & CHOI, J. 2014. A systems toxicology approach to the surface functionality control of graphene-cell interactions. *Biomaterials,* 35**,** 1109-1127.

CHEEMALAPATI, S., PALANISAMY, S., MANI, V. & CHEN, S. M. 2013. Simultaneous electrochemical determination of dopamine and paracetamol on multiwalled carbon nanotubes/graphene oxide nanocomposite-modified glassy carbon electrode. *Talanta,* 117**,** 297-304.

CHEN, D., DOUGHERTY, C. A., ZHU, K. & HONG, H. 2015a. Theranostic applications of carbon nanomaterials in cancer: Focus on imaging and cargo delivery. *Journal of Controlled Release,* 210**,** 230-245.

CHEN, G. Y., CHEN, C. L., TUAN, H. Y., YUAN, P. X., LI, K. C., YANG, H. J. & HU, Y. C. 2014. Graphene Oxide Triggers Toll-Like Receptors/Autophagy Responses In Vitro and Inhibits Tumor Growth In Vivo. *Advanced Healthcare Materials,* 3**,** 1486-1495.

CHEN, G. Y., YANG, H. J., LU, C. H., CHAO, Y. C., HWANG, S. M., CHEN, C. L., LO, K. W., SUNG, L. Y., LUO, W. Y., TUAN, H. Y. & HU, Y. C. 2012. Simultaneous induction of autophagy and toll-like receptor signaling pathways by graphene oxide. *Biomaterials,* 33**,** 6559-6569.

CHEN, L. Q., FANG, L., LING, J., DING, C. Z., KANG, B. & HUANG, C. Z. 2015b. Nanotoxicity of silver nanoparticles to red blood cells: size dependent adsorption, uptake, and hemolytic activity. *Chemical Research in Toxicology,* 28**,** 501-509.

CHEN, M., YIN, J., LIANG, Y., YUAN, S., WANG, F., SONG, M. & WANG, H. 2016a. Oxidative stress and immunotoxicity induced by graphene oxide in zebrafish. *Aquatic Toxicology,* 174**,** 54-60.

CHEN, Y., REN, C., OUYANG, S., HU, X. & ZHOU, Q. 2015c. Mitigation in Multiple Effects of Graphene Oxide Toxicity in Zebrafish Embryogenesis Driven by Humic Acid. *Environmental Science and Technology,* 49**,** 10147-10154.

CHEN, Y. W., SU, Y. L., HU, S. H. & CHEN, S. Y. 2016b. Functionalized graphene nanocomposites for enhancing photothermal therapy in tumor treatment. *Advanced Drug Delivery Review,* 105**,** 190-204.

CHENG, C., LI, S., THOMAS, A., KOTOV, N. A. & HAAG, R. 2017. Functional Graphene Nanomaterials Based Architectures: Biointeractions, Fabrications, and Emerging Biological Applications. *Chemical Reviews,* 117**,** 1826-1914.

CHENG, C., NIE, S., LI, S., PENG, H., YANG, H., MA, L., SUN, S. & ZHAO, C. 2013. Biopolymer functionalized reduced graphene oxide with enhanced biocompatibility via mussel inspired coatings/anchors. *Journal of Materials Chemistry B,* 1**,** 265-275.

CHENG, J. Q., LINDSLEY, C. W., CHENG, G. Z., YANG, H. & NICOSIA, S. V. 2005. The Akt/PKB pathway: molecular target for cancer drug discovery. *Oncogene,* 24**,** 7482-7492.

CHIMENE, D., ALGE, D. L. & GAHARWAR, A. K. 2015. Two-Dimensional Nanomaterials for Biomedical Applications: Emerging Trends and Future Prospects. *Advanced Materials,* 27**,** 7261-7284.

CHOWDHURY, S. M., KANAKIA, S., TOUSSAINT, J. D., FRAME, M. D., DEWAR, A. M., SHROYER, K. R., MOORE, W. & SITHARAMAN, B. 2013. In vitro hematological and in vivo vasoactivity assessment of dextran functionalized graphene. *Scientific Reports,* 3: 2584.

CHU, M., DONG, C., ZHU, H., CAI, X., DONG, H., REN, T., SU, J. & LI, Y. 2013. Biocompatible polyethylenimine-graft-dextran catiomer for highly efficient gene delivery assisted by a nuclear targeting ligand. *Polymer Chemistry,* 4, 2528-2539.

CODOGNO, P., MEHRPOUR, M. & PROIKAS-CEZANNE 2012. "Canonical and non-canonical autophagy: variations on a common theme of self-eating?". *Nature Reviews. Molecular Cell Biology,* 13**,** 7-12.

CONNER, S. D. & SCHMID, S. L. 2003. Regulated Portals of Entry into the Cell. *Nature,* 422**,** 37-44.

CONTRERAS-TORRES, F. F., RODRIGUEZ-GALVAN, A., GUERRERO-BELTRAN, C. E., MARTINEZ-LORAN, E., VAZQUEZ-GARZA, E., ORNELAS-SOTO, N. & GARCIA-RIVAS, G. 2017. Differential cytotoxicity and internalization of graphene family nanomaterials in myocardial cells. *Materials Science & Engineering C-Materials for Biological Applications,* 73**,** 633-642.

DA SILVA MEIRELLES, L., CHAGASTELLES, P. C. & NARDI, N. B. 2006. Mesenchymal stem cells reside in virtually all post-natal organs and tissues. *Journal of Cell Science,* 119**,** 2204-2213.

DAI, L., CHANG, D. W., BAEK, J. B. & LU, W. 2012. Carbon nanomaterials for advanced energy conversion and storage. *Small,* 8**,** 1130-1166.

DARAEE, H., ETEMADI, A., KOUHI, M., ALIMIRZALU, S. & AKBARZADEH, A. 2016. Application of liposomes in medicine and drug delivery. *Artificial Cells, Nanomedicine, and Biotechnology,* 44**,** 381-391.

DAS, R. K., PACHAPUR, V. L., LONAPPAN, L., NAGHDI, M., PULICHARLA, R., MAITI, S., CLEDON, M., DALILA, L. M. A., SARMA, S. J. & BRAR, S. K. 2017. Biological synthesis of metallic nanoparticles: plants, animals and microbial aspects. *Nanotechnology for Environmental Engineering,* 2:18.

DAS, S., SINGH, S., SINGH, V., JOUNG, D., DOWDING, J. M., REID, D., ANDERSON, J., ZHAI, L., KHONDAKER, S. I., SELF, W. T. & SEAL, S. 2013. Oxygenated

Functional Group Density on Graphene Oxide: Its Effect on Cell Toxicity. *Particle & Particle Systems Characterization,* 30**,** 148-157.

DECKER T. & J., L. M. M. 1988. "A quick and simple method for the quantitation of lactate dehydrogenase release in measurements of cellular cytotoxicity and tumor necrosis factor (TNF) activity". *Journal of Immunological Methods* 115**,** 61–69.

DICKENS, L. S., POWLEY, I. R., HUGHES, M. A. & MACFARLANE, M. 2012. The 'complexities' of life and death: death receptor signalling platforms. *Experimental Cell Research,* 318**,** 1269-1277.

DÍEZ, N., ŚLIWAK, A., GRYGLEWICZ, S., GRZYB, B. & GRYGLEWICZ, G. 2015. Enhanced reduction of graphene oxide by high-pressure hydrothermal treatment. *RSC Advances,* 5**,** 81831-81837.

DINESCU, S., IONITA, M., PANDELE, A. M., GALATEANU, B., IOVU, H., ARDELEAN, A., COSTACHE, M. & HERMENEAN, A. 2014. In vitro cytocompatibility evaluation of chitosan/graphene oxide 3D scaffold composites designed for bone tissue engineering. *Bio-medical Materials & Engineering,* 24**,** 2249-2256.

DOBROVOLSKAIA, M. A. & MCNEIL, S. E. 2007. Immunological properties of engineered nanomaterials. *Nature Nanotechnology,* 8**,** 469-478.

DOBROVOLSKAIA, M. A. & MCNEIL, S. E. 2013. Understanding the correlation between in vitro and in vivo immunotoxicity tests for nanomedicines. *Journal of Controlled Release,* 172**,** 456-466.

DONALDSON, K., STONE, V., TRAN, C. L., KREYLING, W. & BORM, P. J. 2004. Nanotoxicology. *Occuptional & Environmental Medicine,* 61**,** 727-728.

DONG, H. S. & QI, S. J. 2015. Realising the potential of graphene-based materials for biosurfaces – A future perspective. *Biosurface and Biotribology,* 1**,** 229-248.

DONG, X., SHI, Y., HUANG, W., CHEN, P. & LI, L. J. 2010. Electrical detection of DNA hybridization with single-base specificity using transistors based on CVD-grown graphene sheets. *Advanced Materials,* 22**,** 1649-1653.

DOS SANTOS, C. A., SECKLER, M. M., INGLE, A. P., GUPTA, I., GALDIERO, S., GALDIERO, M., GADE, A. & RAI, M. 2014. Silver nanoparticles: therapeutical uses, toxicity, and safety issues. *Journal of Pharmacutical Sciences,* 103**,** 1931-1944.

DREWNIAK, S., MUZYKA, R., STOLARCZYK, A., PUSTELNY, T., KOTYCZKA-MORANSKA, M. & SETKIEWICZ, M. 2016. Studies of Reduced Graphene Oxide

and Graphite Oxide in the Aspect of Their Possible Application in Gas Sensors. *Sensors (Basel),* 16:103

DREYER, D. R., PARK, S., BIELAWSKI, C. W. & RUOFF, R. S. 2010. The chemistry of graphene oxide. *Chemical Society Reviews,* 39**,** 228-40.

DU, L., WU, S., LI, Y., ZHAO, X., JU, X. & WANG, Y. 2014. Cytotoxicity of PEGylated graphene oxide on lymphoma cells. *Bio-medical Materials & Engineering,* 24**,** 2135-2141.

EDA, G. & CHHOWALLA, M. 2010. Chemically derived graphene oxide: towards large-area thin-film electronics and optoelectronics. *Advanced Materials,* 22**,** 2392-2415.

ELISA, L. D., ANKOR, G. M., TERESA, P. M., JOSÉ, F. M., FERRER, M. L., FRANCISCO, D. M., CONCEPCIÓN, G. M. & CONCEPCIÓN, S. M. 2015. Subacute Tissue Response to 3D Graphene Oxide Scaffolds Implanted in the Injured Rat Spinal Cord. *Advanced Healthcare Materials,* 4**,** 1861-1868.

ETHERIDGE, M. L., CAMPBELL, S. A., ERDMAN, A. G., HAYNES, C. L., WOLF, S. M. & MCCULLOUGH, J. 2013. The big picture on nanomedicine: the state of investigational and approved nanomedicine products. *Nanomedicine,* 9**,** 1-14.

FADEEL, B. 2013. Nanosafety: towards safer design of nanomedicines. *Journal of Internal Medicine,* 274**,** 578-580.

FADEEL, B., FELIU, N., VOGT, C., ABDELMONEM, A. M. & PARAK, W. J. 2013. Bridge over troubled waters: understanding the synthetic and biological identities of engineered nanomaterials. *Wiley Interdisciplinary Reviews: Nanomedicine & Nanobiotechnology,* 5**,** 111-129.

FADEEL, B., FORNARA, A., TOPRAK, M. S. & BHATTACHARYA, K. 2015. Keeping it real: The importance of material characterization in nanotoxicology. *Biochemical & Biophysical Research Communications,* 468**,** 498-503.

FADEEL, B. & GARCIA-BENNETT, A. E. 2010. Better safe than sorry: Understanding the toxicological properties of inorganic nanoparticles manufactured for biomedical applications. *Advanced Drug Delivery Reviews,* 62**,** 362-374.

FAVALORO, B., ALLOCATI, N., GRAZIANO, V., ILIO, C. D. & LAURENZI, V. D. 2012. Role of apoptosis in diserases. *Aging,* 4**,** 330–349.

FERRARI, A. C. 2007. Raman spectroscopy of graphene and graphite: Disorder, electron–phonon coupling, doping and nonadiabatic effects. *Solid State Communications,* 143**,** 47-57.

FERRARI, A. C. & ROBERTSON, J. 2000. Interpretation of Raman spectra of disordered and amorphous carbon. *Physical reviwe* 61**,** 14095-14107.

FINKEL, T. 2003. oxidant signals and oxidative stress. *Current opinion in cell biology,* 15**,** 247-254.

FIRKOWSKA, OLEK, M.,´Z, N. P.-P., ROJAS-CHAPANA, J. & GIERSIG, M. 2006. Highly Ordered MWNT-Based Matrixes: Topography at the Nanoscale Conceived for Tissue Engineering. *Langmuir,* 22**,** 5427-5434.

FU, C., BAI, H., ZHU, J., NIU, Z., WANG, Y., LI, J., YANG, X. & BAI, Y. 2017. Enhanced cell proliferation and osteogenic differentiation in electrospun PLGA/hydroxyapatite nanofibre scaffolds incorporated with graphene oxide. *PLoS One,* 12:0188352.

FU, C. & YANG, X. 2013. Molecular simulation of interfacial mechanics for solvent exfoliation of graphene from graphite. *Carbon,* 55**,** 350-360.

FU, P. P., XIA, Q., HWANG, H. M., RAY, P. C. & YU, H. 2014. Mechanisms of nanotoxicity: generation of reactive oxygen species. *Journal of Food & Drug Analysis,* 22**,** 64-75.

GAO, X., JANG, J. & NAGASE, S. 2010. Hydrazine and Thermal Reduction of Graphene Oxide: Reaction Mechanisms, Product Structures, and Reaction Design. *The Journal of Physical Chemistry,* 114**,** 832-842.

GE, S., LAN, F., YU, F. & YU, J. 2015. Applications of graphene and related nanomaterials in analytical chemistry. *New Journal of Chemistry,* 39**,** 2380-2395.

GEETHA BAI, R., MUTHOOSAMY, K., SHIPTON, F. N. & MANICKAM, S. 2017. Acoustic cavitation induced generation of stabilizer-free, extremely stable reduced graphene oxide nanodispersion for efficient delivery of paclitaxel in cancer cells. *Ultrasonics Sonochemistry,* 36**,** 129-138.

GEIM, A. K. & NOVOSELOV, K. S. 2007. The rise of graphene. *Nature materials,* 6**,** 183-191.

GOESSLING, W., NORTH, T. E., LOEWER, S., LORD, A. M., LEE, S., STOICK-COOPER, C. L., WEIDINGER, G., PUDER, M., DALEY, G. Q., MOON, R. T. & ZON, L. I. 2009. Genetic interaction of PGE2 and Wnt signaling regulates developmental specification of stem cells and regeneration. *Cell,* 136**,** 1136-147.

GONSALVES, K., LAURENCIN, C. H. T. & NAIR, L. 2007. *Biomedical Nanostructures*, USA, John Wiley & Sons.

GONZALEZ, L., LISON, D. & KIRSCH-VOLDERS, M. 2009. Genotoxicity of engineered nanomaterials: A critical review. *Nanotoxicology,* 2**,** 252-273.

GRAYBILL, R. M. & BAILEY, R. C. 2016. Emerging Biosensing Approaches for microRNA Analysis. *Analytical Chemistry,* 88**,** 431-450.

GU, M., LIU, Y., CHEN, T., DU, F., ZHAO, X., XIONG, C. & ZHOU, Y. 2014. Is graphene a promising nano-material for promoting surface modification of implants or scaffold materials in bone tissue engineering? *Tissue Engineering Part B: Reviews,* 20**,** 477-491.

GUO, J., RAHME, K., HE, Y., LI, L. L., HOLMES, J. D. & O'DRISCOLL, C. M. 2017. Gold nanoparticles enlighten the future of cancer theranostics. *International Journal of Nanomedicine,* 12**,** 6131-6152.

GURUNATHAN, S., HAN, J., PARK, J. H. & KIM, J. H. 2014. An in vitro evaluation of graphene oxide reduced by Ganoderma spp. in human breast cancer cells (MDA-MB-231). *Internaltional Journal of Nanomedicine,* 9**,** 1783-1797.

GURUNATHAN, S., HAN, J. W., EPPAKAYALA, V. & KIM, J. H. 2013. Green synthesis of graphene and its cytotoxic effects in human breast cancer cells. *International Journal of Nanomedicine,* 8**,** 1015-1027.

GURUNATHAN, S., HAN, J. W., KIM, E. S., PARK, J. H. & KIM, J. H. 2015. Reduction of graphene oxide by resveratrol: a novel and simple biological method for the synthesis of an effective anticancer nanotherapeutic molecule. *International Journal of Nanomedicine,* 10**,** 2951-2969.

GURUNATHAN, S. & KIM, J. H. 2016. Synthesis, toxicity, biocompatibility, and biomedical applications of graphene and graphene-related materials. *International Journal of Nanomedicine,* 11**,** 1927-1945.

HARE, J. I., LAMMERS, T., ASHFORD, M. B., PURI, S., STORM, G. & BARRY, S. T. 2017. Challenges and strategies in anti-cancer nanomedicine development: An industry perspective. *Advanced Drug Delivery Reviews,* 108**,** 25-38.

HE, C., HU, Y., YIN, L., TANG, C. & YIN, C. 2010. Effects of particle size and surface charge on cellular uptake and biodistribution of polymeric nanoparticles. *Biomaterials,* 31**,** 3657-3666.

HE, Y. & PARK, K. 2016. Effects of the Microparticle Shape on Cellular Uptake. *Molecular Pharmacutics,* 13**,** 2164-2171.

HENDRICKSON, O. D., ZHERDEV, A. V., GMOSHINSKII, I. V. & DZANTIEV, B. B. 2014. Fullerenes: In vivo studies of biodistribution, toxicity, and biological action. *Nanotechnologies in Russia,* 9**,** 601-617.

HERS, I., VINCENT, E. E. & TAVARE, J. M. 2011. Akt signalling in health and disease. *Cell Signal,* 23**,** 1515-1527.

HINZMANN, M., JAWORSKI, S., KUTWIN, M., JAGIELLO, J., KOZINSKI, R., WIERZBICKI, M., GRODZIK, M., LIPINSKA, L., SAWOSZ, E. & CHWALIBOG, A. 2014. Nanoparticles containing allotropes of carbon have genotoxic effects on glioblastoma multiforme cells. *International Journal of Nanomedicine,* 9**,** 2409-2417.

HU, H., TANG, C. & YIN, C. 2014. Folate conjugated trimethyl chitosan/graphene oxide nanocomplexes as potential carriers for drug and gene delivery. *Materials Letters,* 125**,** 82-85.

HU, W., PENG, C., LV, M., LI, X., ZHANG, Y., CHEN, N., FAN, C. & HUANG, Q. 2011. Protein Corona-Mediated Mitigation of Cytotoxicity of Graphene Oxide. *ACS Nano,* 5**,** 3693-3700.

HUANG, H. C., BARUA, S., SHARMA, G., DEY, S. K. & REGE, K. 2011. Inorganic nanoparticles for cancer imaging and therapy. *Journal of Controlled Release,* 155**,** 344-357.

HUMMERS, W. & OFFEMAN, R. 1958. Preparation of Graphitic Oxide. *American Chemical Society,* 80**,** 1339.

IIJIMA, S. 2002. Carbon nanotubes- past, present, and future. *Physica B,* 323**,** 1-5.

JACOBASCH, H. J., BAUB6CKL, G. & SCHURZ, J. 1985. Problems and results of zeta-potential measurements on fibers. *Colloid and Polymer Science,* 263**,** 3-24.

JANA, A., SCHEER, E. & POLARZ, S. 2017. Synthesis of graphene-transition metal oxide hybrid nanoparticles and their application in various fields. *Beilstein Journal of Nanotechnology,* 8**,** 688-714.

JASIM, D. A., LOZANO, N. & KOSTARELOS, K. 2016. Synthesis of few-layered, high-purity graphene oxide sheets from different graphite sources for biology. *2D Materials,* 3:014006

JAWORSKI, S., HINZMANN, M., SAWOSZ, E., GRODZIK, M., KUTWIN, M., WIERZBICKI, M., STROJNY, B., VADALASETTY, K. P., LIPINSKA, L. & CHWALIBOG, A. 2017. Interaction of different forms of graphene with chicken

embryo red blood cells. *Environmental Science & Pollution Research International,* 24**,** 21671-21679.

JAWORSKI, S., SAWOSZ, E., KUTWIN, M., WIERZBICKI, M., HINZMANN, M., GRODZIK, M., WINNICKA, A., LIPINSKA, L., WLODYGA, K. & CHWALIBOG, A. 2015. In vitro and in vivo effects of graphene oxide and reduced graphene oxide on glioblastoma. *International Journal of Nanomedicine,* 10**,** 1585-1596.

JEONG, J. K., LEE, Y. J., JEONG, S. Y., JEONG, S., LEE, G. W. & PARK, S. Y. 2017. Autophagic flux induced by graphene oxide has a neuroprotective effect against human prion protein fragments. *International Journal of Nanomedicine,* 12**,** 8143-8158.

JIN, M. & KLIONSKY, D. J. 2014. Regulation of autophagy: modulation of the size and number of autophagosomes. *FEBS Letters,* 588**,** 2457-2463.

JOKAR, S., POURJAVADI, A. & ADELI, M. 2014. Albumin–graphene oxide conjugates; carriers for anticancer drugs. *Royal Society of Chemistry Advances,* 4,33001-33006.

JONES, M.-C., TEWARI, P., BLEI, C., HALES, K., POCHAN, D. J. & LEROUX, J.-C. 2006. Self-Assembled Nanocages for Hydrophilic Guest Molecules. *American Chemical Society,* 128**,** 14599-14605.

JONG, W. H. D. & BORM, P. J. 2008. Drug delivery and nanoparticles: Applications and hazards. *Nanomedicine,* 3**,** 133–149.

KAKINEN, A., DING, F., CHEN, P., MORTIMER, M., KAHRU, A. & KE, P. C. 2013. Interaction of firefly luciferase and silver nanoparticles and its impact on enzyme activity. *Nanotechnology,* 24: 345101.

KANG, P., WANG, M. C. & NAM, S. 2016. Bioelectronics with two-dimensional materials. *Microelectronic Engineering,* 161**,** 18-35.

KANIYOOR, A. & RAMAPRABHU, S. 2012. A Raman spectroscopic investigation of graphite oxide derived graphene. *American Institute of Physics Advances,* 2:032183.

KHAN, U., O'NEILL, A., LOTYA, M., DE, S. & COLEMAN, J. N. 2010. High-concentration solvent exfoliation of graphene. *Small,* 6**,** 864-71.

KIEW, S. F., KIEW, L. V., LEE, H. B., IMAE, T. & CHUNG, L. Y. 2016. Assessing biocompatibility of graphene oxide-based nanocarriers: A review. *Journal of Controlled Release,* 226**,** 217-28.

KIM, J., KIM, Y.-R., KIM, Y., LIM, K. T., SEONWOO, H., PARK, S., CHO, S.-P., HONG, B. H., CHOUNG, P.-H., CHUNG, T. D., CHOUNG, Y.-H. & CHUNG, J. H. 2013.

Graphene-incorporated chitosan substrata for adhesion and differentiation of human mesenchymal stem cells. *Journal of Materials Chemistry B,* 1, 933-938.

KIM, J., LEE, J., SON, D., CHOI, M. K. & KIM, D. H. 2016. Deformable devices with integrated functional nanomaterials for wearable electronics. *Nano Convergence,* 3: 4.

KIM, K. H., OH, Y. & ISLAM, M. F. 2012. Graphene coating makes carbon nanotube aerogels superelastic and resistant to fatigue. *Nature Nanotechnology,* 7**,** 562-566.

KIM, K. S., ZHAO, Y., JANG, H., LEE, S. Y., KIM, J. M., KIM, K. S., AHN, J. H., KIM, P., CHOI, J. Y. & HONG, B. H. 2009. Large-scale pattern growth of graphene films for stretchable transparent electrodes. *Nature,* 457**,** 706-710.

KINNEAR, C., MOORE, T. L., RODRIGUEZ-LORENZO, L., ROTHEN-RUTISHAUSER, B. & PETRI-FINK, A. 2017. Form Follows Function: Nanoparticle Shape and Its Implications for Nanomedicine. *Chemical Reviews,* 117**,** 11476-11521.

KLAASSEN, C. D. & WATKINS, J. B. 2008. *Casarett and Doull's, the basic science of poisons,* USA, Mac Graw-hill Medical.

KLAESSIG, F., MARRAPESE, M. & ABE, S. 2011. Current Perspectives in Nanotechnology Terminology and Nomenclature. *Nanotechnology Standards.* USA, Springer Science & business media.

KLIONSKY, D. J., ABDELMOHSEN, K., ABE, A., ABEDIN, M. J., ABELIOVICH, H., ACEVEDO AROZENA, A., ADACHI, H., ADAMS, C. M., ADAMS, P. D., ADELI, K., ADHIHETTY, P. J., ADLER, S. G., AGAM, G., AGARWAL, R., AGHI, M. K., AGNELLO, M., AGOSTINIS, P., AGUILAR, P. V., AGUIRRE-GHISO, J., et al. 2016. Guidelines for the use and interpretation of assays for monitoring autophagy (3rd edition). *Autophagy,* 12**,** 1-222.

KLIONSKY, D. J. & EMR, S. D. 2009. Autophagy as a regulated pathway of cellular degradation. *Science,* 290**,** 1717-1721.

KOSTARELOS, K. 2008. The long and short of carbon nanotube toxicity. *Nature biotechnology,* 26**,** 774-776.

KOSYNKIN, D. V., HIGGINBOTHAM, A. L., SINITSKII, A., LOMEDA, J. R., DIMIEV, A., PRICE, B. K. & TOUR, J. M. 2009. Longitudinal unzipping of carbon nanotubes to form graphene nanoribbons. *Nature,* 458**,** 872-876.

KROTO, H. W., HEATH, J. R., O'BRIEN, S., CURL, R. F. & SMALLEY, R. E. C. 1985. buckminsterfullerene. *Nature,* 318**,** 162-163.

KUEMPEL, E. D., CASTRANOVA, V., GERACI, C. L. & SCHULTE, P. A. 2012. Development of risk-based nanomaterial groups for occupational exposure control. *Journal of Nanopartical Research,* 14:1029.

LACERDA, L., BIANCO, A., PRATO, M. & KOSTARELOS, K. 2006. Carbon nanotubes as nanomedicines: from toxicology to pharmacology. *Advanced Drug Delivery Reviews,* 58**,** 1460-1470.

LACERDA, L., RAFFA, S., PRATO, M., BIANCO, A. & KOSTARELOS, K. 2007. Cell-penetrating CNTs for delivery of therapeutics. *Nano Today,* 2**,** 38-43.

LAMMEL, T., BOISSEAUX, P., FERNÁNDEZ-CRUZ, M.-L. & NAVAS, J. M. 2013. Internalization and cytotoxicity of graphene oxide and carboxyl graphene nanoplatelets in the human hepatocellular carcinoma cell line Hep G2. *Particle and Fibre Toxicology,* 10:27.

LANDRY, J., LAMBERT, H., ZHOU, M., LAVOIE, J. N., HICKEY, E., WEBER, L. A. & ANDRESON, C. W. 1992. human HSP27 is phosphorylated at serines 78 and 82 by heat shock and mitogen-activated kinases that recognize the same amino acid motif as S6 Kinase II. *The journal of bilogical chemistry,* 267**,** 794-803.

LEE, C. H., RAJENDRAN, R., JEONG, M. S., KO, H. Y., JOO, J. Y., CHO, S., CHANG, Y. W. & KIM, S. 2013. Bioimaging of targeting cancers using aptamer-conjugated carbon nanodots. *Chemical Communication (Cambridge),* 49**,** 6543-6545.

LEE, J. & MIN, D. H. 2012. A simple fluorometric assay for DNA exonuclease activity based on graphene oxide. *Analyst,* 137**,** 2024-2026.

LEHMANN, C., SIEG, H., LAMPEN, A. & BRAEUNING, A. 2016. Disturbance of firefly luciferase-based bioassays by different aluminum species. *Analytical Biochemistry,* 504**,** 27-29.

LEON, V., QUINTANA, M., HERRERO, M. A., FIERRO, J. L., DE LA HOZ, A., PRATO, M. & VAZQUEZ, E. 2011. Few-layer graphenes from ball-milling of graphite with melamine. *Chemical Communication (Cambridge),* 47**,** 10936-10938.

LI, Y., LIU, Y., FU, Y., WEI, T., LE GUYADER, L., GAO, G., LIU, R. S., CHANG, Y. Z. & CHEN, C. 2012. The triggering of apoptosis in macrophages by pristine graphene through the MAPK and TGF-beta signaling pathways. *Biomaterials,* 33**,** 402-411.

LI, Y., SUN, L., JIN, M., DU, Z., LIU, X., GUO, C., LI, Y., HUANG, P. & SUN, Z. 2011. Size-dependent cytotoxicity of amorphous silica nanoparticles in human hepatoma HepG2 cells. *Toxicology In Vitro,* 25**,** 1343-1352.

LI, Z., SUN, L., ZHANG, Y., DOVE, A. P., O'REILLY, R. K. & CHEN, G. 2016. Shape Effect of Glyco-Nanoparticles on Macrophage Cellular Uptake and Immune Response. *American Chemical Society Macro Letters,* 5**,** 1059-1064.

LI, Z., WANG, H., YANG, B., SUN, Y. & HUO, R. 2015. Three-dimensional graphene foams loaded with bone marrow derived mesenchymal stem cells promote skin wound healing with reduced scarring. *Materials Science & Engineering C-Materials for Biological Applications,* 57**,** 181-188.

LIAO, K. H., LIN, Y. S., MACOSKO, C. W. & HAYNES, C. L. 2011. Cytotoxicity of graphene oxide and graphene in human erythrocytes and skin fibroblasts. *American Chemical Society Applied Materials & Interfaces,* 3**,** 2607-2615.

LIN, J., CHEN, X. & HUANG, P. 2016. Graphene-based nanomaterials for bioimaging. *Advanced Drug Delivery Reviews,* 105**,** 242-254.

LIU, G., SHEN, H., MAO, J., ZHANG, L., JIANG, Z., SUN, T., LAN, Q. & ZHANG, Z. 2013. Transferrin modified graphene oxide for glioma-targeted drug delivery: in vitro and in vivo evaluations. *American Chemical Society Applied Materials & Interfaces,* 5**,** 6909-6914.

LIU, J., DONG, J., ZHANG, T. & PENG, Q. 2018. Graphene-based nanomaterials and their potentials in advanced drug delivery and cancer therapy. *Journal of Controlled Release,* 286**,** 64-73.

LIU, Y., WANG, X., WANG, J., NIE, Y., DU, H., DAI, H., WANG, J., WANG, M., CHEN, S., HEI, T. K., DENG, Z., WU, L. & XU, A. 2016. Graphene Oxide Attenuates the Cytotoxicity and Mutagenicity of PCB 52 via Activation of Genuine Autophagy. *Environmental Science & Technology,* 50**,** 3154-3164.

LIU, Y., YU, D., ZENG, C., MIAO, Z. & DAI, L. 2010. Biocompatible Graphene Oxide-Based Glucose Biosensors. *Langmuir,* 26**,** 6158-6160.

LIU, Z., DAVIS, C., CAI, W., HE, L., CHEN, X. & DAI, H. 2008a. Circulation and long-term fate of functionalized, biocompatible single-walled carbon nanotubes in mice probed by Raman spectroscopy. *Proceedings of the National Academy of Sciences of U S A,* 105**,** 1410–1415.

LIU, Z., ROBINSON, J. T., SUN, X. & DAI, H. 2008b. PEGylated Nanographene Oxide for Delivery of Water-Insoluble Cancer Drugs. *American Chemical Society,* 130**,** 10876–10877.

LU, B., LI, T., ZHAO, H., LI, X., GAO, C., ZHANG, S. & XIE, E. 2012. Graphene-based composite materials beneficial to wound healing. *Nanoscale,* 4**,** 2978-2982.

LU, Y.-J., LIN, P.-Y., HUANG, P.-H., KUO, C.-Y., SHALUMON, K. T., CHEN, M.-Y. & CHEN, J.-P. 2018. Magnetic Graphene Oxide for Dual Targeted Delivery of Doxorubicin and Photothermal Therapy. *Nanomaterials,* 8:193.

LUO, L., XU, L. & ZHAO, H. 2017a. Biosynthesis of reduced graphene oxide and its in-vitro cytotoxicity against cervical cancer (HeLa) cell lines. *Materials Science & Engneering C- Materials Biological Applications,* 78**,** 198-202.

LUO, N., WEBER, J. K., WANG, S., LUAN, B., YUE, H., XI, X., DU, J., YANG, Z., WEI, W., ZHOU, R. & MA, G. 2017b. PEGylated graphene oxide elicits strong immunological responses despite surface passivation. *Nature Communications,* 8:14537.

MA, J., LIU, R., WANG, X., LIU, Q., CHEN, Y., VALLE, R. P., ZUO, Y. Y., XIA, T. & LIU, S. 2015. Crucial Role of Lateral Size for Graphene Oxide in Activating Macrophages and Stimulating Pro-inflammatory Responses in Cells and Animals. *American Chemical Society Nano,* 9**,** 10498-10515.

MACDONALD, B. T., TAMAI, K. & HE, X. 2009. Wnt/beta-catenin signaling: components, mechanisms, and diseases. *Developmental Cell,* 17**,** 9-26.

MACIA, E., EHRLICH, M., MASSOL, R., BOUCROT, E., BRUNNER, C. & KIRCHHAUSEN, T. 2006. Dynasore, a cell-permeable inhibitor of dynamin. *Developmental Cell,* 10**,** 839-850.

MAGDOLENOVA, Z., COLLINS, A., KUMAR, A., DHAWAN, A., STONE, V. & DUSINSKA, M. 2014. Mechanisms of genotoxicity. A review of in vitro and in vivo studies with engineered nanoparticles. *Nanotoxicology,* 8**,** 233-278.

MANNING, B. D. & CANTLEY, L. C. 2007. AKT/PKB signaling: navigating downstream. *Cell,* 129**,** 1261-1274.

MARCANO, D. C., KOSYNKIN, D. V., BERLIN, J. M., SINITSKII, A., SUN, Z., SLESAREV, A., ALEMANY, L. B., LU, W. & TOUR, J. M. 2010. Improved Synthesis of Graphene Oxide. *American Chemical Society Nano,* 4**,** 4806-4814.

MARTINEZ PAINO, I. M., SANTOS, F. & ZUCOLOTTO, V. 2017. Biocompatibility and toxicology effects of graphene oxide in cancer, normal, and primary immune cells. *Journal of Biomedical Materials Research Part A,* 105**,** 728-736.

MCCALLION, C., BURTHEM, J., REES-UNWIN, K., GOLOVANOV, A. & PLUEN, A. 2016. Graphene in therapeutics delivery: Problems, solutions and future opportunities. *European Journal of Pharmaceutics & Biopharmaceutics,* 104**,** 235-250.

MCILWAIN, D. R., BERGER, T. & MAK, T. W. 2013. Caspase functions in cell death and disease. *Cold Spring Harb Perspectives in Biology,* 5:008656.

MERIC-BERNSTAM, F. & GONZALEZ-ANGULO, A. M. 2009. Targeting the mTOR signaling network for cancer therapy. *Journal of Clinical Oncology,* 27**,** 2278-2287.

METCALFE, C. & BIENZ, M. 2011. Inhibition of GSK3 by Wnt signalling--two contrasting models. *Journal of Cell Science,* 124**,** 3537-3544.

MISHRA, A. R., ZHENG, J., TANG, X. & GOERING, P. L. 2016. Silver Nanoparticle-Induced Autophagic-Lysosomal Disruption and NLRP3-Inflammasome Activation in HepG2 Cells Is Size-Dependent. *Toxicological Sciences,* 150**,** 473-487.

MITTAL, S., KUMAR, V., DHIMAN, N., CHAUHAN, L. K., PASRICHA, R. & PANDEY, A. K. 2016. Physico-chemical properties based differential toxicity of graphene oxide/reduced graphene oxide in human lung cells mediated through oxidative stress. *Scientific Reports,* 6:39548.

MOCHALIN, V. N., SHENDEROVA, O., HO, D. & GOGOTSI, Y. 2011. The properties and applications of nanodiamonds. *Nature Nanotechnology,* 7**,** 11-23.

MOLINA, J., CASES, F. & MORETTO, L. M. 2016. Graphene-based materials for the electrochemical determination of hazardous ions. *Analytica Chimica Acta,* 946**,** 9-39.

MONASTERIO, B. G., ALONSO, B., SOT, J., GARCIA-ARRIBAS, A. B., GIL-CARTON, D., VALLE, M., ZURUTUZA, A. & GONI, F. M. 2017. Coating Graphene Oxide with Lipid Bilayers Greatly Decreases Its Hemolytic Properties. *Langmuir,* 33**,** 8181-8191.

MONTEIRO-RIVIERE, N. A. & INMAN, A. O. 2006. Challenges for assessing carbon nanomaterial toxicity to the skin. *Carbon,* 44**,** 1070-1078.

MULLER, J., DELOS, M., PANIN, N., RABOLLI, V., HUAUX, F. & LISON, D. 2009. Absence of carcinogenic response to multiwall carbon nanotubes in a 2-year bioassay in the peritoneal cavity of the rat. *Toxicological Sciences,* 110**,** 442-448.

MULLICK CHOWDHURY, S., LALWANI, G., ZHANG, K., YANG, J. Y., NEVILLE, K. & SITHARAMAN, B. 2013. Cell specific cytotoxicity and uptake of graphene nanoribbons. *Biomaterials,* 34**,** 283-293.

MUTHOOSAMY, K., BAI, R. G., ABUBAKAR, I. B., SUDHEER, S. M., LIM, H. N., LOH, H. S., HUANG, N. M., CHIA, C. H. & MANICKAM, S. 2015. Exceedingly biocompatible and thin-layered reduced graphene oxide nanosheets using an eco-

friendly mushroom extract strategy. *International Journal of Nanomedicine,* 10**,** 1505-1519.

MV, B., PM, H. & AS, T. 2005. Tetrazolium dyes as tools in cell biology: New insights into their cellular reduction. *Biotechnology annual review,* 11**,** 127-152.

NAAHIDI, S., JAFARI, M., EDALAT, F., RAYMOND, K., KHADEMHOSSEINI, A. & CHEN, P. 2013. Biocompatibility of engineered nanoparticles for drug delivery. *Journal of Controlled Release,* 166**,** 182-194.

NAMVARI, M. & NAMAZI, H. 2014. Sweet graphene I: toward hydrophilic graphene nanosheets via click grafting alkyne-saccharides onto azide-functionalized graphene oxide. *Carbohydrate Research,* 396**,** 1-8.

NANDA, S. S., PAPAEFTHYMIOU, G. C. & YI, D. K. 2015. Functionalization of Graphene Oxide and its Biomedical Applications. *Critical Reviews in Solid State and Materials Sciences,* 40**,** 291-315.

NASIR, S., HUSSEIN, M. Z., ZAINAL, Z. & YUSOF, N. A. 2018. Carbon-Based Nanomaterials/Allotropes: A Glimpse of Their Synthesis, Properties and Some Applications. *Materials (Basel),* 11:295.

NAYAK, T. R., ANDERSEN, H., MAKAM, V. S., KHAW, C., BAE, S., XU, X., PUI-LAIR.EE, AHN, J.-H., BYUNGHEEHONG, GIORGIAPASTORIN & OZYILMAZ, B. 2011. Graphene for Controlled and Accelerated Osteogenic Differentiation of Human Mesenchymal Stem Cells. *American Chemical Society Nano,* 5**,** 4670-4678.

NEL, A. E., NASSER, E., GODWIN, H., AVERY, D., BAHADORI, T., BERGESON, L., BERYT, E., BONNER, J. C., BOVERHOF, D., CARTER, J., CASTRANOVA, V., DESHAZO, J. R., HUSSAIN, S. M., KANE, A. B., KLAESSIG, F., KUEMPEL, E., LAFRANCONI, M., LANDSIEDEL, R., MALLOY, T., MILLER, M. B., MORRIS, J., MOSS, K., OBERDORSTER, G., PINKERTON, K., PLEUS, R. C., SHATKIN, J. A., THOMAS, R., TOLAYMAT, T., WANG, A. & WONG, J. 2013. A Multi-Stakeholder Perspective on the Use of Alternative Test Strategies for Nanomaterial Safety Assessment. *American Chemical Society Nano,* 7**,** 6422-6433.

NETHRAVATHI, C. & RAJAMATHI, M. 2008. Chemically modified graphene sheets produced by the solvothermal reduction of colloidal dispersions of graphite oxide. *Carbon,* 46**,** 1994-1998.

NITULESCU, G. M., MARGINA, D., JUZENAS, P., PENG, Q., OLARU, O. T., SALOUSTROS, E., FENGA, C., SPANDIDOS, D., LIBRA, M. & TSATSAKIS, A. M. 2016. Akt inhibitors in cancer treatment: The long journey from drug discovery to clinical use (Review). *International Journal of Oncology,* 48**,** 869-885.

NOVOSELOV, K. S., FAL'KO, V. I., COLOMBO, L., GELLERT, P. R., SCHWAB, M. G. & KIM, K. 2012. A roadmap for graphene. *Nature,* 490**,** 192-200.

NOVOSELOV, S., GEIM, K., MOROZOV, V., JIANG, D., ZHANG, Y., DUBONOS, V., GRIGORIEVA, V. & FIRSOV, A. 2004. N Electric field effect in atomically thin carbon films. Science. *Science,* 306, 666-669.

NUSSE, R. & CLEVERS, H. 2017. Wnt/beta-Catenin Signaling, Disease, and Emerging Therapeutic Modalities. *Cell,* 169**,** 985-999.

OBERDORSTER, G., MAYNARD, A., DONALDSON, K., CASTRANOVA, V., FITZPATRICK, J., AUSMAN, K., CARTER, J., KARN, B., KREYLING, W., LAI, D., OLIN, S., MONTEIRO-RIVIERE, N., WARHEIT, D., YANG, H. & GROUP, I. R. F. R. S. I. N. T. S. W. 2005. Principles for characterizing the potential human health effects from exposure to nanomaterials: elements of a screening strategy. *Particle & Fibre Toxicology,* 2:8.

OSAKI M & OSHIMURA M, I. H. 2004. "The PI3K-Akt pathway: Its functions and alterations in human cancer". *Apoptosis,* 6**,** 667-676.

OU, L., LIN, S., SONG, B., LIU, J., LAI, R. & SHAO, L. 2017. The mechanisms of graphene-based materials-induced programmed cell death: a review of apoptosis, autophagy, and programmed necrosis. *International Journal of Nanomedicine,* 12**,** 6633-6646.

OU, L., SONG, B., LIANG, H., LIU, J., FENG, X., DENG, B., SUN, T. & SHAO, L. 2016. Toxicity of graphene-family nanoparticles: a general review of the origins and mechanisms. *Particle & Fibre Toxicology,* 13:57.

PANG, J., BACHMATIUK, A., IBRAHIM, I., FU, L., PLACHA, D., MARTYNKOVA, G. S., TRZEBICKA, B., GEMMING, T., ECKERT, J. & RÜMMELI, M. H. 2015. CVD growth of 1D and 2D sp2 carbon nanomaterials. *Journal of Materials Science,* 51**,** 640-667.

PAPINSKI, D. & KRAFT, C. 2014. Atg1 kinase organizes autophagosome formation by phosphorylating Atg9. *Autophagy,* 10**,** 1338-1340.

PARK, E. J., LEE, G. H., HAN, B. S., LEE, B. S., LEE, S., CHO, M. H., KIM, J. H. & KIM, D. W. 2015a. Toxic response of graphene nanoplatelets in vivo and in vitro. *Archives of Toxicology,* 89**,** 1557-1568.

PARK, S. Y., PARK, J., SIM, S. H., SUNG, M. G., KIM, K. S., HONG, B. H. & HONG, S. 2011. Enhanced differentiation of human neural stem cells into neurons on graphene. *Advanced Materials,* 23**,** 263-267.

PARK, Y. H., PARK, S. Y. & IN, I. 2015b. Direct noncovalent conjugation of folic acid on reduced graphene oxide as anticancer drug carrier. *Journal of Industrial and Engineering Chemistry,* 30**,** 190-196.

PAN, C., KUMAR, C., BOHL, S., KLINGMUELLER, U. & MANN, M. 2009. Comparative proteomic phenotyping of cell lines and primary cells to assess preservation of cell type-specific functions. Molecular & Cellular Proteomics, 8, 443-50.

PATIL, Y. P. & JADHAV, S. 2014. Novel methods for liposome preparation. *Chemistry & Physics of Lipids,* 177**,** 8-18.

PECORINO, L. 2008. *Molecular Biology of Cancer* USA, Oxford University Press Inc.

PEI, S. & CHENG, H.-M. 2012. The reduction of graphene oxide. *Carbon,* 50**,** 3210-3228.

PELIN, M., FUSCO, L., MARTIN, C., SOSA, S., FRONTINAN-RUBIO, J., GONZALEZ-DOMINGUEZ, J. M., DURAN-PRADO, M., VAZQUEZ, E., PRATO, M. & TUBARO, A. 2018. Graphene and graphene oxide induce ROS production in human HaCaT skin keratinocytes: the role of xanthine oxidase and NADH dehydrogenase. *Nanoscale,* 10**,** 11820-11830.

PEÑA-BAHAMONDE, J., SAN MIGUEL, V., NGUYEN, H. N., OZISIK, R., RODRIGUES, D. F. & CABANELAS, J. C. 2017. Functionalization of reduced graphene oxide with polysulfone brushes enhance antibacterial properties and reduce human cytotoxicity. *Carbon,* 111**,** 258-268.

PENG, Q. & MU, H. 2016. The potential of protein-nanomaterial interaction for advanced drug delivery. *Journal of Controlled Release,* 225**,** 121-132.

POILLET-PEREZ, L., DESPOUY, G., DELAGE-MOURROUX, R. & BOYER-GUITTAUT, M. 2015. Interplay between ROS and autophagy in cancer cells, from tumor initiation to cancer therapy. *Redox Biology,* 4**,** 184-192.

POLAND, C. A., DUFFIN, R., KINLOCH, I., MAYNARD, A., WALLACE, W. A., SEATON, A., STONE, V., BROWN, S., MACNEE, W. & DONALDSON, K. 2008.

Carbon nanotubes introduced into the abdominal cavity of mice show asbestos-like pathogenicity in a pilot study. *Nature Nanotechnology,* 3**,** 423-428.

QIAN, J., WANG, D., CAI, F. H., XI, W., PENG, L., ZHU, Z. F., HE, H., HU, M. L. & HE, S. 2012. Observation of multiphoton-induced fluorescence from graphene oxide nanoparticles and applications in in vivo functional bioimaging. *Angewandte Chemie International Edition in English,* 51**,** 10570-10575.

QIN, Y., ZHOU, Z. W., PAN, S. T., HE, Z. X., ZHANG, X., QIU, J. X., DUAN, W., YANG, T. & ZHOU, S. F. 2015. Graphene quantum dots induce apoptosis, autophagy, and inflammatory response via p38 mitogen-activated protein kinase and nuclear factor-kappaB mediated signaling pathways in activated THP-1 macrophages. *Toxicology,* 327**,** 62-76.

RAINGEAUD, J., GUPTA, S., ROGERS, J. S., DICKENS, M., HAN, J., ULEVITCH, R. J. & DAVIS, R. J. 1995. pro-inflammatory cytokines and environmetal stress cause p38 mitogen activated protein kinase activation by dual phosporylation on tyrosine and threonine. *The jornal of biological chemistry,* 270**,** 7420-7426.

RANCAN, F., PAPAKOSTAS, D., HADAM, S., HACKBARTH, S., DELAIR, T., PRIMARD, C., VERRIER, B., STERRY, W., BLUME-PEYTAVI, U. & VOGT, A. 2009. Investigation of Polylactic Acid (PLA) Nanoparticles as Drug Delivery Systems for Local Dermatotherapy. *Pharmaceutical Research,* 26**,** 2027-2036.

RAO, T. P. & KUHL, M. 2010. An updated overview on Wnt signaling pathways: a prelude for more. *Circulation Research,* 106**,** 1798-1806.

RAUTOU, P. E., MANSOURI, A., LEBREC, D., DURAND, F., VALLA, D. & MOREAU, R. 2010. Autophagy in liver diseases. *Journal of Hepatology,* 53**,** 1123-1134.

REBRIN, I. & SOHAL, R. S. 2008. Pro-oxidant shift in glutathione redox state during aging. *Advanced Drug Delivery Reviews,* 60**,** 1545-1552.

REINA, G., GONZALEZ-DOMINGUEZ, J. M., CRIADO, A., VAZQUEZ, E., BIANCO, A. & PRATO, M. 2017. Promises, facts and challenges for graphene in biomedical applications. *Chemical Society Reviews,* 46**,** 4400-4416.

RESHMA, S. C., SYAMA, S. & MOHANAN, P. V. 2016. Nano-biointeractions of PEGylated and bare reduced graphene oxide on lung alveolar epithelial cells: A comparative in vitro study. *Colloids & Surfaces B: Biointerfaces,* 140**,** 104-116.

ROBINSON, J. A., WETHERINGTON, M., TEDESCO, J. L., CAMPBELL, P. M., WENG, X., STITT, J., FANTON, M. A., FRANTZ, E., SNYDER, D., VANMIL, B. L., JERNIGAN, G. G., MYERS-WARD, R. L., CHARLES R. EDDY, J. &

GASKILL, D. K. 2009. Correlating Raman spectral signatures with carrier mobility in epitaxial graphene- a guide to achieving high mobility on the wafer scale. *Nano letters,* 9**,** 2873-2876.

ROBINSON, J. T., TABAKMAN, S. M., LIANG, Y., WANG, H., CASALONGUE, H. S., VINH, D. & DAI, H. 2011. Ultrasmall reduced graphene oxide with high near-infrared absorbance for photothermal therapy. *Journal of The American Chemical Society,* 133**,** 6825-6831.

RODRIGUES, A. F., NEWMAN, L., LOZANO, N., MUKHERJEE, S. P., FADEEL, B., BUSSY, C. & KOSTARELOS, K. 2018. A blueprint for the synthesis and characterisation of thin graphene oxide with controlled lateral dimensions for biomedicine. *2D Materials,* 5.

ROUSE, J., COHEN, P., TRIGON, S., MORANGE, M., ALONSO, A., ZAMANILLO, D., HUNT, T. & NEBREDA, A. R. 1994. A noval kinase cascade triggered by stress and heat shock that stimulates MAPKAP kinase-2 and phosphorylation of the small heat shock proteins. *Cell Press,* 78**,** 1027-1037.

ROY, I., RANA, D., SARKAR, G., BHATTACHARYYA, A., SAHA, N. R., MONDAL, S., PATTANAYAK, S., CHATTOPADHYAY, S. & CHATTOPADHYAY, D. 2015. Physical and electrochemical characterization of reduced graphene oxide/silver nanocomposites synthesized by adopting a green approach. *Royal Society of Chemistry Advances,* 5**,** 25357-25364.

RUSSIER, J., TREOSSI, E., SCARSI, A., PERROZZI, F., DUMORTIER, H., OTTAVIANO, L., MENEGHETTI, M., PALERMO, V. & BIANCO, A. 2013. Evidencing the mask effect of graphene oxide: a comparative study on primary human and murine phagocytic cells. *Nanoscale,* 5**,** 11234-11247.

RUTH SCHERZ-SHOUVAL, ELENA SHVETS, EPHRAIM FASS, HAGAI SHORER, GIL, L. & ELAZAR, Z. 2007. Reactive oxygen species are essential for autophagy and specifically regulate the activity of Atg4. *The European Molecular Biology Organisation Journa,l* 26**,** 1749-1760.

SADIK, O. A., ZHOU, A. L., KIKANDI, S., DU, N., WANG, Q. & VARNER, K. 2009. Sensors as tools for quantitation, nanotoxicity and nanomonitoring assessment of engineered nanomaterials. *Journal of Environmental Monitoring,* 11**,** 1782-1800.

SAHAY, G., ALAKHOVA, D. Y. & KABANOV, A. V. 2010. Endocytosis of nanomedicines. *Journal of Controlled Release,* 145**,** 182-195.

SALAS, E. C., SUN, Z., TTGE, A. L. & TOUR, J. M. 2010. Reduction of Graphene Oxide via Bacterial Respiration. *American Chemical Society Nano,* 4**,** 4852-4856.

SALMENA, L., CARRACEDO, A. & PANDOLFI, P. P. 2008. Tenets of PTEN tumor suppression. *Cell,* 133**,** 403-414.

SANCHEZ, V. C., JACHAK, A., HURT, R. H. & KANE, A. B. 2012. Biological interactions of graphene-family nanomaterials: an interdisciplinary review. *Chemical Research in Toxicology,* 25**,** 15-34.

SANGTANI, A., NAG, O. K., FIELD, L. D., BREGER, J. C. & DELEHANTY, J. B. 2017. Multifunctional nanoparticle composites: progress in the use of soft and hard nanoparticles for drug delivery and imaging. *Wiley Interdisciplinary Reviews: Nanomedicine & Nanobiotechnology,* 9.

SCHERZ-SHOUVAL, R. & ELAZAR, Z. 2011. Regulation of autophagy by ROS: physiology and pathology. *Trends in Biochemical Sciences,* 36**,** 30-8.

SEABRA, A. B., PAULA, A. J., DE LIMA, R., ALVES, O. L. & DURAN, N. 2014. Nanotoxicity of graphene and graphene oxide. *Chemical Research in Toxicology,* 27**,** 159-168.

SHAMAS-DIN, A., KALE, J., LEBER, B. & ANDREWS, D. W. 2013. Mechanisms of action of Bcl-2 family proteins. *Cold Spring Harb Perspectives in Biology,* 5:008714.

SHANG, L., NIENHAUS, K. & NIENHAUS, G. U. 2014. Engineered nanoparticles interacting with cells- size matters. *Journal of nanobiotechnology,* 12**,** 1-11.

SHEN, H., ZHANG, L., LIU, M. & ZHANG, Z. 2012. Biomedical applications of graphene. *Theranostics,* 2**,** 283-294.

SHEN, J., YAN, B., SHI, M., MA, H., LI, N. & YE, M. 2011. One step hydrothermal synthesis of TiO2-reduced graphene oxide sheets. *Journal of Materials Chemistry,* 21, 3415-3421.

SHIBATA, M. T. M. & NIKI, E. 2001. ESTIMATION OF LIPID PEROXIDATION OF LIVE CELLS USING A FLUORESCENT PROBE, DIPHENYL-1-PYRENYLPHOSPHINE. *Free Radical Biology & Medicine,* 31**,** 164-174.

SHIEH, Y.-T., HUANG, B.-R. & TSAI, M.-L. 2015. Graphene Oxide-Assisted Dispersion of Carbon Nanotubes in Sulfonated Chitosan-Modified Electrode for Simultaneous Detections of Sodium Nitrite, Hydroquinone, and Catechol. *Internaltional Journal of Electrochemical Science,* 10**,** 3867-3884.

SINGH, Z. 2016. Applications and toxicity of graphene family nanomaterials and their composites. *Nanotechnology, Science & Applications,* 9**,** 15-28.

SLONCZEWSKI, J. C. & WEISS, P. R. 1958. Band Structure of Graphite. *Physical Review,* 109**,** 272-279.

SMALLEY, R. E. 1991. Great balls of carbon: The story of Buckminsterfullerene. *Sciences,* 31**,** 22–28.

SMITH, S. M., WUNDER, M. B., NORRIS, D. A. & SHELLMAN, Y. G. 2011. A simple protocol for using a LDH-based cytotoxicity assay to assess the effects of death and growth inhibition at the same time. *PLoS One,* 6:26908.

SONG, J., WANG, X. & CHANG, C.-T. 2014. Preparation and Characterization of Graphene Oxide. *Journal of Nanomaterials,* 2014**,** 1-6.

SONG, Y., CHEN, Y., FENG, L., REN, J. & QU, X. 2011. Selective and quantitative cancer cell detection using target-directed functionalized graphene and its synergetic peroxidase-like activity. *Chemical Communications (Cambridge),* 47**,** 4436-4438.

STANKOVICH, S., DIKIN, D. A., PINER, R. D., KOHLHAAS, K. A., KLEINHAMMES, A., JIA, Y., WU, Y., NGUYEN, S. T. & RUOFF, R. S. 2007. Synthesis of graphene-based nanosheets via chemical reduction of exfoliated graphite oxide. *Carbon,* 45**,** 1558-1565.

STONE, V., POZZI-MUCELLI, S., TRAN, L., ASCHBERGER, K., SABELLA, S., VOGEL6, U., POLAND, C., BALHARRY, D., FERNANDES, T., GOTTARDO, S., HANKIN, S., HARTL, M. G., HARTMANN, N., HRISTOZOV, D., HUND-RINKE, K., JOHNSTON, H., MARCOMINI, A., PANZER, O., RONCATO, D., SABER, A. T., WALLIN, H. K. & SCOTT-FORDSMAND, J. J. 2014. ITS-NANO - Prioritising nanosafety research to develop a stakeholder driven intelligent testing strategy. *Particle and Fibre Toxicology,* 11:9.

STOUT, D. A., DURMUS, N. G. & WEBSTER, T. J. 2013. Synthesis of carbon based nanomaterials for tissue engineering applications. *Nanomaterials in Tissue Engineering.*USA, Woodhead Publishing Limitted.

STROJNY, B., KURANTOWICZ, N., SAWOSZ, E., GRODZIK, M., JAWORSKI, S., KUTWIN, M., WIERZBICKI, M., HOTOWY, A., LIPINSKA, L. & CHWALIBOG, A. 2015. Long Term Influence of Carbon Nanoparticles on Health and Liver Status in Rats. *PLoS One,* 10:0144821.

SU, C.-Y., LU, A.-Y., XU, Y., CHEN, F.-R., KHLOBYSTOV, A. N. & LI, L.-J. 2011. High-Quality Thin Graphene Films from Fast Electrochemical Exfoliation. *American Chemical Society Nano,* 5**,** 2332–2339.

SUN, C., WAKEFIELD, D. L., HAN, Y., MULLER, D. A., HOLOWKA, D. A., BAIRD, B. A. & DICHTEL, W. R. 2016. Graphene Oxide Nanosheets Stimulate Ruffling and Shedding of Mammalian Cell Plasma Membranes. *Chem,* 1**,** 273-286.

SUZUKI, H., TOYOOKA, T. & IBUK, Y. 2007. Simple and Easy Method to Evaluate Uptake Potential of Nanoparticles in Mammalian Cells Using a Flow Cytometric Light Scatter Analysis. *Environmental Science and Technology,* 41**,** 3018-3024.

SWATHI, R. S. & SEBASTIAN, K. L. 2009. Long range resonance energy transfer from a dye molecule to graphene has (distance)(-4) dependence. *Journal of Chemical Physics,* 130:086101.

SZABO, T. S., BERKESI, O., FORGO, P. T., JOSEPOVITS, K., SANAKIS, Y., PETRIDIS, D. &´NY, I. D. K. 2006. Evolution of Surface Functional Groups in a Series of Progressively Oxidized Graphite Oxides. *Chemistry of Materials,* 18**,** 2740-2749.

TABISH, T. A., ZHANG, S. & WINYARD, P. G. 2018. Developing the next generation of graphene-based platforms for cancer therapeutics: The potential role of reactive oxygen species. *Redox Biology,* 15**,** 34-40.

TADI, K. K., NARAYANAN, T. N., AREPALLI, S., BANERJEE, K., VISWANATHAN, S., LIEPMANN, D., AJAYAN, P. M. & RENUGOPALAKRISHNAN, V. 2015. Engineered 2D nanomaterials–protein interfaces for efficient sensors. *Journal of Materials Research,* 30**,** 3565-3574.

TAKAHIRO SHINTANI, D. J. K. 2004. Autophagy in Health and Disease: A Double-Edged Sword. *Science,* 306**,** 990-995.

TANG, Z., ZHAO, L., YANG, Z., LIU, Z., GU, J., BAI, B., LIU, J., XU, J. & YANG, H. 2018. Mechanisms of oxidative stress, apoptosis, and autophagy involved in graphene oxide nanomaterial anti-osteosarcoma effect. *International Journal of Nanomedicine,* 13**,** 2907-2919.

TAYLOR, A., WILSON, K. M., MURRAY, P., FERNIG, D. G. & LEVY, R. 2012. Long-term tracking of cells using inorganic nanoparticles as contrast agents: are we there yet? *Chemical Society Reviews,* 41**,** 2707-2717.

THEMA, F. T., MOLOTO, M. J., DIKIO, E. D., NYANGIWE, N. N., KOTSEDI, L., MAAZA, M. & KHENFOUCH, M. 2013. Synthesis and Characterization of

Graphene Thin Films by Chemical Reduction of Exfoliated and Intercalated Graphite Oxide. *Journal of Chemistry,* 2013**,** 1-6.

THOMAS, H. R., VALLÉS, C., YOUNG, R. J., KINLOCH, I. A., WILSON, N. R. & ROURKE, J. P. 2013. Identifying the fluorescence of graphene oxide. *Journal of Materials Chemistry. C,* 1**,** 338-342.

TIWARI, J. N., VIJ, V., KEMP, K. C. & KIM, K. S. 2016. Engineered Carbon-Nanomaterial-Based Electrochemical Sensors for Biomolecules. *American Chemical Society Nano,* 10**,** 46-80.

TIWARI, R. N., ISHIHARA, M., TIWARI, J. N. & YOSHIMURA, M. 2012. Synthesis of graphene film from fullerene rods. *Chemical Communications (Cambridge),* 48**,** 3003-3005.

TODUKA, Y., TOYOOKA, T. & IBUKI, Y. 2012. Flow cytometric evaluation of nanoparticles using side-scattered light and reactive oxygen species-mediated fluorescence-correlation with genotoxicity. *Environmental Science & Technology,* 46**,** 7629-7636.

TONELLI, F. M., GOULART, V. N. A., GOMES, K. N., LADEIRA, M. S., SANTOS, A. K., LORENÇON, E., LADEIRA, L. O. & RESENDE, R. R. 2015. Graphene-based nanomaterials- biological and medical applications and toxicity. *Nanomedicine,* 10**,** 2423-2450.

TRIPATHI, A., SARAF, S. & SARAF, S. 2015. Carbon Nanotropes: A Contemporary Paradigm in Drug Delivery. *Materials,* 8**,** 3068-3100.

TROCOLI, A., BENSADOUN, P., RICHARD, E., LABRUNIE, G., MERHI, F., SCHLAEFLI, A. M., BRIGGER, D., SOUQUERE, S., PIERRON, G., PASQUET, J., SOUBEYRAN, P., REIFFERS, J., SEGAL-BENDIRDJIAN, E., TSCHAN, M. P. & DJAVAHERI-MERGNY, M. 2014. "p62/SQSTM1 upregulation constitutes a survival mechanism that occurs during granulocytic differentiation of acute myeloid leukemia cells". *Cell death and differentiation,* 21**,** 1852-1861.

VANCE, M. E., KUIKEN, T., VEJERANO, E. P., MCGINNIS, S. P., HOCHELLA, M. F., JR., REJESKI, D. & HULL, M. S. 2015. Nanotechnology in the real world: Redeveloping the nanomaterial consumer products inventory. *Beilstein Journal of Nanotechnology,* 6**,** 1769-1780.

VASUDEVAN, K. M., GURUMURTHY, S. & RANGNEKAR, V. M. 2004. Suppression of PTEN Expression by NF- B Prevents Apoptosis. *Molecular and Cellular Biology,* 24**,** 1007-1021.

VERMA, A. & STELLACCI, F. 2010. Effect of surface properties on nanoparticle-cell interactions. *Small,* 6**,** 12-21.

VERMES, I., HAANEN, C., STEFFENS-NAKKEN, H. & REUTELINGSPERGER, C. 1995. A novel assay for apoptosis "Flow cytometric detection of phosphatidylserine expression on early apoptotic cells using fluorescein labelled Annexin V". *Journal of Immunological Methods,* 184**,** 39-51.

VILA, M., PORTOLES, M. T., MARQUES, P. A., FEITO, M. J., MATESANZ, M. C., RAMIREZ-SANTILLAN, C., GONCALVES, G., CRUZ, S. M., NIETO, A. & VALLET-REGI, M. 2012. Cell uptake survey of pegylated nanographene oxide. *Nanotechnology,* 23:465103.

VRANIC, S. & KOSTARELOS, K. 2017. High-Accuracy Determination of Cytotoxic Responses from Graphene Oxide Exposure Using Imaging Flow Cytometry. *Biomedical Nanotechnology: Methods in Molecular Biology,* 1570**,** 287-300.

VRANIC, S., RODRIGUES, A. F., BUGGIO, M., NEWMAN, L., WHITE, M. R. H., SPILLER, D. G., BUSSY, C. & KOSTARELOS, K. 2018. Live Imaging of Label-Free Graphene Oxide Reveals Critical Factors Causing Oxidative-Stress-Mediated Cellular Responses. *American Chemical Society Nano,* 12**,** 1373-1389.

WAN, B., WANG, Z. X., LV, Q. Y., DONG, P. X., ZHAO, L. X., YANG, Y. & GUO, L. H. 2013. Single-walled carbon nanotubes and graphene oxides induce autophagosome accumulation and lysosome impairment in primarily cultured murine peritoneal macrophages. *Toxicology Letters,* 221**,** 118-127.

WANG, A., PU, K., DONG, B., LIU, Y., ZHANG, L., ZHANG, Z., DUAN, W. & ZHU, Y. 2013. Role of surface charge and oxidative stress in cytotoxicity and genotoxicity of graphene oxide towards human lung fibroblast cells. *Journal of Applied Toxicology,* 33**,** 1156-1164.

WANG, D., ZHU, L., CHEN, J. F. & DAI, L. 2015a. Can graphene quantum dots cause DNA damage in cells? *Nanoscale,* 7**,** 9894-9901.

WANG, J., YU, Y., LU, K., YANG, M., LI, Y., ZHOU, X. & SUN, Z. 2017a. Silica nanoparticles induce autophagy dysfunction via lysosomal impairment and inhibition of autophagosome degradation in hepatocytes. *International Journal of Nanomedicine,* 12**,** 809-825.

WANG, J., ZHANG, H., HUNT, M. R., CHARLES, A., TANG, J., BRETCANU, O., WALKER, D., HASSAN, K. T., SUN, Y. & SILLER, L. 2017b. Synthesis and

Characterisation of Reduced Graphene Oxide/Bismuth Composite for Electrodes in Electrochemical Energy Storage Devices. *ChemSusChem,* 10**,** 363-371.

WANG, K., RUAN, J., SONG, H., ZHANG, J., WO, Y., GUO, S. & CUI, D. 2011. Biocompatibility of Graphene Oxide. *Nanoscale Research Letters,* 6:8.

WANG, X., LIU, L. H., RAMSTROM, O. & YAN, M. 2009. Engineering nanomaterial surfaces for biomedical applications. *Experimental Biology & Medicine (Maywood),* 234**,** 1128-1139.

WANG, X., WEN, X., LIU, Z., TAN, Y., YUAN, Y. & ZHANG, P. 2012. Rapid and efficient synthesis of soluble graphene nanosheets using N-methyl-p-aminophenol sulfate as a reducing agent. *Nanotechnology,* 23:485604.

WANG, Y., SANTOS, A., EVDOKIOU, A. & LOSIC, D. 2015b. An overview of nanotoxicity and nanomedicine research: principles, progress and implications for cancer therapy. *Journal of Materials Chemistry B,* 3**,** 7153-7172.

WANG, Y. X. 2015. Current status of superparamagnetic iron oxide contrast agents for liver magnetic resonance imaging. *World Journal of Gastroenterology,* 21**,** 13400-13402.

WATANABE, R., WEI, L. & HUANG, J. 2011. mTOR signaling, function, novel inhibitors, and therapeutic targets. *Journal of Nuclear Medicine,* 52**,** 497-500.

WEI, X. Q., HAO, L. Y., SHAO, X. R., ZHANG, Q., JIA, X. Q., ZHANG, Z. R., LIN, Y. F. & PENG, Q. 2015. Insight into the Interaction of Graphene Oxide with Serum Proteins and the Impact of the Degree of Reduction and Concentration. *American chemical Society Applied Materials & Interfaces,* 7**,** 13367-13374.

WEIKEL, K. A., CACICEDO, J. M., RUDERMAN, N. B. & IDO, Y. 2016. Knockdown of GSK3beta increases basal autophagy and AMPK signalling in nutrient-laden human aortic endothelial cells. *Bioscience Reports,* 36:00382.

WELSHER, K., LIU, Z., SHERLOCK, S. P., ROBINSON, J. T., CHEN, Z., DARANCIANG, D. & DAI, H. 2009. A route to brightly fluorescent carbon nanotubes for near-infrared imaging in mice. *Nature Nanotechnology,* 4**,** 773-780.

WEST, K. A., CASTILLO, S. S. & DENNIS, P. A. 2002. Activation of the PI3K:Akt pathway and chemotherapeutic resistance. *Drug Resistance Updates,* 5**,** 234-248.

WHITE, J. C. & XING, B. 2016. Environmental Nanotoxicology. *Environmental Science & Technology,* 50**,** 5423.

WICK, P., LOUW-GAUME, A. E., KUCKI, M., KRUG, H. F., KOSTARELOS, K., FADEEL, B., DAWSON, K. A., SALVATI, A., VAZQUEZ, E., BALLERINI, L., TRETIACH, M., BENFENATI, F., FLAHAUT, E., GAUTHIER, L., PRATO, M.

& BIANCO, A. 2014. Classification framework for graphene-based materials. *Angewandte Chemie International Edition in English,* 53**,** 7714-7718.

WU, J., DANG, Y., SU, W., LIU, C., MA, H., SHAN, Y., PEI, Y., WAN, B., GUO, J. & YU, L. 2006. Molecular cloning and characterization of rat LC3A and LC3B--two novel markers of autophagosome. *Biochemical & Biophysical Research Communications,* 339**,** 437-442.

WU, S. Y., AN, S. S. & HULME, J. 2015. Current applications of graphene oxide in nanomedicine. *International Journal of Nanomedicine,* 10 **,** 9-24.

WU, X., XING, Y., ZENG, K., HUBER, K. & ZHAO, J. X. 2018. Study of Fluorescence Quenching Ability of Graphene Oxide with a Layer of Rigid and Tunable Silica Spacer. *Langmuir,* 34**,** 603-611.

XIE, L., LING, X., FANG, Y., ZHANG, J. & LIU, Z. 2009. Graphene as a substrate to suppress fluorescence in resonance Raman spectroscopy. *Journal of The American Chemical Society*, 131**,** 9890-9891.

XIE, X., LIAO, J., SHAO, X., LI, Q. & LIN, Y. 2017. The Effect of shape on Cellular Uptake of Gold Nanoparticles in the forms of Stars, Rods, and Triangles. *Scientific Reports,* 7**,** 3827.

XU, J., WANG, J., NIU, L., ZHANG, J., JU, C., NAN, X. & FENG, C. 2015. Effect of Particle Size on Dispersibility of Antimony Nanoparticles in Lubricating Oil. *Synthesis and Reactivity in Inorganic, Metal-Organic, and Nano-Metal Chemistry,* 46**,** 477-482.

YAN, L., WANG, Y., XU, X., ZENG, C., HOU, J., LIN, M., XU, J., SUN, F., HUANG, X., DAI, L., LU, F. & LIU, Y. 2012. Can graphene oxide cause damage to eyesight? *Chemical Research in Toxicology,* 25**,** 1265-1270.

YÁÑEZ-SEDEÑO, P., CAMPUZANO, S. & PINGARRÓN, J. 2017. Carbon Nanostructures for Tagging in Electrochemical Biosensing: A Review. *Journal of Carbon Research,* 3:3.

YANG, C., HUANG, X., LIU, H., XIAO, F., WEI, J., YOU, L. & QIAN, W. 2017a. PDK1 inhibitor GSK2334470 exerts antitumor activity in multiple myeloma and forms a novel multitargeted combination with dual mTORC1:C2 inhibitor PP242. *Oncotarget,* 8**,** 39185-39197.

YANG, D., FENG, L., DOUGHERTY, C. A., LUKER, K. E., CHEN, D., CAUBLE, M. A., BANASZAK HOLL, M. M., LUKER, G. D., ROSS, B. D., LIU, Z. & HONG, H.

2016. In vivo targeting of metastatic breast cancer via tumor vasculature-specific nano-graphene oxide. *Biomaterials,* 104**,** 361-371.

YANG, H. W., LU, Y. J., LIN, K. J., HSU, S. C., HUANG, C. Y., SHE, S. H., LIU, H. L., LIN, C. W., XIAO, M. C., WEY, S. P., CHEN, P. Y., YEN, T. C., WEI, K. C. & MA, C. C. 2013a. EGRF conjugated PEGylated nanographene oxide for targeted chemotherapy and photothermal therapy. *Biomaterials,* 34**,** 7204-7214.

YANG, K., GONG, H., SHI, X., WAN, J., ZHANG, Y. & LIU, Z. 2013b. In vivo biodistribution and toxicology of functionalized nano-graphene oxide in mice after oral and intraperitoneal administration. *Biomaterials,* 34**,** 2787-2795.

YANG, S., LUO, S., LIU, C. & WEI, W. 2012a. Direct synthesis of graphene-chitosan composite and its application as an enzymeless methyl parathion sensor. *Colloids & Surfaces B: Biointerfaces,* 96**,** 75-79.

YANG, X., NIU, G., CAO, X., WEN, Y., XIANG, R., DUAN, H. & CHEN, Y. 2012b. The preparation of functionalized graphene oxide for targeted intracellular delivery of siRNA. *Journal of Materials Chemistry,* 22, 6649-6654.

YANG, Y., QIN, Z., ZENG, W., YANG, T., CAO, Y., MEI, C. & KUANG, Y. 2017b. Toxicity assessment of nanoparticles in various systems and organs. *Nanotechnology Reviews,* 6, 279-289.

YILDIRIMER, L., THANH, N. T., LOIZIDOU, M. & SEIFALIAN, A. M. 2011. Toxicology and clinical potential of nanoparticles. *Nano Today,* 6**,** 585-607.

YONGBIN ZHANG, SYED F. ALI, ENKELEDA DERVISHI, YANG XU, ZHONGRUI LI, DANIEL CASCIANO & BIRIS, A. S. 2010. Cytotoxicity Effects of Graphene and Single-Wall Carbon Nanotubes in Neural Phaeochromocytoma-Derived PC12 Cells. *American Chemical Society Nano,* 4**,** 3181-3186.

YOON, Y. H., CHO, K. S., HWANG, J. J., LEE, S. J., CHOI, J. A. & KOH, J. Y. 2010. Induction of lysosomal dilatation, arrested autophagy, and cell death by chloroquine in cultured ARPE-19 cells. *Investigative Ophthalmology & Visual Science,* 51**,** 6030-6037.

YUE, H., WEI, W., YUE, Z., WANG, B., LUO, N., GAO, Y., MA, D., MA, G. & SU, Z. 2012. The role of the lateral dimension of graphene oxide in the regulation of cellular responses. *Biomaterials,* 33**,** 4013-4021.

YUE, Z. G., WEI, W., LV, P. P., YUE, H., WANG, L. Y., SU, Z. G. & MA, G. H. 2011. Surface charge affects cellular uptake and intracellular trafficking of chitosan-based nanoparticles. *Biomacromolecules,* 12**,** 2440-2446.

ZHANG, B., WEI, P., ZHOU, Z. & WEI, T. 2016. Interactions of graphene with mammalian cells: Molecular mechanisms and biomedical insights. *Advanced Drug Delivery Reviews,* 105**,** 145-162.

ZHANG, L., XIA, J., ZHAO, Q., LIU, L. & ZHANG, Z. 2010. Functional graphene oxide as a nanocarrier for controlled loading and targeted delivery of mixed anticancer drugs. *Small,* 6**,** 537-544.

ZHANG, M., ZHOU, N., YUAN, P., SU, Y., SHAO, M. & CHI, C. 2017a. Graphene oxide and adenosine triphosphate as a source for functionalized carbon dots with applications in pH-triggered drug delivery and cell imaging. *Royal Society of Chemistry Advances,* 7**,** 9284-9293.

ZHANG, Q., WU, Z., LI, N., PU, Y., WANG, B., ZHANG, T. & TAO, J. 2017b. Advanced review of graphene-based nanomaterials in drug delivery systems: Synthesis, modification, toxicity and application. *Materials Science & Engineering C-Materials for Biological Applications,* 77**,** 1363-1375.

ZHANG, T.-X., ZHU, G.-Y., LU, B.-Y. & PENG, C.-L. Z. Q. 2017c. Concentration-dependent protein adsorption at the nano–bio interfaces of polymeric nanoparticles and serum proteins. *Nanomedicine,* 22**,** 2757–2769.

ZHANG, W., GUO, Z., HUANG, D., LIU, Z., GUO, X. & ZHONG, H. 2011. Synergistic effect of chemo-photothermal therapy using PEGylated graphene oxide. *Biomaterials,* 32**,** 8555-8561.

ZHANG, X., HU, W., LI, J., TAO, L. & WEI, Y. 2012a. A comparative study of cellular uptake and cytotoxicity of multi-walled carbon nanotubes, graphene oxide, and nanodiamond. *Toxicology Research,* 1, 62-68.

ZHANG, Y., TEKOBO, S., TU, Y., ZHOU, Q., JIN, X., DERGUNOV, S. A., PINKHASSIK, E. & YAN, B. 2012b. Permission to enter cell by shape: nanodisk vs nanosphere. *American Chemical Society Applied Materials & Interfaces,* 4**,** 4099-4105.

ZHAO, J., LU, H., WONG, S., LU, M., XIAO, P. & STENZEL, M. H. 2017. Influence of nanoparticle shapes on cellular uptake of paclitaxel loaded nanoparticles in 2D and 3D cancer models. *Polymer Chemistry,* 8**,** 3317-3326.

ZHOU, K., ZHU, Y., YANG, X., JIANG, X. & LI, C. 2011. Preparation of graphene–TiO2composites with enhanced photocatalytic activity. *New Journal of Chemistry.,* 35**,** 353-359.

ZHOU, T., ZHANG, B., WEI, P., DU, Y., ZHOU, H., YU, M., YAN, L., ZHANG, W., NIE, G., CHEN, C., TU, Y. & WEI, T. 2014. Energy metabolism analysis reveals the mechanism of inhibition of breast cancer cell metastasis by PEG-modified graphene oxide nanosheets. *Biomaterials,* 35**,** 9833-9843.

ZHOU, X., TAN, B., ZHENG, X., KONG, D. & LI, Q. 2015. Interfacial electron transfer of glucose oxidase on poly(glutamic acid)-modified glassy carbon electrode and glucose sensing. *Analytical Biochemistry,* 489**,** 9-16.

ZHOU, Y., BAO, Q., TANG, L. A. L., ZHONG, Y. & LOH, K. P. 2009. Hydrothermal Dehydration for the "Green" Reduction of Exfoliated Graphene Oxide to Graphene and Demonstration of Tunable Optical Limiting Properties. *Chemistry of Materials,* 21**,** 2950-2956.

ZHU, C., GUO, S., FANGA, Y. & DONG, S. 2010a. Reducing Sugar- New Functional Molecules for the Green Synthesis of Graphene Nanosheets. *American Chemical Society Nano,* 4**,** 2429-2437.

ZHU, Y., JAMES, D. K. & TOUR, J. M. 2012. New routes to graphene, graphene oxide and their related applications. *Advanced Materials,* 24**,** 4924-4955.

ZHU, Y., MURALI, S., CAI, W., LI, X., SUK, J. W., POTTS, J. R. & RUOFF, R. S. 2010b. Graphene and graphene oxide: synthesis, properties, and applications. *Advanced Materials,* 22**,** 3906-3924.

ZHU, Z., YANG, R., YOU, M., ZHANG, X., WU, Y. & TAN, W. 2010c. Single-walled carbon nanotube as an effective quencher. *Analytical & Bioanalytical Chemistry,* 396**,** 73-83.

ZÓLYOMI, V., KOLTAI, J. & KÜRTI, J. 2011. Resonance Raman spectroscopy of graphite and graphene. *Physica Status Solidi (b),* 248**,** 2435-2444.